Hyperon production in Cabibbo suppressed reactions induced by antineutrinos in nucleons and nuclei

UNIVERSIDAD
DE GRANADA

María Benítez Galán

TESIS DOCTORAL

Programa de Doctorado en Física y Matemáticas

March 13, 2024

Dirigido por: Ignacio Luis Ruiz Simó

Departamento de Física Atómica, Molecular y Nuclear

Facultad de Ciencias

Universidad de Granada

Editor: Universidad de Granada. Tesis Doctorales
Autor: María Benítez Galán
ISBN: 978-84-1195-372-6
URI: https://hdl.handle.net/10481/92925

"Lo esencial es invisible a los ojos."
Antoine de Saint-Exupéry, *El Principito*

Agradecimientos

Antes que nada, quiero dedicar unas palabras a la experiencia de pasar más de cuatro años en Granada, donde he tenido la oportunidad de sumergirme en el fascinante mundo de los neutrinos y los hiperones. Esta ciudad se ha convertido en mucho más que un lugar de trabajo y estudio; se ha convertido en casa. Agradezco profundamente el privilegio de haber vivido esta etapa de mi vida aquí.

Primero quiero comenzar expresando mi agradecimiento a mi director de tesis, Nacho, por su guía y apoyo durante estos años. Por tus pacientes explicaciones, tus consejos y dedicación, todo ello ha sido clave para el desarrollo de esta tesis. Ser tu primera estudiante de doctorado ha sido, es y será un verdadero placer.

Por otro lado quiero expresar mi más sincero agradecimiento a mis colaboradores. A Manolo y Luis, quienes me acogieron durante mis estancias en el IFIC, en Valencia. Les agradezco profundamente por su generosidad, orientación y las interesantísimas conversaciones que tuvimos con las que tanto he aprendido. Y a Rafi, nuestro estimado colaborador en la India, I would like to extend my heartfelt gratitude for your invaluable assistance since the beginning of my thesis.

También quiero agradecer a esas personas del departamento que durante estos cuatro años hemos compartido más de un café, agradezco cada consejo recibido. Un agradecimiento especial a Enrique, Quique, Pablo, María y Paloma, quien me ha enseñado todo lo que había que saber de Grana'.

No quiero dejar de agradecer a las personas que hicieron mis estancias en Valencia una experiencia inolvidable. Agradezco enormemente a Eulogio, Juan, Raquel, Miguel, Albert, Melahat y Amador, así como a mis compañeros de comidas y despacho durante esas estancias Gustavo, Víctor, los Fer y Neus.

Quiero expresar mi agradecimiento a todas las personas que me han acompañado durante estos años, brindándome su ánimo y apoyo. En especial, quiero agradecer al "neutron team" por las cenas compartidas donde hemos transitado juntos nuestros caminos doctorales. A Murias, Montes, Raúl, Jen, Carlos y Adri, gracias.

Para ir terminando quiero agradecerle a mi familia, por su apoyo y paciencia constante. A mis padres, mi hermano y a mi croquetilla peluda, por empujarme siempre ha cumplir mis sueños y no dejarme tirar la toalla. En especial a mi madre que escucha siempre mis explicaciones ambiguas sobre esos antineutrinos que reaccionan y producen esos hiperones. Y a mi hermano, Eddie, por nuestra busqueda incesante del positrino.

Y para finalizar, quiero agradecer a Adri, mi Drian, por ser la compañia perfecta en este camino. Por tener siempre las palabras de ánimo que necesito y aún así ser la voz de la razón y la lógica. Es una fortuna tenerte conmigo.

A todos ellos, gracias de corazón.

Resumen

En esta tesis, investigamos la producción de hiperones Λ y Σ suprimida Cabibbo inducidas por antineutrinos muónicos a través de corrientes débiles cargadas con cambio de extrañeza. En nuestro modelo consideramos el mecanismo cuasielástico (QE) y un mecanismo inelástico en el cual el hiperón se produce junto a un pion ($Y\pi$). Ambos mecanismos han sido estudiados anteriormente pero en el caso de la producción $Y\pi$ solo a partir de nucleones libres. Por lo que estudiamos la producción $Y\pi$ tanto a partir de nucleones libres como en núcleos, enfocándonos en la región de energía de antineutrinos $E_{\bar{\nu}} < 2$ GeV, relevante para numerosos experimentos de dispersión y oscilación de neutrinos. Incluiremos en nuestro estudio las interacciones de estado final (FSI) de los hiperones en su salida del núcleo.

Los estudios teóricos de las secciones eficaces de las interacciones antineutrino-núcleo son esenciales para analizar datos de experimentos de dispersión y oscilación de neutrinos. Un componente clave de estas secciones eficaces es el modelo primario de interacción antineutrino-nucleón. Por lo tanto, comenzamos esta tesis estudiando reacciones de producción $Y\pi$ a partir de nucleones libres. Nuestro modelo se basa en los Lagrangianos quirales SU(3) efectivos de orden más bajo en presencia de una corriente débil cargada externa y contiene los términos de background o Born y el mecanismo de excitación de resonancias bariónicas del decuplete que pueden contribuir a estos canales de reacción. Hemos considerado relevantes las resonancias $\Delta(1232)$ y $\Sigma^*(1385)$.

Continuamos con el estudio de la producción de hiperones en núcleos. La producción de hiperones en este rango de energía procede principalmente a través de la dispersión QE, por lo que hemos considerado este tipo de reacción, además de la producción $Y\pi$. Los efectos nucleares los incluimos estudiando el movimiento de Fermi de los nucleones del blanco nuclear mediante el modelo de gas de Fermi con la aproximación de densidad local. Comparamos dos versiones de la interacción de estado final experimentada por los hiperones en el núcleo. Una utiliza un enfoque más simple, mientras que la otra tiene en cuenta el potencial de la Lambda debido a la limitada información experimental disponible sobre el potencial de la Sigma.

La FSI la consideramos mediante una cascada intranuclear Monte Carlo. También estimamos la absorción de piones, producidos en el mecanismo $Y\pi$, por el núcleo utilizando una aproximación eikonal.

A partir de nucleones libres, encontramos que la resonancia $\Sigma^*(1385)$ predomina notablemente en las reacciones $\Lambda\pi$ pero tiene menos importancia en los canales $\Sigma\pi$. Además, observamos la importancia de los diagramas cruzados de Δ o polos de nucleón cruzado, especialmente en algunas de las reacciones $\Sigma\pi$. También estudiamos las secciones eficaces totales convolucionadas con los flujos de antineutrinos de experimentos pasados (MiniBooNE, SciBooNE) y actuales (detectores cercanos y lejanos de T2K, Minerva) de oscilación y dispersión de neutrinos. Igualmente comparamos y discutimos nuestros resultados con otros que siguen enfoques similares y muy diferentes de la literatura reciente y pasada.

Mostramos los resultados para la producción de hiperones a partir de núcleos. La producción $Y\pi$ tiene un umbral de producción más alto en comparación con los mecanismos QE. Sin embargo, observamos que sus secciones eficaces muestran un crecimiento más rápido con la energía del antineutrino en comparación con la dispersión QE. Comprobamos que los canales $Y\pi$ desempeñan un papel significativo en la caracterización de la producción de hiperones dentro de los núcleos. Específicamente, contribuyen de manera significativa a la producción de Σ^+ y generan una parte sustancial de la sección eficaz total en otros canales: confirmamos que debido al porcentaje de absorción de piones por el núcleo, mayor a bajas energías del antineutrino, los mecanismos podrían confundirse experimentalmente entre sí. No tener en cuenta estos mecanismos introduciría sesgos en el análisis experimental y la interpretación de los resultados. En este contexto, determinamos que las distribuciones de ángulos relativos leptón-hiperón sirven como observables útiles para distinguir entre procesos QE y $Y\pi$. Por lo que, consideramos necesaria la inclusión de la producción $Y\pi$ en los generadores Monte Carlo de eventos de neutrinos, como GENIE o NuWro.

Finalmente, estudiamos la producción de Λ en argón en las condiciones de la reciente medida de MicroBooNE. Convolucionamos nuestras secciones eficaces con el flujo de antineutrinos e imponemos la restricción en el espacio fásico adecuada. Obtenemos resultados consistentes con el valor experimental de baja estadística y observamos que el mecanismo $\Lambda\pi$ representa un tercio de la sección eficaz total. Asimismo, obtenemos resultados para la producción de hiperones convolucionando las secciones eficaces con el flujo de antineutrinos del experimento SBND. Nos llevan a confirmar la importancia del mecanismo $Y\pi$ debido a la posibilidad de confundir ambos mecanismos al producirse absorción de piones por el núcleo. Y en el caso de producción de Σ^+, el mecanismo $\Sigma^+\pi$ sería el predominante al no producirse de manera primaria a través de la producción QE.

Abstract

In this thesis, we study the Cabibbo suppressed hyperon (Λ and Σ) production induced by muonic antineutrinos in strangeness changing weak charged currents interactions. Our model considers the quasielastic mechanism (QE) and an inelastic mechanism in which the hyperon is produced alongside a pion ($Y\pi$). Both mechanisms have been previously studied, but $Y\pi$ production has only been examined from free nucleons. Therefore, we explore $Y\pi$ production both from free nucleons and within nuclei, focusing on the antineutrino energy region $E_{\bar{\nu}} < 2$ GeV, which is relevant for numerous neutrino scattering and oscillation experiments. We also include in our study the final state interactions (FSI) of hyperons as they exit the nucleus.

Theoretical studies of the cross sections for antineutrino-nucleus interactions are crucial for analyzing data from neutrino scattering and oscillation experiments. A crucial component of these cross sections is the primary antineutrino-nucleon interaction model. Therefore, we initiate this thesis by investigating $Y\pi$ production reactions from free nucleons. Our model is based on the lowest order effective SU(3) chiral Lagrangians in the presence of an external weak charged current. It contains Born background terms and the lowest-lying decuplet resonant mechanism that can contribute to these reaction channels. We include the resonances $\Delta(1232)$ and $\Sigma^*(1385)$.

We continue with the study of hyperon production in nuclei. The hyperon production in this energy range primarily proceeds through quasielastic scattering (QE). Therefore, we have considered this type of reaction in addition to the $Y\pi$ production. Nuclear effects are accounted for by studying the Fermi motion of target nucleons using the Fermi gas model with the local density approximation. We compare two versions of the final state interaction experienced by hyperons in the nucleus. One employs a simpler approach, while the other takes into account the potential of the Lambda due to limited experimental information on the Sigma potential. Final state interactions are considered through an intranuclear Monte Carlo cascade. Additionally, we estimate the absorption of pions produced in the $Y\pi$ mechanism by the nucleus using an eikonal approximation.

From the results for the $Y\pi$ mechanism from free nucleons, we find that the $\Sigma^*(1385)$ resonance notably predominates in $\Lambda\pi$ reactions but is less important in $\Sigma\pi$ channels. Additionally, we observe the significance of crossed Δ or nucleon-pole diagrams, especially in some of the $\Sigma\pi$ reactions. We also calculate the total cross sections convoluted with the antineutrino fluxes from past experiments (MiniBooNE, SciBooNE) and current ones (T2K at near and far detectors, Minerva) for neutrino oscillation and scattering. Furthermore, we compare and discuss our results with others that employ similar and different approaches from both recent and past literature.

We study hyperon production from nuclei, where the predominant process at the antineutrino energies we are working with is quasielastic production. The $Y\pi$ production has a higher production threshold compared to QE mechanisms. However, we observe that its cross sections exhibit a faster growth with antineutrino energy compared to QE scattering. We verify that $Y\pi$ channels play a significant role in characterizing hyperon production within nuclei. Specifically, they contribute significantly to the production of Σ^+ and generate a substantial portion of the total cross section in other channels: we confirm that, due to the higher percentage of pion absorption by the nucleus at low antineutrino energies, these mechanisms could be experimentally confused with each other. Neglecting these mechanisms would introduce biases in the experimental analysis and result interpretation. In this context, we determine that relative lepton-hyperon angle distributions serve as useful observables to distinguish between QE and $Y\pi$ processes. Therefore, we consider necessary to include $Y\pi$ production in Monte Carlo neutrino event generators such as GENIE or NuWro.

Finally, we investigate the production of Λ in argon under the conditions of the recent MicroBooNE measurement. We convolute our cross sections with the antineutrino flux and impose the appropriate phase space restriction. We obtain results consistent with the low-statistics experimental value and observe that the $\Lambda\pi$ mechanism accounts for one-third of the total cross section. Additionally, we obtain results for hyperon production by convoluting the cross sections with the antineutrino flux from the SBND experiment. These results confirm the importance of the $Y\pi$ mechanism due to the potential confusion between both mechanisms caused by pion absorption by the nucleus. In the case of Σ^+ production, the $\Sigma^+\pi$ mechanism would be predominant, as it does not occur primarily through QE production.

Contents

Chapter 1

Introduction

1.1 Neutrino in history

The understanding and development of neutrino physics have been amazing and full of surprises since the "birth" of the neutrino. Today, neutrinos continue to challenge our expectations. Let's take a look at some of the key events in their history.

In 1930, Wolfgang Pauli proposed the idea of the neutrino, originally called "neutron", as a neutral, weakly interacting, spin 1/2 particle. Pauli suggested the existence of the neutrino to explain the problem of energy conservation in beta decay [1]. Three years after, Enrico Fermi, who popularized the term "neutrino", proposed a theory that included Pauli's hypothesized particle, his theory later referred as the theory of the weak interaction [2, 3]. In 1935, Maria Goeppert Mayer predicted a special kind of radioactive decay called double beta decay [4], a phenomenon that is nowadays much studied. Ettore Majorana, in 1937, also theorized that neutrinos could potentially be their own antiparticles [5]. Even today, the nature of the neutrino remains unknown - is it his own antiparticle or is it a Dirac particle?

However, the neutrino was extremely challenging to detect due to its weak interaction with matter. Several decades passed before a successful experiment to detect the neutrino was carried out. The difficulty of experimentally studying neutrino interactions with matter led Pauli to claim "I did a terrible thing, which no theorist should do, I postulated a particle that can not be detected". It was not until 1956, over 25 years later, that Frederick Reines and Clyde Cowan were able to observe neutrinos in the first reactor-neutrino experiment at Los Alamos National Laboratory [6] and sent a telegram to Pauli announcing their discovery "We are happy to inform you that we have definitely detected neutrinos....". The neutrino is still referred to as a "ghostly" particle today.

A year after the discovery, Pontecorvo in a paper published in the Soviet Journal of Physics in 1959, in which he proposed that neutrinos could appear in different classes, according to a new property, which he called flavor [7]. He proposed the existence of electron neutrinos (associated electron) and muon neutrinos (associated with the muon). He also prediced the supernova neutrinos. In the same year, Richard Feynman and Murray Gell-Mann formulated the V-A theory of weak interactions [8]. A few years later, in 1962, Lederman, Schwartz and Steinberger discovered a new flavor of neutrino related to the muon [9]. The third flavor of neutrino, the tau neutrino, was postulated after the detection the charged tau lepton, in 1975. The first detection of this neutrino flavor was by the DONUT collaboration in 2000 at Fermilab [10].

With the discovery of the tau lepton in 1975 and various hadrons with heavy quark contents like the charm (c), beauty (b), and top (t) quarks and analyses of their weak decays, the V-A theory of weak interactions was reformulated in terms of leptons and quarks using the concept of quark mixing proposed by Cabibbo [11] and extended by Kobayashi and Maskawa [12], described in terms of the Cabibbo-Kobayashi-Maskawa (CKM) matrix. Experimental analyses of various weak interaction processes were performed using the phenomenological V-A theory.

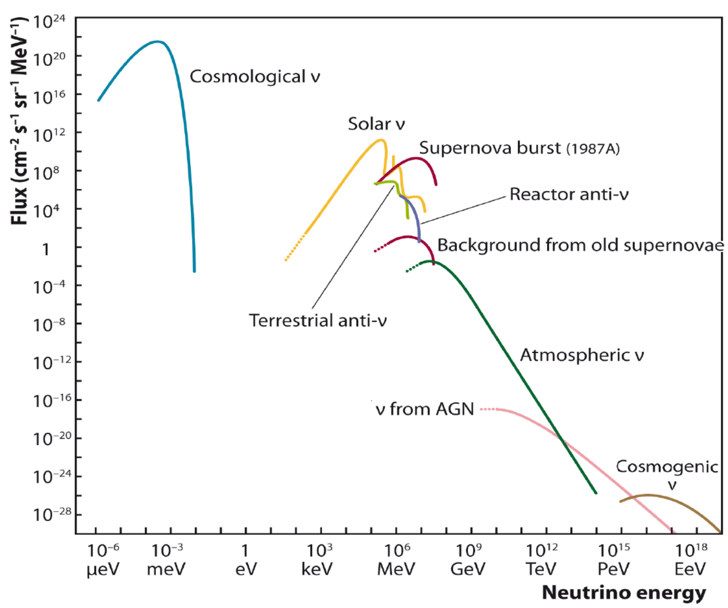

Figure 1.1: Flux of neutrinos from various sources as a function of their energies [13]

In 1967, Glashow, Weinberg and Salam formulated the Standard model (SM) that incorporates the Higgs mechanism (P.W.Higgs, 1964). In 1968, Brookhaven National Laboratory detected electron neutrinos produced by the sun, known as solar neutrinos [14]. In 1985, Kamiokande and the IMB collaborations detected atmospheric neutrinos. An anomaly was observed between the number of neutrinos detected and those expected in both detections. As predicted by Pontecorvo, the Kamiokande and IMB collaborations also detected neutrinos emitted by Supernova 1987A in 1987, making the first recorded observation of supernova neutrinos [15]. In 1998, the Super-Kamiokande collaboration announced the first evidence of neutrino oscillations [16], indicating that neutrinos must have mass. In 2002, Sudbury Neutrino Observatory (SNO) confirmed neutrino oscillations using solar neutrinos [17], and two years later, KamLAND provided evidence of antineutrino oscillation [18]. In the last decades, the neutrinoless double-beta decay experiments like GERDA [19], SNO+ [20], NEXT [21] and nEXO [22] are searching for the detection of this process in order to classify the neutrino as a Majorana or Dirac particle.

Currently, various collaborations are working to measure the parameters of the Pontecorvo-Maki-Nakagawa-Sakata (PMNS) matrix with greater precision including the mixing angles and the CP violation phase [23]. It is now well established that neutrinos are massive particles. Although the Standard Model can explain most electroweak processes, the neutrino oscillation, CP-violation, and the absence of flavor-changing neutral currents (FCNC) open new possibilities for physics beyond the standard model [24]. The search for sterile neutrinos, hypothetical particles that do not interact through the known forces and could potentially explain certain unexplained experimental observations, is also an ongoing field of research. Neutrino interactions with matter provide opportunities for research in a wide range of fields, from astrophysics and cosmology to multimessenger astronomy and the study of the baryonic matter-antimatter asymmetry. There are neutrino experiments aiming to study the neutrino cosmic background radiation, which are neutrinos that were generated in the early stages of the universe and are still propagating [25]. Neutrinos coming from astrophysical events such as supernovae, neutron stars, and black holes are also being investigated to gather information about the physical processes in these extreme environments . Even neutrinos have been proposed as potential candidates to explain dark matter and dark energy in the universe [26]. In hadronic physics, neutrinos are essential for gaining a better understanding of the structure of the nucleon, baryonic resonances, and form factors. They also play a crucial role in checking the validity of hadronic current models. In nuclear physics, neutrino experiments will lead to a more accurate description of nuclear effects, as nuclear interactions can cause in-correct identification of reaction channels. A theoretical understanding of nuclear effects and neutrino-nucleus interactions is crucial for interpreting experimental results.

While neutrinos are involved in many areas of physics, they are elusive particles, difficult to be detected, that provide answers to important questions across these fields. Through this history of the particle, it is clear that a deeper understanding of neutrinos would benefit research in nuclear and particle physics, cosmology, and astrophysics.

1.2 Properties of neutrino

We now know that there are at least three distinct types of neutrinos, known as flavors, that form a doublet with their corresponding charged leptons (electron, muon and tau). In 1996, the LSND experiment at Los Alamos National Laboratory suggested the possibility of the existence of a fourth type of neutrino, known as the sterile neutrino, which does not interact with anything except gravity. Due to the experimental discrepancies in the results [27], the hypothesis of sterile neutrinos was considered as a possible explanation for these observations. The existence of sterile neutrinos would indicate new physics beyond the Standard Model. Neutrinos are particles with zero charge, of spin 1/2 with helicity -1 and with the ability to change flavor through a process known as oscillation. This implies that their mass is not zero, which is in contrast to the assumptions of the Standard Model. Furthermore, as we have mentioned in the previous section, there is still a debate on whether the neutrino is its own antiparticle (Majorana neutrino) or has a distinct antiparticle (Dirac neutrino). The electroweak theory developed by Weinberg, Salam and Glashow in the 1970s describes the weak interaction of neutrinos with matter, which is much weaker than the electromagnetic interaction and results in very small cross sections and this is why the neutrinos are so difficult to detect.

Neutrinos in the Standard Model

The Standard Model, which was proposed in the 1970s, describes the strong, electromagnetic and weak interactions of elementary particles. The electromagnetic (EM) and weak interactions are unified in the SM by the electroweak $SU(2)_L \times U(1)_Y$ theory of Glashow-Weinberg-Salam [28, 29, 30]. Its experimental confirmation came in the 1980s with the discovery of the W and Z bosons. The weak isospin (T) is the quantum number associated to the symmetry group $SU(2)_L$ of the SM. Under this symmetry, fermionic fields with left-handed chirality are grouped into weak isospin doublets

$$\Psi_L = \begin{pmatrix} \nu_{eL} \\ e_L \end{pmatrix}, \qquad \begin{pmatrix} \nu_{\mu L} \\ \mu_L \end{pmatrix}, \qquad \begin{pmatrix} \nu_{\tau L} \\ \tau_L \end{pmatrix} \tag{1.1}$$

In the SM, the neutrino fields have only left-handed components [31], this implies that it is a massless particle. Meanwhile the other fermions have right-handed components (e_R, μ_R and τ_R). These right-handed components of charged fermions transform as weak isospin singlets under the action of the $SU(2)_L$ group.

The weak interaction takes place through the exchange of heavy W and Z bosons. The W bosons appear in scattering processes with charge exchange, processes with charged currents (CC) (the ones to be studied in this work), while the Z boson is associated with processes without charge exchange, processes with neutral currents (NC) which are flavor-blind. This refers to the fact that since neutrinos cannot be directly detected, it is experimentally impossible to determine with certainty the flavor of the initial and final neutrinos in the reaction.

The Lagrangian density, which describes only the weak interactions in the SM in terms of the neutral and charged currents coupled to the corresponding gauge bosons, is given by

$$\mathcal{L}_{int} = -\frac{g}{2cos\theta_W} J^{\mu}_{NC} Z_{\mu} - \frac{g}{2\sqrt{2}} \left(J^{\mu}_{CC} W^{\dagger}_{\mu} + h.c \right), \tag{1.2}$$

where Z_μ and W_μ stand for the fields of the massive bosons. J_{NC} and J_{CC} correspond to the neutral and charged currents and at the quark level with the three lightest quark flavors can be written as

$$\begin{aligned} J^{\mu}_{NC} &= \bar{\Psi}_u \gamma^{\mu} (1 - \frac{8}{3} \sin^2\theta_W - \gamma_5) \Psi_u \\ &- \bar{\Psi}_d \gamma^{\mu} (1 - \frac{4}{3} \sin^2\theta_W - \gamma_5) \Psi_d \\ &- \bar{\Psi}_s \gamma^{\mu} (1 - \frac{4}{3} \sin^2\theta_W - \gamma_5) \Psi_s \\ &= V^{\mu}_{NC} - A^{\mu}_{NC} \end{aligned} \tag{1.3}$$

$$J^{\mu}_{CC} = \bar{\Psi}_u \gamma^{\mu} (1 - \gamma_5)(\cos\theta_C \Psi_d + \sin\theta_C \Psi_s) = V^{\mu}_{CC} - A^{\mu}_{CC} \tag{1.4}$$

The angle θ_W, called the Weinberg angle, defines the ratio of the vector boson masses and also relates the strength of the electromagnetic interaction with the weak coupling, g,

$$cos\theta_W = \frac{M_W}{M_Z}, \qquad sin\theta_W = \frac{e}{g}. \tag{1.5}$$

The Fermi constant, $G_F = 1.116 \times 10^{-5}\ GeV^{-2}$, is connected to the weak coupling by

$$\frac{G_F}{\sqrt{2}} = \frac{g^2}{8M_W^2}. \tag{1.6}$$

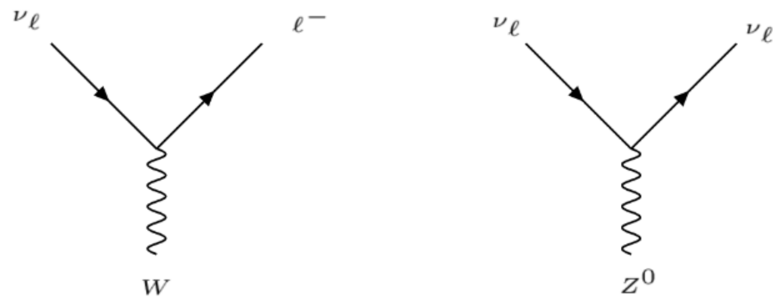

Figure 1.2: CC and NC diagrams

For the resolution of the problems treated in this thesis, it is important to emphasize that we will work within the SM framework, with the following assumptions:

- There are three distinct flavors of neutrinos (ν_e, ν_μ and ν_τ) whose masses are so small that we consider them massless particles. The absolute values of the masses are currently unknown. The relationship between the three mas states (ν_1, ν_2 and ν_3) and the three flavor states is given by the Pontecorvo-Maki-Nakagawa-Sakata (PMNS) matrix. This matrix depends on the mixing angles (θ_{12}, θ_{13} and θ_{23}) that determine the degree of mixing between the mass and flavors eigenstates, as well as the CP violation phase. So, we consider the (anti)neutrinos as massless particles.

- The flavor of the lepton is conserved, the lepton flavor number assigned is $L_i = +1(-1)$ for the neutrino(antineutrino) flavors. Neutrinos of different flavors interact only with other leptons of the same flavor. It is not possible the lepton flavor changing process. Hence, the lepton flavor number is conserved.

- Neutrinos have negative helicity (left-handed) and antineutrinos have positive helicity (right-handed). This reflects parity violation in weak interactions; if we consider neutrinos as massive particles, this situation could be modified. In addition, as we have already mentioned, the nature of the neutrino is unknown, we do not know if it is a Dirac particle or a Majorana particle. As we said, at present, there are experiments trying to prove the existence of the double beta decay without neutrinos where the Majorana nature would be proved in the case that the neutrinos annihilate each other.

- Neutrinos interact, through the exchange of massive charged vector fields $W_\mu^\pm$, with the charged leptons and quarks with the same strength for all the flavors (CC). These currents transform as $V_\mu - A_\mu$ theory.

- The weak interactions between neutrinos and hadrons involve changes in charge. Being S the strangeness quantum number, the hadronic currents obey ΔS=0 or |ΔS|=1 rule. The processes through ΔS=1 are suppressed with respect to those with ΔS=0 channels by a factor $tan^2\theta_c$ where θ_c is the Cabibbo angle. In the range of antineutrino energies $E_{\bar{\nu}}$ = 1 - 3 GeV, the production of strange particles through ΔS=0 processes is suppressed by phase space. Because it occurs through associated production, where one has to produce a kaon ($S = 1$) and a hyperon ($S = -1$), and the kaon masses are larger than the lighter meson masses, whether compared to hyperon and a pion production or simply compared to zero, which is what happens in quasielastic hyperon production [32]. In this region both processes are comparable. Nevertheless, neutral currents (NC) are significantly suppressed in the |ΔS| = 1 sector, upholding the principle of the absence of flavor-changing neutral currents(FCNC).

The $V - A$ theory satisfactorily describes neutrino interactions with matter at low energies and lies within the Standard Model. Among the neutrino properties that cannot be explained by the SM and that we will not take into account for the realization of the thesis are:

- The neutrino oscillations imply that neutrinos are massive and the mixing of flavors.

- CP violation in neutrino interactions.

- Additional neutrino flavors. Sterile neutrinos. Not yet been proven in other experiments.

Neutrino-nucleus interaction

The study of the interaction of neutrinos with nuclei at the energies range of hundreds of MeV up to tens of GeV plays a crucial role in the analysis of neutrino scattering and oscillation experiments. As the energy of the neutrino increases, the dynamics of the interactions becomes more complex. In this energy range, there are three main possibilities: Quasielastic scattering (QE), Resonance production (RES) and Deep Inelastic scattering (DIS).

In the lower neutrino energy range, quasielastic scattering processes dominate (the $E_\nu \leq 1$ GeV region). In this energy region, the most commonly studied process is Charged Current Quasi-elastic (CCQE) scattering (ν_l + A -> l + A') in which a neutrino of any flavor interacts with a nucleus via charged current interaction. The final nuclear target can be in the ground state or in the excited states, which then can decay by emitting neutrinos, leptons, photons or nucleons. As the energy of the incident neutrino increases, inelastic channels such as π production, hyperon production, baryonic resonances and kaon production become more important. These particles are emitted along with the residual nucleus in the final state. In nuclei, multi-nucleon mechanisms also come into play. In the few GeV energy region, single pion production channels may play a crucial role. At higher energies, Deep Inelastic Scattering becomes dominant, in which a jet of hadrons with a charged lepton are produced in the final state. As described below:

- **Quasielastic scattering (QE):** As we said, QE is a type of neutrino-nucleus interaction that dominates in the lower energy range, typically below 1 GeV. In this process, neutrinos and antineutrinos of all flavors interact with a nucleon through both charged current (CC) and neutral current (NC) interactions. In particle physics, the term of "quasielastic" is used specifically for charged current interactions, while "elastic" is used for neutral current interactions, meanwhile in nuclear physics both interactions are called "quasielastic". In QE scattering through CC interactions, the neutrino interacts with a nucleon in the target nucleus, resulting in the production of a charged lepton and a residual nucleus. This process can occur with and without change of strangeness. It is important to note that in the case of antineutrinos, single hyperon production (such as Λ, Σ,...) can occur in the final state, while it is prohibited in the case of neutrinos due to the ΔS = ΔQ and FCNC rules.There are many models that have been developed to study QE scattering in nuclei [33, 34]. These include the SuperScaling approximation and exchange currents-[35, 36], Final State Interactions (FSI) and SuperScaling-[37] and FSI and Random Phase Approximation (RPA) corrections [38, 39].

- **Resonance production (RES):** In the intermediate energy range, between 1 - 10 GeV, neutrino-nucleus interactions can excite the target nucleon to a resonance state, known as resonance production. The baryonic resonance that is produced, such as Δ, Λ, Σ^* or N^*, then decays into a variety of possible mesonic final states, resulting in combinations of nucleons and mesons. At higher energies, which implies large Q^2 values, neutrinos gain access to inelastic scattering processes. These inelastic scattering processes, which start with single pion production, are dominated by the Δ resonance [40]. A good understanding of pion production is crucial for interpreting neutrino oscillation experiments. The production and decay of nucleon resonances in neutrino interactions is a significant part of the total neutrino cross section in the few GeV region, and these resonances have been explored using electron scattering experiments as well. However, in the case of neutrino scattering, different form factors contribute. For higher neutrino energies, other channels involving strange particles may also become relevant. One must note that, although Cabibbo suppressed ($\Delta S = \pm 1$) cross sections are typically smaller, they can be larger (up to $\sim$ 1.5 GeV) than those for associated production ($\Delta S = 0$ and not Cabibbo suppressed) due to the different thresholds.

- **Deep Inelastic Scattering (DIS):** At higher energies, typically above 10 GeV, the dominant process in neutrino-nucleus interactions is DIS. In this process, the neutrino interacts with the nucleon through the exchange of a virtual boson (W or Z boson), and scatters off the quarks and gluons inside the nucleon. The DIS process can be described by the nucleon structure functions, which can be written in terms of Parton Distribution Functions (PDFs) for quarks, antiquarks and gluons [41]. These PDFs describe the probability of finding a quark or gluon inside a nucleon as a function of its momentum fraction. The neutrino can scatter directly off any of the quarks inside the nucleon, including the "sea" of quarks and anti-quarks that is constantly being created and annihilated. Nuclear effects in DIS have extensively studied using muon and electron beams. However, the study of nuclear effects in neutrino DIS has been relatively limited. This is in part because neutrino beams have lower intensities.

Overall, understanding the different types of neutrino-nucleus scattering is crucial for interpreting neutrino oscillation experiments, as the dominant process at the range of energies and how it can affect the measured cross sections. Furthermore, neutrino-nucleus scattering is also important for studying the properties of the nucleons and nuclei, as well as for understanding the dynamics of weak interactions in nuclei.

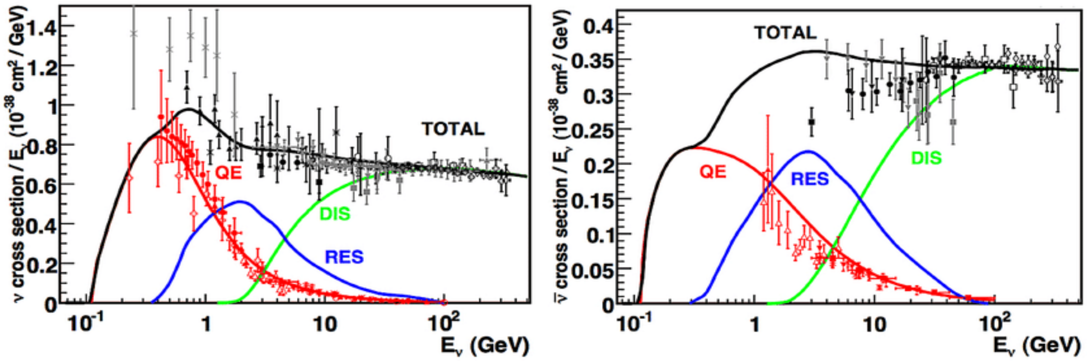

Figure 1.3: Total neutrino (left panel) and antineutrino (right panel) per nucleon CC cross sections divided by neutrino energy and plotted as a function of energy (E_ν). In this (anti)neutrino energy region the processes that contribute are: Quasielastic scattering (QE), resonance production (RES) and Deep Inelastic scattering (DIS). Figure taken from [42].

1.3 Neutrino experiments

As mentioned above, neutrinos are elusive particles that interact only weakly with matter, making their cross sections very small. This requires the use of large detectors to detect the interactions of neutrinos with nuclear targets. Since the initial proposal of their existence, many experiments have been conducted to study these particles. The first observation of antineutrinos was made in 1956 at Los Alamos National Laboratory in the Poltergeist project [6]. Experiments can be broadly classified into two types: those that use natural neutrino sources such as cosmic, solar, atmospheric and nuclear reactor neutrinos (e.g. Kamiokande, SNO, Double Chooz), and those that produce intense neutrino beams using accelerators (e.g. J-PARC, CERN, Fermi National Lab).

The earliest neutrino experiments were of the first type. In 1968, the Homestake experiment observed solar neutrinos for the first time [14] and discovered the so-called solar neutrino problem anomaly, caused by the detection of only electron neutrinos and not muon neutrinos. The solar neutrino puzzle was confirmed by experiments such as GALLEX and SAGE (Kamiokande collaboration) [43]. In 1998, the SuperKamiokande experiment confirmed the phenomenon of neutrino oscillation [16]. A few years later, in 2001, the SNO experiment measured the total solar neutrino flux and confirmed the disappearance of electron neutrinos [17]. These solar neutrino experiments are sensitive to the θ_{12} mixing angle and work on the estimation of mixing angles and mass differences between electron and muon neutrinos. The Kamiokande experiment was the first to demonstrate oscillations with atmospheric neutrinos [16], we know that the dominant process in this case is characterized by the parameters θ_{23} and Δm^2_{23}. There are other experiments that have worked on constraining these parameters such as MINOS [44] and T2K [45]. The new generation of atmospheric neutrino experiments, like PINGU in IceCube [46], ORCA in KM3NeT [47] and Hyper-Kamiokande [48], will focus on determining the mass order or hierarchy and the CP violation in the lepton sector. Finally, the third mixing angle θ_{13} has been determined by experiments that measure the reactor antineutrinos, such as JUNO [49], Daya Bay [50], Double Chooz [51], PROSPECT [52] and RENO [53]. Most of the experiments mentioned in this section are searching for the existence of sterile neutrinos, dark matter... among other measurements of oscillation parameters.

The experiments that generate neutrino beams have detectors located at short-baseline distances (a few hundred metres from the source) and long-baseline distances (hundreds of kilometres away). These experiments typically measure neutrino energies in the range of hundreds of MeV to a few GeV, such as T2K [45], MiniBooNE [54], SciBooNE [55], MicroBooNE [56] and NOvA [57]. The new generation of experiments will focus on the long-baseline measurements to determine the CP phase-violation and mass hierarchy, such as the DUNE [58] and T2HK [41] experiments. These experiments use intermediate energies (around 1 - 20 GeV) and select charged-current quasielastic scattering processes as their main measure channel. Processes induced by neutral currents (ν + A $\rightarrow$ ν + A'), where the outgoing neutrino is undetectable, are not chosen. The goal of these experiments is to detect muons or electrons, as well as other outgoing particles. Nuclear interactions and effects can scatter or absorb these particles, making the theoretical study of these processes important and a source of systematic uncertainty. We will briefly describe the experiments whose neutrino fluxes have been used by us to carry out some calculations:

- **MiniBooNE:** was a neutrino oscillation experiment that used a beam of muon neutrinos produced at Fermilab. The experiment started collecting data in 2002. The neutrino beam was directed at a 12.2 meter diameter spherical detector filled with 800 tons of mineral oil (ultra-refined methylene compounds) and lined with 1,280 photomultiplier tubes. The experiment's primary goal was to confirm or refute the LSND (Liquid Scintillator Neutrino Detector) experiment result, which found evidence of neutrino oscillations at a baseline of 30 meters and an energy of around 1 GeV. MiniBooNE collected data from both muon neutrino and anti-neutrino interactions and searched for evidence of oscillations between the two types. The experiment's results had important implications for our understanding of neutrino properties and the possibility of a fourth neutrino species. The neutrino energy spectrum of MiniBooNE was peaked at 0.7 GeV, where the Quasi-Elastic (QE) scattering process dominates. The experiment had collected a large amount of data from Charged Current Quasi-Elastic (CCQE) interactions, Charged Current pion production, and Neutral Current (NC) cross sections.

- **SciBooNE:** (SciBar Booster Neutrino Experiment) was a neutrino oscillation experiment that used a beam of neutrinos produced at Fermilab by a detector filled with 100 tons of liquid argon. The SciBooNE experiment also aimed to measure the low-energy neutrino cross sections on iron and carbon targets, which is important for understanding the neutrino background in long-baseline neutrino oscillation experiments. The SciBooNE detector had three subsystems: SciBar, the EC (electron catcher) and the MRD (muon range detector). The experiment ran in conjunction with the Booster Neutrino Beam (BNB) at Fermilab and used a near detector to measure the neutrino flux and energy spectra. Data collection for the experiment was completed in 2008. SciBooNE was considered the first phase of the MiniBooNE experiment and the neutrino beam used in SciBooNE was continued to the MiniBooNE detector, located approximately 540 meters downrange from the target.The SciBooNE data provided information about neutrino interactions and was crucial for the design and interpretation of future neutrino experiments.

- **MicroBooNE:** is an experiment located on the Booster Neutrino Beamline at Fermilab and detected by a large liquid-argon time projection chamber (LArTPC) to acquire a high statistics sample of neutrino interactions. The experiment is designed to study the so-called "liquid argon anomaly", a discrepancy between the expected and observed number of electron neutrino interactions in the liquid argon used in the detector. The MicroBooNE detector is designed to perform detailed studies of neutrino interactions in liquid argon and to search for evidence of new physics beyond the standard model. The experiment is also designed to make precise measurements of neutrino cross sections on argon and to study the properties of neutrinos, including their oscillations. In 2022, they have reported the first measurement of Λ quasielastic production. And luckily, the situation is poised for improvement as the statistical significance on Argon targets. The number of recorded events are expected to increase, thanks to the data collected between 2017 and 2020 by MicroBooNE, which are currently awaiting analysis [59].

- **The Short-Baseline Near Detector (SBND):** is currently under construction and is expected to begin operation in 2023. It will be one of three liquid argon neutrino detectors located in the Booster Neutrino Beam (BNB) at Fermilab as part of the Short-Baseline Neutrino Program. MicroBooNE and ICARUS are the intermediate and far detectors in the program, respectively. SBND is a 112-ton active volume liquid argon time projection chamber (LArTPC) that will be located only 110 m from the BNB neutrino source. The experiment is expected to provide important information for future long-baseline neutrino experiments such as DUNE. Larger statistics of hyperon production are expected to be obtained in SBND ($\sim$1000 Λ events) [60, 61].

- **T2K:** (Tokai-to-Kamioka) is a long-baseline neutrino oscillation experiment located in Japan. It uses a beam of muon neutrinos produced at the Japan Proton Accelerator Research Complex (J-PARC) and detected by the ND280 near detector, located 280 meters from the source, and the Super-Kamiokande detector in Kamioka (almost 300 kilometers away from the neutrino source), Japan. The far detector will be replaced by the Hyper-Kamiokande experiment. The experiment's primary goal is to measure the mixing angle called θ_{13}, which is a key parameter in understanding the properties of neutrinos. T2K also aims to measure the mixing angle θ_{13} and the mass hierarchy of neutrinos, as well as to search for evidence of CP violation in the lepton sector [62]. The experiment uses a unique off-axis beam that allows for the measurement of neutrino interactions with a high precision. T2K has been running since 2010 and continues to collect data, with the goal of increasing the precision of its measurements and searching for new physics beyond the standard model.

- **Minerνa:** (Main INjector ExpeRiment for ν-A) is a neutrino scattering experiment located at Fermilab. It is designed to study neutrino-nucleus interactions by using a high-intensity beam to study neutrino reactions with different nuclei (including hydrogen, carbon, iron, lead, and titanium). The experiment consists of 200 hexagonal detector panels, each one made up of 127 triangular scintillator plastic strips with fiber optic cable running down their centers, that allows for the measurement of multiple final state particles and is able to distinguish between neutrino and anti-neutrino interactions. The front of the detector is referred to as the nuclear target region, which contains five detector panels made of varying configurations of solid carbon, iron, and lead, separated by eight scintillator panels. This variety of nuclear targets allows researchers to compare reactions of neutrinos with the lightest nuclear target, helium, to the heaviest, lead. The goal of MINERvA is to make precise measurements of neutrino cross sections in order to improve our understanding of the interactions of neutrinos with matter and to provide information for future long-baseline neutrino experiments such as NOvA and T2K.

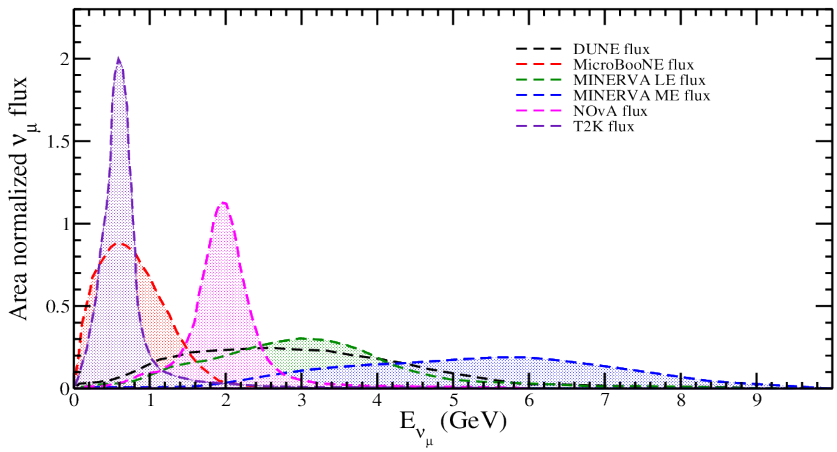

Figure 1.4: Muon neutrino flux as a function of neutrino energy (E_ν) from current and future accelerator based neutrino experiments. Figure taken from [63].

In conclusion, research on neutrino oscillations has revived the theoretical study of the neutrino-matter interaction cross sections. As previously discussed, there are different dominant regions depending on the energy range. Currently, there is no single theoretical model that can accurately describe all channels, even at the free nucleon level. This has led to the development of event generators, which combine different models. These event generators typically treat the primary interaction as a (anti)neutrino-nucleon interaction, with the exception of deep inelastic scattering (DIS). After the primary interaction is treated, it is further analyzed at the nuclear level and the final state interaction of the resulting particles is simulated. Most of the generators to be mentioned below are designed to simulate neutrino interactions in a wide range of energies, from low energy neutrino beams to high energy neutrino beams, and it can simulate interactions with various types of nuclei. It is built on a modular structure, which allows it to be easily extended to include new physics models. They are based on the standard model of particle physics and it includes a variety of models to describe neutrino-nucleus interactions, such as the Local Fermi gas (LFG) model, a variation of the original LFG model, called the correlated Fermi gas (CFG), Valencia model and SuSAv2 for quasielastic scattering, the Rein-Sehgal model to describe pion production in the resonance region, the Bodek-Yang model and the Bodek-Ritchie model for deep inelastic scattering. Most of them have the ability to simulate the response of different detector types, such as liquid argon, water Cherenkov and scintillation detectors. It also includes a detailed simulation of detector response, including the effect of multiple scattering and final state interactions. None of these generators include the final state interaction (FSI) to study the hyperon production induced by antineutrinos. Several event generators are currently available and are widely used in the field:

- **GENIE:** (General Neutrino Interaction Generator) is a widely used event generator for simulating neutrino interactions in various detectors. It is the most used generator. In use by NOvA, MicroBooNE, MINERvA, SBND, ICARUS and DUNE. Also being tested in MINERvA, and used by T2K's near-detector analyses. GENIE is based on the standard model of particle physics and it includes a variety of models to describe neutrino-nucleus interactions [64].

- **NEUT:** (Neutrino Event Generator) is another widely used event generator for simulating neutrino interactions in various detectors [65]. In use by Hyper- Kamiokande, Super-Kamiokande, T2K's far and near detectors. It can simulate interactions with various types of nuclei. This generator is updated according to experiments needs.

- **NuWro:**(Nucleon Weak Response to Oscillations) is a Monte Carlo neutrino event generator, created at the University of Wroclaw [66]. It is driven by theorist. It simulates neutrino-nucleon and neutrino-nucleus reactions for energies from threshold to TeV. The generator has a detector geometry module and can handle realistic neutrino beams, which make it suitable to use in neutrino experiments. It is also used in combination with other generators such as GENIE and NEUT to improve the simulation of neutrino interactions.

- **AChilLES:**(A CHIcagoLand Lepton Event Simulator) is a novel lepton-nucleus event generator from theorist that separates the primary interaction from hadron propagation within the nucleus [67]. Novel observables are also proposed to assess lepton-nucleus scattering models. Furthermore, ACHILLES can be readily extended to simulate neutrino-nucleus scattering events.

- **FLUKA (NUNDIS):** NUNDIS (NeUtrino DIS integrated flux) is a module of FLUKA that is specifically designed for simulating neutrino interactions in a variety of target materials [68].

- **GiBUU:** (Generator of Interacting BUU) is a Monte Carlo event generator for simulating neutrino interactions in nuclei [69]. The code is based on the BUU (Boltzmann-Uehling-Uhlenbeck) transport theory. GiBUU also includes the effects of the nuclear medium, such as Fermi motion, binding energy and Pauli blocking, which are important in the understanding of neutrino-nucleus interactions. It can predict ν/e/hadron scattering in the same framework. This generator is very different to the other generators.

1.4 Hyperons

We will study in detail hyperon production through two differents mechanism, the quasielastic production off nuclei and the inelastic processes where the hyperon is produced along with a pion in the final state off free nucleons and nuclei. Let us delve into the specifics of hyperons. Hyperons are subatomic particles that are composed of three quarks, just like protons and neutrons. They belong to the baryon family, which means they have a baryon number of 1. To distinguish hyperons from other baryons, almost one of the quark in their composition is a strange quark. The discovery of the strange quark dates back to the 1950s and was achieved through a series of experiments studying subatomic particles and strong interactions. This discovery went hand in hand with the study of strange baryons. The most common hyperons are the Lambda (Λ), Sigma (Σ) and Xi (Ξ) particles. They are formed in high energy interactions and are short-lived, decaying into other particles within an extremely brief timeframe. These particles are composed of one up or down quark and one or two strange quarks.

The hyperons produced in our reactions are Lambdas (Λ) and the three Sigmas (Σ^-, Σ^0 and Σ^+) which belong to the group of hyperons composed of two "normal" quarks (up and down) and one strange quark (Fig.1.5). They have a lifetime of about $\sim 10^{-10}$ s, except the Σ^0 particle, whose lifetime is approximately $\sim 10^{-20}$ s because it decays electromagnetically into a Λ and a photon. The hyperon's lifetime is considerably very much shorter than the lifetime of protons and neutrons [70]. This makes them difficult to detect and study. These particles are produced in high-energy collisions, such as those occurring in particle accelerators. They can also be produced in cosmic ray interactions with the Earth's atmosphere. Due to their short lifetimes and the high energies required to produce them, much of what we know about hyperons comes from studying their decays. Strange baryons are significant in the study of the strong force, which binds quarks together in protons and neutrons. They also provide insight into the properties of strange quarks and the behavior of matter under high densities and temperatures.

The term hyperon was proposed by Louis Leprince-Ringuet in 1953 [71]. Although hyperons are unstable particles, they can be part of a strange nucleus which is named hypernucleus. The first hyperon to be discovered was the Lambda (Λ) particle, which was discovered by V. D. Hopper and S. Biswas of the University of Melbourne and it was detected in cosmic ray interactions, in a lead block above the cloud chamber, by a team of scientists led by Cecil Powell in 1947 [72]. The discovery of the Lambda particle was significant because it was the first known particle that exhibited the existence of a "strange" quark in its composition, challenging previous ideas about hadron structure. The term "strangeness" in the name of the quark originated precisely from the unusual behavior observed in Λ and similar particles. In the initial experiment conducted by Cecil Powell and his colleagues, the cloud chamber only provided limited information about the trajectory of particles, making it difficult to distinguish between the Kaon and Lambda hyperon. To overcome this challenge, Powell and his team conducted a more detailed experiment to clearly distinguish between the two types of particles. The experiment was performed at the Cavendish Laboratory at the University of Cambridge using a device called a cloud chamber. In the cloud chamber, a beam of subatomic particles is passed through a chamber filled with vapor of water or liquid alcohol. When the particles pass through the chamber, they ionize the vapor molecules and create a visible trail of small liquid droplets that indicate the trajectory of the particles. In the experiment, Powell and his colleagues passed a cosmic ray beam through a cloud chamber that was surrounded by a magnetic field. The scientists knew that kaons and Lambda hyperons are deflected differently in a magnetic field due to their electric charges and magnetic moments. Powell and his colleagues analyzed the trajectories of the subatomic particles observed in the cloud chamber and used the differences in their behavior in the magnetic field to distinguish between kaons and Lambda hyperons. Kaons were deflected in one direction, while Lambda hyperons were deflected in another direction. The scientists also analyzed the decay properties of the particles to confirm their identities. They found that kaons decay into three different particles, while Lambda hyperons decay into two different particles.

In 1950, the CalTech Group [73] confirmed with several examples the existence of events similar to those observed by Rochester and Butler. Over the following years, several other hyperons were discovered, including the Sigma (Σ) and Xi (Ξ) particles. The first identified (Ξ) particle was published by the Manchester group in 1952, it was the first identified because its decay was so characteristic and its sign so out of place for a heavy particle. The main characteristic of these particles, and the reason they are called cascade particles, is their unstable state, which leads them to rapidly decay into lighter particles through a chain of decays. These discoveries were made by teams of scientists using bubble chamber detectors, which allowed them to detect and study the short-lived hyperons. As technology and experimental techniques advanced, scientists made significant progress in studying hyperons in more detail, including their properties, decays, and interactions. The baryonic nature of the Σ^+ was established by A. Bonetti and his Milano group in 1953. Building upon that, in 1954, the Diffusion Chamber group of Brookhaven discovered the Σ^- hyperon. In 1957, the Σ^0 was discovered at Brookhaven by Steinberger and his collaborators. This discovery involved a pair emitted in the decay $\Sigma^0 \rightarrow \Lambda + \gamma$.

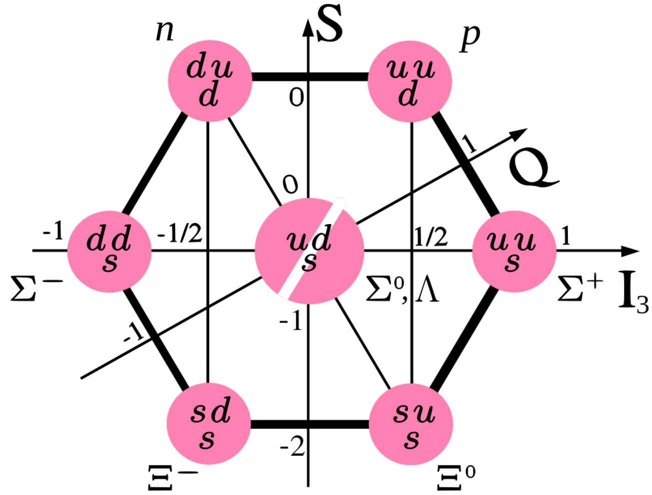

Figure 1.5: Baryon octet grouped according to the SU(3) scheme. (Wikipedia archive)

In 1953, Gell-Mann explained the decay of these new particles, the hyperons. Nishijima had the same idea and published it three months later. The term strangeness was introduced by Gell-Mann. This property explained the fact that these particles (kaons and hyperons) were created easily but decayed more slowly than expected. This new property, the strangeness, is conserved during the strong and the electromagnetic interactions, but not during the weak interactions. In the decade of 1960s, Murray Gell-Mann and other physicists developed the theory of quarks, which explained that hyperons and other subatomic particles were composed of quarks. The quark theory provided an explanation for many properties and characteristics of hyperons, such as their neutral electric charge and strange flavor charge. In 1954, Powell published a paper summarizing everything that was known up to that point about hyperons in the Ref.-[74]

During the 1970s and 1980s, experiments conducted at the Brookhaven National Laboratory and CERN played a crucial role in establishing the properties of hyperons, including their masses, lifetimes, and decay modes. In the 1990s and 2000s, experiments at the Relativistic Heavy Ion Collider (RHIC) and Large Hadron Collider (LHC) provided new insights into the properties of hyperons, including their interactions with other particles in a hot and dense environment, such as those that existed in the early universe.

Today, the study of hyperons continues to be an active area of research, with ongoing experiments planned at existing and future facilities. These experiments aim to deepen our understanding of the properties of these strange particles and the behavior of matter at high densities and temperatures.

Y	Quarks	Mass(MeV/c^2)	I	J^P	Mean lifetime(s)	Decays
Λ	uds	1115.683 ± 0.006	0	$\frac{1}{2}^+$	$(2.632 \pm 0.020) \times 10^{-10}$	$p + \pi^- // n + \pi^0$
Σ^-	dds	1197.449 ± 0.030	1	$\frac{1}{2}^+$	$(1.479 \pm 0.011) \times 10^{-10}$	$n + \pi^-$
Σ^0	uds	1192.642 ± 0.024	1	$\frac{1}{2}^+$	$(7.4 \pm 0.7) \times 10^{-20}$	$\Lambda + \gamma$
Σ^+	uus	1189.37 ± 0.07	1	$\frac{1}{2}^+$	$(0.8018 \pm 0.0026) \times 10^{-10}$	$p + \pi^0 // n + \pi^+$

Table 1.1: Main properties of the hyperons with $S = -1$ studied in this work.

The hyperons we will focus on are Λ and Σ's, we have collected their main properties in the table 1.1. In the next chapters, we will see in detail how hyperons interact with the nucleons in the interior of the nuclei to follow them by the Final State Interactions.

Several experiments have reported strange particle production induced by neutrinos and antineutrinos. Some of them are:

- Gargamelle: this experiment in the 70s at CERN presented cross sections for Λ and Σ^0 using bubble chambers filled first with freon (CF3Br) [75], with propane and a small admixture of freon (CF3Br) [76] and just with propane [77]. They reported on the first observation of hyperon production induced by neutrinos.

- ANL (Argonne National Laboratory): In 1974, the experiment reported seven cases of strange particle production [78]. The bubble chamber used in this case was filled with deuterium.

- BNL (Brookhaven National Laboratory): At the end of the 1970s, this experiment presented a study of Λ production in antineutrino-hydrogen reactions [79, 80].

- Fermilab: In the 1980s, they reported the cross section of the quasielastic reactions $\bar{\nu}_\mu p \to \mu^+\Lambda(\Sigma^0)$, the bubble chamber was filled with deuterium [81] and with a heavy neon-hydrogen mixture [82].

- SKAT: It is an experiment using the bubble chamber filled with heavy freon (CF3Br). In 1989, the collaboration presented the cross section for Λ production induced by antineutrinos [83].

1.5 Motivation and structure of this thesis

In this tesis, we are going to study a model of semi-inclusive hyperon production off free nucleons and nuclei induced by muonic antineutrino and driven by the weak charged current. Our model consists in the quasielastic mechanism (QE) and the inelastic mechanism where the hyperon is produced alongside a light meson, specifically a pion ($Y\pi$). This last mechanism had only been studied on free nucleons before. The processes of pion production from nucleons and nuclei at intermediate neutrino energies are important tools for studying the structure of hadrons. We focus on the neutrino energy region $E_{\bar{\nu}} < 2$ GeV, which is particularly relevant for numerous scattering and oscillation neutrino experiments. Furthermore, it must be taken into account in all cases that the hyperons produced in the primary scattering travel through the nucleus experiencing final state interactions (FSI). These FSI interactions entail collisions with the nucleons, alterations in the hyperon direction, energy loss or even turning into a different hyperon species before getting out of the nucleus and being detected. To account for these effects, we use a Monte Carlo simulation that incorporates the FSI, to follow the propagation of hyperons inside the nuclear medium.

Theoretical studies of the cross sections of antineutrino-nucleus interactions are essential for analyzing neutrino scattering and oscillation experiments data. For the hyperon production in the antineutrino energy region of few GeV, the dominant weak process is the quasielastic production. Also in this energy region, the inelastic processes where pions are produced alongside the hyperon by weak charged currents. These reactions can play an important role as background in those experiments. So, that once the primary reactions (on free nucleons) have been studied, it is important studying the production of hyperons through scattering on nuclear targets. However, this introduces significant complexities in the analysis and interpretation of theoretical and experimental results.

The study of the production of hyperons induced by antineutrinos has been previously studied. A brief overview of the theoretical work done on the subject so far shows that on the one hand the quasielastic mechanism has been studied on several occasions. It has been examined for both nucleonic and nuclear targets in various works [84, 85, 86, 87, 88]. In our work, we will follow the quasielastic model proposed in [85]. In these scenarios, the weak interaction occurs on a bound nucleon within the nuclear target. Various theoretical approaches have been employed to describe the initial nucleus, including global [88] and local [85, 87, 88] Fermi gas approximations. And some descriptions take into account the nuclear mean field and nucleon-nucleon correlations [87]. It is crucial to consider the subsequent propagation of hyperons produced in the primary scattering through the nucleus, as they undergo final state interactions (FSI). During FSI, hyperons can collide with nucleons, change direction, lose energy, or even transform into different hyperon species before exiting the nucleus and being detected. To handle these FSI effects, semiclassical methods have been employed [85, 87, 88], which have a substantial impact on observables, surpassing the influence of the nuclear initial state treatment [87].

In contrast to quasielastic (QE) hyperon production, the $Y\pi$ mechanisms in nuclei have not yet been extensively studied. It is worth noticing that in the case of quasielastic scattering, there are some special channels, for instance there is no direct Σ^+ production on a single nucleon. This hyperon could only appear due to final state interactions or re-scattering of other hyperons inside the nucleus. However, allowing for the presence of additional pions, namely the $Y\pi$ channel, the Σ^+ hyperon can be directly produced from a single proton. Although the $Y\pi$ production off nuclear targets is not studied yet, the process of Cabibbo enhanced single pion production off nucleons has been a topic of theoretical study as in Refs. [40, 84, 89, 90, 91] and measurements as in Refs. [92, 93, 94, 95, 96, 97] for several decades. Despite the lack of research on this topic, the Cabibbo-suppressed hyperon-pion production from nucleons has the potential to provide valuable insights into the nature of the strong interaction and the dynamics of hadron formation. In the course of this thesis, we have studied models of hyperon production from free nucleons [98] and nuclei [99]. Different approaches have been employed in previous works [100, 101, 102, 103]. In Ref. [100], a coupled-channel chiral unitary approach is utilized to dynamically generate the $\Lambda(1405)$ resonance, which significantly contributes to the $\pi\Sigma$ reaction channel. In Refs. [101, 102], a non-relativistic 3-quark model, effective $V - A$ theory with experimental form factors, and the relativistic quark model with the harmonic interaction of Feynman, Kislinger, and Ravndal [104] are employed to calculate the cross section for $\Sigma^0(1385)$ resonance production off a proton, among other channels. Lastly, in Ref. [103], a model incorporating background or Born terms is used to compute a wide range of reactions involving the production of strange particles, specifically focusing on the πY channel while explicitly excluding N^* and Y^* exchange mechanisms.

Although theoretical studies have been carried out on both mechanisms of hyperon production, there is still a continuous effort in order to understand aspects of crucial importance in the development of these models. For example, to obtain the vector and axial-vector form factors [105, 106] and the possible SU(3) breaking effects using QCD and QCD-inspired models on the theoretical front. Various methods, such as 1/Nc expansions, chiral perturbation theory, quark models, and lattice QCD, have been employed to achieve this goal. However, our current understanding of these form factors remains unsatisfactory due to the limited availability of experimental data, primarily derived from hyperon semileptonic decays with low momentum transfers. This means that the experimental data available to us is restricted to a very small part of the full momentum transfer space. Therefore, researchers have been continuously exploring new ways to gather more experimental data to improve our understanding of these form factors. For instance, there are ongoing efforts to develop new experimental techniques to measure these form factors at higher momentum transfers. Overall, these mechanisms have been studied previously by several groups with consistent results, exploring, among other things, the sensitivity to the transition form factors, to the axial mass, SU(3) symmetry breaking or the existence of second class currents

On the other hand, in the experimental aspect, the quasielastic reaction $\bar{\nu}_l + N \to l^+ + Y$, which provides a better way of probing the momentum transfer dependence of the $N \to Y$ form factors, has not been explored extensively. Currently, there are only a few observed Λ and Σ production events before the 1990s, using bubble chambers. These detectors "can see" the decay of the hyperon into another particles such as $\Lambda \to \pi^- + p$. Such as Gargamelle, filled with freon [75, 76] and propane [77] (reported events of $\mu^+ + \Lambda$ ($\Lambda \to \pi^- + p$) and $\mu^+ + \Sigma^0$ ($\Sigma^0 \to \gamma + \Lambda$)), ANL 12-foot filled with deuterium [107] (reported events of Λ production), BNL 7-foot filled with hydrogen [79, 80] (reported events of $\mu^+ + \Lambda$ ($\Lambda \to \pi^- + p$)), Fermilab 15-foot filled with a heavy neon-hydrogen mixture [82] (reported events of $\mu^+ + \Lambda$ ($\Lambda \to \pi^- + p$), $\mu^+ + \Sigma^0$ ($\Sigma^0 \to \gamma + \Lambda$) and $\mu^+ + \Lambda + \pi^0$), and deuterium [81], as well as SKAT filled with freon [83] (reported events of $\mu^+ + \Lambda$ ($\Lambda \to \pi^- + p$)). Despite the low statistics and uncertainties in the incoming flux, these experiments have provided cross sections for low-energy

$E_\nu < 20$ GeV, $\Delta S = -1$, single Λ, Σ, and $\Delta S = 0$ ΛK production, as well as YX and YKX production, where X represents additional hadrons. Further experiments have been conducted to obtain higher energy cross sections and rates, as well as hyperon yields and polarization measurements, using bubble chambers (see Ref. [108] for a comprehensive list of references) and by the NOMAD experiment [60, 61]. However, given the limited experimental data available, there is still much to be learned about the momentum transfer dependence of the $N \to Y$ form factors. As such, researchers continue to explore new experimental techniques to better understand these processes and further our understanding of neutrinos and hyperons.

In 2022, the MicroBooNE Collaboration [59] reported the first measurement of $\bar{\nu_\mu} +^{40} Ar \to \mu^+ + \Lambda + X$, where X denotes the final state content without strangeness. So far only five quasielastic Λ production events have been identified analyzing the exposure of the MicroBooNE liquid argon to the off-axis NUMI beam at FNAL. However, there is good news as the situation is expected to improve significantly with the large data sample collected by MicroBooNE, which is still awaiting analysis [59], and the much larger data sample expected at the SBND detector [60, 61]. We want to prove that the hyperon-pion production is a relevant channel to take into account in the experiments that find hyperon production induced by antineutrinos. To do this, we will compare our results with the measurement presented by the MicroBooNE collaboration. We will calculate the flux-folded cross sections using the SBND flux to check the relative importance of the $Y\pi$ production in the total value of the cross sections.

During the development of this thesis, we investigate the production of Λ and Σ hyperons off free nucleons and nuclei driven by charged current interactions induced by muonic antineutrinos. We have focused on the inelastic process where the hyperon is produced alongside a pion. We have developed this process from the most primary version, in which the reaction is produced off free nucleons. Then we extended to nuclear models and compared this process with the dominant one in the chosen neutrino energy range (quasielastic mechanism). We consider both the inelastic $Y\pi$ channel and the QE process. By focusing on laboratory energies within the range of $E_{\bar{\nu}} \lesssim 2$ GeV, which is probed by MicroBooNE and SBND experiments, we can neglect hyperon production accompanied by multiple pions, the associated YK reaction channel, and secondary hyperon production induced by $\bar{K}$. Additionally, we incorporate FSI effects by employing a Monte Carlo simulation to account for hyperon propagation in the nuclear medium. Finally, we compared our complete model of hyperon production with the first measurements presented in the last 30 years. Our model is applied to the recent measurement by MicroBooNE [59]. In this way, we wanted to verify the implications of the hyperon-pion production process and the validity of our work. More analyzed hyperon production results from the MicroBooNE and SBND collaborations are expected to be presented in the coming years.

In order to achieve the objectives of this thesis we will use quantum mechanics and quantum field theory. For the description of the hadronic degrees of freedom and resonances present in the models we will employ hadronic and nuclear physics. For the computation of the cross sections in nuclei we will apply the local Fermi gas model. In general we will start from lagrangians that describe the interaction between baryons, mesons and weak charged currents. This will allow us to obtain the vertices of the Feynman diagrams relevant to the reactions. Once these currents are obtained by applying the Feynman rules to the diagrams, we will obtain the reduced matrix elements of the transition and therefore the cross section. To include the final state interactions (FSI) we will simulate a Monte Carlo intranuclear cascade with the hyperon-nucleon scattering cross sections.

The structure of this thesis will be the following: in Chapter 2 we discuss the theoretical model used to describe the primary antineutrino-induced hyperon-pion production off nucleons through strangeness-changing weak charged current; in Chapter 3, we present the formalism of quasielastic mechanism and hyperon-pion process in the nucleus. In this chapter, we also explain how we incorporate and simulate the hyperon final state interactions. We present the results obtained in Chapter 4. In the Chapter 5, we compare our solutions obtained with the measurement presented by MicroBooNE collaboration and we show the cross sections convoluted with the SBND flux. This thesis concludes with the insights presented in Chapter 6.

Chapter 2

Hyperon-pion production off the nucleon

As discussed in the previous chapter, understanding (anti)neutrino-nucleon cross sections is crucial for the analysis of neutrino scattering and oscillation experiments [109, 110, 111, 112, 113]. Before considering nuclear effects, it is essential to have a thorough understanding of the primary (anti)neutrino-nucleon interaction in order to provide a theoretical description of the cross sections. This primary reaction plays a significant role in describing the interaction between neutrinos and nuclear matter. Therefore, it is crucial for these models to accurately predict experimental data on nucleon targets before incorporating these elementary interactions into the nuclear medium. Nuclear effects introduce distortions to the final signal detected in neutrino scattering experiments. At intermediate neutrino energies, there are limited calculations available for the antineutrino production of strange baryons from free nucleons. In the energy range of a few GeV, the Cabibbo suppressed single pion production channels may also play a crucial role, even when quasielastic hyperon production dominates, particularly in the case of the production of Σ^+. It is important to consider these processes as potential sources of background in neutrino oscillation experiments.

The Cabibbo enhanced single pion production off nucleons, as it has already been explained in the Sec.1.5, is a well-known theoretical process that has been studied and measured over the years. However, its Cabibbo-suppressed counterpart, where a pion is produced along with a $S = -1$ hyperon (Σ or Λ, in this work) in the final state, is a scarcely studied set of reactions. In these antineutrino induced reactions, a single pion can be produced along with a hyperon. One of the main challenges in developing this model is the fact that the reaction involves three final particles (a meson, a hyperon and a lepton). The hyperon-pion production involves a strangeness change of $\Delta S = -1$, the first effect of that change is that the reaction can only be induced by antineutrinos due to the selection rule for the strangeness-changing weak charged current, $\Delta S = \Delta Q = -1$, for the hadrons. Given that the strangeness-changing weak charged current changes an u quark into a s quark ($W^- + u \to s$) (or a $\bar{s}$ antiquark into an $\bar{u}$ one), there are also the selection rules $\Delta I = \frac{1}{2}$ and $\Delta I_z = -\frac{1}{2} = \frac{\Delta Q}{2}$, where (I, I_z) are the strong isospin and its third component. Another point to take into account, as we said, is that this kind of reactions is Cabibbo suppressed. In order to explain briefly the suppression of the strength of $\Delta S = \pm 1$ currents as compared to $\Delta S = 0$ currents, Gell-Mann, Levi [114] and Cabibbo [11] proposed that the strength of the strangeness-changing current in the hadronic sector is suppressed as compared to the non-strangeness-changing currents by a factor described by a parameter to be determined experimentally from β-decays of hyperons. The weak transition of β-decay corresponds to $u \leftrightarrows d$ transition in $\Delta S = 0$ case, and $s \to u$ in $\Delta S = \pm 1$ currents. In the Cabibbo model [11] formulated in terms of the quark model of the hadrons, the weak hadronic charged current is written as

$$J_\mu^{\text{Cabibbo}}(x) = \cos\theta_C \bar{\psi}_u(x)\gamma_\mu(1-\gamma_5)\psi_d(x) + \sin\theta_C \bar{\psi}_u(x)\gamma_\mu(1-\gamma_5)\psi_s(x), \quad (2.1)$$

in which the $\Delta S = \pm 1$ currents are suppressed by a factor $\tan\theta_C$, its experimental value was determined to be $\tan\theta_C$=0.237 [115]. However, even with this suppression by a factor $\tan\theta_C$, in the low neutrino energy region ($E_\nu \sim 1 - 3$ GeV), the associated production of strange particles through $\Delta S = 0$ processes is suppressed by phase space. This suppression arises from the fact that, in $\Delta S = 0$ processes, a kaon ($S = +1$) must be generated alongside the hyperon ($S = -1$), and the mass of the kaon exceeds that of the pion. Therefore, in this low energy region, the cross sections for the hyperon production through $|\Delta S| = 1$ and $\Delta S = 0$ currents become comparable.

In previous works, various authors followed different approaches. The reader can find more information about their approaches in Sec. 1.5. We have developed a model for antineutrino-induced $Y\pi$ production off free nucleon induced by the weak charged current interactions. The model is based on the lowest order effective SU(3) chiral Lagrangians and includes both a non-resonant mechanism (background terms), which relies on the chiral Lagrangian and SU(3) flavor symmetry, and a resonant mechanism that involves both non-strange ($\Delta(1232)$) and strange ($\Sigma^*(1385)$) resonances.

The structure of this chapter is as follows: in Sect. 2.1 we discuss the formalism in detail; in Sect.2.2 we describe the Born or background terms; in Sect. 2.3 the resonance terms; and finally, in Sect. 2.4 we discuss our results of the calculations of the total cross sections convoluted with the fluxes of different experiments.

2.1 Formalism

The set of antineutrino induced charged current hyperon production reactions that we describe formally in this section is given by

$$\bar{\nu}_l(k) + N(p) \quad \longrightarrow \quad l^+(k') + \pi(p_m) + Y(p_Y), \tag{2.2}$$

where N can be a proton or neutron, l^+ is an antilepton which has the same flavor as the incoming antineutrino $\bar{\nu}_l$. In this thesis, we will mostly work with muonic antineutrinos, so the antilepton will be referred to as an antimuon. π is a pion, Y is a Σ or Λ hyperon, and the four-momenta of particles are given in parentheses. For induced reactions off protons, we can produce all the hyperons, the allowed $Y\pi$ final states are $\Lambda\pi^0$, $\Sigma^0\pi^0$, $\Sigma^+\pi^-$ and $\Sigma^-\pi^+$; while for the neutron channel the possibilities are $\Lambda\pi^-$, $\Sigma^0\pi^-$ and $\Sigma^-\pi^0$.

We show in Fig. 2.1, all the Feynman diagrams that we have included in our $Y\pi$ production model. For the background (Fig. 2.1a), we consider six different channels: we include in our model the contact term (CT), the kaon pole (KP), the kaon-in-flight (KF), the direct Λ and Σ channels (s-Λ and s-Σ) and the nucleon crossed diagram (u-N). Our model is very similar to that followed in Ref. [40, 100, 116, 117, 118, 119] but including the lowest-lying decuplet resonances $\Delta(1232)$ and $\Sigma^*(1385)$ as explicit degrees of freedom (shown in Fig. 2.1b). In this thesis, we do not consider the $\Lambda(1405)$ resonance channel, as done in the Ref.[100], this will be explained later.

We use effective $V-A$ strangeness-changing weak charged current with vector and axial-vector form factors for the transitions between nucleons and hyperons. The vector form factors are related to the electromagnetic nucleon form factors using the Cabibbo theory, under the assumption that the strangeness-changing weak vector current belongs to an SU(3) octet of flavor currents. The same is applied to the axial-vector currents, D-type (symmetric) and F-type (antisymmetric) couplings arise between two octets $\{8\} \otimes \{8\}$ that are connected through an SU(3) octet axial current. Whereas, the dependence of the form factors on the momentum transfer q^2 is introduced by assuming a similar form for both D and F couplings, taking the form of a dipole [85, 119]. In the case of the strong vertices $\pi NN'$ and $\pi YY'$, we assume pseudo-vector couplings with the derivative of the pseudo-scalar meson field. These assumptions are consistent with the lowest order baryon-meson chiral Lagrangians in the presence of a weak charged external current, as shown in Ref. [120].

The expression for the unpolarized differential cross section in the laboratory

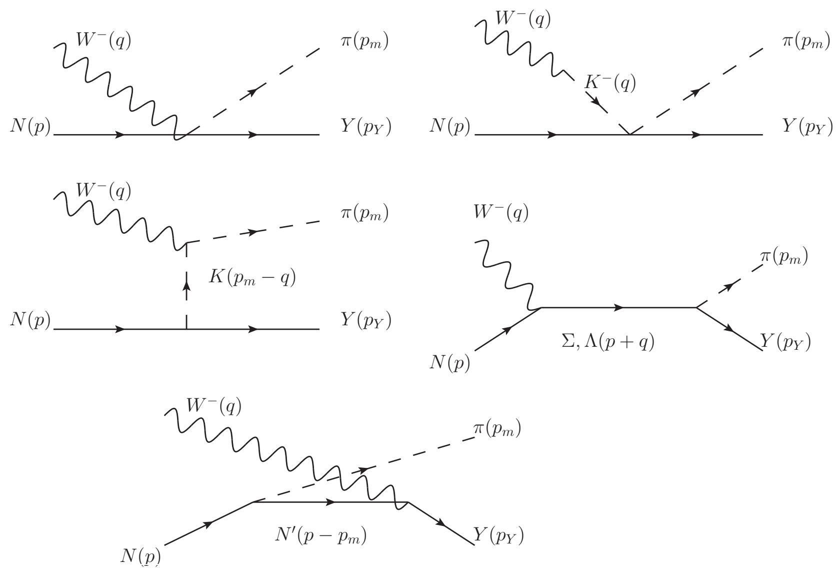

(a) Background or Born terms of our model. From top to bottom and from left to right, we find the contact term (CT), the kaon pole (KP), the kaon-in-flight (KF), the s-channel Σ and Λ (s-Σ and s-Λ) and the u-channel N (u-N) diagrams, respectively.

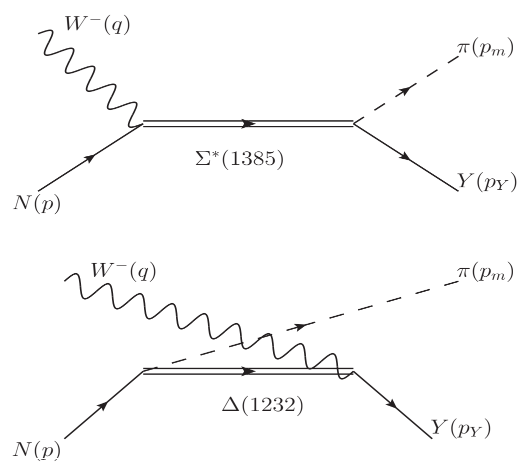

(b) Resonance diagrams included in our model. The s-channel $\Sigma^*(1385)$ diagram is shown in the upper figure, while the u-channel $\Delta(1232)$ diagram is depicted in the lower figure.

Figure 2.1: Feynman diagrams included in our model for the Cabibbo suppressed πY production process off nucleons induced by antineutrinos.

(lab) frame corresponding to the reactions shown in Eq. (2.2) is

$$d^9\sigma = \delta^4(p + q - p_Y - p_m)\frac{1}{(2\pi)^5\, 4ME_{\bar{\nu}}}\frac{d^3k'}{2E'_l(\mathbf{k}')}\;\frac{d^3p_m}{2E_m(\mathbf{p}_m)}\;\frac{d^3p_Y}{2E_Y(\mathbf{p}_Y)}\overline{\sum}\sum|\mathcal{M}|^2\,, \tag{2.3}$$

where k and k' are the 3-momenta of the incoming and outgoing leptons in the lab frame, the energy of the outgoing lepton $E'_l = (\mathbf{k}'^2 + m_l^2)^{\frac{1}{2}}$, the mass of this lepton (muon in this case) is $m_\mu = 105.65$ MeV. The pion lab momentum is p_m having energy E_m, p_Y is the hyperon lab momentum with energy E_Y, M is the nucleon mass and p is the nucleon lab momentum. This CC reaction is mediated via a W^- boson of transferred momentum $q = k - k'$. The symbol $\overline{\sum}\sum|\mathcal{M}|^2$ is the square of the scattering amplitude $\mathcal{M}$ averaged and summed over the spins of the initial and final states, respectively. In the limit $|q^2| \ll M_W^2$, our expression for the reduced transition matrix element is given by the Fermi theory of contracted product of weak lepton and hadron currents, and in this limit, the propagator of the W boson and the weak coupling constants at both currents can be written in terms of the Fermi constant. At low energies, this amplitude can be written as

$$\mathcal{M} = \frac{G_F}{\sqrt{2}}\,\ell_\mu J_H^\mu, \tag{2.4}$$

with $G_F = \frac{\sqrt{2}g^2}{8M_W^2} = 1.1664 \times 10^{-5}$ GeV^{-2} as the Fermi coupling constant [121], and ℓ_μ and J_H^μ are the leptonic and hadronic currents, respectively. The leptonic current for processes with charged currents is

$$l^\mu = \overline{v}_{\nu_l}(\mathbf{k})\gamma^\mu(1-\gamma_5)v_l(\mathbf{k}'), \tag{2.5}$$

and the total hadron current is calculated as the sum of the individual hadron currents of each one of the diagrams depicted in Fig. 2.1.

In the present calculations, we take initial nucleons as unpolarized; however, antineutrinos are fully polarized under these assumptions, the expression of the reduced transition matrix element squared $\overline{\sum}\sum|\mathcal{M}|^2$ leads to:

$$\overline{\sum}\sum|\mathcal{M}|^2 = 2\,G_F^2\,L^{\mu\nu}(k,k')\sum_{\lambda_N,\lambda_Y} J_\mu^{CC}(J_\nu^{CC})^*. \tag{2.6}$$

In the above expression, $L^{\mu\nu}(k,k')$ is the lepton tensor calculated from leptonic currents, and given by

$$L^{\mu\nu}(k,k') = k^\mu k'^\nu + k^\nu k'^\mu - g^{\mu\nu}(k\cdot k') - i\,\epsilon^{\mu\nu\alpha\beta}k_\alpha k'_\beta, \tag{2.7}$$

with $\epsilon^{0123} = 1$ and the metric $g^{\mu\nu} = (+, -, -, -)$. Finally, the sum over the spins of the initial and final baryons ($\lambda_{N,Y}$) gives rise to traces over chains of Dirac matrices; the hadron tensor is thus given by

$$\begin{aligned} W_{\mu\nu} &= \sum_{\lambda_N,\lambda_Y} J^H_\mu (J^H_\nu)^* = \sum_{\lambda_N,\lambda_Y} \left[\bar{u}_{\lambda_Y}(\mathbf{p}_Y) j_\mu u_{\lambda_N}(\mathbf{p})\right] \\ &\quad \left[\bar{u}_{\lambda_N}(\mathbf{p})\gamma^0 j^\dagger_\nu \gamma^0 u_{\lambda_Y}(\mathbf{p}_Y)\right] = \\ &= \mathrm{Tr}\left[j_\mu(\not{p} + M)\gamma^0 j^\dagger_\nu \gamma^0(\not{p}_Y + M_Y)\right], \end{aligned} \tag{2.8}$$

where j_μ is the total hadron current J^{CC}_μ, but without Dirac spinors, also known as amputated current. The structure of the baryonic part is complicated because hadrons interact strongly. For the calculation of Dirac traces, we have used the Mathematica package Feyncalc [122, 123, 124]. The hadronic current for CC-induced interaction is given by

$$J^{CC}_\mu = \bar{u}_{\lambda_Y}(\mathbf{p}_Y) j_\mu u_{\lambda_N}(\mathbf{p}) = \bar{u}_{\lambda_Y}(\mathbf{p}_Y)\left(V^{CC}_\mu - A^{CC}_\mu\right) u_{\lambda_N}(\mathbf{p}) \tag{2.9}$$

as it will be shown later. Where V^{CC}_μ and A^{CC}_μ are the CC weak vector and axial-vector hadron currents.

The Eq. (2.3) can be integrated over the momentum of the final hyperon with the δ-function of momentum conservation in the LAB frame, defined as the frame where the initial nucleon is at rest ($\mathbf{p} = 0$). We impose with the 3-momentum δ-function that $\mathbf{p_Y} = \mathbf{q} - \mathbf{p_m}$ (The reader can find more information about the kinematic in Appendix C). Then we have the 6-fold differential cross section

$$\begin{aligned} d^6\sigma &= \frac{1}{(2\pi)^5\, 4ME_{\bar{\nu}}} \frac{d^3k'}{2E'_l(\mathbf{k'})} \frac{d^3p_m}{2E_m(\mathbf{p}_m)} \frac{\delta(M + q^0 - E_Y(\mathbf{q} - \mathbf{p}_m) - E_m(\mathbf{p}_m))}{2E_Y(\mathbf{q} - \mathbf{p}_m)} \\ &\quad \overline{\sum}\sum |\mathcal{M}|^2 . \end{aligned} \tag{2.10}$$

In Eq. (2.10), we can use the δ-function of energy conservation to integrate over the polar angle θ_m that the three-momentum of the meson $\mathbf{p_m}$ forms with the direction of the three-momentum transfer $\mathbf{q}$ ($\theta^0_m = \cos^{-1}[\hat{q}\cdot\hat{p}_m]$). To that end, we have to fix the polar angle θ^0_m which makes the argument of the δ-function to be zero.

$$\begin{aligned} M + q^0 - E_Y(\mathbf{q} - \mathbf{p}_m) - E_m(\mathbf{p}_m) = 0 \\ M + q^0 - \sqrt{|\mathbf{q} - \mathbf{p_m}|^2 + M_Y^2} - E_m(\mathbf{p}_m) = 0. \end{aligned} \tag{2.11}$$

The cosine of this polar angle is given by

$$\cos\theta_m^0 = \frac{M_Y^2 + \mathbf{q}^2 + \mathbf{p}_m^2 - (M + q^0 - E_m)^2}{2\,|\mathbf{q}|\,|\mathbf{p}_m|}. \tag{2.12}$$

Note that the values of this cosine depend, in general, on other external integration variables such as $(q^0, \cos\theta_l', E_m)$.

In Eq. (2.10), if we define the solid angles $(d\Omega_{\hat{k}'}, d\Omega_{\hat{p}_m})$, the one for the final lepton with respect to the direction of incident antineutrino momentum $\mathbf{k}$, which defines the Z-axis, we can write $d^3k' = |\mathbf{k}'|^2\, d|\mathbf{k}'|\, d\Omega_{\hat{k}'} = |\mathbf{k}'| E_l'\, dE_l'\, d\Omega_{\hat{k}'}$ and the pion solid angle with respect to the direction of trimomentum transfer $\mathbf{q}$, $d^3p_m = |\mathbf{p_m}| E_m\, dE_m\, d\Omega_{\hat{p}_m}$. And integrating over the polar angle θ_m we obtain the 5-fold differential cross section,

$$d^5\sigma = \frac{1}{(2\pi)^5\, 4ME_{\bar{\nu}}}\, \frac{|\mathbf{k}'|}{8\,|\mathbf{q}|}\, \overline{\sum}\sum |\mathcal{M}|^2\, \Theta(1 - \cos^2\theta_m^0)\, dE_l'\, d\Omega_{\hat{k}'}\, dE_m\, d\phi_m, \tag{2.13}$$

where ϕ_m is the azimuthal angle of the three-momentum of the π meson on the reaction plane, measured in a plane orthogonal to the trimomentum transfer q, with respect to the $\bar{\nu}-l^+$ scattering plane. The step function (Θ) puts a constraint on the cosine of theta (θ_m^0).

Finally, integrating eq. (2.13) with respect to all the variables for a fixed antineutrino energy $E_{\bar{\nu}}$, we obtain the next expression

$$\begin{aligned}\sigma(E_{\bar{\nu}}) \;&=\; \frac{1}{(2\pi)^5\, 4ME_{\bar{\nu}}} \int d\Omega_{\hat{k}'} \int_{m_l}^{E'_{l\max}} dE_l'\, \frac{|\mathbf{k}'|}{8\,|\mathbf{q}|} \\ &\quad \int_{m_\pi}^{E_m^{\max}} dE_m\; \Theta(1 - \cos^2\theta_m^0) \int_0^{2\pi} d\phi_m\, \overline{\sum}\sum |\mathcal{M}|^2 . \end{aligned} \tag{2.14}$$

For the upper limits of integration in the energies of the final lepton and the π meson, we have chosen $E'_{l\max} = E_{\bar{\nu}} + M - M_Y - m_\pi$ and $E_m^{\max} = E_{\bar{\nu}} - E_l' + M - M_Y$. We know that these upper limits are not the most restrictive ones and, for some energies between these values, the cosine given by eq. 2.12 is out of range. In these kinematic situations the unit step function $\Theta(1 - \cos^2\theta_m^0)$ gets rid of the problem. In fact, the most restrictive bounds in the integration of the π meson energy can be found by requiring the cosine of eq. 2.12 to be always between -1 and 1. This imposes more restrictive constraints in the upper and lower limits of integration in E_m, of course, but then they also depend on the outermost integration variables (E_l', θ_l') or equivalently (q^2, q^0) in a more cumbersome way. There is axial symmetry around the Z axis, defined by the momentum of the antineutrino $\mathbf{k}$. This means that one can fix $\phi_l' = 0$ and solve the integral for this value. What happens for any other angle value will be equivalent to the result for

$\phi_l' = 0$, then it is sufficient to multiply the result of the integral for $\phi_l' = 0$ by 2π, which is the range that the azimuthal angle of the final lepton covers.

2.2 Born term model

The process of hyperon-pion production involves both non-resonant and resonant contributions. The non-resonant (NR) or background terms have been calculated using a model based on the SU(3) chiral Lagrangians, which describe the interactions between mesons and baryons in the limit of small quark masses [120]. The chiral Lagrangians constitute the low energy effective field theory of QCD, sharing its same relevant global symmetries in the limit of massless quarks: chiral symmetry, the pattern of spontaneous breaking of this symmetry,... In addition to spontaneuous symmetry breaking, these Lagrangians also incorporate terms to account for the explicit breaking of the chiral symmetry, thus providing the pseudo-Goldstone bosons (the octet of pseudoscalar mesons) with masses.

We use these chiral Lagrangians at the lowest order in the presence of an external weak charged current [120] as a tool to calculate the relevant vertices and mechanisms for the processes in order to apply the Feynman rules.

The relevant parameters for the description of the scattering amplitudes are the pion decay constant f_π, the Cabibbo angle θ_C, and the symmetric D and antisymmetric F axial-vector constants appearing in the coupling of two octets of baryon fields with another octet of pseudoscalar meson fields to form a singlet SU(3) Lagrangian. Some of these parameters are obtained from the analysis of the semileptonic decays of neutrons and hyperons [106].

Some other assumptions are used, as the Current Vector Conservation (CVC) hypothesis, in order to relate some vector form factors with others, by using SU(3) symmetry. The Partial Conservation of the Axial Current (PCAC) is used to relate the induced pseudoscalar form factor with the axial-vector one.

Meson - meson interaction

Following the Ref. [120], the lowest order chiral effective Lagrangian in the SU(3) flavor scheme for pseudoscalar mesons in the presence of an external weak charged current is written as

$$\mathcal{L}_M^{(2)} = \frac{f_\pi^2}{4}\mathrm{Tr}\left[D_\mu U (D^\mu U)^\dagger\right] + \frac{f_\pi^2}{4}\mathrm{Tr}\left[\chi U^\dagger + U\chi^\dagger\right], \tag{2.15}$$

where $f_\pi = 93$ MeV is the pion decay constant, U is the SU(3) representation of the pseudo-scalar meson octet fields

$$U(x) = \exp\left(i\frac{\phi(x)}{f_\pi}\right), \tag{2.16}$$

where

$$\phi(x) = \begin{pmatrix} \pi^0 + \frac{\eta}{\sqrt{3}} & \sqrt{2}\pi^+ & \sqrt{2}K^+ \\ \sqrt{2}\pi^- & -\pi^0 + \frac{\eta}{\sqrt{3}} & \sqrt{2}K^0 \\ \sqrt{2}K^- & \sqrt{2}\bar{K}^0 & -\frac{2}{\sqrt{3}}\eta \end{pmatrix}. \tag{2.17}$$

$D_\mu U$ and $D^\mu U^\dagger$ are the covariant derivatives, given by

$$D_\mu U = \partial_\mu U - ir_\mu U + iUl_\mu, \tag{2.18}$$
$$D^\mu U^\dagger = \partial^\mu U^\dagger + iU^\dagger r^\mu - il^\mu U^\dagger, \tag{2.19}$$

where l_μ and r_μ are left and right-handed external currents coupled to the meson fields. In the particular case of the weak charged current, these currents are

$$r_\mu = 0 \qquad l_\mu = -\frac{g}{\sqrt{2}}\left(W_\mu^+ T_+ + W_\mu^- T_-\right), \tag{2.20}$$

with $W_\mu^\pm$ the weak vector boson fields, $g = \frac{e}{sin\theta_W}$ the weak coupling constant, $\sin\theta_W$ is the sine of the Weinberg angle, and $T_\pm$ the 3×3 matrices containing the Cabibbo-Kobayashi-Maskawa matrix elements relevant for the three flavor scheme,

$$T_+ = \begin{pmatrix} 0 & V_{ud} & V_{us} \\ 0 & 0 & 0 \\ 0 & 0 & 0 \end{pmatrix}; \quad T_- = \begin{pmatrix} 0 & 0 & 0 \\ V_{ud} & 0 & 0 \\ V_{us} & 0 & 0 \end{pmatrix}. \tag{2.21}$$

Their magnitudes are $V_{ud} = cos\theta_C = 0.97435 \pm 0.00016$ and $V_{us} = sin\theta_C = 0.22500 \pm 0.00067$ [121] and θ_C being the Cabibbo angle.

Finally, in Eq. (2.15), the second term in this equation is not relevant to our study. It incorporates the explicit breaking of chiral symmetry due to the finite quark masses. With the Lagrangian given in eq. (2.15) we can obtain the relevant $WK\pi$ and $W\bar{K}$ vertices necessary for the KP and KF diagrams shown in Fig. 2.1a.

Baryon - meson interaction

For the baryons, we follow the same procedure as we do for the mesons. The lowest-order interaction between the octet of baryons, the octet of pseudoscalar mesons and the weak external current can also be introduced (following Ref. [120]) as

$$\begin{aligned}\mathcal{L}_{MB}^{(1)} &= \mathrm{Tr}\left[\bar{B}(i\not{D}-M)B\right] \\ &+ \frac{D}{2}\mathrm{Tr}\left[\bar{B}\gamma^\mu\gamma_5\left\{u_\mu,B\right\}\right]+\frac{F}{2}\mathrm{Tr}\left[\bar{B}\gamma^\mu\gamma_5\left[u_\mu,B\right]\right], \end{aligned}\tag{2.22}$$

where M denotes the mass of the baryon octet, $D(=0.804)$ and $F(=0.463)$ are the symmetric and antisymmetric axial-vector coupling constants for the baryon octet determined from the semileptonic decays of the neutron and hyperons [106]. The two independent couplings appear because in the Clebsch-Gordan series of the direct product $\{8\}\otimes\{8\}$ of two SU(3) octets, the $\{8\}$ representation is contained twice. And $B(x)$ is the SU(3) representation of the baryon fields

$$B=\begin{pmatrix} \frac{1}{\sqrt{2}}\Sigma^0+\frac{1}{\sqrt{6}}\Lambda & \Sigma^+ & p \\ \Sigma^- & -\frac{1}{\sqrt{2}}\Sigma^0+\frac{1}{\sqrt{6}}\Lambda & n \\ \Xi^- & \Xi^0 & -\frac{2}{\sqrt{6}}\Lambda \end{pmatrix}. \tag{2.23}$$

In this case, the covariant derivative of the baryon fields is given in terms of the connection Γ_μ as

$$D_\mu B=\partial_\mu B+\left[\Gamma_\mu,B\right], \tag{2.24}$$

with

$$\Gamma_\mu=\frac{1}{2}\left[u^\dagger\left(\partial_\mu-ir_\mu\right)u+u\left(\partial_\mu-il_\mu\right)u^\dagger\right]. \tag{2.25}$$

In Eq. (2.25) we have introduced

$$u=\sqrt{U}=\exp\left(i\frac{\phi(x)}{2f_\pi}\right)$$

Also, in Eq. (2.22), the definition of the so-called vielbein, u_μ, is given by

$$u_\mu=i\left[u^\dagger\left(\partial_\mu-ir_\mu\right)u-u\left(\partial_\mu-il_\mu\right)u^\dagger\right]. \tag{2.26}$$

The Lagrangian of Eq. (2.22) allows extracting all the necessary vertices NYK, $NYK\pi$, $NYW\pi$, and the leading order vector and axial-vector terms for the $N-Y$ strangeness-changing weak transitions for the diagrams depicted in Fig. 2.1a.

Hadronic current

In order to calculate the hadronic current for CC-induced interaction, the matrix elements of the vector (V_μ) and the axial-vector (A_μ) currents between a hyperon Y (Λ, Σ^-, Σ^0 and Σ^+) and a nucleon N (p and n) are given by

$$\begin{aligned}
\langle Y(p_Y)| V^\mu |N(p)\rangle &= \bar{u}_Y(\mathbf{p}_Y)[f_1^{NY}(q^2)\gamma^\mu \\
&+ i\frac{f_2^{NY}(q^2)}{M+M_Y}\sigma^{\mu\nu}q_\nu + \frac{f_3^{NY}(q^2)}{M+M_Y}q^\mu]u_N(\mathbf{p}) \qquad (2.27)\\
\langle Y(p_Y)| A^\mu |N(p)\rangle &= \bar{u}_Y(\mathbf{p}_Y)[g_1^{NY}(q^2)\gamma^\mu\gamma_5 \\
&+ i\frac{g_2^{NY}(q^2)}{M+M_Y}\sigma^{\mu\nu}\gamma_5 q_\nu + \frac{g_3^{NY}(q^2)}{M+M_Y}q^\mu\gamma_5]u_N(\mathbf{p}). \qquad (2.28)
\end{aligned}$$

where $q^2 = (k-k')^2$ is the four momentum transfer squared. M and M_Y are the initial nucleon and the final hyperon masses, respectively. $f_1^{NY}(q^2)$, $f_2^{NY}(q^2)$ and $f_3^{NY}(q^2)$ are the vector, weak magnetic and induced scalar N - Y transition form factors and $g_1^{NY}(q^2)$, $g_2^{NY}(q^2)$ and $g_3^{NY}(q^2)$ are the axial-vector, induced pseudotensor (or weak electric) and induced pseudoscalar form factors, respectively. We follow the Bjorken Drell [126] conventions for the Dirac matrices when defining these transition matrix elements.

Form factors

The weak transition form factors $f_i^{NY}(q^2)$ and $g_i^{NY}(q^2)$ are determined using Cabibbo theory, which is extended to the strange sector with the application of SU(3) symmetry. Time reversal invariance requires that the form factors be real. The Cabibbo assumptions reduce the number of independent form factors. The conserved vector current (CVC) hypothesis, proposed by Gershtein and Zeldovich [127] and Feynman and Gell-Mann [8], leads to the vector part of the weak charged current being conserved. They proposed a stronger hypothesis of the isotriplet of the vector currents. This hypothesis implies that the form factors of the weak vector current can be described in terms of the electromagnetic form factors of nucleons. Specifically, the vector form factors are expressed in terms of the electromagnetic form factors $f_{1,2}^{p,n}(q^2)$, where $f_1^{p,n}(q^2)$ and $f_2^{p.n}(q^2)$ are the Dirac and Pauli form factors for the proton and neutron, respectively. Unlike the vector current, the axial-vector current is not conserved. To obtain the axial-vector form factors, we use the partial conservation of axial vector current (PCAC). The axial form factors come from the Lagrangian, at $q^2 = 0$. PCAC is used to relate the pseudoscalar form factor ($g_3(q^2)$) to the axial form factor ($g_1(q^2)$). This assumed relationship, which is assumed to be exact, since deriving it does assume the conservation of the axial current, would be like this if the meson masses were zero. As they are not zero, but are small, there is no conservation of the axial current, but rather its partial conservation, which would be exact in the limit where the Goldstone bosons had zero mass. To take into account the q^2-dependence of the couplings obtained from the Lagrangians, we assume the validity of the Cabibbo model. This implies that the relevant vector form factors can be related to the proton and neutron electromagnetic ones due to the assumption of SU(3) symmetry and the conservation of the vector current (CVC) hypothesis. On the other hand, for the axial-vector form factors, we assume that symmetric (d-type) and antisymmetric (f-type) form factors have the same q^2-dependence and we relate them to the axial-vector form factor of the nucleon.

The Lagrangian of Eq. (2.22) provides the values for the vector and axial couplings (form factors at $q^2 = 0$) $f_1^{NY}(0)$ and $g_1^{NY}(0)$, but not for the others, which appear at higher orders of the chiral expansion. Particularly, we are interested in the relevant couplings $f_2^{NY}(0)$ and $g_3^{NY}(0)$. These couplings are known as the weak magnetism and the induced pseudoscalar ones, respectively. However, using symmetry arguments, some of these form factors can be neglected, as we will explain in the following lines. For example, the weak electric form factor ($g_2^{NY}(q^2)$) and the scalar form factor ($f_3^{NY}(q^2)$) transform as second-class currents under G-parity [128] and are neglected in the present calculations. We assume that G-parity is a good quantum number for strong interactions, and in the Standard Model there are no second-class currents. Thus, G-parity invariance leads to neglecting the contribution of g_2 and f_3. Additionally, the CVC hypothesis, which implies $\partial_\mu V^\mu(x) = 0$, requires $f_3(q^2) = 0$. Some properties of the form factors can be extracted from the behaviour of the different components of the current under the discrete symmetries of the Dirac theory. Time reversal ($\mathcal{T}$) invariance implies that the form factors $f_i^{NY}(q^2)$ and $g_i^{NY}(q^2)$ have to be real [129].

Therefore, in the case of CC interactions, the hadronic currents contain two vector form factors $f_{1,2}^{NY}(q^2)$, which can be related to linear combinations of the electromagnetic Dirac $f_{1,2}^p(q^2)$ and Pauli $f_{1,2}^n(q^2)$ form factors using SU(3) symmetry. To obtain the form factors of the axial-vector current, we work in the limit of $m_\pi \to 0$, where the axial-vector current is conserved, and using the hypothesis of Partial Conservation of the Axial Current (PCAC), we can relate the pseudoscalar $g_3^{NY}(q^2)$ form factor with the axial $g_1^{NY}(q^2)$ one in this limit. Later, we extrapolate the meson pole to incorporate the meson mass. The non-zero form factors are obtained using the SU(3) symmetry and PCAC.

In the present scheme, the most standard way to obtain the $f_2(0)$ couplings is to include the relevant pieces of the next higher order meson-baryon chiral Lagrangian [120] and to match the low energy constants to well-known $f_2(0)$ transition form factors, which can be obtained from Table I of Ref.[106]. For this purpose, we add the relevant piece

$$\mathcal{L}^{(2)}_{MB} = d_4 \mathrm{Tr}\left[\bar{B}\sigma^{\mu\nu}\left\{f^+_{\mu\nu}, B\right\}\right] + d_5 \mathrm{Tr}\left[\bar{B}\sigma^{\mu\nu}\left[f^+_{\mu\nu}, B\right]\right], \tag{2.29}$$

where the tensor flavor matrix $f^+_{\mu\nu}$ can be reduced to

$$f^+_{\mu\nu} = \partial_\mu l_\nu - \partial_\nu l_\mu - i\left[l_\mu, l_\nu\right]. \tag{2.30}$$

Furthermore, these new terms couple two octet baryons to the derivative of the $W^\pm_\mu$ bosons, resulting in the appearance of a contracted four-momentum transfer (q) carried by them with the Lorentz index of the Dirac matrices $\sigma^{\mu\nu}$ after applying the Feynman rules. By appropriately matching the two low energy constants d_4 and d_5 to give the correct $f_2(0)$ couplings for the weak transitions $n \longrightarrow p$ and $p \longrightarrow \Lambda$, in accordance with the data provided in Table I of Ref.[106], we obtain

$$d_4 = \frac{-3\mu_n}{16M}; \qquad d_5 = \frac{2\mu_p + \mu_n}{16M}, \tag{2.31}$$

where μ_p and μ_n are the anomalous magnetic moments of the proton and neutron, respectively. After matching these low-energy constants, all the $f_2^{NY}(0)$ weak couplings for all the possible transitions between a nucleon and a hyperon are uniquely determined. Their q^2-dependence can be expressed in terms of the electromagnetic $f_2^p(q^2)$ and $f_2^n(q^2)$ Pauli form factors, which are normalized such that $f_2^p(0) = \mu_p$ and $f_2^n(0) = \mu_n$, respectively.

These results could also have been obtained by assuming exact SU(3) symmetry and noticing that the weak vector currents and the electromagnetic current belong to the same octet of current operators of the SU(3) group. As the octet $\{8\}$ representation appears twice in the Clebsch-Gordan series for the tensor product of two octets

$$\{8\} \otimes \{8\} = \{1\} \oplus \{8\} \oplus \{8'\} \oplus \{10\} \oplus \left\{\overline{10}\right\} \oplus \{27\}, \tag{2.32}$$

this implies that *any octet irreducible tensor operator connecting two octet baryons has two independent irreducible matrix elements.* Therefore, it is necessary to explicitly calculate two independent matrix elements for an octet operator. Later, using the SU(3) Wigner-Eckart theorem, all the non-vanishing matrix elements between octet states connected through an octet current operator can be related using the SU(3) Clebsch-Gordan coefficients, which can be found in the Ref. [130], along with the previous explicitly calculated two matrix elements. In the case of the octet of vector currents, these two irreducible matrix elements can be expressed in terms of the proton and neutron electromagnetic current matrix elements, $\langle p| J^\mu_{\rm em} |p\rangle$ and $\langle n| J^\mu_{\rm em} |n\rangle$. This facilitates us to express all the $N \rightleftharpoons Y$ transition vector form factors in terms of those, $f^{p,n}_{1,2}(q^2)$, of the electromagnetic interaction, that is well measured. They are summarized in Table 2.1, and for this work we use the Galster parametrization [131] of the electromagnetic form factors.

$i = 1, 2$	$Y = \Lambda$	$Y = \Sigma^0$	$Y = \Sigma^-$
$f_i^{pY}(q^2)$	$-\sqrt{\frac{3}{2}} f_i^p(q^2)$	$-\frac{1}{\sqrt{2}}\left(f_i^p(q^2) + 2 f_i^n(q^2)\right)$	0
$f_i^{nY}(q^2)$	0	0	$-\left(f_i^p(q^2) + 2 f_i^n(q^2)\right)$

Table 2.1: Dirac and Pauli vector form factors for the weak strangeness-changing transitions considered in this work.

We can express the Dirac and Pauli form factors of the two nucleons in terms of the electric and magnetic form factors of the proton and the neutron, with $\tau = \frac{q^2}{4M^2}$, as

$$f_1^{p,n} = \frac{G_E^{p,n} - \tau G_M^{p,n}}{1-\tau}; \qquad f_2^{p,n} = \frac{G_M^{p,n} - G_E^{p,n}}{1-\tau}. \tag{2.33}$$

The explicit expressions for the electric and magnetic form factors and for present [131]

$$\begin{aligned} G_E^p &= \frac{1}{\left(1 - \frac{q^2}{M_V^2}\right)^2}; \qquad G_M^p = (1+\mu_p)\, G_E^p \\ G_E^n &= \frac{\tau \mu_n}{(1-\tau\lambda_n)^2} G_E^p; \qquad G_M^n = \mu_n G_E^p \end{aligned} \tag{2.34}$$

with $M_V = 0.84$ GeV (The numerical value of the vector dipole mass is taken from experimental data on electron proton scattering [125]), $\mu_p = 1.792$, $\mu_n = -1.913$, and $\lambda_n = 5.6$.

Something similar happens for the axial-vector currents in the Cabibbo model. However, in this case, there are not two well-measured independent transition matrix elements to be used to express univocally the rest of the transition matrix elements driven by the weak axial current. The only one we have is the $n \longrightarrow p$ weak transition, from where one can extract the axial coupling of the nucleon,

$g_A(0) = g_1^{np}(0) = 1.267$, which is determined experimentally from the β decay of the neutron. Normally, its q^2 - dependence is assumed to take a dipole form with an axial mass of $M_A = 1.03$ GeV,

$$g_A(q^2) = \frac{g_A(0)}{\left(1 - \frac{q^2}{M_A^2}\right)^2}, \tag{2.35}$$

where $g_A(0) = D + F$. One assumption that has been extensively used in past works ([85, 86, 119, 132, 133]) is that the q^2 - dependence acquired by the D and F couplings is identical and driven by the dependence on q^2 of the nucleon axial form factor $g_A(q^2)$. Under this assumption, we can write

$$\begin{aligned} g_1^{NY}(q^2) &= aD_A(q^2) + bF_A(q^2) = \frac{aD + bF}{\left(1 - \frac{q^2}{M_A^2}\right)^2} \\ &= \frac{aD + bF}{D + F} \frac{g_A(0)}{\left(1 - \frac{q^2}{M_A^2}\right)^2} = \frac{aD + bF}{D + F} g_A(q^2), \end{aligned} \tag{2.36}$$

where a and b are factors related to the SU(3) Clebsch-Gordan coefficients, and D_A and F_A are normalized to D and F couplings at $q^2 = 0$. The values for these axial-vector form factors are tabulated in Table 2.2 for the transitions of interest for our work.

	$Y = \Lambda$	$Y = \Sigma^0$	$Y = \Sigma^-$
$g_1^{pY}(q^2)$	$-\sqrt{\frac{1}{6}}(1 + 2x)g_A(q^2)$	$\frac{1}{\sqrt{2}}(1 - 2x)g_A(q^2)$	0
$g_1^{nY}(q^2)$	0	0	$(1 - 2x)g_A(q^2)$

Table 2.2: $g_1^{NY}(q^2)$ axial-vector form factors for the weak strangeness-changing transitions considered in this work. The definition of $x = \frac{F}{D+F}$ is taken for simplicity in the formulae.

Finally, invoking Partial Conservation of the Axial Current (PCAC) in the chiral limit, we can relate the induced pseudo-scalar $g_3^{NY}(q^2)$ form factor with the axial one, $g_1^{NY}(q^2)$. The hypothesis of PCAC is that the axial current coupled to $W_\mu^\pm$ bosons is the derivative of a pseudo-scalar charged meson field ($\pi^\pm$ and $K^\pm$ mesons) because both operators carry the same quantum numbers of an axial current. Under this assumption, the derivative of the axial current is proportional to the meson field and its mass, by using the equations of motion of a Klein-Gordon spinless field,

$$A^\mu(x) = \partial^\mu \phi(x) \Longrightarrow \partial_\mu A^\mu = \partial_\mu \partial^\mu \phi = -m_\phi^2 \phi, \tag{2.37}$$

where $\phi(x)$ is any of the charged meson fields of Eq.(2.17). In the chiral limit, $m_\phi \longrightarrow 0$, the axial current is divergenceless and conserved in this limit. This allows us to take the divergence in momentum space (contraction with $q_\mu = p_{Y\mu} - p_\mu$) of Eq. (2.28) and equate it to zero. Making use of the Dirac equations for the on-shell spinors, we obtain the following relation between the pseudoscalar $g_3^{NY}(q^2)$ form factor the axial one, $g_1^{NY}(q^2)$:

$$g_3^{NY}(q^2) = -g_1^{NY}(q^2)\frac{(M+M_Y)^2}{q^2}. \tag{2.38}$$

Lastly, to take into account the non-vanishing meson masses, the denominator is extrapolated from q^2 to a kaon pole, $q^2 - M_K^2$, for strangeness-changing axial weak charged currents. This is called the kaon-pole dominance [134], and it is equivalent to assuming that the induced pseudoscalar form factor is generated through the coupling of the W^- boson to the baryons through a K^-, as depicted in Fig. 2.2. Although the kaon-pole dominance is expected to work worse than the pion-pole dominance for non-strangeness-changing weak axial currents, the contribution of the pseudo-scalar form factor $g_3^{NY}(q^2)$ is proportional to q^μ in every axial current. When contracted this momentum transfer with the lepton tensor, its contribution is proportional to the final charged lepton mass, and therefore really minor for muon and electron antineutrinos induced reactions.

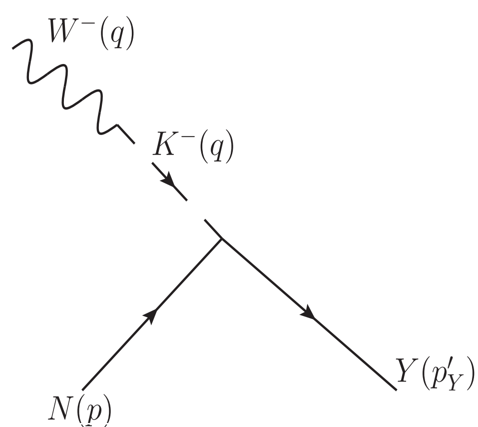

Figure 2.2: Feynman diagram illustrating the generation of the pseudo-scalar term in the axial-vector current.

While deriving eq. (2.38), the baryons in Fig. 2.2 are taken as on-shell. The off-shellness of intermediate baryons in the s-Σ, s-Λ and u-N diagrams (shown in Fig. (2.1a)) can be restored by replacing the $(M + M_Y)$ in the numerator with an operator that reduces to this factor when both baryons are on-shell. That can easily be achieved by substituting the axial vertex of eq. (2.28) by

$$\langle Y(p_Y)|\, A^\mu \,|N(p)\rangle = g_1^{NY}(q^2)\, \bar{u}_Y(\mathbf{p}_Y) \left(\gamma^\mu\gamma_5 - \frac{q^\mu \not{q}}{q^2 - M_K^2}\gamma_5\right) u_N(\mathbf{p}), \qquad (2.39)$$

where we used the relationship,

$$\bar{u}_Y(\mathbf{p}_Y)\not{q}\gamma_5 u_N(\mathbf{p}) = (M + M_Y)\, \bar{u}_Y(\mathbf{p}_Y)\gamma_5 u_N(\mathbf{p}) \qquad (2.40)$$

when both baryons are on-shell.

Finally, once the form factors is known (the vector $f_{1,2}^{NY'}(q^2)$ and axial-vector $g_1^{NY'}(q^2)$ form factors given in Tables 2.1 and 2.2, respectively), we can write the vector and axial-vector weak vertices as

$$V^\mu_{NY'}(q) = f_1^{NY'}(q^2)\gamma^\mu + \frac{i f_2^{NY'}(q^2)}{M + M_{Y'}}\sigma^{\mu\nu}q_\nu \qquad (2.41)$$

$$A^\mu_{NY'}(q) = g_1^{NY'}(q^2)\left(\gamma^\mu - \frac{q^\mu\not{q}}{q^2 - M_K^2}\right)\gamma_5. \qquad (2.42)$$

Now, applying the Feynman rules to the vertices and propagators appearing in Fig. 2.1a, which can be extracted from the Lagrangians given in Eqs. (2.15) and (2.22), we obtain the following hadron currents for the Born term diagrams:

$$J^\mu_{\mathrm{CT}} = i\, V_{us}\, \mathcal{A}_{\mathrm{CT}}^{N\to Y\pi}\; F_D(q^2)\; \bar{u}_Y(\mathbf{p}_Y)\left[\gamma^\mu - a^{N\to Y\pi}\gamma^\mu\gamma_5\right] u_N(\mathbf{p}) \qquad (2.43)$$

$$J^\mu_{\mathrm{KP}} = i\, V_{us}\, \mathcal{A}_{\mathrm{KP}}^{N\to Y\pi}\; F_D(q^2)\; \frac{q^\mu}{q^2 - M_K^2}\; \bar{u}_Y(\mathbf{p}_Y)\left[\not{q} - \frac{(M_Y - M)}{2}\right] u_N(\mathbf{p}) \qquad (2.44)$$

$$J^\mu_{\mathrm{KF}} = i\, V_{us}\, \mathcal{A}_{\mathrm{KF}}^{N\to Y\pi}\; F_D(q^2)\; \frac{2p_m^\mu - q^\mu}{(p_m - q)^2 - M_K^2}\; (M_Y + M)\, \bar{u}_Y(\mathbf{p}_Y)\gamma_5 u_N(\mathbf{p}) \qquad (2.45)$$

$$J^\mu_{\mathrm{s-Y'}} = i\, V_{us}\, \mathcal{A}_{\mathrm{s-Y'}}^{N\to Y\pi}\; \bar{u}_Y(\mathbf{p}_Y)\not{p}_m\gamma_5\; \frac{\not{p} + \not{q} + M_{Y'}}{(p+q)^2 - M_{Y'}^2}\; \left[V^\mu_{NY'}(q) - A^\mu_{NY'}(q)\right] u_N(\mathbf{p}) \qquad (2.46)$$

$$J^\mu_{\mathrm{u-N'}} = i\, V_{us}\, \mathcal{A}_{\mathrm{u-N'}}^{N\to Y\pi}\; \bar{u}_Y(\mathbf{p}_Y)\left[V^\mu_{N'Y}(q) - A^\mu_{N'Y}(q)\right] \frac{\not{p} - \not{p}_m + M}{(p - p_m)^2 - M^2}\; \not{p}_m\gamma_5 u_N(\mathbf{p}), \qquad (2.47)$$

where $Y, Y' = \Sigma, \Lambda$; $N, N' = p, n$; $F_D(q^2)$ is a global dipole form factor for the CT, KP and KF diagrams to treat on a similar footing these diagrams with those with a hyperon Y' or a nucleon N' propagating, which also have form factors in the weak vertices. We assume for simplicity the following form for this dipole form factor

$$F_D(q^2) = \frac{1}{\left(1 - \frac{q^2}{M_D^2}\right)^2}, \quad M_D \simeq 1 \text{ GeV}. \tag{2.48}$$

This same assumption for this global dipole form factor has also been taken in other works such as those of Refs. ([100],[116]-[118]). In Eqs. (2.43)-(2.47), the $\mathcal{A}_i^{N\to Y\pi}$ are global constants that depend on the particular reaction, and they are given in Table 2.3.

Reaction	$\mathcal{A}_{\rm CT}^{N\to Y\pi}$	$a^{N\to Y\pi}$	$\mathcal{A}_{\rm KP}^{N\to Y\pi}$	$\mathcal{A}_{\rm KF}^{N\to Y\pi}$	$\mathcal{A}_{\rm s-\Sigma}^{N\to Y\pi}$	$\mathcal{A}_{\rm u-N'}^{N\to Y\pi}$	$\mathcal{A}_{\rm s-\Lambda}^{N\to Y\pi}$
$p\to\pi^0+\Lambda$	$\frac{\sqrt{3}}{2\sqrt{2}f_\pi}$	$F+\frac{D}{3}$	$-\frac{\sqrt{3}}{2\sqrt{2}f_\pi}$	$-\frac{(D+3F)}{2\sqrt{6}f_\pi}$	$\frac{D}{\sqrt{3}f_\pi}$	$\frac{D+F}{2f_\pi}$	0
$n\to\pi^-+\Lambda$	$\frac{\sqrt{3}}{2f_\pi}$	$F+\frac{D}{3}$	$-\frac{\sqrt{3}}{2f_\pi}$	$-\frac{(D+3F)}{2\sqrt{3}f_\pi}$	$\frac{D}{\sqrt{3}f_\pi}$	$\frac{D+F}{\sqrt{2}f_\pi}$	0
$p\to\pi^0+\Sigma^0$	$\frac{1}{2\sqrt{2}f_\pi}$	$F-D$	$-\frac{1}{2\sqrt{2}f_\pi}$	$\frac{(D-F)}{2\sqrt{2}f_\pi}$	0	$\frac{D+F}{2f_\pi}$	$\frac{D}{\sqrt{3}f_\pi}$
$p\to\pi^-+\Sigma^+$	$\frac{1}{\sqrt{2}f_\pi}$	$F-D$	$-\frac{1}{\sqrt{2}f_\pi}$	$\frac{(D-F)}{\sqrt{2}f_\pi}$	$-\frac{F}{f_\pi}$	0	$\frac{D}{\sqrt{3}f_\pi}$
$p\to\pi^++\Sigma^-$	0	0	0	0	$\frac{F}{f_\pi}$	$\frac{D+F}{\sqrt{2}f_\pi}$	$\frac{D}{\sqrt{3}f_\pi}$
$n\to\pi^-+\Sigma^0$	$-\frac{1}{2f_\pi}$	$F-D$	$\frac{1}{2f_\pi}$	$\frac{(F-D)}{2f_\pi}$	$\frac{F}{f_\pi}$	$\frac{D+F}{\sqrt{2}f_\pi}$	0
$n\to\pi^0+\Sigma^-$	$\frac{1}{2f_\pi}$	$F-D$	$-\frac{1}{2f_\pi}$	$\frac{(D-F)}{2f_\pi}$	$-\frac{F}{f_\pi}$	$-\frac{D+F}{2f_\pi}$	0

Table 2.3: Constants $\mathcal{A}_i^{N\to Y\pi}$ and $a^{N\to Y\pi}$ (for the axial-vector piece of the CT diagram) for each $\bar{\nu}_l + N \to l^+ + \pi + Y$ reaction and diagram in our model.

For explain why some of the values of the $\mathcal{A}_i^{N\to Y\pi}$ constants are zero, we provide the following arguments

- If the initial nucleon is a neutron, the $\mathcal{A}_{\rm s-\Lambda}^{n\to Y\pi}$ is always zero because the transition $n\to\Lambda$ by absorbing a W^- is forbidden by charge conservation in the weak vertex.

- For the channel $p\to\Lambda+\pi^0$, while the weak vertex is allowed, the strong one is forbidden because of the non-conservation of the isospin. Indeed, the coupling of isospin 0 (that of the Λ particle) with isospin 1 of the pion cannot give total isospin 0 (that of the intermediate propagating Λ). Because of this and the previous argument, the final Λ and Σ production channels off neutrons are going to be much less affected by the presence of Λ resonances, in particular the $\Lambda(1405)$, whose role was studied in Ref. [100] for antineutrino induced $\Lambda(1405)$ production off protons, and its effect was particularly studied in the final $\Sigma\pi$ channel. However, it is impossible for the $\Lambda(1405)$

to strongly decay into a Lambda and a pion regardless of the initial nucleon due to isospin non-conservation.

- The constant $\mathcal{A}_{\mathrm{s-\Sigma}}^{p\to\Sigma^0\pi^0}$ is zero because the intermediate Σ hyperon is a neutral one and the coupling $\Sigma^0\Sigma^0\pi^0$ is proportional to the Clebsch-Gordan coefficient for the composition of two states $|1,0\rangle \otimes |1,0\rangle$ to give again a state of isospin $|1,0\rangle$. This Clebsch- Gordan coefficient is zero.

- The constants $\mathcal{A}_{\mathrm{u-N'}}^{p\to\Sigma^+\pi^-}$ and $\mathcal{A}_{\mathrm{KF}}^{p\to\Sigma^-\pi^+}$ are also zero because these diagrams would involve the interchange of a nucleon (N^{++}) and a kaon (K^{++}) with impossible charge states, respectively.

- The fact that the CT and KP diagrams for the $p \to \Sigma^-\pi^+$ channel are zero and not for the other ones can be explained with the help of Figs. 2.3a and 2.3b. The key is not to need to emit gluons in these diagrams, i.e, that the virtual $s\bar{u}$ pair (K^-) in which the W^- decays could be redistributed along with the valence quarks of the initial nucleon in the two final hadrons, the hyperon and the pion, but without the need of emitting gluons to create a $q\bar{q}$ pair of the same flavor. It seems to be a kind of OZI forbidding rule because the valence quarks of the initial W^-N state get fully redistributed into the final $Y\pi$ state without any gluon emission. This is totally possible for all the channels except for the $W^-p \to \Sigma^-\pi^+$ as shown in Fig. 2.3b. Notice that the $\bar{u}$ antiquark coming out from the decay of the W^- is not present in the final state. Therefore, it is completely necessary to annihilate it with an u quark via gluon emission to have the right quarks in the final state.

  As the $s\bar{u}$ quark-antiquark pair has the same quantum numbers as the K^-, this argument holds not only for the CT diagram but for the KP as well.

2.3 Resonance model

To describe the currents of the resonance diagrams depicted in Fig. 2.1b, we use the same approach followed in Refs. ([40, 84, 117, 119]) and include the lowest lying resonances belonging to the decuplet representation of the SU(3) group. At intermediate energies, the weak excitation of the $\Delta(1232)$ resonance and its subsequent decay into $N\pi$ dominates in pion production processes [40]. The resonance channels that we are considering in the $Y\pi$ production are those involving the $\Delta(1232)$ and $\Sigma^*(1385)$ resonances. These resonant states, when there is a change in strangeness (as in the cases we are studying in this thesis),

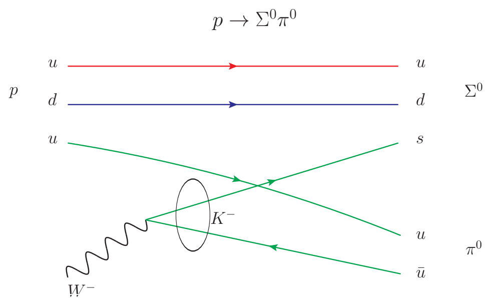

(a) In this diagram for the channel $p \to \Sigma^0\pi^0$, the valence quarks of the initial state particles can be fully accommodated in the final state particles without any gluon emission.

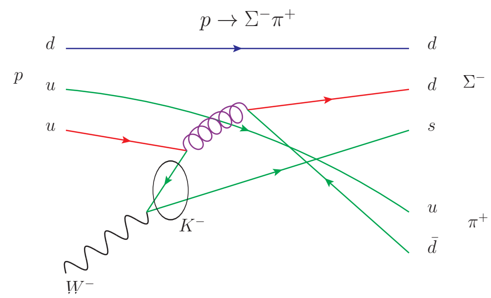

(b) In this diagram for the channel $p \to \Sigma^-\pi^+$, all the valence quarks of the initial state particles cannot be fully accommodated in the final state particles without gluon emission and the creation of a $d\bar{d}$ pair.

Figure 2.3: Two possible Feynman diagrams in terms of quarks and gluons to explain why the CT and KP diagrams are forbidden for the $p \to \Sigma^-\pi^+$ reaction channel but not for the others. The colored quark lines represent their possible colors in QCD to make colorless initial and final hadrons.

which may appear in the s-channel and u-channel are $\Sigma^*(1385)$ and $\Delta(1232)$, respectively. Though the $\Delta(1232)$ resonances are widely studied in the literature, there is less information available for the $\Sigma^*(1385)$ resonances. However, we know that both $\Sigma^*(1385)$ and $\Delta(1232)$ are members of the same decuplet, therefore under the assumption of exact SU(3) flavor symmetry for the couplings and using the Eq. (2.32), the weak transition form factors connecting an octet state to a decuplet state can be obtained. That means. in the end, it involves connecting a state of the octet with one of the decuplet using a current operator that belongs to the octet representation of the SU(3) flavor group. To connect one state to the other, there must be an operator that allows for that transition, and that operator is precisely the charged weak current that changes strangeness.

Hadronic current

All the weak transition form factors from an octet state to a decuplet state can be related between themselves (assuming exact SU(3) flavor symmetry for the couplings) if one knows these couplings for just one transition matrix element. The reason for this is, again, the assumption that the weak charged current belongs to the octet representation of current operators of the SU(3) group, and to couple one octet state with one decuplet state through an octet current operator, the representation $\{10\}$ appears only once in the Clebsch-Gordan series of eq. (2.32). Therefore, there is only one independent reduced matrix element. We will take for the latter the transition matrix element as:

$$\left\langle \Delta^+(p_R)\right| j^\mu_{\Delta S=0} \left|n(p)\right\rangle = \bar{u}_\alpha(\mathbf{p}_R)\Gamma^{\alpha\mu}(p,q)u(\mathbf{p}), \tag{2.49}$$

with $p_R = p+q$. In eq. (2.49), $\Gamma^{\alpha\mu}(p,q)$ is the vertex function given by

$$\begin{aligned}
\Gamma^{\alpha\mu}(p,q) &= [V^{\alpha\mu}\gamma_5 - A^{\alpha\mu}\mathbb{I}_4] \\
&= \left[\frac{C_3^V}{M}\left(g^{\alpha\mu}\not{q} - q^\alpha\gamma^\mu\right) + \frac{C_4^V}{M^2}\left(g^{\alpha\mu} q\cdot(p+q) - q^\alpha(p+q)^\mu\right)\right. \\
&+ \left.\frac{C_5^V}{M^2}\left(g^{\alpha\mu} q\cdot p - q^\alpha p^\mu\right) + C_6^V g^{\alpha\mu}\right]\gamma_5 + \left[\frac{C_3^A}{M}\left(g^{\alpha\mu}\not{q} - q^\alpha\gamma^\mu\right)\right. \\
&+ \left.\frac{C_4^A}{M^2}\left(g^{\alpha\mu} q\cdot(p+q) - q^\alpha(p+q)^\mu\right) + C_5^A g^{\alpha\mu} + \frac{C_6^A}{M^2} q^\alpha q^\mu\right],
\end{aligned} \tag{2.50}$$

$V^{\alpha\mu}$ and $A^{\alpha\mu}$ represent the vector and axial-vector currents for transitions from a spin-parity $\frac{1}{2}^+$ baryon to a spin-parity $\frac{3}{2}^+$ resonances, $\bar{u}_\alpha(\mathbf{p}_R)$ is a Rarita-Schwinger spinor describing spin-$\frac{3}{2}$ particles, C_i^V and C_i^A are the vector and axial-vector CC transition form factors which are functions of q^2. The conserved vector current hypothesis leads to $C_6^V(q^2) = 0$. And $j^\mu_{\Delta S=0}$ is the strangeness-preserving weak charged current coupled to an incoming W^+ boson, which at the quark level is given by

$$j^\mu_{\Delta S=0} = \bar{Q}\gamma^\mu\left(1-\gamma_5\right)\left(F_1 + iF_2\right)Q, \tag{2.51}$$

with $F_i = \frac{\lambda_i}{2}$, $Q = (uds)^T$ the triplet of the light quarks, and λ_i the Gell-Mann matrices, that are summarised in Appendix A. The above current transforms under SU(3) group as an isovector current carrying "magnetic" quantum numbers $(1,1,0)$ of SU(3) for (I, I_3, Y), being I the total isospin, I_3 its third component and Y the hypercharge. Note that the Cabibbo-Kobayashi-Maskawa matrix element, V_{ud}, which would go into the current, is not being considered in the discussion of the transformation properties of this current operator under SU(3).

However, for our weak transitions of Fig. 2.1b, we are interested in the strangeness-changing weak charged current, given at the quark level by

$$j^\mu_{\Delta S=-1} = \bar{Q}\gamma^\mu\left(1-\gamma_5\right)\left(F_4 - iF_5\right)Q, \tag{2.52}$$

This current transform as an isodoublet carrying "magnetic" quantum numbers $\left(\frac{1}{2}, -\frac{1}{2}, -1\right)$ of SU(3), i.e, it can change the total isospin of the initial state by $\pm\frac{1}{2}$, its third component by $-\frac{1}{2}$, and the hypercharge (and therefore the strangeness) by -1.

Nevertheless, both currents (Eqs. (2.51) and (2.52)) belong to the octet representation of SU(3) currents and their reduced matrix element for the composition $\{8\} \otimes \{8\} \to \{10\}$ is the same. This means that all the vector and axial-vector $C_i^{V,A}(q^2)$ transition form factors appearing in eq. (2.50) for all the allowed transitions can be written just in terms of those for a known transition.

A systematic way of obtaining the relationships (SU(3) factors) between the weak vertices for all the allowed transitions and that for the $n \to \Delta^+$ (given in eq. (2.50)) is to use the lowest order Lagrangian that couples the decuplet baryons with the octet baryons and mesons in the presence of an external current [135, 136] and that was already used in Refs. [117, 118, 119]. Its form is

$$\mathcal{L}_{\rm dec} = \mathcal{C}\left(\epsilon^{abc}\,\overline{T}^{\mu}_{ade}(u_\mu)^d_b\,B^e_c + \epsilon^{abc}\bar{B}^c_e(u_\mu)^b_d\,T^{\mu}_{aed}\right), \tag{2.53}$$

where the parameter $\mathcal{C}$ is the decuplet-baryon-meson strong coupling constant, B is given by Eq. (2.23), u_μ is the vielbein of Eq. (2.26), and T^{μ}_{aed} is the SU(3) representation of the Rarita-Schwinger fields for the decuplet baryons. This representation is completely symmetric, which in the present notation is given by a 3 x 3 x 3 array of the next matrices

$$T_{ubc} = \begin{pmatrix} \Delta^{++} & \frac{1}{\sqrt{3}}\Delta^{+} & \frac{1}{\sqrt{3}}\Sigma^{*+} \\ \frac{1}{\sqrt{3}}\Delta^{+} & \frac{1}{\sqrt{3}}\Delta^{0} & \frac{1}{\sqrt{6}}\Sigma^{*0} \\ \frac{1}{\sqrt{3}}\Sigma^{*+} & \frac{1}{\sqrt{6}}\Sigma^{*0} & \frac{1}{\sqrt{3}}\Xi^{*0} \end{pmatrix}, \tag{2.54}$$

$$T_{dbc} = \begin{pmatrix} \frac{1}{\sqrt{3}}\Delta^{+} & \frac{1}{\sqrt{3}}\Delta^{0} & \frac{1}{\sqrt{6}}\Sigma^{*0} \\ \frac{1}{\sqrt{3}}\Delta^{0} & \Delta^{-} & \frac{1}{\sqrt{3}}\Sigma^{*-} \\ \frac{1}{\sqrt{6}}\Sigma^{*0} & \frac{1}{\sqrt{3}}\Sigma^{*-} & \frac{1}{\sqrt{3}}\Xi^{*-} \end{pmatrix} \tag{2.55}$$

and

$$T_{sbc} = \begin{pmatrix} \frac{1}{\sqrt{3}}\Sigma^{*+} & \frac{1}{\sqrt{6}}\Sigma^{*0} & \frac{1}{\sqrt{3}}\Xi^{*0} \\ \frac{1}{\sqrt{6}}\Sigma^{*0} & \frac{1}{\sqrt{3}}\Sigma^{*-} & \frac{1}{\sqrt{3}}\Xi^{*-} \\ \frac{1}{\sqrt{3}}\Xi^{*0} & \frac{1}{\sqrt{3}}\Xi^{*-} & \Omega^{-} \end{pmatrix}. \tag{2.56}$$

in the three flavor indices (u, d, s), and where the indices b and c of each matrix label rows and columns in the order (u, d, s), is understood in Eq. (2.53). It is worth relating the T_{abc} representation to the physical states as

$$\begin{aligned}
&T_{111} = \Delta^{++}; \quad T_{112} = \frac{\Delta^{+}}{\sqrt{3}}; \quad T_{122} = \frac{\Delta^{0}}{\sqrt{3}} \\
&T_{222} = \Delta^{-}; \quad T_{113} = \frac{\Sigma^{*+}}{\sqrt{3}}; \quad T_{123} = \frac{\Sigma^{*0}}{\sqrt{6}} \\
&T_{223} = \frac{\Sigma^{*-}}{\sqrt{3}}; \quad T_{133} = \frac{\Xi^{*0}}{\sqrt{3}}; \quad T_{233} = \frac{\Xi^{*-}}{\sqrt{3}} \\
&T_{333} = \Omega^{-}. \qquad (2.57)
\end{aligned}$$

Form factors

The Lagrangian of Eq. (2.53) only provides the leading weak axial coupling $C_5^A(0)$ for all the allowed weak transitions. Knowing that $C_5^A(0)|_{n\to\Delta^+} \simeq \frac{2\mathcal{C}}{\sqrt{3}}$ with $\mathcal{C} \sim 1$, one can relate all the other leading axial couplings for the other weak transitions to that for the $n \to \Delta^+$. These relative factors are then applied to all the vector $C_i^V(q^2)$ and axial $C_i^A(q^2)$ form factors, thus assuming exact SU(3) symmetry for the couplings (In Appendix B, we give an equivalent formulation based on flavor SU(3) symmetry.). Note that the strong coupling $\mathcal{C} \simeq 1$ is obtained to match the Δ width at its nominal mass. We choose the form factors for the $n \to \Delta^+$ transition from Ref. [40], and apply the above mentioned SU(3) relative factors to obtain the strangeness-changing octet-to-decuplet transition form factors. The three vector form factors C_i^V, $i = 3, 4, 5$ are given in terms of the isovector electromagnetic form factors for $p \longrightarrow \Delta^+$ transition as

$$C_3^V(q^2) = \frac{2.13}{(1-\frac{q^2}{M_V^2})^2} \times \frac{1}{1-\frac{q^2}{4M_V^2}}, \qquad (2.58)$$

$$C_4^V(q^2) = \frac{-1.51}{(1-\frac{q^2}{M_V^2})^2} \times \frac{1}{1-\frac{q^2}{4M_V^2}}, \qquad (2.59)$$

$$C_5^V(q^2) = \frac{0.48}{(1-\frac{q^2}{M_V^2})^2} \times \frac{1}{1-\frac{q^2}{0.776M_V^2}}, \qquad (2.60)$$

with the vector dipole mass taken as $M_V = 0.84$ GeV. As we said, the conserved vector current hypothesis implies $C_6^V = 0$.

The most significant contribution among the axial form factors comes from C_5^A. The axial-vector form factors information comes mainly from two bubble chamber experiments, ANL [137] and BNL [138]. The form factors are determined from the analysis of weak pion production experiments using Adler's model, which is consistent with the hypothesis of PCAC and the generalized Golderger-Treiman relation.

The q^2 - dependence of $C_3^A(q^2)$ and $C_5^A(q^2)$ are obtained in Adler's model as

$$C_4^A(q^2) = -\frac{1}{4}C_5^A(q^2), \quad C_3^A(q^2) = 0. \tag{2.61}$$

For $C_5^A(q^2)$ and $C_6^A(q^2)$

$$C_5^A(q^2) = \frac{1.2}{(1 - \frac{q^2}{M_{A\Delta}^2})^2} \times \frac{1}{1 - \frac{q^2}{3M_{A\Delta}^2}}, \quad M_{A\Delta} = 1.05 \text{ GeV}. \tag{2.62}$$

These considerations give $C_6^A(q^2)$ in terms of $C_5^A(q^2)$

$$C_6^A(q^2) = C_5^A(q^2)\frac{M^2}{M_K^2 - q^2}, \tag{2.63}$$

which appears when one imposes PCAC for the transition similar to Fig. 2.2 with the final hyperon replaced by the $\Sigma^*(1385)$ resonance.

The N$\Delta\pi$ and $\Sigma^* Y\pi$ vertices

The Lagrangian of Eq. (2.53) also provides the strong $\Sigma^* Y\pi$ and $N\Delta\pi$ vertices. From this Lagrangian, we obtain the following one, in this case where the resonances have spin 3/2 in a more general form, is given by

$$\mathcal{L}_{D\to B\phi} = \frac{f_{DB\phi}}{f_\phi}\bar{\Psi}^\mu_{\frac{3}{2}}\partial_\mu\phi^a T_a \Psi, \tag{2.64}$$

where f_ϕ is the meson decay constant, $f_{DB\phi}$ is the coupling strength for spin 3/2 resonances and $\Psi^\mu_{\frac{3}{2}}$ is the field associated with this resonance. Ψ is the spin-1/2 octet baryon field, ϕ^a the mesonic field (in the case of pion it will be a triplet of pion fields) and $T_a = T^\dagger$ is the isospin transition operator. The index a ranges from 1 to 8 in order to establish connections between the baryon octet and the Rarita-Schwinger fields of the resonances. In fact, this operator is essentially a matrix of Clebsch-Gordan coefficients. And the general form for the resonance width $\Gamma_{D\to B\phi}$ in its rest frame is given by

$$\Gamma_{D\to B\phi} \;=\; \frac{1}{32\pi^2 M_D^2}\int |\mathbf{k}_\phi|\, d\,|\mathbf{k}_\phi|\, d\Omega_{\hat{k}_\phi}\delta(|\mathbf{k}_\phi| - p_{final})\bar{\Sigma}\Sigma\,|\mathcal{M}|^2\,, \tag{2.65}$$

$\mathbf{k}_\phi$ is the meson momenta. For the sum over the final spin of the baryon and the average over the initial spin projections of the unpolarized resonance in the squared transition matrix element, we obtain

$$\bar{\Sigma}\Sigma\,|\mathcal{M}|^2 = \frac{1}{4}\left(\frac{\mathcal{C}}{f_\pi}\right)^2 k_\phi^\alpha k_\phi^\beta \ \mathrm{Tr}(\mathcal{P}_{\alpha\beta}(p_D)(\not{p}' + M_B)), \tag{2.66}$$

where $\mathcal{P}_{\alpha\beta}(p_D)$ is the spin-$\frac{3}{2}$ projector operator appearing in the propagator of Rarita-Schwinger fields is defined as

$$\mathcal{P}_{\alpha\beta}(P) = -\left(\not{P} + M_D\right)\left[g_{\alpha\beta} - \frac{1}{3}\gamma_\alpha\gamma_\beta - \frac{2}{3}\frac{P_\alpha\,P_\beta}{M_D^2} + \frac{1}{3}\frac{P_\alpha\,\gamma_\beta - P_\beta\,\gamma_\alpha}{M_D}\right], \tag{2.67}$$

with M_D the corresponding mass of the decuplet baryon, either the Δ or the Σ^*, and P the four-momentum carried by these particles.

The Dirac delta function in Eq. 2.65 only selects one possible modulus of the meson 3-momentum

$$p_{final} = \frac{\lambda^{\frac{1}{2}}(M_D^2, M_B^2, m_\phi^2)}{2M_D}, \tag{2.68}$$

where $\lambda(x, y, z) = x^2 + y^2 + z^2 - 2xy - 2xz - 2yz$ is the Källen λ-function. The resonance width has the form

$$\begin{aligned}\Gamma_{D\to B\phi} &= \frac{C_{DB\phi}}{192\pi}\left(\frac{\mathcal{C}}{f_\pi}\right)^2 \frac{((W + M_B)^2 - m_\phi^2)}{W^5}\lambda^{\frac{3}{2}}(W^2, M_B^2, m_\phi^2)\\ &\times\ \Theta(W - M_B - m_\phi),\end{aligned} \tag{2.69}$$

where W is the invariant mass of the resonance, when $W = M_D$, the resonance width should then recover the value at the nominal mass. $C_{DB\phi}$ is a factor that depends on the decay channel and $\Theta(W - M_B - m_\phi)$ is the unit step function.

If we apply the Feynman rules to the diagrams depicted in Fig. 2.1b, we obtain the following amplitudes:

$$J^\mu_{\mathrm{s}-\Sigma^*} = i\,V_{us}\,\mathcal{A}^{N\to Y\pi}_{\mathrm{s}-\Sigma^*}\,\frac{p_m^\beta}{p_{\Sigma^*}^2 - M_{\Sigma^*}^2 + iM_{\Sigma^*}\Gamma_{\Sigma^*}}\,\bar{u}_Y(\mathbf{p}_Y)\,\mathcal{P}_{\beta\alpha}(p_{\Sigma^*})\,\Gamma^{\alpha\mu}(p, q)\,u_N(\mathbf{p}) \tag{2.70}$$

$$J^\mu_{\mathrm{u}-\Delta} = i\,V_{us}\,\mathcal{A}^{N\to Y\pi}_{\mathrm{u}-\Delta}\,\frac{p_m^\beta}{p_\Delta^2 - M_\Delta^2 + iM_\Delta\Gamma_\Delta}\,\bar{u}_Y(\mathbf{p}_Y)\,\tilde{\Gamma}^{\mu\alpha}(p_Y, q)\,\mathcal{P}_{\alpha\beta}(p_\Delta)\,u_N(\mathbf{p}), \tag{2.71}$$

where $p_{\Sigma^*} = p + q$, $p_\Delta = p - p_m$, $\tilde{\Gamma}^{\mu\alpha}(p_Y, q) = \gamma^0 \left[\Gamma^{\alpha\mu}(p_Y, -q)\right]^\dagger \gamma^0$, $\mathcal{P}_{\alpha\beta}(p_D)$ is the spin-$\frac{3}{2}$ projector operator appearing in the propagator of Rarita-Schwinger fields. The constants $\mathcal{A}_i^{N\to Y\pi}$ appearing in Eqs. (2.70) and (2.71) are given in table 2.4. The decuplet baryon-propagator has the next form

$$G^{\mu\nu}(p_D) = \frac{\mathcal{P}^{\mu\nu}(p_D)}{p_D^2 - M_D^2 + iM_D\Gamma_D}, \tag{2.72}$$

where M_D is the resonance mass ($\sim$ 1232 MeV for Δ case, and $\sim$ 1385 MeV for the Σ^* one, respectively). Finally, $\Gamma_D(s)$ is the energy dependence resonance width in its rest frame.

The constants $\mathcal{A}_i^{N\to Y\pi}$ already incorporate the weak SU(3) factors relating the different vector and axial $\{8\} \longrightarrow \{10\}$ transition vertices with that for the $n \longrightarrow \Delta^+$ weak transition, as well as the factors appearing in the $\Sigma^* Y\pi$ or $N\Delta\pi$ strong vertices.

Reaction	$\mathcal{A}_{\text{s}-\Sigma^*}^{N\to Y\pi}$	$\mathcal{A}_{\text{u}-\Delta}^{N\to Y\pi}$
$\bar{\nu}_l + p \to l^+ + \pi^0 + \Lambda$	$\frac{\mathcal{C}}{\sqrt{2}f_\pi}$	0
$\bar{\nu}_l + n \to l^+ + \pi^- + \Lambda$	$\frac{\mathcal{C}}{f_\pi}$	0
$\bar{\nu}_l + p \to l^+ + \pi^0 + \Sigma^0$	0	$2\sqrt{\frac{2}{3}}\frac{\mathcal{C}}{f_\pi}$
$\bar{\nu}_l + p \to l^+ + \pi^- + \Sigma^+$	$\frac{\mathcal{C}}{\sqrt{6}f_\pi}$	$\frac{\mathcal{C}\sqrt{6}}{f_\pi}$
$\bar{\nu}_l + p \to l^+ + \pi^+ + \Sigma^-$	$-\frac{\mathcal{C}}{\sqrt{6}f_\pi}$	$\sqrt{\frac{2}{3}}\frac{\mathcal{C}}{f_\pi}$
$\bar{\nu}_l + n \to l^+ + \pi^- + \Sigma^0$	$-\frac{\mathcal{C}}{\sqrt{3}f_\pi}$	$-\frac{2\mathcal{C}}{\sqrt{3}f_\pi}$
$\bar{\nu}_l + n \to l^+ + \pi^0 + \Sigma^-$	$\frac{\mathcal{C}}{\sqrt{3}f_\pi}$	$\frac{2\mathcal{C}}{\sqrt{3}f_\pi}$

Table 2.4: Constants $\mathcal{A}_i^{N\to Y\pi}$ for each reaction and the resonances (s-Σ^* and u-Δ) diagrams of Fig. 2.1b in our model.

Some simple arguments can be done to explain why some diagrams are forbidden for some reaction channels in table 2.4:

- For final Λ production there cannot be u-Δ diagrams at all. This is because the weak strangeness-changing charged current is able to change the total isospin by $\Delta I = \pm\frac{1}{2}$. Therefore, it can change the isospin of the $\Delta(1232)$ from $\frac{3}{2} \longrightarrow 1$, thus giving a Σ hyperon, but it is not possible to give final isospin 0, that of the Λ particle.

- The reason for which the constant $\mathcal{A}_{\text{s}-\Sigma^*}^{p\to\Sigma^0\pi^0} = 0$ is exactly the same for which the corresponding constant for the s-Σ background channel was. This is because the intermediate propagating resonance is a Σ^{*0}, and the strong coupling $g_{\Sigma^{*0}\Sigma^0\pi^0}$ is proportional to the Clebsch-Gordan for coupling two $|1,0\rangle$ states to another $|1,0\rangle$ state. In virtue of the symmetries of the SU(2) Clebsch-Gordan coefficients, this is zero.

The decay width corresponding to $\Delta(1232)$, following the Ref. [40], is given by

$$\begin{aligned}\Gamma_{\Delta\to N\pi} &= \frac{1}{6\pi}\left(\frac{f^*}{m_\pi}\right)^2 \frac{M}{W}\frac{\lambda^{3/2}(W^2,M^2,m_\pi^2)}{8W^3} \\ &\times\ \Theta(W-M-m_\pi), \end{aligned} \tag{2.73}$$

where M is the nucleon mass and m_π is the pion mass.

Finally, in Eq. (2.70), Γ_{Σ^*} is the energy dependent $\Sigma^*(1385)$ width, given by

$$\Gamma_{\Sigma^*} = \Gamma_{\Lambda\pi} + \Gamma_{\Sigma\pi} + \Gamma_{N\bar{K}} + \Gamma_{\Sigma\eta} + \Gamma_{\Xi K},$$

where the different strong partial widths $\Gamma_{B\phi}$ can be calculated at tree level with the vertices from the Lagrangian given in Eq. (2.53). Their expressions are always the same up to an SU(3) factor, and are given by

$$\begin{aligned}\Gamma_{\Sigma^*\to B\phi} &= \frac{C_{B\phi}}{192\pi}\left(\frac{\mathcal{C}}{f_\pi}\right)^2 \frac{(W+M_B)^2-m_\phi^2}{W^5} \\ &\lambda^{3/2}(W^2,M_B^2,m_\phi^2)\ \Theta(W-M_B-m_\phi), \end{aligned} \tag{2.74}$$

where M_B and m_ϕ are the final baryon and meson masses in the decay of the Σ^*, Θ is the unit step function allowing the Σ^* to decay in the $B\phi$ channel only when the invariant mass W of the resonance is higher than the channel threshold $(M_B + m_\phi)$. Finally, the SU(3) factors $C_{B\phi}$ are 1 for $\Lambda\pi$ and $\Sigma\eta$, while they are $\frac{2}{3}$ for the $\Sigma\pi$, $N\bar{K}$ and ΞK decay channels.

In eq. (2.71), it is not necessary to take into account the $\Delta(1232)$ width because as being an u-channel diagram, the pole of the denominator is never reached. Indeed, it can be shown that

$$p_\Delta^2 = (p-p_m)^2 = M^2 + m_\pi^2 - 2ME_\pi \tag{2.75}$$

where E_π is the pion energy in the LAB frame. For the allowed kinematics by energy-momentum conservation, this energy is always greater than its rest mass. Therefore, we can write

$$p_\Delta^2 = M^2 + m_\pi^2 - 2ME_\pi \leqslant (M-m_\pi)^2 < (M+m_\pi)^2 < M_\Delta^2. \tag{2.76}$$

This leads to the Δ width equals zero as $p_\Delta^2 < (M+m_\pi)^2$ holds for all the kinematics regions under consideration.

2.4 Flux-integrated total cross section

We have also evaluated the flux-folded total cross section for antineutrino fluxes of several experiments. In the results section 4, we show the fluxes for those experiments. We have chosen antineutrino fluxes peaked at intermediate energies $\langle E_{\overline{\nu}}\rangle \backsimeq 1-3$ GeV, where the four-momentum transfers are expected to be low enough for our model, based on chiral expansions, to be more reliable.

For some of the reaction channels, we have also applied a kinematic cut of $W < 1.4$ GeV, as done in other works [40]. The outgoing $Y\pi$ invariant mass W varies in this case between

$$W_{min} = M_Y + m_\pi \leq W \leq 1.4 \text{ GeV} \tag{2.77}$$

We have applied this cut when we have considered that higher lying strange resonances, such as the $\Lambda(1405)$, can play a very important role for hadronic invariant masses larger than 1.4 GeV. Although this cut in the invariant final hadronic mass does not mean that our model is going to be more reliable than without the cut, the experiments can implement the kinematic cut in their events, thus rejecting all the events where the final $Y\pi$ system has $W > 1.4$ GeV. If such cuts are done, then the final sample of events can be more reliable compared with our cross sections predictions.

The definition of the flux-integrated total cross section, $\langle\sigma\rangle$, for a given antineutrino flux $\Phi(E_{\bar{\nu}})$ of some experiment, can be obtained as

$$\langle\sigma\rangle = \frac{\int_{E_{\bar{\nu}}^{\rm th}}^{E^{max}} \Phi(E_{\bar{\nu}})\, \sigma(E_{\bar{\nu}})\, dE_{\bar{\nu}}}{\int_0^{E^{max}} \Phi(E_{\bar{\nu}})\, dE_{\bar{\nu}}}. \tag{2.78}$$

In eq. (4.4), the lower limit in the integral of the numerator can be also zero, but it is not necessary, because the total cross section $\sigma(E_{\bar{\nu}})$ is zero for $E_{\bar{\nu}} < E_{\bar{\nu}}^{\rm th}$, where $E_{\bar{\nu}}^{\rm th}$ is the threshold antineutrino energy in the LAB frame for the reaction to take place. Its expression is given by

$$E_{\bar{\nu}}^{\rm th} = \frac{(M_Y + m_\pi + m_l)^2 - M^2}{2M}, \tag{2.79}$$

thus giving $E_{\bar{\nu}}^{\rm th} \simeq 0.515$ GeV for final Λ production and $E_{\bar{\nu}}^{\rm th} \simeq 0.630$ GeV for final Σ production induced by muon antineutrinos. Note that for the masses of the particles we have taken isospin average masses for the Σ hyperon, for the nucleon and for the pions.

Notice also that in eq. (4.4), the upper limit in the antineutrino energy does not need to go up to infinity. This is a formal expression where the cut in the energy has to be taken when the flux is negligible, but one also has to take care that the product of the flux and the total cross section in the numerator decreases fast enough at the higher energies to make the flux-folded total cross section meaningful.

Chapter 3

Hyperon production off the nucleus

In this chapter, we present the theoretical model for the semi-inclusive production of hyperons off nuclear targets. The study of hyperon production for nuclear matter is important in understanding the properties of strange particles, as well as the behaviour of weak interactions in nuclei. In the previous chapter, we detailed the formalism used for the $Y\pi$ production off free nucleons induced by antineutrinos. Our model is based on the lowest-order effective SU(3) chiral Lagrangian, which describes the interactions of the lightest mesons and baryons in the presence of an external weak charged current. It explicitly includes resonance degrees of freedom in addition to background terms, which are essential for describing the complex dynamics of the reaction. This primary hyperon production serves as the foundation for the nuclear model. To expand on this model, beyond $Y\pi$ production, we include the hyperon quasielastic mechanism. The presence of multiple nucleons can affect the reaction dynamics. This requires the inclusion of nuclear effects and the final state interactions (FSI). It is also interesting to calculate the probability for pions to be absorbed by the nucleus.

To complement our model and be able to compare our results with the first experimental data presented by the MicroBooNE collaboration for quasielastic Λ production [59]. And from this studied model, to be able to determine the shape of the cross sections with the flux from other current and future experiments. We also include the quasielastic hyperon production model studied in Ref. [85]. As most of the neutrino experiments work in the low and intermediate (anti)neutrino energy range (0.5 GeV $<$ $E_{\nu(\bar{\nu})}$ $<$ 2 GeV), this reaction is the main source of strange baryon production at intermediate energies with antineutrino beams, except for the primary Σ^+ production, which cannot be produced without FSI in the quasielastic channel.

In summary, in this chapter, we present a formalism for calculating the total and differential cross sections for quasielastic hyperon production and $Y\pi$ production in a nuclear environment. The simplest nuclear model to study these reactions is the Fermi gas model. Our formalism takes into account the effects of the nuclear medium, such as Fermi motion and final-state interactions (FSI) through the use of intranuclear reinteraction models for the primary produced hyperons. We also provide a detailed explanation of the incorporation of FSI effects into our model in the section 3.4 of this chapter. We present two models of FSI cascade. The second model represents an improvement over the first one, considering that hyperons could get trapped in the nucleus. We also include an estimate of the probability that the pion, in the $Y\pi$ production, is absorbed by the nucleus. It is important to notice that both models, the quasielastic model and the $Y\pi$ production model, use the same approaches to include the nuclear effects and the FSI.

3.1 Nuclear effects

In a nucleus, nucleons are not stationary or devoid of interactions, giving rise to a range of nuclear effects with both kinematic and dynamical origins. In nuclear reactions involving the production of hyperons, the dynamic of these particles is affected by the movement of nucleons within the nucleus, known as Fermi motion. Nuclear effects refer to the ways in which the properties of nuclei, such as their binding energy, size, and shape, can influence the behaviour of subatomic particles, particularly neutrinos and other weakly interacting particles. Additional effects include Pauli blocking, final-state interactions, and nucleon-nucleon correlations, among others. Some of these effects can be studied using theoretical models, including the simplest model called Fermi gas model. In the Fermi gas model, the nucleon momentum is constrained by an upper limit known as the Fermi momentum, denoted as k_F, which is expressed in terms of the nucleon density ρ within the nucleus

$$k_F^i(r) = (3\pi^2\rho_i(r))^{\frac{1}{3}}, \tag{3.1}$$

the index 'i' refers to both types of nucleons: protons and neutrons.

In this thesis, the Fermi motion effects are determined using the Local Fermi gas model (LFG). The Local Fermi gas model is a theoretical model that combines the Fermi gas model with the local density approximation (LDA). In the local density approximation, it is assumed that nuclear density does not remain constant, as it does in nuclear matter, but instead, it varies based on the position within the nucleus. This method incorporates the finite-size effects of the nucleus, unlike nuclear matter, where the density and Fermi momentum are constant. Nuclear matter behaves like a Fermi gas with an infinite number of nucleons in an infinite volume, maintaining a constant ratio between them (the density). Consequently, this model does not account for finite nuclear size effects.

The Fermi gas model is a theoretical model used to describe the behaviour of a system of non-interacting fermions at low temperatures. It is based on the Pauli exclusion principle, which states that no two fermions can occupy the same quantum state simultaneously. This model is based on the assumption that the system of fermions is in thermal equilibrium and that the density of states can be approximated by the density of states of a non-interacting gas of fermions. This model is widely used in the study of nuclear physics, quantum mechanics, and condensed matter physics. In the Local Fermi Gas (LFG) model, the momenta of the nucleons range from 0 to their respective Fermi momenta at the interaction point ($\mathbf{r}$). This means that the properties of the nucleus are described by the density profiles of protons and neutrons. While this simplifies the physical situation, compared to other models such as shell-models, which provide a more detailed structure of nuclei, it can still be useful in certain applications.

Nucleus	a (fm)	b (fm)	w	Fermi profile function
^{12}C	2.355	0.5224	-0.149	3pF
^{16}O	2.608	0.513	-0.051	3pF
^{40}Ar	3.53	0.542		2pF
^{40}Ca	3.766	0.586	-0.161	3pF
^{56}Fe	4.106	0.519		2pF

Table 3.1: Charge density distribution parameters to calculate the proton density profile given in Eq. 3.6 for different nuclei used in this thesis [139].

In the local density approximation (see eq. 3.2), the nuclear cross section is calculated as an incoherent sum of the single-nucleon cross section weighted by the density of nucleons of each type. In this approach, the incoming antineutrino scatters from a nucleon (proton or neutron) moving in a finite nucleus A, where the density of the nucleon is $\rho_N(r)$ and r is the distance from the interaction or scattering point to the center of the nucleus. The differential cross section for antineutrino-nucleus scattering is given by

$$\left(\frac{d^2\sigma}{dE_l d\Omega_l}\right)_{\bar{\nu}A\to f} = \sum_{i=p,n} \int d^3r\, \rho_i(r) \left(\frac{d^2\sigma}{dE_l d\Omega_l}\right)_{\bar{\nu}N_i\to f} \tag{3.2}$$

The nucleon density in the nucleus is given by

$$\rho_i(r) = \frac{N_i}{V} = 2\int_0^{k_F^i(r)} \frac{d^3p}{(2\pi)^3} = 2\int \frac{d^3p}{(2\pi)^3} n_i(\mathbf{p},\mathbf{r}), \tag{3.3}$$

where the factor 2 is to take into account the nucleon spin degrees of freedom. Each nucleon occupies a volume of $(2\pi)^3$. A is the total number of nucleons and V is the volume of the nucleus. And $n_N(\mathbf{p},\mathbf{r})$ is the occupation number defined as

$$n(\mathbf{p},\mathbf{r}) = \theta(k_F(r) - |\mathbf{p}|), \tag{3.4}$$

all states below the maximum momentum k_F are filled and the momentum states higher than this momentum are unoccupied. We have taken the proton densities from Ref. [139] and they are scaled with a factor N/Z for neutrons. This is important because for the $Y\pi$ production reactions, in general, both types of nucleons contribute, as it will be seen later.

Finally, we write the differential cross section for antineutrino-nucleus scattering as

$$\left(\frac{d^2\sigma}{dE_l d\Omega_l}\right)_{\bar{\nu}A\to f} = 2\sum_{i=p,n}\int d^3r \int \frac{d^3p}{(2\pi)^3}\, n_i(\mathbf{p},\mathbf{r}) \left(\frac{d^2\sigma}{dE_l d\Omega_l}\right)_{\bar{\nu}N_i\to f} \tag{3.5}$$

In this thesis, we use the Fermi distribution function:

$$3\text{pF}: \qquad \rho(r) = \frac{\rho_0\left(1 + w\frac{r^2}{a^2}\right)}{1+\exp((r-a)/b)}, \tag{3.6}$$

where, in the case $w = 0$, this profile function reduces to a 2pF. 3pF and 2pF are Fermi-type distributions with 3 or 2 parameters, respectively. The parameters for the nuclei used as nuclear targets are compiled in Table 3.1.

In the neutrino energy region on a few GeV, we neglect the effect of Coulomb distortion on the charged lepton wave function. We treat the hyperons as long-lived particles, with a well-defined energy for a given momentum.

3.2 Quasielastic hyperon production

In this section, we provide a detailed description of the formalism used in Ref. [85] for the quasielastic hyperon production model. It is not the aim of this thesis to delve into the details of QE hyperon production, but as we complement our results with QE results, we must provide a brief explanation. To help the reader to understand the development, we begin by briefly outlining the primary model off free nucleons. For a more in-depth understanding, the reader is referred to Ref. [85]. Then, we present the modifications made to the model when quasielastic reactions take place in a nucleus, taking into account the effects of the nuclear medium such as Fermi motion and final-state interactions (FSI). This include the use of intranuclear reinteraction models for the primary produced hyperons, as well as a detailed explanation of how we incorporate these effects into our model.

As a consequence of the selection rule for weak strangeness-changing processes $\Delta S = \Delta Q$, the possible quasielastic weak hyperon production ($\Delta S = -1$) induced by antineutrinos processes are

$$\begin{aligned} \bar{\nu}_l(k) + p(p) &\rightarrow l^+(k') + \Lambda(p_Y), &(3.7)\\ \bar{\nu}_l(k) + p(p) &\rightarrow l^+(k') + \Sigma^0(p_Y), &(3.8)\\ \bar{\nu}_l(k) + n(p) &\rightarrow l^+(k') + \Sigma^-(p_Y). &(3.9)\end{aligned}$$

Different approaches to these reactions have been followed in previous works [85, 87]. For the description of the quasielastic mechanism, we follow completely the formalism of Ref. [85]. The differential cross section for the hyperon production off free nucleons can be written as

$$d\sigma = \frac{1}{(2\pi)^2}\frac{1}{4E_{\bar{\nu}}^{\mathrm{CM}}\sqrt{s}}\delta^4(k+p-k'-p_Y)\frac{d^3k'}{2E_l'(\mathbf{k}')}\,\frac{d^3p_Y}{2E_Y(\mathbf{p}_Y)}\,|\mathcal{M}|^2\,, \quad (3.10)$$

where $s = (k+p)^2$, $q = p_Y - p = k - k'$, and $E_{\bar{\nu}}^{\mathrm{CM}} = \frac{s-M^2}{2\sqrt{s}}$ is the antineutrino energy in the antineutrino-nucleon center of mass (CM) frame. M is the nucleon mass and the scattering amplitude matrix element is

$$\mathcal{M} = \frac{G_F}{\sqrt{2}}a_C\bar{v}(k)\gamma^\mu(1-\gamma^5)v(k')\langle Y(p_Y)\left|V_\mu - A_\mu\right|N(p)\rangle, \quad (3.11)$$

where $a_C = \sin\theta_C$ is the sine of the Cabibbo angle for $\Delta S = -1$ processes, $G_F = 1.1664\times10^{-5}$ GeV^{-2} is the Fermi coupling constant, and $\langle Y(p_Y)\left|V_\mu\right|N(p)\rangle$ and $\langle Y(p_Y)\left|A_\mu\right|N(p)\rangle$ are the nucleon-to-hyperon transition matrix elements of the vector and axial-vector weak currents, which are defined as

$$\langle Y(p_Y)\left|V_\mu(q)\right|N(p)\rangle = \bar{u}_Y(p_Y)\left[f_1^{NY}(q^2)\gamma_\mu + \frac{if_2^{NY}(q^2)}{M+M_Y}\sigma_{\mu\nu}q^\nu\right]u_N(p) \quad (3.12)$$

$$\langle Y(p_Y)\left|A_\mu(q)\right|N(p)\rangle = \bar{u}_Y(p_Y)\left[g_1^{NY}(q^2)\left(\gamma_\mu - \frac{q_\mu \not{q}}{q^2-M_K^2}\right)\gamma_5\right]u_N(p). \quad (3.13)$$

The reader can find the details and discussion of these transition matrix elements and their weak form factors values in Ref. [85]. Nevertheless, the form factors used in the quasielastic case are the same as those presented in the previous chapter, in Tables 2.1 and 2.2. The nuclear effects are calculated with the Fermi Gas model and the LDA, where the Fermi momentum of each nucleon species depends on its nuclear density as $k_F^{p(n)}(r) = (3\pi^2\rho_{p(n)}(r))^{\frac{1}{3}}$.

The differential cross section for the QE hyperon production from a nucleus can be written as

$$\begin{aligned} d\sigma = & \frac{1}{(2\pi)^2} 2 \int d^3r \, \frac{d^3p}{(2\pi)^3} \, n(\mathbf{p},\mathbf{r}) \, \delta^4(k + p - k' - p_Y) \\ & \times \frac{d^3k'}{2E'_l(\mathbf{k'})} \, \frac{d^3p_Y}{2E_Y(\mathbf{p}_Y)} \frac{1}{4E_{\bar{\nu}}^{\mathrm{CM}}\sqrt{s}} \overline{\sum} \sum |\mathcal{M}|^2 \, , \end{aligned} \tag{3.14}$$

where $n(\mathbf{p},\mathbf{r})$ is the local occupation number of the initial nucleon of momentum $\mathbf{p}$ localized at a radius r in the nucleus. And from now on, the square of the summation over final spins and averaging over initial spins of the scattering matrix element squared will be written as $\overline{\sum}\sum |\mathcal{M}|^2 = \overline{|\mathcal{M}|^2}$. It is worth noting that eq. (3.14) for the QE reactions (3.7-3.9) gives the cross section for a single nucleon type, therefore the Fermi momenta refer to that nucleon species. The primary hyperon produced only comes from one type of nucleon. As we said, we have taken the densities from Table 3.1, calculated the protons densities and they are scaled with a factor N/Z for neutrons. This is important because for the $Y\pi$ production reactions, in general, both types of nucleons contribute.

Using the δ-function of momentum conservation, we integrate over the hyperon momentum $\mathbf{p_Y}$, which selects only that $\mathbf{p_Y} = \mathbf{p} + \mathbf{k} - \mathbf{k'} = \mathbf{p} + \mathbf{q}$.

$$\begin{aligned} d\sigma = & \frac{2}{(2\pi)^5} \int d^3r \, d^3p \; n(\mathbf{p},\mathbf{r}) \, \frac{\delta(E_{\bar{\nu}} + E_p - E_{k'} - E_Y(\mathbf{p}+\mathbf{k}-\mathbf{k'}))}{2\,E_Y(\mathbf{p}+\mathbf{k}-\mathbf{k'})} \\ & \times \frac{d^3k'}{2E'_l(\mathbf{k'})} \, \frac{1}{4E_{\bar{\nu}}^{\mathrm{CM}}\sqrt{s}} \overline{|\mathcal{M}|^2}, \end{aligned} \tag{3.15}$$

Note that the integrand above only depends on r, and not at all on $\Omega_{\hat{r}}$, therefore we can integrate immediately over the full solid angle giving 4π of the r position inside the nucleus. This gives:

$$\begin{aligned} d\sigma = & \frac{2 \times 4\pi}{16(2\pi)^5} \int r^2 dr \, d^3p \; n(\mathbf{p},r) \, \frac{\delta(E_{\bar{\nu}} + E_p - E_{k'} - E_Y(\mathbf{p}+\mathbf{k}-\mathbf{k'}))}{E_Y(\mathbf{p}+\mathbf{k}-\mathbf{k'})} \\ & \times \frac{d^3k'}{E'_l(\mathbf{k'})} \, \frac{1}{E_{\bar{\nu}}^{\mathrm{CM}}\sqrt{s}} \overline{|\mathcal{M}|^2}, \end{aligned} \tag{3.16}$$

with the aid of the δ-function of energy conservation, we integrate over the cosine of the relative angle between $\mathbf{p}$ and $\mathbf{q} = \mathbf{k} - \mathbf{k}'$. We have to find the polar angle $\theta^0_{\hat{p}\hat{q}}$ which makes the argument of the δ-function to be zero.

$$\begin{aligned} E_{\bar\nu} + E_p - E_{k'} - E_Y(\mathbf{p}+\mathbf{q}) &= 0 \\ E_{\bar\nu} + E_p - E_{k'} &= \sqrt{|\mathbf{p}+\mathbf{q}|^2 + M_Y^2}. \end{aligned} \tag{3.17}$$

We fix the cosine of the angle $\theta^0_{\widehat{pq}}$ from the external integration variables $(r, \mathbf{k}', |\mathbf{p}|, \phi_{\widehat{pq}})$

$$\cos\theta^0_{\widehat{pq}} = \frac{q^2 + M^2 - M_Y^2 + 2E_p q^0}{2\,|\mathbf{p}|\,|\mathbf{q}|}, \tag{3.18}$$

where E_p is the on-shell nucleon energy, $q^0 = E_{\bar\nu} - E_{k'}$ and $\phi_{\widehat{pq}}$ is the azimuthal angle of the nucleon momentum as measured in a plane perpendicular to $\mathbf{q}$. Therefore, $\mathbf{k} - \mathbf{k}'$ defines the Z-axis. Using that $n(\mathbf{p}, r) = \theta(k_F(r) - |\mathbf{p}|)$, we can write

$$\begin{aligned} d\sigma = \quad & \frac{1}{64\pi^4} \int r^2 dr \int_0^{2\pi} d\phi_{\widehat{pq}} \int_0^{k_F(r)} dp\, d^3k' \\ & \frac{p}{E_l'(\mathbf{k}')|\mathbf{k}-\mathbf{k}'|} \frac{|\mathcal{M}|^2}{E_{\bar\nu}^{\mathrm{CM}}\sqrt{s}} \Theta(1 - \cos^2\theta^0_{\widehat{pq}}). \end{aligned} \tag{3.19}$$

Therefore, finally, we obtained the differential cross section for quasielastic hyperon production from nuclei.

All the kinematic variables are defined in the integral itself, except that the cosine of the polar angle between $\mathbf{p}$ and $\mathbf{q}$ is fixed by Eq. (3.18).

The threshold of this mechanism is given by

$$E_{\bar\nu}^{\mathrm{th}} = \frac{(M_Y + m_l)^2 - M^2}{2M}, \tag{3.20}$$

its value is important as a reference for the minimum antineutrino energy for the QE reaction to take place off the nucleus in its rest frame.

3.3 Hyperon-pion production

In chapter 2, we studied, in detail, the hyperon production along with a light meson (pion) off free nucleons induced by antineutrinos driven by the strangeness-changing weak charged current. As mentioned then, the reaction is

$$\bar\nu_l(k) + N(p) \to l^+(k') + \pi(p_m) + Y(p_Y). \tag{3.21}$$

Recalling what was discussed in chapter 2 , the allowed $Y\pi$ final states are $\Lambda\pi^0$, $\Sigma^0\pi^0$, $\Sigma^-\pi^+$ and $\Sigma^+\pi^-$ for the proton channel and $\Lambda\pi^-$, $\Sigma^0\pi^-$ and $\Sigma^-\pi^0$ for the neutron one. It is important remember that our model for $Y\pi$ production off free nucleons contains explicit resonant ($\Sigma^*(1385)$ and $\Delta(1232)$) channels as well as background or Born terms obtained from lowest order chiral Lagrangians.

Now, let us extend our model when the reactions take place in a nucleus,

$$\bar{\nu}_l(k) + A \rightarrow l^+(k') + \pi(p_m) + Y(p_Y) + X, \tag{3.22}$$

where X is the residual nucleus that we do not consider to be detected. The dynamics of the particles are influenced by the Fermi motion of the nucleons. In the same way, as in section 3.2, we include the nuclear effects through the Fermi Gas model in the local density approximation (LDA).

We are interested in producing one type of hyperon along with a pion. In general, for each kind of hyperon, both types of nucleons, protons and neutrons, contribute to its primary production. The only exception is the Σ^+ production, that only happens off protons. Therefore, our differential cross section is the sum of both contributions

$$d\sigma_{\bar{\nu}+A\rightarrow l^+ + Y + \pi} = \sum_{i=p,n} d\sigma^A_{\bar{\nu}+N_i\rightarrow l^+ + Y + \pi}. \tag{3.23}$$

Therefore, the nuclear differential cross section, in general, is written as

$$\begin{aligned} d\sigma_{\bar{\nu}+A\rightarrow l^+ + Y + \pi} &= \frac{2}{(2\pi)^5} \sum_{i=p,n} \int d^3r \, \frac{d^3p}{(2\pi)^3} \, n_i(\mathbf{p},\mathbf{r}) \delta^4(k + p - k' - p_m - p_Y) \\ &\times \frac{d^3k'}{2E'_l(\mathbf{k'})} \frac{d^3p_m}{2E_m(\mathbf{p}_m)} \frac{d^3p_Y}{2E_Y(\mathbf{p}_Y)} \frac{1}{4E^{\mathrm{CM}}_{\bar{\nu}}\sqrt{s}} \left|\mathcal{M}_{i\rightarrow Y\pi}\right|^2. \end{aligned} \tag{3.24}$$

In this case, the nuclear differential cross section, for each type of nucleon, is written as

$$\begin{aligned} d\sigma &= \frac{2}{(2\pi)^5} \int d^3r \, \frac{d^3p}{(2\pi)^3} \, n(\mathbf{p},\mathbf{r}) \delta^4(k + p - k' - p_m - p_Y) \\ &\times \frac{d^3k'}{2E'_l(\mathbf{k'})} \frac{d^3p_m}{2E_m(\mathbf{p}_m)} \frac{d^3p_Y}{2E_Y(\mathbf{p}_Y)} \frac{1}{4E^{\mathrm{CM}}_{\bar{\nu}}\sqrt{s}} \overline{|\mathcal{M}|^2}. \end{aligned} \tag{3.25}$$

In the above equation, we are interested only in a definite hyperon production, regardless of the charge of their accompanying pion. It is important to note that, unlike the QE hyperon production cross section described in Eq. (3.14), the production of the same hyperon generally involves contributions from both types of nucleons, with the only exception of Σ^+ production, which is solely attributed to protons. As a result, we must take into account contributions from both types of nucleons separately. In general, for non-symmetric nuclei ($Z \neq N$), there is a difference on the local Fermi momentum distributions, where $n_i(\mathbf{p}, \mathbf{r}) = \theta(k_F^i(r) - |\mathbf{p}|)$. There is radial symmetry in the nuclear density, as $k_F^i(r) = (3\pi^2 \rho_i(r))^{\frac{1}{3}}$ only depends on r but not on the angles $d\Omega_{\hat{r}}$, so it can be directly integrated over the solid angle, resulting in a factor of 4π.

$$\begin{aligned} d\sigma &= \frac{4}{(2\pi)^7} \int r^2 dr \int d^3p\, n(\mathbf{p}, \mathbf{r})\, \delta^4(k + p - k' - p_m - p_Y) \\ &\times \frac{d^3k'}{2E_l'(\mathbf{k'})} \frac{d^3p_m}{2E_m(\mathbf{p}_m)} \frac{d^3p_Y}{2E_Y(\mathbf{p}_Y)} \frac{1}{4E_{\bar{\nu}}^{\mathrm{CM}}\sqrt{s}} \overline{|\mathcal{M}|^2}. \end{aligned} \tag{3.26}$$

We integrate over the hyperon momentum using the δ-function of momentum conservation, which selects only $\mathbf{p_Y} = \mathbf{p} + \mathbf{q} - \mathbf{p_m} = \mathbf{p} + \mathbf{q_m}$, where $\mathbf{q_m} = \mathbf{q} - \mathbf{p_m}$, the nuclear differential cross section reads now as

$$\begin{aligned} d\sigma &= \frac{1}{1024\pi^7} \int r^2 dr \int d^3p\, n(\mathbf{p}, \mathbf{r})\, \frac{\delta(E_p + q^0 - E_Y(\mathbf{p} + \mathbf{q_m}) - E_m(\mathbf{p_m}))}{E_Y(\mathbf{p} + \mathbf{q_m})} \\ &\times \frac{d^3k'}{E_l'(\mathbf{k'})} \frac{d^3p_m}{E_m(\mathbf{p}_m)} \frac{1}{E_{\bar{\nu}}^{\mathrm{CM}}\sqrt{s}} \overline{|\mathcal{M}|^2}. \end{aligned} \tag{3.27}$$

With the aid of the δ-function of energies, we solve the integral for the polar angle between $\mathbf{p}$ and $\mathbf{q_m} = \mathbf{q} - \mathbf{p_m}$, with $\mathbf{q} = \mathbf{k} - \mathbf{k'}$. Thus, making the argument of the δ-function to be zero

$$\begin{aligned} E_{\bar{\nu}} + E_p - E_l' - E_Y(\mathbf{p} + \mathbf{q_m}) - E_m(\mathbf{p_m}) = 0 \\ E_{\bar{\nu}} + E_p - E_l' - E_m = \sqrt{|\mathbf{p} + \mathbf{q_m}|^2 + M_Y^2}, \end{aligned} \tag{3.28}$$

we fix the cosine of the angle between the nucleon momentum $\mathbf{p}$ and $\mathbf{q_m}$:

$$\cos\theta^0_{\widehat{pq}_m} = \frac{(E(\mathbf{p}) + q^0 - E_m(\mathbf{p_m}))^2 - |\mathbf{p}|^2 - |\mathbf{q_m}|^2 - M_Y^2}{2\,|\mathbf{p}|\,|\mathbf{q_m}|}. \tag{3.29}$$

Now, using that $n_i(p, r) = \theta(k_F^i(r) - |p|)$, our expression can be written as

$$\begin{aligned} d\sigma &= \frac{1}{1024\pi^7} \int r^2 dr \int_0^{k_F^i} \frac{|\mathbf{p}|}{|\mathbf{q_m}|} d|\mathbf{p}|\, d\phi_{\widehat{pq}_m} \frac{d^3k'}{E_l'(\mathbf{k'})} \frac{d^3p_m}{E_m(\mathbf{p}_m)} \\ &\times \frac{\overline{|\mathcal{M}|^2}}{E_{\bar{\nu}}^{\mathrm{CM}}\sqrt{s}}\, \Theta(1 - \cos^2\theta^0_{\widehat{pq}_m}). \end{aligned} \tag{3.30}$$

Finally, using that $d^3k' = |\mathbf{k}'|^2\, d|\mathbf{k}'|\, d\Omega_{\hat{k}'} = |\mathbf{k}'| E'_l\, dE'_l\, d\Omega_{\hat{k}'}$ and $d^3p_m = |\mathbf{p_m}| E_m\, dE_m\, d\Omega_{\hat{p}_m}$, we obtain the next simplified expression for the contribution to the total nuclear cross section from only one type of nucleon

$$\begin{aligned} d\sigma &= \frac{1}{512\pi^6} \int r^2 dr \int dE'_l\, d\cos\theta_{\widehat{kk}'} \int dE_m\, d\Omega_{\hat{p}_m} \\ & \int_0^{k_F^i(r)} d|\mathbf{p}| \int_0^{2\pi} d\phi_{\widehat{pq}_m} \Theta(1-\cos^2\theta^0_{\widehat{pq}_m}) \frac{|\mathbf{p}|\,|\mathbf{k}'|\,|\mathbf{p_m}|}{|\mathbf{q_m}|} \frac{\overline{|\mathcal{M}|^2}}{E_{\bar{\nu}}^{\mathrm{CM}}\sqrt{s}}. \end{aligned} \quad (3.31)$$

In eq. (3.31), $\theta_{\widehat{kk}'}$ is the scattering angle of the final lepton with respect to the direction of the antineutrino; $\phi_{\widehat{pq}_m}$ is the azimuthal angle of the three-momentum of the nucleon measured on a plane orthogonal to $\mathbf{q_m}$, which can be chosen to define the Z-axis; and the solid angle of the pion, $\Omega_{\hat{p}_m}$, is referred with respect to the three-momentum transfer $\mathbf{q}$.

In the hyperon-pion mechanism, the threshold energy for the reaction to take place off free nucleons is

$$E_{\bar{\nu}}^{\mathrm{th}} = \frac{(M_Y + m_\pi + m_l)^2 - M^2}{2M}, \quad (3.32)$$

which will make a difference in the antineutrino energy range where this mechanism will be relevant if compared to the quasielastic hyperon production.

3.4 Final state interactions

Once the hyperon has been produced from one of the nucleons in the target nucleus, it interacts with other nucleons through elastic or inelastic scattering processes. Different approaches have been employed to study the hyperon final state interaction [85, 87, 88]. The effects of hyperon final state interactions (FSI) are particularly significant when the primary reaction involves quasielastic production. This is very interesting in the quasielastic case because Σ^+ hyperons only appear through charge exchange scattering processes, which can occur within nuclei ($\Lambda + p \to \Sigma^+ + n$ and $\Sigma^0 + p \to \Sigma^+ + n$). This is different from the $Y\pi$ processes, where the Σ^+, or any other hyperon, can already be produced in the primary interaction without the effect of FSI. In the $Y\pi$ production mechanism, the Σ^+ can be produced off protons in contrast to the other hyperons which can be produced off neutrons too. However, for both types of mechanisms, the effect of FSI is relevant for determining the type of hyperon finally emitted.

To estimate the FSI effects on the QE hyperon and $Y\pi$ production processes, we use a Monte Carlo code presented in Ref. [85, 99]. The algorithm calculates the propagation of hyperons in the nuclear medium and uses the available experimental data of hyperon-nucleon scattering cross sections to determine the probabilities of hyperon interaction. The primary reaction produces a hyperon (QE primary processes Eq. 3.7-3.9, $Y\pi$ primary production 2.2) which travels through the nucleus interacting with the nucleons and experiments changes of direction, energy and/or the kind of hyperon through elastic and inelastic $Y+N \to Y'+N'$ reactions. We enhance the method used for calculating FSI by incorporating a couple of improvements, including the hyperon potentials and the possibility of the hyperon becoming trapped in the nucleus, among others. We discuss these differences between the original and improved FSI models in more detail later. While the main objective of this thesis is to compare both types of hyperon production (QE and $Y\pi$) in the results, we also assess the impact of the different FSI algorithms on the cross section for various hyperons.

3.4.1 Old algorithm

We sketch here the procedure we follow: first, we fixed the hyperon produced in the primary interaction, Λ, Σ^- or Σ^0 for QE processes or Λ, Σ^-, Σ^0 or Σ^+ for hyperon-pion production processes. We obtain the profile function $\frac{d^6\sigma}{d^3r d^3k'}$ integrating the Eq. 3.14 and $\frac{d^9\sigma}{d^3r d^3k' d^3p_m}$ integrating the Eq. 3.25, over the rest of the variables. In our Monte Carlo simulation, we use that profile function as input, which is the weight assigned to the events. According to that, we generate a random hyperon position $\mathbf{r}$ (where the primary reaction takes place) and calculate its momentum $\mathbf{p_Y}$. To calculate the hyperon position we generate a random radius or distance r with respect to the center of the nucleus, an isotropic angular position (θ_r,ϕ_r) on the surface of a sphere with radius r where the hyperon is produced, namely, $\mathbf{r} = (r\cos\phi_r \sin\theta_r, r\sin\phi_r\sin\theta_r, r\cos\theta_r)$. The momentum of the initial nucleon is generated isotropically, with $|\mathbf{p}| \leq k_F(r)$. Those of the outgoing lepton, $\mathbf{k'}$, and pion, $\mathbf{p_m}$, (if applicable) are also randomly generated after energy conservation is imposed. The hyperon momentum at this initial coordinate is constrained by momentum conservation as $\mathbf{p_Y} = \mathbf{k} - \mathbf{k'} + \mathbf{p}$ (QE) or $\mathbf{p_Y} = \mathbf{k} - \mathbf{k'} + \mathbf{p} - \mathbf{p_m}$ ($Y\pi$). As we assume that the initially produced hyperon is on-shell, its energy is given by $E_Y = \sqrt{M_Y^2 + \mathbf{p}_Y^2}$.

We assume the real part of the hyperon nuclear potential to be weak compared with their kinetic energies and propagate them following straight lines till they are out of the nucleus. We expect this to be a good approximation. For instance, typical mean field potentials for the Λ are $\sim -30\rho/\rho_0$ MeV [140]. In Refs. [87, 88], the authors considered the Lambda potential in their FSI calculations. We follow their approach for our improved simulation. We neglect the quantum effects in this simulation but we expect those effects become especially important at low energies. This hyperon potential is taken into account in the improved algorithm that we explain in the subsection 3.4.2.

Once the initial properties of the event have been fixed, we start the simulation of the propagation of the hyperons and their possible scattering with the nucleons of the nuclear medium until they are out of the nucleus or until they have a kinetic energy below 30 MeV. First, we propagate the hyperon on a short distance $dl = \frac{\mathbf{p}_Y}{|\mathbf{p}_Y|}\Delta x$ (Δx fixed to 0.35 fm), along its momentum direction, such that $P_Y dl \ll 1$, where P_Y is the probability of interaction per unit length of a hyperon at point $\mathbf{r}$, and is given by

$$P_Y = \sum_{f,f'} \{\sigma_{Yn\to f}(\bar{s})\rho_n(r) + \sigma_{Yp\to f'}(\bar{s})\rho_p(r)\}, \tag{3.33}$$

where the sum is performed over all possible hyperon-nucleon final states and ρ_n, ρ_p are their local densities. The total cross sections $\sigma_{Y+N\to Y'+N'}(\bar{E})$ are extracted and parameterized from the available experimental data which are compiled in the Appendix of Ref. [85]. The threshold energy cut in the hyperon energy is fixed to 30 MeV for quasielastic interaction ($\Lambda \to \Lambda$, $\Sigma \to \Sigma$). Below this cut, we only consider $\Sigma \to \Lambda$ processes. Thus, the kinetic energy spectra of the final hyperons at these low kinetic energies are not meaningful because other much more relevant effects, such as hyperon potentials and hyperon absorption effects, among others not accounted for in the FSI model, are absent in the simulation.

Then we generate a random number $x \in [0, 1]$. The interaction between the hyperon and a nucleon of the nuclei occurs when $P_Y dl > x$. If it does not occur, we move the hyperon dl again. The Δx value is kept fixed to 0.35 fm unless the new hyperon position is near the limit of the nuclear size, in this case, Δx is fixed to $0,5$ fm. If the interaction has occurred we select the interaction channel according to their respective probabilities. Once we know the possible interaction channel, we check Pauli blocking. To implement Pauli blocking, we first select a random nucleon at rest in the local Fermi sea which depends on the initial hyperon and the possible final one. Assuming isotropic cross sections in the hyperon-nucleon CM system, we generate a random scattering angle to calculate the final hyperon and nucleon momenta in that system. We boost these momenta to the laboratory frame and check the Pauli blocking. If the final nucleon momentum squared is larger than $k_F^2(r)$, we have a new type of hyperon and/or a new direction and energy. If not, we consider that the interaction did not take place and the hyperon continues its movement with the same initial properties.

We repeat this procedure until the hyperon escapes the nucleus or until the hyperon is a Λ and its kinetic energy is smaller than 30 MeV. In this last case, we assume that the Λ hyperon exits the nucleus without any other interaction.

3.4.2 Improved algorithm

As part of our enhancements to the original FSI code outlined in Ref. [85], we integrated the real component of hyperon-nucleus potentials. To incorporate this into the cascade, we followed the algorithm detailed in Ref. [88]. In addition, we introduced a novel feature by considering the impact of the hyperon potential on hyperon trajectories between collisions, achieved by solving classical Hamilton equations. Efforts have been made to ascertain the hyperon-nucleus potential through pion-nucleus scattering events where the presence of a kaon is detected in the final state [141, 142, 143]. Concerning hyperon potentials, we have set the Lambda potential to approximately $-30\rho/\rho_0$ MeV [141]. However, we have omitted the Sigma potentials due to the lack of consensus on their values, as discussed in [143].

The propagation of a given hyperon produced in one of the possible primary interactions of a $\bar{\nu}_\mu$ with laboratory energy $E_{\bar{\nu}_\mu}$, as in the simplest FSI simulation, starts at a random position r_0 inside the nucleus. The momentum of the initial nucleon, $\mathbf{p}$, is generated isotropically. The outgoing lepton momentum, $\mathbf{k}'$, and pion momentum, $\mathbf{p_m}$, (if applicable) are also randomly generated after energy conservation is imposed. In the same way, the hyperon momentum at this initial coordinate is constrained as $\mathbf{p_Y} = \mathbf{k} - \mathbf{k}' + \mathbf{p}$ (QE) or $\mathbf{p_Y} = \mathbf{k} - \mathbf{k}' + \mathbf{p} - \mathbf{p_m}$ $(Y\pi)$.

Being the hamiltonian

$$H = \frac{p^2}{2m} + V(r), \tag{3.34}$$

where the hyperon potentials are

$$\begin{aligned} V(r) &= -30\rho/\rho_0 \text{ MeV for } \Lambda, \\ V(r) &= 0 \text{ MeV for } \Sigma, \end{aligned} \tag{3.35}$$

and the classical Hamilton equations are given by

$$\frac{\partial p_i}{\partial t} = -\frac{\partial H}{\partial q_i} = -\frac{\partial r}{\partial q_i}\frac{\partial V(r)}{\partial r} = -\frac{q_i}{r}\frac{\partial V(r)}{\partial r}, \tag{3.36}$$

$$\frac{\partial q_i}{\partial t} = \frac{\partial H}{\partial p_i} = \frac{p_i}{m}. \tag{3.37}$$

Once we fix the hyperon kinematic properties, we can calculate its propagation within the nucleus and how the hyperon momentum changes under the influence of the potential, specifically in the case of the Λ particle, by following the classical Hamiltonian equations. Consequently, the alterations in both position and momentum can be expressed as follows

$$\mathbf{r} = \mathbf{r_0} + \Delta\mathbf{r} = \mathbf{r_0} + \frac{\mathbf{p_{Y}}_0}{|\mathbf{p_{Y}}_0|}\Delta x, \tag{3.38}$$

$$\mathbf{p_Y} = \mathbf{p_Y}_0 + \frac{\Delta x}{|\mathbf{p_Y}_0|}\mathbf{r_0} V'_{eff}(r_0). \tag{3.39}$$

The derivative of the effective potential is

$$V'_{eff}(r_0) = -\frac{m_Y}{r_0} V'(r_0), \tag{3.40}$$

where the potential $V(r_0)$ is given in the Eq. 3.35.

It is important to note that the Σ hyperons move in straight lines, just as they do in the simplest version of the FSI simulation, as they are not influenced by any potential. In this new improved algorithm, the initially set momentum is regarded as the hyperon asymptotic momentum ($\mathbf{p_Y}_{asym}$). In the case of the Λ, this $\mathbf{p_\Lambda}$ is regarded as the asymptotic momentum the hyperon would have in the absence of FSI. To account for the potential, the Λ initial energy is increased by $-V_\Lambda(r_0)$. We have to calculate the initial momentum (p_{Y0}) in the presence of the potential in the case of the Λ at the production point in order to propagate an on-shell hyperon through the intranuclear cascade of FSI. We do this by applying conservation of energy

$$T_{asym} = T(r_0) + V(r_0) = \sqrt{M_Y^2 + \mathbf{p_Y}_{asym}^2} - M_Y. \tag{3.41}$$

We calculate the initial momentum to be propagated from $T(r_0)$. Once we have calculated the hyperon kinetic properties (r_0, $\mathbf{p_Y}_0$), we proceed to propagate the hyperon, following the same steps as in the initial algorithm. In this new cascade, after verifying Pauli blocking, we calculate the total energy of the final hyperon in the $YN \to Y'N'$ interaction. We check whether the hyperon is trapped in the nucleus due to the potential.

Following Ref. [88] we implement further adjustments in this algorithm, which are required to account for the Λ potential. In case of a $\Lambda N \to \Lambda N$ interaction one should check that after the collision $\sqrt{m_\Lambda^2 + \mathbf{p_\Lambda}^2} + V_\Lambda(r) > m_\Lambda$. Otherwise, the Λ is trapped in the attractive potential, its propagation is ceased and the hyperon is not counted as an asymptotic final state. A fraction of bound Λ hyperons weakly decays into $p\pi^-$ and could be experimentally detected through these decay products. However, identifying the Λ becomes challenging due to the distortion of the emitted pion and nucleon within the nucleus. Additionally, measurement limitations imposed by detection thresholds further complicate the process. Lastly, it is crucial to note that a semiclassical cascade model is inadequate to explain the formation and decay of Λ hypernuclei. Next, if a secondary Λ is born in a $\Sigma N \to \Lambda N'$, its energy is increased by $-V_\Lambda(r)$ and its momentum is re-adjusted to continue its propagation as an on-shell particle. Finally, after a $\Lambda N \to \Sigma N'$ FSI, the Σ energy has to be decreased by $V_\Lambda(r)$ and its momentum adjusted to correspond to an on-shell Σ at position $\mathbf{r}$, unless $\sqrt{m_\Sigma^2 + \mathbf{p_\Sigma}^2} + V_\Lambda(r) < m_\Sigma$. In the latter case, no Σ hyperon can actually be created, so the interaction is disregarded and the original Λ continues its propagation

The new final state interaction ends when the hyperon exits the nucleus, or if the hyperon becomes trapped inside the nucleus. Meanwhile, the process is repeated, and we must recalculate the momentum for an on-shell hyperon from its kinetic energy, and in the next propagation, this momentum is used to propagate the hyperon between one collision and the possible next one.

$YN \to Y'N'$ cross sections

We have followed the parametrization indicated in the appendix of Ref. [85]. In order to help the reader we include below a summary of the contents of that appendix.

The parametrizations used in our MC code for the $YN \to Y'N'$ cross sections correspond to the best fits to data with the chosen functional form. The data used in the fits have been obtained from http://nn-online.org. During the course of this work, we checked the latest data available for these $NY \to N'Y'$ cross sections [144, 145, 146, 147] and found that there were no significant changes with the data initially available. The fitting described in the appendix of Ref. [85] would be validly adjusted to these new data, so we continue to use that fitting. Despite the new data presented for these reactions in recent years, the cross sections are still poorly known. The statistical errors of the data are quite large and one should use these numbers as simple estimates. Note that the momenta in the next formulas always refer to the hyperons.

- $\Lambda + N \to \Lambda + N$
  $\sigma = (39.66 - 10.45x + 92.44x^2 - 21.40x^3)/p_{LAB}$, where $x = \min(2.1, p_{LAB})$. Fitted to data for $\Lambda p \to \Lambda p$ scattering from Refs. [148, 149, 150].

- $\Lambda + N \to \Sigma^0 + N$

$\sigma = (31.10 - 30.94x + 8.16x^2)p^{\Sigma}_{CM}/p^{\Lambda}_{CM}$, where $x = \min(2.1, p_{LAB})$. Fitted to data for $\Lambda p \to \Sigma^0 p$ scattering from Ref. [150].

- $\Sigma^+ + p \to \Sigma^+ + p$
  $\sigma = 11.77/p_{LAB} + 19.07$. Fitted to data for $\Sigma^+ p \to \Sigma^+ p$ scattering from Refs. [151, 152].

- $\Sigma^- + p \to \Sigma^- + p$
  $\sigma = 22.40/p_{LAB} - 1.08$. Fitted to data for $\Sigma^- p \to \Sigma^- p$ scattering from Ref. [151, 152].

For the rest of the channels, in the appendix of Ref. [85], the authors have used isospin symmetry and detailed balance. They assumed a similar size and energy dependence to the available channels. Therefore, using isospin symmetry

$$\begin{aligned}
\sigma_{\Lambda+n\to\Sigma^-+p} &= \sigma_{\Lambda+p\to\Sigma^++n} = 2\sigma_{\Lambda+n\to\Sigma^0+n} = 2\sigma_{\Lambda+p\to\Sigma^0+p} \\
\sigma_{\Sigma^-+n\to\Sigma^-+n} &= \sigma_{\Sigma^++p\to\Sigma^++p} \\
\sigma_{\Sigma^++n\to\Sigma^++n} &= \sigma_{\Sigma^-+p\to\Sigma^-+p}
\end{aligned}$$

To obtain the channels with a Λ in the final state, the authors used the principle of detailed balance

$$p_{ab}^2 \sigma_{ab\to cd} = p_{cd}^2 \sigma_{cd\to ab}$$

where p_{ab} and p_{cd} are the corresponding CM momenta.

The rest of the ΣN processes have been taken with a cross section equal to the elastic processes $\Sigma^- + p \to \Sigma^- + p$

$$\sigma_{\Sigma^-+p\to\Sigma^-+p} = \sigma_{\Sigma^0+N\to\Sigma^0+N} = \sigma_{\Sigma^-+p\to\Sigma^0+n} = \sigma_{\Sigma^0+p\to\Sigma^++n}.$$

For the case $\Sigma^- + p \to \Sigma^0 + n$ there are few data points compatible with this value [153].

Pion absorption

In the $Y\pi$ channel, there is the possibility of pion absorption. In this case, the inelastic hyperon production can be confused with quasielastic channels. Although the main objective of this thesis is to assess total hyperon production, it may also be worthwhile to contemplate the final state interaction of the pions generated through the hyperon-pion mechanism. This consideration is important because if pions could be detected in future experiments, it could contribute to a more comprehensive understanding of the processes involved. The idea is to calculate the probability of pion absorption and how it depends on the initial antineutrino energy, the size of the nucleus, and the type of hyperon. The absorption of pions can occur at any point within the nucleus. We do not perform a comprehensive calculation of the pion final state interaction, as pions on their way out could scatter and change energy, direction and charge, among other effects . However, since this thesis does not primarily focus on this aspect, we instead focus on estimating the potential pion absorption using an eikonal approximation. This approach has been successfully employed in the analysis of various pion production processes in nuclei induced by pions [154] or neutrinos [155, 156].

Following the Refs. [157, 158], we can write the probability for a pion absorption in terms of the probability of reaction per unit time P and the pion self-energy Π

$$Pdt = -\frac{1}{\omega}\mathrm{Im}\,\Pi dt = -\frac{1}{|\mathbf{p_m}|}\mathrm{Im}\,\Pi dl, \tag{3.42}$$

where $\omega = \sqrt{|\mathbf{p_m}|^2 + m_\pi^2}$, $|\mathbf{p_m}|$ is the modulus of the pion three-momentum and $\mathrm{Im}\,\Pi_{\mathrm{abs}}$ indicates the imaginary part of the pion self-energy related to absorption in the nuclear medium. This self-energy has been taken from Refs. [157, 158]. In our case, we work with the probability of reaction per unit length, being $dl = |\mathbf{p_m}|\,/\omega dt$, we write the expression as

$$P_{abs} = -\frac{1}{|\mathbf{p_m}|}\mathrm{Im}\,\Pi_{\mathrm{abs}}. \tag{3.43}$$

To delve into the details of the calculation of the pion absorption probability in the nucleus, we sum the contributions of the s-wave and p-wave components to this probability per unit length.

$$P_{abs} = P_{s-wave}(\hat{p}_m, \vec{r}) + P_{p-wave}(\hat{p}_m, \vec{r}) \tag{3.44}$$

where $\vec{r}$ is the production point. The expression of the s-wave absorption probability per unit length is given by

$$P_{s-wave}(\hat{p}_m, \vec{r}) = \frac{4\pi}{p_m}\left(1 + \frac{\omega}{2M}\right)\mathrm{Im}B_0\rho(\vec{r})^2. \tag{3.45}$$

where $\rho(\vec{r})$ is the sum of both nucleon densities (proton and neutron). The term B_0 is associated with s-wave pion absorption and it has the following dependence on the pion mass

$$\mathrm{Im}B_0 \approx \frac{0.035}{m_\pi^4}. \tag{3.46}$$

For the p-wave part, the pion absorption probability is

$$P_{p-wave}(\hat{p}_m, \vec{r}) = \frac{4}{9}\left(\frac{f^*}{m_\pi}\right)^2 p_m^2 \left|\tilde{G}_\Delta(p_m + p)\right|^2 (-\mathrm{Im}\Sigma_\Delta)\rho(\vec{r}), \tag{3.47}$$

where $\tilde{G}_\Delta(p_m + p)$ is the Δ propagator. In the absorption process, the Δ self-energy depends only on two-body and three-body absorption cuts

$$-\mathrm{Im}\Sigma_\Delta = [C_{A2}(\rho/\rho_0)^\beta + C_{A3}(\rho/\rho_0)^\gamma], \tag{3.48}$$

the terms C_{Ai} (where i can be 2 or 3, in the absorption case), β and $\gamma = 2\beta$ are parametrized as in Ref.[157] and are expressed as follows

$$\begin{aligned} C_{A2} &= 1.06x^2 - 6.64x + 22.66 \\ C_{A3} &= -13.46x^2 + 46.17x - 20.34 \\ \beta &= -0.038x^2 + 0.204x + 0.613, \end{aligned} \tag{3.49}$$

where $x = T_m/m_\pi$, being T_m the pion kinetic energy. In our calculation of pion absorption probability, we consider the Pauli blocking of nucleons in the nuclear medium.

In this approximation, the probability for a pion to escape from the nucleus is given by

$$P_{no\ abs} = \exp\left[-\frac{1}{p_m}\int_0^\infty \mathrm{Im}\,\Pi_{abs}(\vec{r} + \lambda\,\frac{\mathbf{p_m}}{|\mathbf{p_m}|})\,d\lambda\right]. \tag{3.50}$$

Chapter 4

Analysis and results

4.1 $Y\pi$ production off the nucleon

In this section, we start with the discussion of the results obtained for the $Y\pi$ production off free nucleons induced by antineutrinos driven by the strangeness-changing weak charged current. It is important to analyse and understand the functioning of the primary inelastic hyperon-pion production to allow us to better understand how this production behaves inside a nucleus, because the nuclear effects distort the final signal detected. This kind of reactions has been very scarcely analysed so far. As we said, we have considered in our model the $\Delta(1232)$ and $\Sigma^*(1385)$ resonances to study how dominant and important they can be in our processes. We also compare our results with previous works that follow different approaches. In Ref. [100], the authors considered the $\Lambda(1405)$ resonance. A non-relativistic 3-quark model (NR3QM) was followed by the authors in Ref. [101]. In Ref. [102], they used a relativistic quark model to calculate cross sections for Λ and Σ resonances by antineutrinos. Dewan's model considered Born terms to estimate $Y\pi$ cross section [103]. A relativistic quark model with harmonic interaction is used in Ref. [104], where the authors calculated the cross section for $\Sigma^*(1385)$ resonance production off protons.

This section is divided into four subsections. First, we present the results for the total cross section. In the second subsection, we show the hyperon energy distributions. In the third, we compare with those of other similar models. Finally, in the fourth, we present the results for the flux-folded total cross section and hyperon energy distribution for muon antineutrino fluxes from various experiments, including MiniBooNE, SciBooNE, T2K and Minerva.

4.1.1 Total cross sections

The possible reactions allowed by the selection rules of the strangeness-changing weak charged current are:

$$\begin{array}{rcl}
\bar{\nu}_\mu + p & \longrightarrow & \mu^+ + \pi^0 + \Lambda \\
\bar{\nu}_\mu + n & \longrightarrow & \mu^+ + \pi^- + \Lambda \\
\bar{\nu}_\mu + p & \longrightarrow & \mu^+ + \pi^0 + \Sigma^0 \\
\bar{\nu}_\mu + p & \longrightarrow & \mu^+ + \pi^+ + \Sigma^- \\
\bar{\nu}_\mu + p & \longrightarrow & \mu^+ + \pi^- + \Sigma^+ \\
\bar{\nu}_\mu + n & \longrightarrow & \mu^+ + \pi^0 + \Sigma^- \\
\bar{\nu}_\mu + n & \longrightarrow & \mu^+ + \pi^- + \Sigma^0
\end{array}$$

In Figs. 4.1, 4.2 and 4.3, we present the results for the total cross sections of hyperon-pion production off proton and neutron targets as a function of the muon-antineutrino energy in the laboratory (LAB) frame. In order to better understand the dynamics of the different possible channels in each reaction, we show the contribution from individual diagrams of Figs 2.1a and 2.1b, where applicable. We want to know what contribution is more important in each reaction, whether the behaviour is repeated in all reactions and whether resonances play a crucial role in the sum of the contributions. The relation between the cross sections of the different reactions is shown in Appendix B via the SU(3) relationships between the hadron amplitudes. The values for the $\mathcal{A}_i^{N\to Y\pi}$ constants are indicative of the relationships between the distinct channels of reactions. In the "Total" line (black solid line) we sum over all the contributions. It represents the full model, taking into account the contribution from the resonance channel. The purple solid line corresponds to the coherent sum of the background terms. The antineutrino energy range is between 0.5 - 2.0 GeV. The cross sections of these primary reactions are about $\sim 10^{-41}\,\mathrm{cm}^2$.

It is worth noting that we do not present the results for all the channels. We do not represent the contributions from the Kaon-Pole diagram that appear in Fig. 2.1a. In these figures, we have not plotted the KP contributions at all because the hadron tensor associated with the KP diagram alone is proportional to $q^\mu q^\nu$, and when contracted with the lepton tensor, it is proportional to the square of the lepton mass, making its individual contributions negligible for electron and muon antineutrinos. However, their contributions are present in the "Total" result. As we said, the reader can note that the size of the contributions of many mechanisms depicted in Figs. 2.1a and 2.1b can be understood in terms of their couplings alone, given by the constants $\mathcal{A}_i^{N\to Y\pi}$ of tables 2.3 and 2.4.

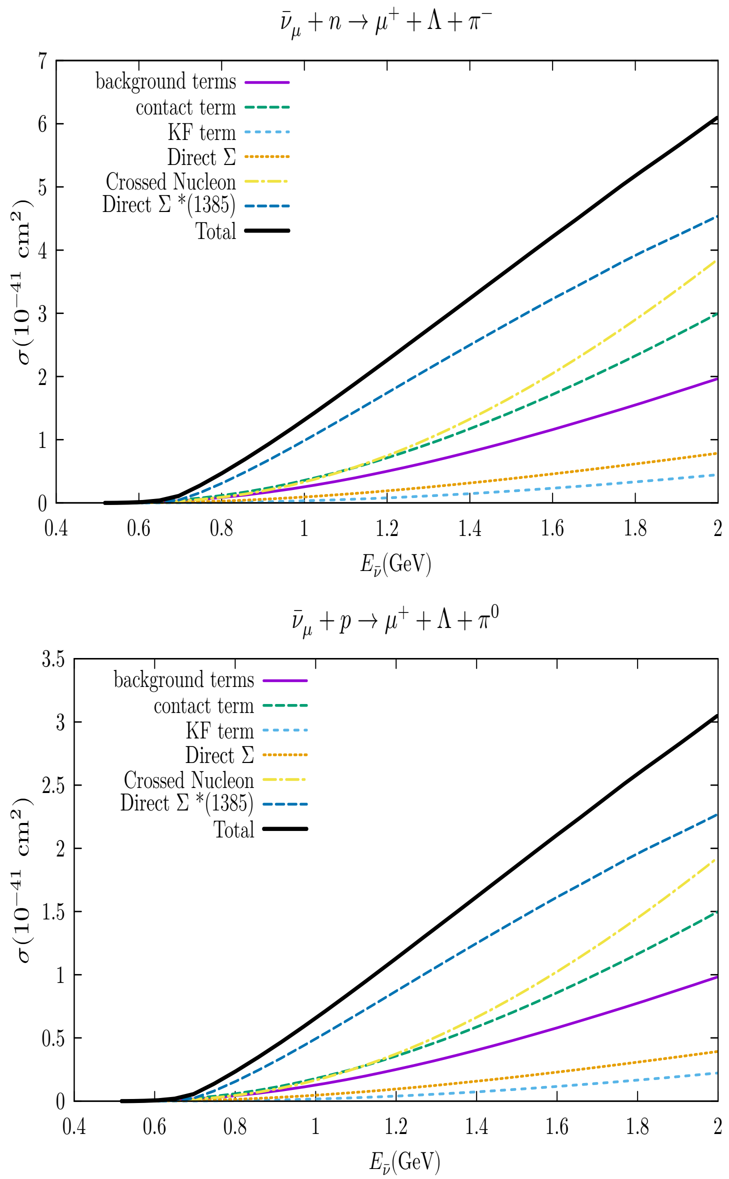

Figure 4.1: Total cross sections for the Λ hyperon production off neutrons (top panel) and protons (bottom panel). Some of the contributions of individual diagrams of Figs. 2.1a and 2.1b have been singled out. Note that the nature is identical in both panels, except for the scale on the vertical axis. This is because the total cross section for neutrons is exactly twice that for protons (see Appendix B).

The cross sections for the $\Lambda\pi$ final state on the neutron and proton target are shown in Fig. 4.1. Apart from the individual contributions, we also present results for the background terms, where we add all the diagrams of Fig. 2.1a coherently. We find that the background terms are comparable with the resonance contribution. Undoubtedly, the channel that contributes the most is the $\Sigma^*(1385)$ resonance, and this is because this resonance strongly decays into a Lambda and a pion [70]. Furthermore, if we look at the constants $\mathcal{A}_{s-\Sigma^*}^{N\to Y\pi}$ for the resonance channel, the values are higher for the $\Lambda\pi$ production for both initial nucleons, being higher in the case of having an initial neutron. We want to denote that the channels that contribute most to the total cross section are (in order) the direct $\Sigma^*(1385)$ resonance, the crossed nucleon (proton in these cases) and the contact term. One particular feature of the $\Lambda\pi$ production cross section is that the cross section off neutron targets is exactly twice that for proton targets; see Appendix B for the SU(3) relationships derived for the different amplitudes (hadronic currents). So the dynamics are the same in both cases.

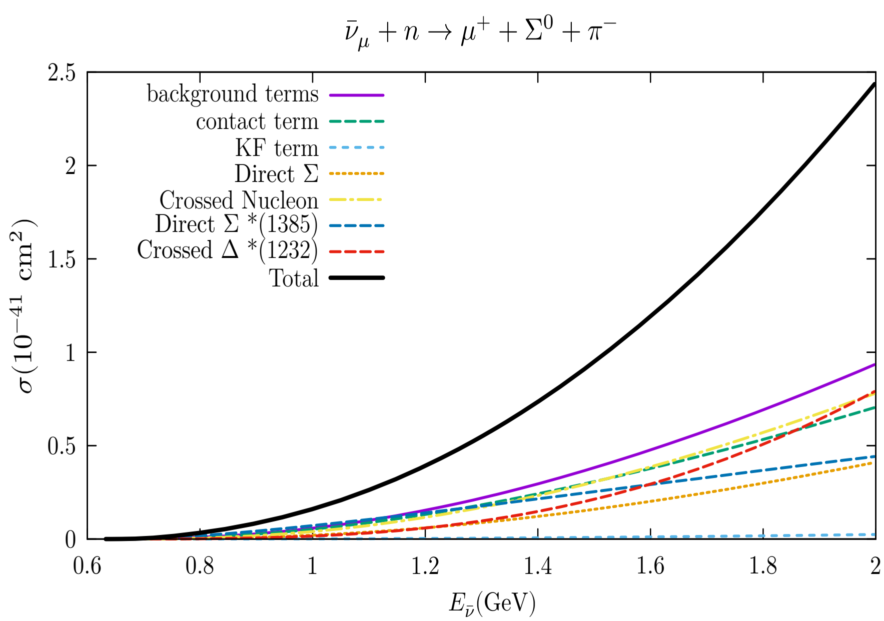

Figure 4.2: Total cross sections for the $\Sigma^0\pi^-$ and $\Sigma^-\pi^0$ production off neutrons. We present here the results for $\Sigma^0\pi^-$ production only. The results for the $\Sigma^-\pi^0$ are identical as the hadron amplitude is the same up to a relative sign (see Appendix B). We also present individual contributions of some of the diagrams following Fig. 4.1.

Let us examine the shapes of the cross sections of the diagrams contributing to the $\Sigma\pi$ production off neutrons, as depicted in Fig. 4.2. In this case, the possible final states are $\Sigma^0\pi^-$ and $\Sigma^-\pi^0$. Both final charge channels cross sections are exactly identical and the results are shown for only one of the channels ($\bar{\nu}_\mu + n \to \mu^+ + \Sigma^0 + \pi^-$). This can be understood from their isospin relations as given in Appendix B, where the moduli of the isospin factors are the same for both channels.

$$\left|\left\langle \Sigma^0\pi^- \right| j^\mu_{\rm sc} \left| n \right\rangle\right| = \left|\left\langle \Sigma^-\pi^0 \right| j^\mu_{\rm sc} \left| n \right\rangle\right| . \tag{4.1}$$

In these cases, the most important contribution comes from the sum of all background terms (purple solid line). The resonance $\Sigma^*(1385)$ diagram has not the same importance as in the production of Λs, this is because the decay fraction of this resonance into $\Sigma\pi$ is 11.7%, which is much small compared to the decay fraction into $\Lambda\pi$ of 87% [70]. Moreover, the reaction threshold for producing Σs is higher, this implies that there is less phase space available at the same antineutrino energy. If we compare the Figs. 4.2 and 4.1, we note that the full model grows faster with the antineutrino energy for the $\Sigma\pi$ reaction than for $\Lambda\pi$ production. The contribution of the kaon in flight channel is smaller than in the $\Lambda\pi$ production case. The most important channels, in order, are the crossed nucleon (with the crossed nucleon being a proton for $\Sigma^0\pi^-$ and a neutron for $\Sigma^-\pi^0$) and the contact term. Another essential difference between both figures is that, in the case of $\Sigma\pi$ production, the crossed channel of the $\Delta(1232)$ resonance contributes, which does not play a role in the production of Λ.

In Fig. 4.3, we show the total cross section for $\Sigma\pi$ production off protons. In contrast to the same production off neutrons, the contributions are very different between the distinct reactions. The total cross section is greater for $\Sigma^+\pi^-$ production. This is important because the primary Σ^+ production is only possible through this inelastic reaction, not with QE process. As this hyperon can only be produced off protons, if its primary production cross section were already smaller at the nucleon level, it would be even smaller compared with the primary production of the other Sigma's, because these could be produced off protons and neutrons in nuclei. The $\Delta(1232)$ resonance channel is the most important for $\Sigma^0\pi^0$ and $\Sigma^+\pi^-$ production followed by the background terms. Meanwhile, the crossed nucleon channel is the principal contribution to the $\Sigma^-\pi^+$ production, being a rather significant contribution compared to the rest of the diagrams. We can also observe that, as it happened in the case of the production off neutrons, the $\Sigma^*(1385)$ resonance has less importance alone than in the case of $\Lambda\pi$ production. Note, for instance, that in the case of $\Sigma^0\pi^0$ production, it is not even an allowed channel.

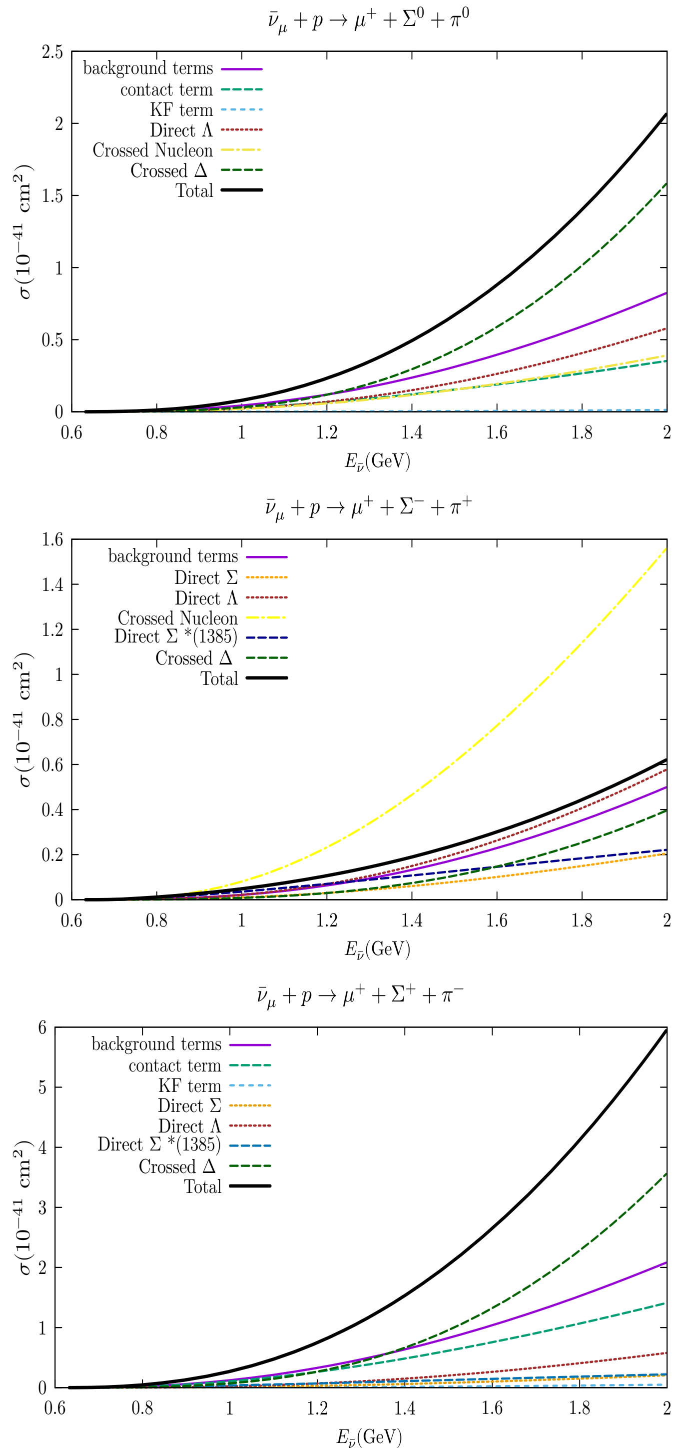

Figure 4.3: Total cross sections for the Σ hyperon production off protons, $\Sigma^0\pi^0$ on the top panel, $\Sigma^-\pi^+$ on the middle one and $\Sigma^+\pi^-$ on the bottom. The individual contributions are also shown, similar to Fig. 4.1.

The reader may note that the total cross section starts at distinct antineutrino energies for Λ and Σ production. This is because the value of the threshold antineutrino energy for the reactions to take place because the Λ mass is smaller than the Σ's ones. This is going to be more important when we compare the $Y\pi$ production off nuclei with the quasielastic production. The threshold plays an important role in the comparison.

We compare the main differences between the different hyperon-pion productions and initial nucleons. The relative size of the contributions of many mechanisms depicted in Figs. 2.1a and 2.1b can be understood in terms of their couplings given by the constants $\mathcal{A}_i^{N\to Y\pi}$ of tables 2.3 and 2.4. If we compare, first, the behavior of the total cross section as a function of the antineutrino energy for the $\Sigma\pi$ production off neutrons and protons (Figs. 4.2 and 4.3), we can notice that the interferences between the distinct channels are very different for both types of nucleons. The total cross section increases significantly for production off neutrons. The interferences are, thus, constructive. For the protons, in general, the interferences between the different mechanisms (diagrams) are significant and destructive, except for the $p \to \Sigma^+\pi^-$ channel (see Fig. 4.3), where the incoherent sum of all the contributions give roughly the total cross section of about 6×10^{-41} cm^2 at $E_{\bar{\nu}} = 2$ GeV. But this reaction channel is the exception. In the others, the interference is important and reduces the total cross section as compared with the incoherent sum of the singled-out contributions. In some cases, like in the reaction $\bar{\nu}_\mu + p \to \mu^+ + \Sigma^- + \pi^+$ (see Fig. 4.3) the crossed nucleon mechanism is much larger than the total cross section. Similar results are found for the $\Lambda\pi$ production, as might be seen in Fig. 4.1. Here we must point out that the chiral Lagrangian fixes the relative sign between all background diagrams, at least close to the threshold. In the $\Lambda\pi$ case, even having destructive interferences, the total cross section is larger than anyone of the single contributions of the different mechanisms. We can say that, in general, for all cases of hyperon-pion production except for the Σ^+ and the $\Sigma\pi$ production off neutrons, the interferences between all the diagrams contributing to these productions are destructive to a greater or lesser extent.

We want to recall that the Kaon-pole term (KP) result does not appear in any figures but it has been taken into account in the background and total contributions. For instance, the smallness of the Kaon-in-Flight (KF) contributions in the Σ production reaction channels (Figs. 4.2 and 4.3) can be explained because their cross sections are proportional to the square of $(D - F)$, while for the Λ production reaction channels (Fig. 4.1), these are proportional to the square of $(D+3F)$, which is much larger. Also, there are threshold effects that are not negligible at all, because the threshold energy for producing a Λ particle is smaller than that for producing a Σ ($M_\Lambda < M_\Sigma$), thus allowing a larger phase space for the same antineutrino energy. However, the virtual kaon in the KF diagram carries a four-momentum which is highly off-shell, which also suppresses its contribution in all of the reactions. Indeed, following an argument similar to that for Eq. (2.76),

$$p_K^2 = (p - p_Y)^2 \leqslant (M - M_Y)^2 \ll M_K^2. \tag{4.2}$$

In fact, if the reader consults the Refs. [116, 117, 118], one can see that this kind of contribution is more sizeable when the mass of the exchanged meson is lighter, as it is the case of the πP diagrams with respect to the ηP ones, if one inspects some of the figures depicted in Refs. [116, 117, 118].

Next, let us focus on the behavior of the crossed-nucleon diagrams. In general, the crossed-nucleon channels are important because of two main reasons:

- The constants of the diagrams $\mathcal{A}^{N\to Y\pi}_{\mathrm{u-N'}}$ are proportional to $(D+F)$ coupling coming from the $NN'\pi$ vertex (see table 2.3), which is also large.
- The four-momentum squared carried by the intermediate nucleon (N') is closer to its squared mass, given that the mass of the final π meson is lighter. Following the Eq. (2.76) with M_Δ^2 replaced by M^2, it is given by

$$p'^2 = M^2 + m_\pi^2 - 2ME_\pi \leqslant (M - m_\pi)^2 < M^2. \tag{4.3}$$

Therefore, in this case, the difference in the intermediate nucleon propagator, $(p - p_m)^2 - M^2$, exhibits a smaller absolute value compared to the crossed-Δ propagator. This channel is especially important for the $\Sigma^-\pi^+$ production off protons, although the interferences have a destructive impact, compared with the production of the other types of Σ. The relative size of the crossed-diagrams for the different channels can be understood by referring to the table 2.3 along with tables 2.1 and 2.2. Particularly interesting, in Fig. 4.3, where the ratio $\sigma_{u-N'}(\Sigma^0\pi^0) : \sigma_{u-N'}(\Sigma^-\pi^+)$ is $1:4$. If the reader looks only at the values of the table 2.3 one sees only a factor $\sqrt{2}$ of difference between the constants $\mathcal{A}_i$ for both reactions, which would imply only a ratio of $1:2$. However, there is an additional $\sqrt{2}$ factor hidden in the vector and axial-vector transition form factors for $p \to \Sigma^0$ and $n \to \Sigma^-$ in tables 2.1 and 2.2. This results in the contribution of this diagram to the cross section $p \to \Sigma^0\pi^0$ being four times smaller than that for the reaction $p \to \Sigma^-\pi^+$. Something similar happens with the neutron-induced $\Sigma\pi$ reactions presented in Fig. 4.2, but in this case, the factors compensate each other, giving the same contribution (a $1:1$ ratio) to the cross section.

In the s-channel we find that, normally, the direct Λ contributions are larger than the direct Σ contributions in $\Sigma\pi$ production off protons by a factor of ~ 3

when both diagrams are present in the same reaction channel. This observation can be more or less understood because $\frac{D}{\sqrt{3}} \sim F$ and if one neglects (which is a reasonable approximation for the vector form factors) the impact of the charge form factor $f_1^n(q^2)$ (certainly not good for the magnetic $f_2^n(q^2)$), the ratio of direct Λ over direct Σ is roughly $\left(\frac{D}{F}\right)^2 \sim 3$. Additionally, it is important to consider the presence of the pure axial-vector contribution and the vector-axial interference in these diagrams, which tend to cancel. Otherwise, the observed ratio of 3:1 would not be as accurate as it turns out to be. It is worth noting that the direct Λ contributions are absent in other hyperon production channels, while the direct Σ contributions exist, but they are not the dominant ones.

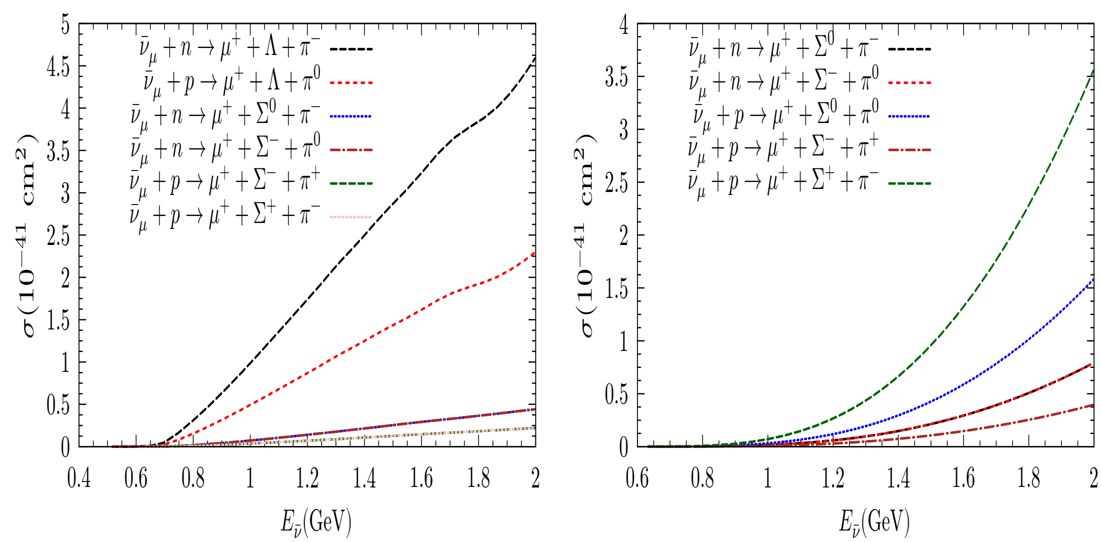

Figure 4.4: Total cross sections for all hyperon production reactions off neutrons and protons for the resonance channels. In the left panel, we show the direct $\Sigma^*(1385)$ contributions, and in the right one, the crossed $\Delta(1232)$ channel.

It is essential to evaluate the relevance of the resonance channels incorporated into our model for each one of the possible $Y\pi$ production reactions. As previously mentioned, this thesis has exclusively taken into account the channels involving the $\Delta(1232)$ and the $\Sigma^*(1385)$ resonances. In Fig. 4.4, a comparison of all feasible reactions is presented. Nevertheless, other studies consider supplementary channels that encompass various resonances, including the $\Lambda(1405)$. We also compare later our findings with those that have incorporated this resonance [100].

The contribution of direct Σ^* resonance channel plays a crucial role in the final $\Lambda\pi$ production reactions of Fig. 4.1, and gradually decreases for $\Sigma\pi$ production off neutrons (Fig. 4.2) and it has an even smaller impact in the case of proton-induced reactions (Fig. 4.3). There are various possible explanations:

- As we have mentioned previously, the $\Sigma^*(1385)$ resonance diagram is more significant in the case of $\Lambda\pi$ production than $\Sigma\pi$. This is because the decay fraction of this resonance into a Lambda and a pion is 87%, whereas into a Sigma and a pion, it is only 11.7% [70]. This is a threshold effect because the $\Sigma^*(1385)$ resonance has more phase space available to decay into $\Lambda\pi$ than into $\Sigma\pi$, precisely because the mass of the Λ is lower than that of the Σ. Even though there are more possibilities for final $\Sigma\pi$ states due to charge states in which any charge state of $\Sigma^*(1385)$ can decay. It also happens that to produce $\Sigma\pi$, more neutrino energy is needed than to produce $\Lambda\pi$. In fact, this mechanism is dominant in the $\Lambda\pi$ production channel, which has a lower threshold than the $\Sigma\pi$ one. This threshold effect allows the phase space to have grown for the $\Lambda\pi$ reaction when the $\Sigma\pi$ starts to be feasible.

- The $\mathcal{A}_{s-\Sigma^*}$ couplings of the second column of table 2.4 are a factor $\sqrt{3}$ (a factor 3 of reduction in the cross section) smaller for the $n \to \Sigma\pi$ channels than it is for the $n \to \Lambda\pi^-$ one (the largest one); for the reaction off protons there is even an additional $\sqrt{2}$ factor of reduction in the amplitude, thus implying a factor 6 of reduction in the cross section.

The presence of this threshold effect, together with mainly the smaller couplings for the $\Sigma\pi$ channels diminishes the contribution of the Σ^* resonance for the final production of $\Sigma\pi$.

Finally, the crossed-Δ diagrams are important for the $\Sigma\pi$ reaction channels, especially when induced off protons (see Fig. 4.3). It is important to note that this channel does not contribute to the $\Lambda\pi$ production due to the isospin selection rule. In fact, according to their coupling constants of the third column of table 2.4, their individual contributions to the cross sections for the channels $p \to \Sigma^+\pi^-$, $p \to \Sigma^0\pi^0$, $n \to \Sigma\pi$ and $p \to \Sigma^-\pi^+$ are found in the relative ratios $9 : 4 : 2 : 1$, respectively.

Now that we have a comprehensive understanding of the contributions of the different diagrams to each possible reaction, it is time to conduct a thorough comparison of the total cross section values for these reactions, which encompass both the background and resonance terms.

In Fig. 4.5, we present the total cross sections for the full model corresponding to all the possible $Y\pi$ channels induced by muon antineutrinos off nucleons. These cross sections are plotted as a function of the antineutrino energy in the LAB frame. It is interesting to see that the total cross sections have the same

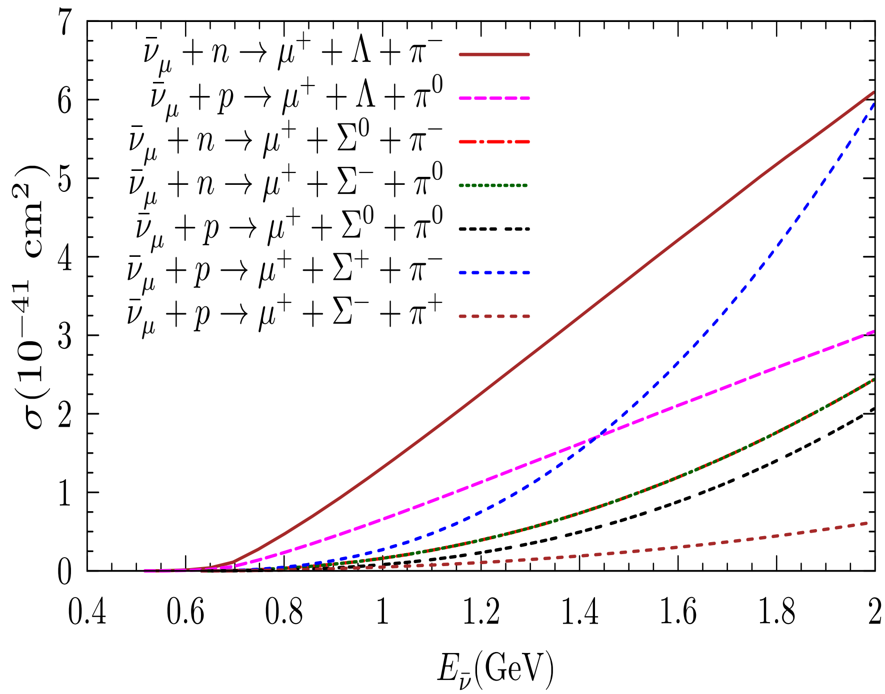

Figure 4.5: Plot of the total cross sections for $Y\pi$ production off nucleons induced by muon antineutrinos as a function of the antineutrino energy in the LAB frame.

order of magnitude as the single K and $\bar{K}$ production cross sections off nucleons studied in Refs. [116, 117]. Additionally, these total cross sections are roughly two orders of magnitude smaller than their Cabibbo-enhanced counterparts, specifically referring to the charged-current weak single pion production cross sections off nucleons that do not involve strangeness-changing processes. This reduction in magnitude can be attributed to the transformation from $V_{ud}^2 \to V_{us}^2$ in the cross sections, which amounts to a factor of roughly $\sim 5.3 \times 10^{-2}$, neglecting the higher production thresholds for the reactions studied here.

When comparing, in Fig. 4.5, the form of the total cross section of the $\Lambda\pi$ and $\Sigma\pi$ production, we can see that, in general, the values grow faster with antineutrino energy in the $\Sigma\pi$ production, especially in the case of $\Sigma^+\pi^-$. As we said, this is partly due to the fact that the total cross section for $\Lambda\pi$ production starts in energy earlier than in the Σ case because of the lower threshold associated with Λ. It is also worth mentioning that the smallest total cross section corresponds to the production of $\Sigma^-\pi^+$ when considering proton targets in the range of antineutrino energies considered in Fig. 4.5.

Finally, in Figs. 4.6 and 4.7, we present a comparative analysis of the total cross sections for $Y\pi$ production induced by electron antineutrinos and muon antineutrinos, with respect to antineutrino energy in the LAB frame. As expected, the most remarkable feature of these cross sections is that the electron antineutrinos ones are larger than their muon counterparts. This characteristic arises from the lower production thresholds associated with electron antineutrinos, a consequence of the significantly smaller electron mass when contrasted with the muon mass. The shape of the cross sections remains the same for both types of antineutrinos.

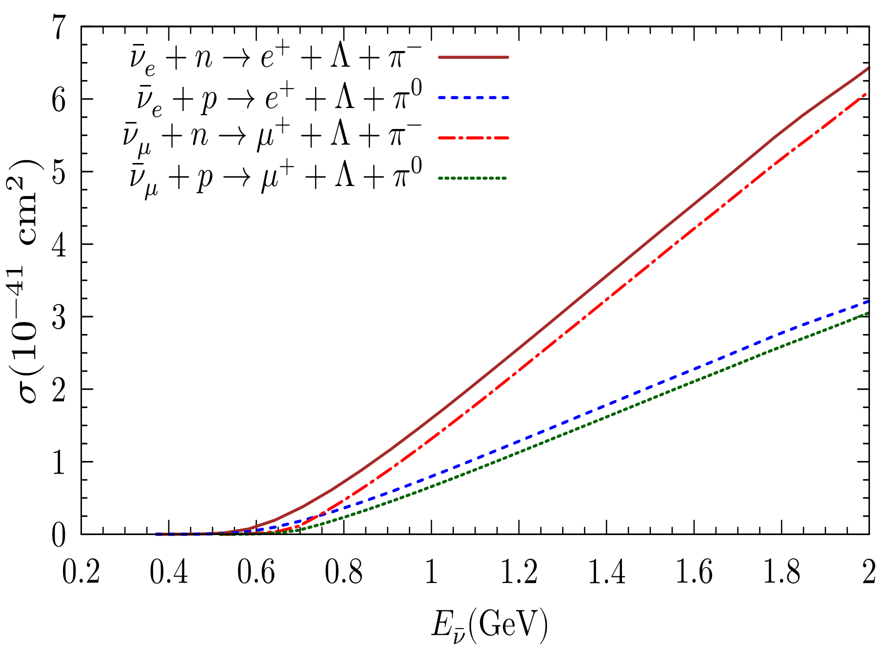

Figure 4.6: Comparison between electron antineutrino and muon antineutrino induced total cross sections off nucleons in terms of the antineutrino energies in the LAB frame. We display the $\Lambda\pi$ reaction channels

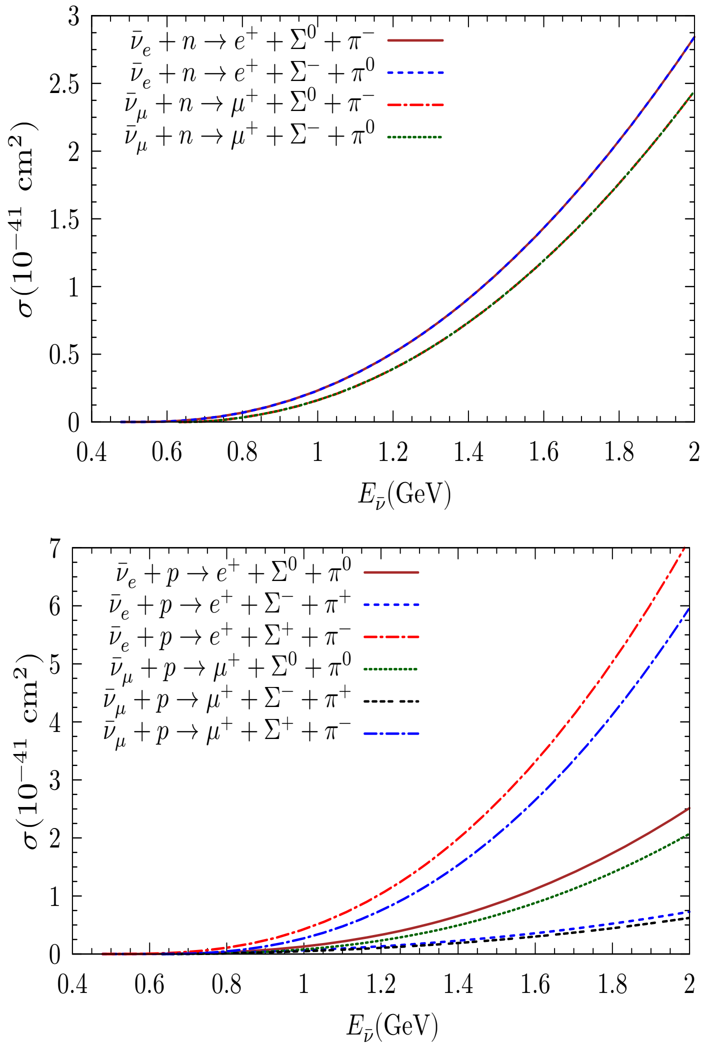

Figure 4.7: Comparison between electron antineutrino and muon antineutrino induced total cross sections off nucleons in terms of the antineutrino energies in the LAB frame. In the top panel we display the $\Sigma\pi$ production channels off neutrons. Finally, in the bottom panel we plot the $\Sigma\pi$ reactions off protons.

4.1.2 Hyperon energy distribution

In Fig. 4.8, we show the hyperon energy distributions for the $Y\pi$ production at an antineutrino energy of 2 GeV. We have used ^{12}C as the nuclear target to obtain these figures. By not considering the final state interaction, the nuclear effects taken into account are minimal. We make the comparison between the production off protons and neutrons. In the solid black lines, we show the hyperon production off neutrons, and it is worth noting that in the Σ^+ production, this line is absent because this kind of hyperon can only be produced off protons. On the other hand, the dashed red lines present the hyperon production off protons. In general, the values of the energy distribution are larger for the neutron case than for the production off protons. This is important because when we expand our model on the nucleus we do not work only with symmetric nuclei. This becomes particularly pertinent as major neutrino oscillation and scattering experiments employ asymmetric nuclei as their target materials.

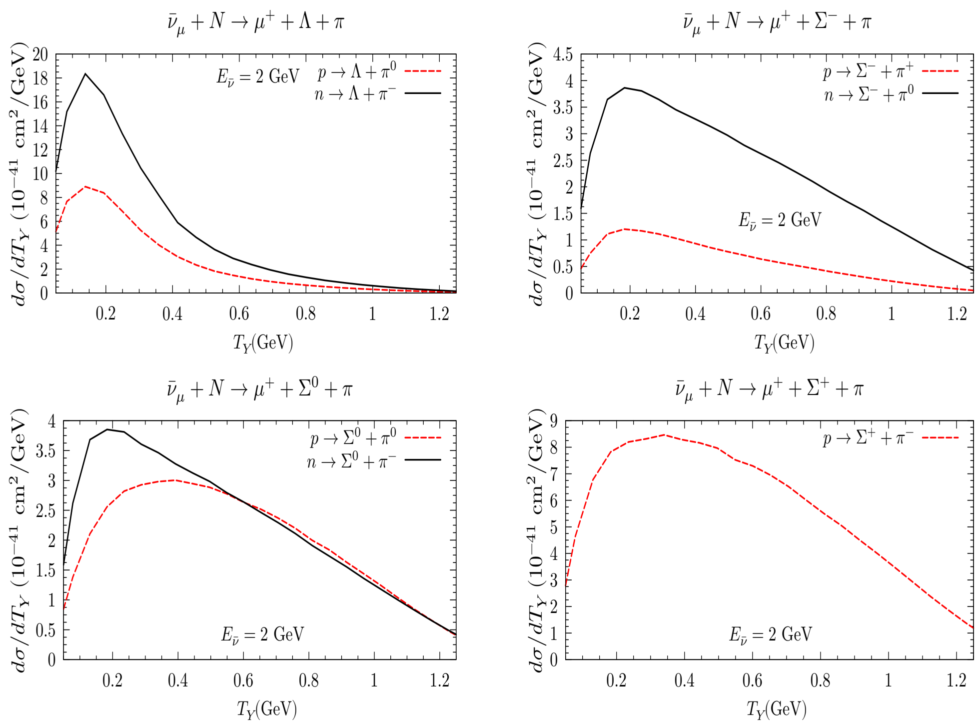

Figure 4.8: Hyperon energy distributions for hyperon-pion production off both nucleons. The antineutrino energy is fixed at 2 GeV. Note that in the case of the Σ^+ production, the process occurs only off protons.

The kinetic energy distribution of the Λ is peaked around the mass of the resonances, as the invariant mass is close to that value. Beyond the resonance region, the distribution values decay sharply. In contrast, for the production of any of the Σs, the resonances are not as crucial. The invariant mass distribution in the production of Σs has a significant contribution beyond the resonance region. Therefore, the results of the Σs decrease more gradually at higher kinetic energies.

4.1.3 Comparisons with other models

To the best of our knowledge, our calculations regarding the $Y\pi$ production are one of the first in studying these processes, alongside Refs. [100, 101, 102, 103]. To validate our model, we make some comparisons with the results obtained in these previous works prior to ours.

To initiate the analyses, in Fig. 4.9, therefore, we present a comparative analysis of our muon antineutrino induced total cross sections off protons considering only the mechanism of s-Σ^* diagram. We compare our results with those of Ref. [101], where the authors calculate the quasifree production of an on-shell $\Sigma^{*0}(1385)$ resonance. To compare the production cross sections of specific $Y\pi$ channels, we have taken into account the primary decay channels of Σ^*: $\Lambda\pi^0$ and $\Sigma\pi$ with branching ratios 87% and 11.7% respectively. These branching ratios have been taken from the PDG [70]. Furthermore, to separate the inclusive $\Sigma\pi$ decay channel into the different charged channels, $\Sigma^{\pm}\pi^{\mp}$ and $\Sigma^0\pi^0$ we have also multiplied the latter branching ratio by the SU(2) Clebsch-Gordan coefficients squared for the coupling of two $I = 1$ particles to another $I = 1$ state. The coefficient for $\Sigma^0\pi^0$ is zero, while those for $\Sigma^{\pm}\pi^{\mp}$ are $\frac{1}{2}$ for each channel. In this study, they provided results for the V-A approach and calculations performed using the non-relativistic 3-quark model (NR3QM-single). In contrast, in Ref. [102], the authors employ a relativistic quark model to compute the cross sections for the Lambda and Sigma resonances.

In the upper panel of Fig. 4.9, where the two models show a remarkable coincidence, the solid lines correspond to our model, while the dashed lines are those of Ref. [101] with the V-A approach. They used an axial mass $M_A =$ 1.05 GeV for the axial form factor $C_5^A(q^2)$. The reader should note that, in this thesis, the axial mass used is $M_A = 1.03$ GeV. The coincidence was, a priori, expectable, but it is also remarkable. Nevertheless, in our model, certain off-shell effects introduce a slight discrepancy at the highest energies within the top panel, particularly in the context of the $\Sigma^{\pm}\pi^{\mp}$ production channel. In this same panel, we include dotted lines with filled squares to represent the corresponding outcomes from Ref. [102]. The coincidence for the decay channel $p \to \Sigma^{*0}(1385) \to \Lambda\pi^0$ at the higher energies shown in the plot is remarkable.

On the other hand, in the lower panel of Fig. 4.9, we show the same solid curves as in the top one. In this part of the figure, we compare our results with the calculations with the non-relativistic 3 quark model (NR3QM-single) discussed in Ref. [101]. In this case, it is worth noting that discrepancies tend to be more pronounced at lower antineutrino energies, as anticipated. This is because the cross sections calculated within the NR3QM-single approach were already smaller than those calculated within the V-A approach, as demonstrated in Fig. 10 of Ref. [101]. Nevertheless, it is noteworthy that the cross sections in both cases remain within the same order of magnitude, even when compared with the less favorable approach.

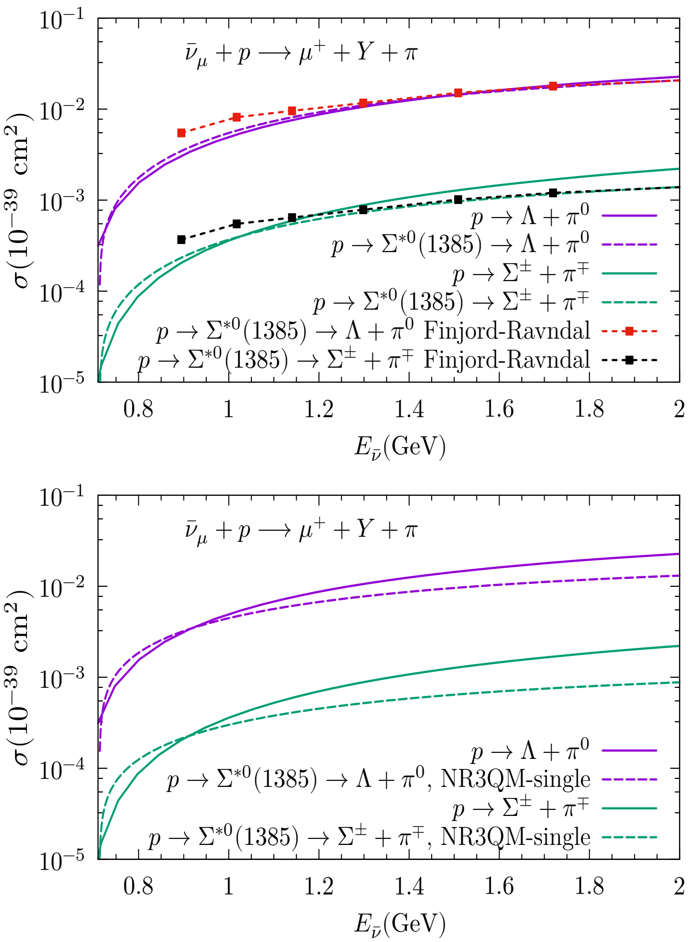

Figure 4.9: Comparison for the reaction of Cabibbo suppressed single pion production off protons with the mechanism of intermediate Σ^{*0} alone. We compare it with the results obtained in Ref. [101], where the authors calculated the quasi-free production of an on-shell Σ^{*0} off protons induced by muon antineutrinos. In both panels, solid lines represent our model with only s-Σ^* reaction mechanism. In the top panel, dashed lines show the results from Ref. [101] using the V-A approach, and in the lower panel, they represent the NR3QM-single approach. On the top panel, we also display as dotted lines with filled squares the results of Ref. [102].

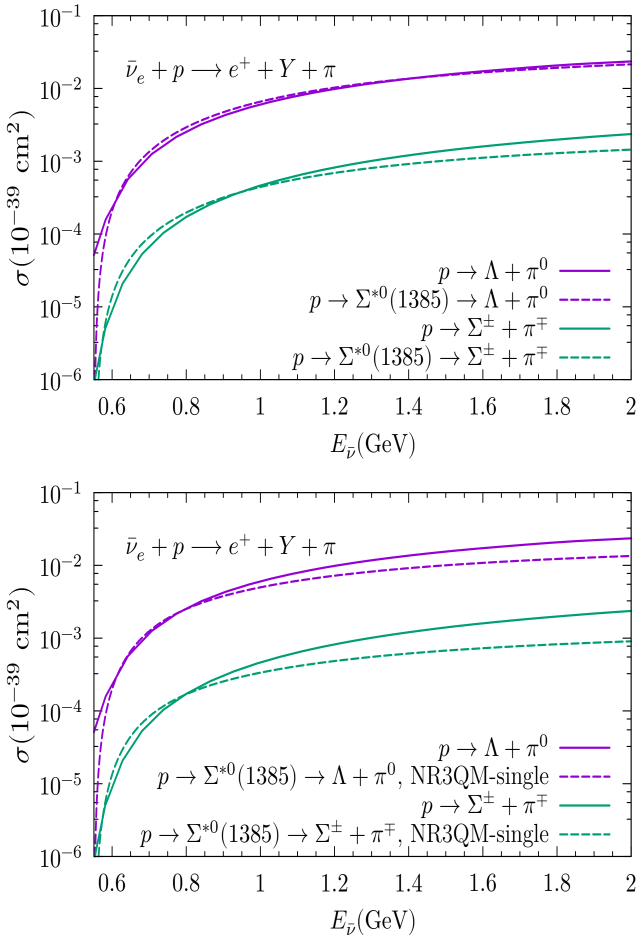

Figure 4.10: Same as Fig. 4.9 but for the reactions induced by electron antineutrinos off protons. Panels and lines have the same meaning as in Fig. 4.9.

In Fig. 4.10, we present a similar comparison to that shown in Fig. 4.9, but now with the results from Ref. [101] for the reactions induced by electron antineutrinos off protons. In this case, the thresholds are slightly lower, but the general features found in Fig. 4.9 remain the same. One should note that the comparison on the upper panel of Fig. 4.10 with the V-A approach of Ref. [101] is very good because our approach is similar, with the primary distinction being the off-shell production of the Σ^{*0} (1385) resonance in our model, while in Ref. [101], the production is on-shell. However, on the lower panel, the agreement with the NR3QM-single approach is more inadequate as it already was in the bottom panel of Fig. 4.9.

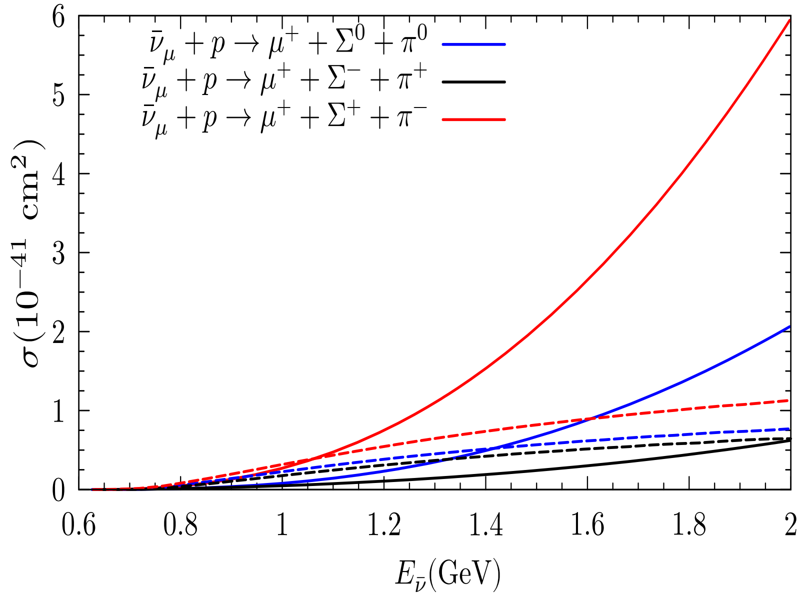

Figure 4.11: Comparison between the total cross sections for the three $\Sigma\pi$ reaction channels for our model (solid lines) and that of Ref. [100] (short-dashed lines).

Lastly, in Fig. 4.11, we present the comparison between the results of the total cross sections for the three charge $\Sigma\pi$ states production channels off protons in our model (solid lines) and the results from the Ref. [100] (short-dashed lines). The model used in Ref. [100] is based on a chiral unitary approach, where all the meson-baryon pairs with $S = -1$ produced in a primary contact term, kaon-pole or meson-in-flight diagram are allowed to interact in a coupled channels approach to dynamically generate the Λ (1405) resonance. This is achieved by solving the Bethe-Salpeter equation with an interaction potential derived from the lowest-order chiral Lagrangian, as described in Ref. [100].

If we inspect Fig. 4.11, it becomes evident and clear that the total cross sections derived in our model are generally much larger than those of Ref. [100]. Particularly significant is the remarkable growth observed in the $\Sigma^+\pi^-$ channel, with amounts to almost a factor 6 at $E_{\bar{\nu}} = 2$ GeV. The growth in the $\Sigma^0\pi^0$ channel is more moderate, while in the $\Sigma^-\pi^+$ channel, our cross section is smaller than its counterpart of Ref. [100]. Nevertheless, it is worth noting that, near the threshold, all three cross sections in Ref. [100] surpass those in our model, even although we explicitly incorporate a resonant diagram with a $\Sigma^*(1385)$ resonance which is below the $\Lambda(1405)$ resonance and above the $\Sigma\pi$ threshold. This clearly indicates the significant role played by the $\Lambda(1405)$ in describing these reactions near the threshold for the $\Sigma\pi$ production channels. Probably the reason for this is that the $\Lambda(1405)$ appears in s-wave coupled channels and these are going to be much more important close to the threshold. Nonetheless, the $\Sigma^*(1385)$ is a p-wave resonance, similar to the Δ, and its contribution, which is already small due to its couplings (as shown in Fig. 4.3) for these reactions, starts to contribute more at higher antineutrino energies. In Fig. 4.11, however, it does not appear the $\Lambda\pi$ production. This is because the $\Lambda(1405)$ resonance is not going to play any role in the $\Lambda\pi^0$ production off protons. After all, it appears in the I=0 channel and the final one has I=1. We think the most reliable and unaffected by the presence of higher lying strange resonances are those reaction channels with a Λ as a final hyperon.

One similarity between the results of Ref. [100] and ours is that the order of the channels with larger cross sections is exactly the same, i.e, the cross section for $\Sigma^+\pi^-$ production is larger than that for $\Sigma^0\pi^0$ and the latter larger than the $\Sigma^-\pi^+$ production channel in both approaches. This consistency provides a degree of self-confidence in our results within our model. Also note that in the calculations of Ref. [100], a non-relativistic reduction of the amplitudes was carried out. These approximations can also have an impact on the differences observed in the size of the cross sections for the same range of antineutrino energies shown in Fig. 4.3. However, we cannot at the present moment quantify how much of the difference comes from the non-relativistic approximation and/or from other relevant ingredients present in the model of Ref. [100] and absent in ours, or vice versa.

Finally, it is also worth noticing that the way these cross sections rise in our model is very similar to how the crossed or u-channel diagrams do it, especially the crossed Δ diagrams plotted in Fig. 4.3, which are very relevant by themselves, especially for the $\Sigma^+\pi^-$ and $\Sigma^0\pi^0$ reaction channels, which are those with the largest cross sections. This could point to the importance of crossed diagrams, not only for Δ intermediate states but also for N^* resonances that are not considered here. Nonetheless, taking into account these differences from the model presented in Ref. [100] for $\Sigma\pi$ production, we focus on examining how our model behaves for this type of Σ production with nuclear targets in Sect. 4.2.

4.1.4 Flux-integrated total cross sections

As mentioned in the section 2.4, we have also estimated the flux-folded total cross sections for antineutrino fluxes of several experiments like MiniBooNE [159], SciBooNE [160], T2K [161, 162] and Minerva [163]. In the introduction of this thesis, specifically in Sec. 1.3, the reader can find a brief explanation of these experiments, among others. The energy dependence of these fluxes is shown in Fig. 4.12. All these fluxes are normalized concerning their total flux, i.e., the value for each energy bin has been divided by the total integrated flux. We choose antineutrino fluxes that peak at intermediate energies, $\langle E_{\bar{\nu}} \rangle \simeq 1 - 3$ GeV. At these energies, the four-momentum transfers are expected to be low enough to carry out chiral expansions, making the results of the present model more reliable. It is important to bring back the definition of the flux-integrated total cross section, $\langle \sigma \rangle$, for a given antineutrino flux $\Phi(E_{\bar{\nu}})$ of some experiment

$$\langle \sigma \rangle = \frac{\int_{E_{\bar{\nu}}^{\rm th}}^{E^{max}} \Phi(E_{\bar{\nu}})\, \sigma(E_{\bar{\nu}})\, dE_{\bar{\nu}}}{\int_0^{E^{max}} \Phi(E_{\bar{\nu}})\, dE_{\bar{\nu}}}. \tag{4.4}$$

In table 4.1, we show the flux-folded total cross sections for muon antineutrinos fluxes from the different experiments.

Reaction	MiniBooNE	SciBooNE	T2K ND280	T2K SK	Minerva
$p \to \pi^0 + \Lambda$	3.42	1.95	2.17	1.68	23.8
$n \to \pi^- + \Lambda$	6.84	3.90	4.33	3.36	47.7
$p \to \pi^0 + \Sigma^0$	0.935	0.713	0.0684	0.0546	0.623
$p \to \pi^- + \Sigma^+$	2.88	2.13	0.290	0.231	2.85
$p \to \pi^+ + \Sigma^-$	0.369	0.254	0.111	0.0887	1.36
$n \to \pi^- + \Sigma^0$	1.38	0.954	0.263	0.211	2.96
$n \to \pi^0 + \Sigma^-$	1.38	0.954	0.263	0.211	2.96

Table 4.1: Flux-folded total cross sections for $\bar{\nu}_\mu$ fluxes from different experiments, in units of 10^{-42} cm^2. The cut in the final invariant hadronic mass $W \leqslant 1.4$ GeV has been applied to the calculations for the T2K and Minerva fluxes. The uncertainties are in the last significant figure.

The T2K (both at the near detector ND280 and at SuperKamiokande one) and Minerva fluxes have larger tails ranging up to 20 GeV. Our model, which is based on a chiral expansion, cannot be considered reliable for these larger energies. At such energies, the potential for high momentum transfers and significant invariant masses becomes accessible as antineutrino energy increases. In fact, there is another problem related to the aforementioned argument: the cross sections, in particular the $p \to \Sigma^+\pi^-$ in Fig. 4.5, exhibit a very faster growth rate with energy, much faster than the fall rate of the neutrino fluxes of these experiments with it, thus not providing a clearly decreasing product $\Phi(E_{\bar{\nu}})\sigma(E_{\bar{\nu}})$ for higher

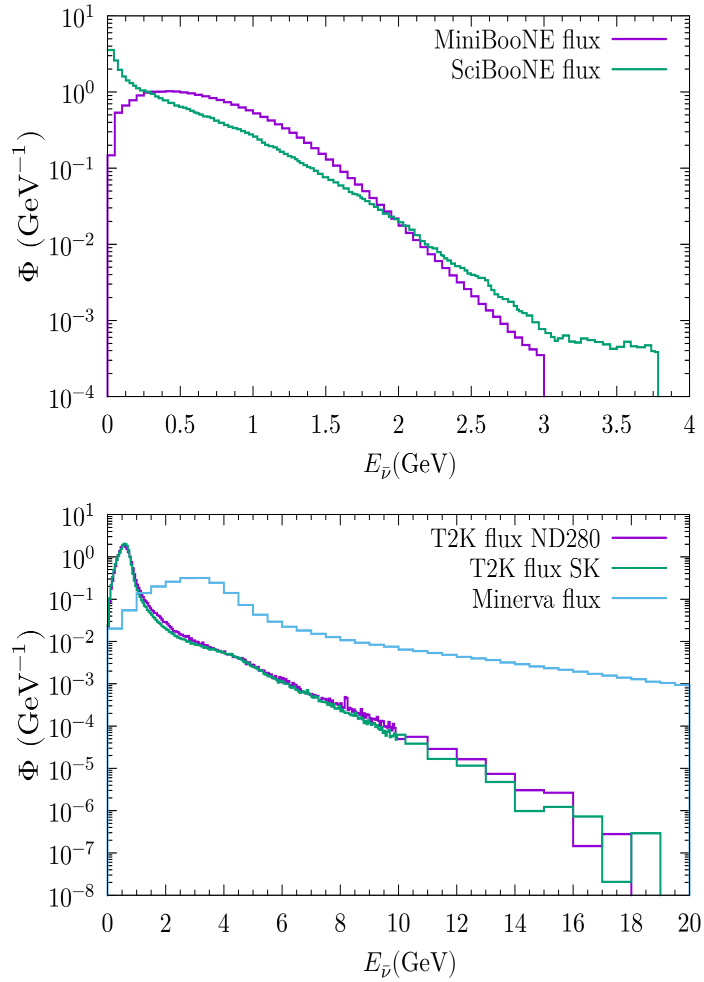

Figure 4.12: Fluxes from different experiments. On the upper panel, the $\bar{\nu}_\mu$ fluxes from MiniBooNE [159] and SciBooNE [160]. On the bottom panel, the T2K fluxes at the near detector ND280 and the Super-Kamiokande far detector [161, 162], and the enriched $\bar{\nu}_\mu$ Minerva flux [163]. The fluxes are normalized to their total flux, i.e, the integral of the fluxes shown in this figure is 1.

and higher antineutrino energies for the numerator of Eq. (4.4). This makes the flux-averaged total cross section somehow ill-defined, because the larger the antineutrino energy up to one integrates, the larger the flux-folded total cross section is.

In order to overcome this difficulty, we have put a constraint in the final invariant hadronic mass reached by the $Y\pi$ pair. We constrain this invariant mass to be below 1.4 GeV (as detailed in Eq. 2.77). This approach resolves two problems: on one hand, we are sure that higher lying strange resonances above the $\Sigma^*(1385)$, such as the $\Lambda(1405)$ (which has been shown in Fig. 4.11 to contribute importantly to the $\Sigma\pi$ production channel near threshold), are not going to contribute for these kinematically constrained total cross sections; on the other hand, the imposition of an invariant mass cutoff results in significantly lower total cross sections, which exhibit slower growth with increasing antineutrino energy. This allows us to calculate a well-defined flux-averaged total cross section with the fluxes of T2K and Minerva (low energy mode). Moreover, this constraint offers an advantage, as it can also be enforced experimentally, thereby rejecting $Y\pi$ events with measured invariant masses exceeding $W > 1.4$ GeV. In such a scenario, the flux-averaged total cross sections, if measured, could be reliably compared with the numbers provided in table 4.1 for the T2K and Minerva experiments. It is important to note also that the SuperKamiokande flux is provided in Refs. [161, 162] for the non-oscillation scenario. However, the flux is altered by neutrino oscillation at the far detector, leading to different measured values. To provide these values, the calculations in the fifth column of table 4.1 would need to be performed using the oscillated flux, which is not currently available.

In order to analyze the results shown in table 4.1, it is important to emphasize that the flux-folded total cross sections do not depend on the total flux, because they are normalized to it. They depend basically on the shape of the flux, particularly where the flux is mostly peaked and whether its tails are longer or shorter. And also on how large the total cross section is in the energy region where the flux is sizeable. With this in mind, we can understand the calculations shown in table 4.1.

The first comparison we analyse is between the flux-averaged cross sections for MiniBooNE [159] and SciBooNE [160] experiments. Note that the flux taken for MiniBooNE, Ref. [159], corresponds to the antineutrino enhanced sample; while the flux for SciBooNE is taken from figure 1 of Ref. [160] and corresponds also to the $\bar{\nu}_\mu$ flux, but in this case, this is not the predominant component of the flux, because the latter is the muon neutrino component. Nonetheless, the differences in the fluxes can be seen in the upper panel of Fig. 4.12. The fluxes from MiniBooNE and SciBooNE are generally similar, with the notable exception that the SciBooNE flux peaks at antineutrino energies below the threshold for the reaction to occur. In addition, the SciBooNE flux has a longer tail which decreases a bit more gradually than the MiniBooNE one. The MiniBooNE flux decreases by three orders of magnitude in roughly ~ 2 GeV, while the SciBooNE one does the same in ~ 2.5 GeV. Although not a significant difference, therefore, the flux-averaged cross sections are expected to be similar in both experiments.

Indeed, they are if one inspects the corresponding columns in table 4.1. These cross sections are always higher for MiniBooNE because its flux is larger in the region between 0.5 and 2 GeV. The presence of the SciBooNE tail has minimal impact, particularly for the $\Lambda\pi$ production channels, even though the cross section in this region is increasing (without the cut in the hadronic invariant mass).

However, there is a difference in the averaged cross sections for the reactions $p \to \Lambda\pi^0$ and $p \to \Sigma^+\pi^-$ in both experiments. The first reaction has a higher flux-folded cross section with the MiniBooNE flux, while the opposite occurs with the SciBooNE flux. The reason for this difference must be sought in the behavior of the cross sections for these two reactions in the higher energy tails of the fluxes. Observing Fig. 4.5, we can see how the cross section for $p \to \Sigma^+\pi^-$ grows clearly more steeply with the antineutrino energy than the $p \to \Lambda\pi^0$ cross section does. The result for this reaction is much larger than that for the production of Lambda starting from ~ 1.4 GeV. If we now focus on the upper panel of Fig. 4.12, we can see that from ~ 1.75 GeV onwards, the gradually decreasing tail of SciBooNE has a compensating effect for the $p \to \Sigma^+\pi^-$ reaction. In the region of this tail, the cross section for $p \to \Sigma^+\pi^-$ is much larger than for the $p \to \Lambda\pi^0$ channel. This makes the flux-folded $p \to \Sigma^+\pi^-$ cross section the second highest in magnitude with the SciBooNE flux, while it is the third for the MiniBooNE flux.

In the results presented in table 4.1, for the flux-folded total cross sections with the T2K near detector ND280, and Super-Kamiokande far detector fluxes [161, 162], and with the Minerva flux [163], we have applied the cut $W \leq 1.4$ GeV in the final hadronic invariant mass. We wanted to verify the decrease in the cross section due to the cut in the invariant mass. This cut has the obvious effect of reducing the size of the total cross sections, as can be observed in Fig. 4.13. However, the reduction in size is much more prominent for the $\Sigma\pi$ reactions than for the $\Lambda\pi$ ones. The reason for this behaviour is because the cut in the invariant mass is much closer to the threshold for $\Sigma\pi$ production ($W_{\text{th}}^{\Sigma\pi} = M_\Sigma + m_\pi \simeq 1.33$ GeV) than it is for the $\Lambda\pi$ production channels ($W_{\text{th}}^{\Lambda\pi} = M_\Lambda + m_\pi \simeq 1.25$ GeV). In fact, obviously, if the applied cut had been below the $\Sigma\pi$ threshold, all these cross sections would have been exactly zero.

Therefore, the substantial decrease in the size of the total cross sections for the $\Sigma\pi$ reaction channels, resulting from the application of the cut in the invariant mass, explains why the flux-averaged total cross sections with the T2K and Minerva fluxes are so small if compared with their $\Lambda\pi$ counterparts in table 4.1. The reduction attributed to the cut in the invariant mass is approximately one order of magnitude smaller for the $\Sigma\pi$ reactions. There is even a specific reaction channel, $p \to \Sigma^0\pi^0$, where the reduction of the cross section due to the cut in the invariant mass is especially significant, as it can be observed in the lower panel of Fig. 4.13.

This channel has the smallest cross section of the $\Sigma\pi$ channels, while this was not the case when there was no cut in the final hadronic invariant masses. In fact, for this particular reaction channel, the reduction in the flux-averaged total cross sections is already about two orders of magnitude than for the $\Lambda\pi$ reactions. For this reason, we have plotted in logarithmic scale the cross sections for the $\Sigma\pi$ channels when comparing them with the cut and without it in the bottom panel of Fig. 4.13. This choice is made because, on a linear vertical scale, the cross sections with the cut in the invariant mass were nearly imperceptible.

Something interesting happens when we apply the cut on the final invariant hadronic mass, and it is the similarity in the flux-averaged total cross sections for the $p \to \Sigma^+\pi^-$ and $n \to \Sigma\pi$ channels (both final charge channels have exactly the same cross section). If we observe first the results obtained for these channels in table 4.1, for such different fluxes as those of T2K and Minerva, which are centred at completely different antineutrino energies and have truly distinct tails, as shown in the bottom panel of Fig. 4.12. The results are practically identical among the three channels when compared with the differences observed with the MiniBooNE and SciBooNE fluxes, where we did not apply the cut on the invariant mass. However, the flux-averaged cross section for the $p \to \Sigma^+\pi^-$ channel is higher than that for the $n \to \Sigma\pi$ channels for the T2K fluxes, as these peak below 1 GeV, where the cross section for the $p \to \Sigma^+\pi^-$ production channel is slightly larger. For the Minerva flux, the results are the opposite because this flux peaks around 3 GeV, although the differences, as discussed, are truly minor. Now, if we focus on the bottom panel of Fig. 4.13, the reduced total cross sections (due to the cut) for both channels are so similar (compare the short-dashed blue and long-dashed black lines), whereas the cross sections without the cut in the invariant hadronic mass are clearly different, as we have observed in all the figures shown so far.

It is also worth mentioning that even although both T2K fluxes at near and far detectors are almost equal (see the bottom panel of Fig. 4.12), the flux-folded total cross sections are systematically smaller when convoluted with the flux at the SuperKamiokande detector for all the reactions. The reason for this has to be searched in the slightly smaller tail of the T2K flux at SK, compared with that at the ND280, especially in the region between 1 and 4 GeV of muon antineutrino energies, where its contribution is still relevant for the flux-integrated total cross section.

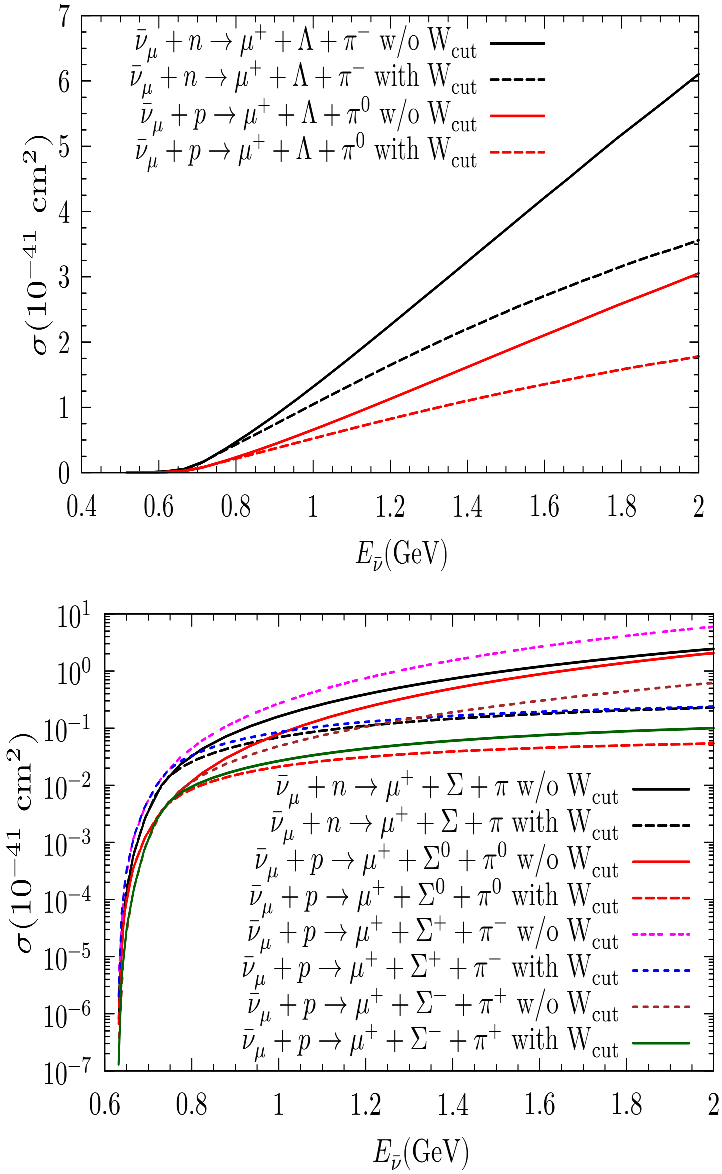

Figure 4.13: Plots of the total cross sections for the $Y\pi$ production as a function of the antineutrino energy with the effect of the kinematic cut in the final hadronic invariant mass $W \leq 1.4$ GeV. In the top panel, we show the results for $\Lambda\pi$ production, while in the bottom one, we display those for the $\Sigma\pi$ case. For this latter case, the y-axis is logarithmic because of the huge reduction in the cross sections when the cut $W \leq 1.4$ GeV is imposed.

Finally, the substantial values observed in the flux-averaged total cross sections, particularly for the $\Lambda\pi$ production channels, as depicted in the final column of table 4.1, stand out prominently when contrasted with the corresponding figures for the T2K fluxes. This notable difference can be attributed to the unique characteristics of the Minerva flux. The Minerva flux exhibits a pronounced peak around 3 GeV, a range in which the cross sections experience a substantial increase compared to the region where the T2K fluxes reach their maximum values. Moreover, it is crucial to highlight the impact of the larger and gradually decreasing tail of the Minerva flux, as evident in the solid cyan line on the bottom panel of Fig. 4.12. This tail plays a significant role in augmenting the flux-convoluted total cross sections for Minerva. The extended influence of the Minerva flux's tail is a key factor in enhancing the overall cross sections for this experiment when compared to the outcomes obtained for T2K. The combined effects of the peaked energy distribution and the extended tail contribute to the distinctive and much larger flux-averaged total cross sections observed with the Minerva flux.

4.2 Hyperon production off the nucleus

We present all the results corresponding to hyperon production processes off nuclei induced by muonic antineutrino beams. We evaluate numerically the effects of the nuclear medium on the quasielastic hyperon production using Eq. 3.19 and of the $Y\pi$ production using Eq. 3.31. The final state interaction effects are calculated using the two Monte Carlo simulations detailed in Sect. 3.4. We compare both results for the FSI to check how they can affect to the comparison with the experimental data. The range of energies has been limited such that the associated production of strange particles (hyperon + kaon) through $\Delta S = 0$ processes, not Cabibbo suppressed, is still small by phase space constraints.

We focus especially on the comparison between these two types of mechanisms (QE and $Y\pi$) and we study the effect of the final state interaction and its possible relevance. In one of the possible FSI simulations, we study the effect of the hyperon potential inside the nucleus. The selected nuclei for our study are ^{12}C, ^{16}O (light size), ^{40}Ca, ^{40}Ar and ^{56}Fe (medium size). The first three are symmetric nuclei (with the same number of protons and neutrons), and the last two are asymmetric. These nuclei are abundantly used in neutrino detectors. We also compare the results for the two kinds of hyperon production processes for symmetrical and asymmetrical nuclei and we study the dependence of the cross section on the nuclear size. After considering the QE mechanism in earlier studies, we focus on $Y\pi$ and the comparison between the two mechanisms. For most results, light ^{16}O and medium-size ^{40}Ar nuclei, present in modern neutrino detectors, are selected.

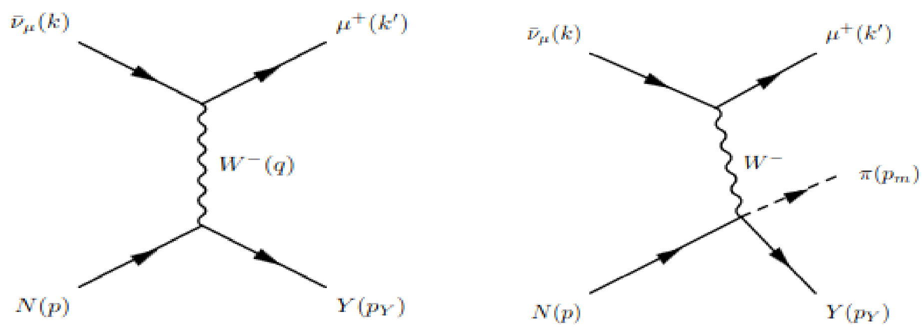

Figure 4.14: Feynman diagrams for quasielastic hyperon production (left figure) and hyperon-pion production (right figure).

As discussed in the introduction, the predictions for hyperon production are reliable for $\Delta S = -1$ QE and $Y\pi$ processes, restricting incoming neutrino energies to $E_{\bar{\nu}} \lesssim 2$ GeV. The $\Delta S = 0$ process is suppressed in measurements where no kaons are allowed in the final state.

4.2.1 Integrated cross sections

To initiate our analysis, Figure 4.15 provides a comparative examination of the two distinct FSI simulations delineated in Sec. 3.4, showing the integrated cross sections for ^{16}O for the quasielastic process, hyperon-pion production, and the cumulative effects of both contributions. In this first figure, the initial comparison focuses on the shape of the integrated cross sections, without delving into describing how both mechanisms behave. The aim is to observe how the effects of the two possible FSI simulations influence the same process. It is important to remind the reader at this point that in the description of the two FSI simulations, one took into account the potentials experienced by hyperons ("Improved FSI", subsection 3.4.2), while the other did not. Let us recall that the potential for the Λ is around $\sim -30\rho/\rho_0$ MeV, while it is absent for the Σ's. Another enhancement included in this "Improved FSI" model is that the Λ hyperon does not move in a straight line within the nucleus; instead, it follows the Hamilton equations since both momentum and position are changed by the hyperon-nucleus potential in its way out of the nucleus. In this simulation, we have also accounted for the possibility of the hyperon getting trapped in the nucleus due to the presence of potentials. In contrast, in the other simulation (no improvement, subsection

3.4.1), the hyperon always exited the nucleus, and therefore, it was always taken into account in our results as a final particle.

In Fig. 4.15, we present the integrated cross sections for QE (blue lines), $Y\pi$ (green lines), and the sum of both contributions (black lines). In the left panels, we observe the results obtained with the initial FSI; and in the right panels, those obtained with the enhanced FSI. As shown in Figure 4.15, the most significant difference induced by the intranuclear cascade effect occurs in the upper panels, namely, in Λ production. In contrast, there is not a significant difference between the two possible simulations in the Σ production. With the initial FSI, the cross section for Λ production increased compared to the result without FSI. With the enhanced FSI, there is still growth, but it is minimal compared to the initial FSI. This is attributed to the existence of the Lambda potential and the possibility of the Λ hyperon getting trapped inside the nucleus.

We present, in Fig. 4.16, the results for the integrated cross sections for ^{16}O and ^{40}Ar as a function of the muon antineutrino energy in the LAB frame. We show the contribution to the different hyperons production, for Λ and $\Sigma^{+,0,-}$ in the final state. The two kinds of processes (QE and $Y\pi$) and the sum of both contributions are shown with and without the inclusion of the enhanced FSI. We have selected these nuclei because we want to compare the differences between a symmetric nucleus and an asymmetric one, and the dependence on the nuclear size. The QE production calculations are represented by the blue dashed lines and $Y\pi$ production calculations in green ones. The black lines represent the sum of both contributions. The final sum of both contributions has been done using a cubic spline program that interpolates each distribution at the midpoint of its respective bin, and then both contributions have already been summed over the whole drawn range using the splines corresponding to each contribution at the same point. We can see that the effects of the FSI can be considered relevant in the two modes of hyperon production.

We observe the clear dominance of Λ production. This channel has a substantially larger cross section than the other ones taken together. This is partly due to FSI, which favors the $\Sigma \to \Lambda$ transitions. The initial calculation of Λ production is increased a little when we include the cascade effects. While for Σ^- and Σ^0 it is considerably reduced when applying the FSI effects. In the case of Σ^+ production, it only appears with FSI for the QE production, while in the inelastic case, it is reduced with respect to the initial production without FSI. The total cross sections for Σ^+ production are mostly dominated by the inelastic channel. Notice that for $E_{\bar{\nu}} < 1.2$ GeV, a large fraction of the cross section comes from the QE production, which only appears for this hyperon because of the FSI effect. This is not common for the rest of the hyperons where the QE cross section is clearly more relevant than the hyperon-pion ones at this range of energies. We observe the same relation between the results with and without FSI effects in the hyperon kinetic energy distribution. Going back to the scenario of Λ production, as mentioned, the integrated cross section shows a slight increase due to the FSI effect. However, this growth is not substantial. Despite the FSI favoring the transition from $\Sigma \to \Lambda$, the consideration of the Λ potential and the possibility of this particle getting trapped inside the nucleus counteract the overall increase, resulting in a moderated effect in the presence of FSI. The reader should take into account that, in all channels, the $Y\pi$ mechanisms have a higher threshold that implies that these mechanisms start to contribute at higher antineutrino energies. We can also observe that the $Y\pi$ contribution grows faster than the QE with the antineutrino energy. This effect is clearly visible in the case of Σ^0 production, but it also happens for the rest of the $Y\pi$ production channels. Despite this faster growth of the $Y\pi$ production with respect to the QE, overall, the cross sections for QE processes are, in general, larger than the $Y\pi$ production ones.

We should recall here that our model for the inelastic processes involves the decuplet non-strange resonance $\Delta(1232)$ and the strange resonance $\Sigma^*(1385)$. As the reader can see in Sect. 4.1, the $\Sigma^*(1385)$ channel provides the biggest contribution to $\Lambda\pi$ production. Meanwhile, the $\Delta(1232)$ channel contributes the most to the primary total cross section for the production of $\Sigma^0\pi$ and $\Sigma^+\pi$. However, this model does not include the $\Lambda(1405)$ resonance channel in the Σ production. In Ref. [100], the authors include the s-wave $\Lambda(1405)$ resonance. This resonance could play a moderate role in the $\Sigma\pi$ reaction channels at low energies. But the $\Lambda\pi$ production is not affected at all by the $\Lambda(1405)$ resonance, because it only decays to $\Sigma\pi$ and $\bar{K}N$ due to isospin conservation. Besides, the $\Lambda(1405)$ mechanisms are s-wave and grow rather slowly as a function of the energy. As a consequence, after inspection of the Refs. [98, 100], we find that they would only be competitive with the other $\Sigma\pi$ inelastic production mechanisms for the Σ^- and Σ^0 cases and at energies E_ν <1.4 GeV, where QE production is already much larger. Thus, we neglect them, as the net contribution would be small and these mechanisms would only be relevant for the investigation of some exclusive measurements where also a pion would be detected.

In summary, the QE results exhibit larger values compared to those obtained for the $Y\pi$ ones. Besides, the integrated cross section for $Y\pi$ grows faster with the antineutrino energy. We also observed, in the specific case of Λ production, the FSI effect increases slightly the value of the total cross section in both types of hyperon production. However, in Σ production reactions decreases the values. The exception is the cross section for Σ^+, because it is zero for the QE production without FSI, and the principal contribution comes from the $Y\pi$ production.

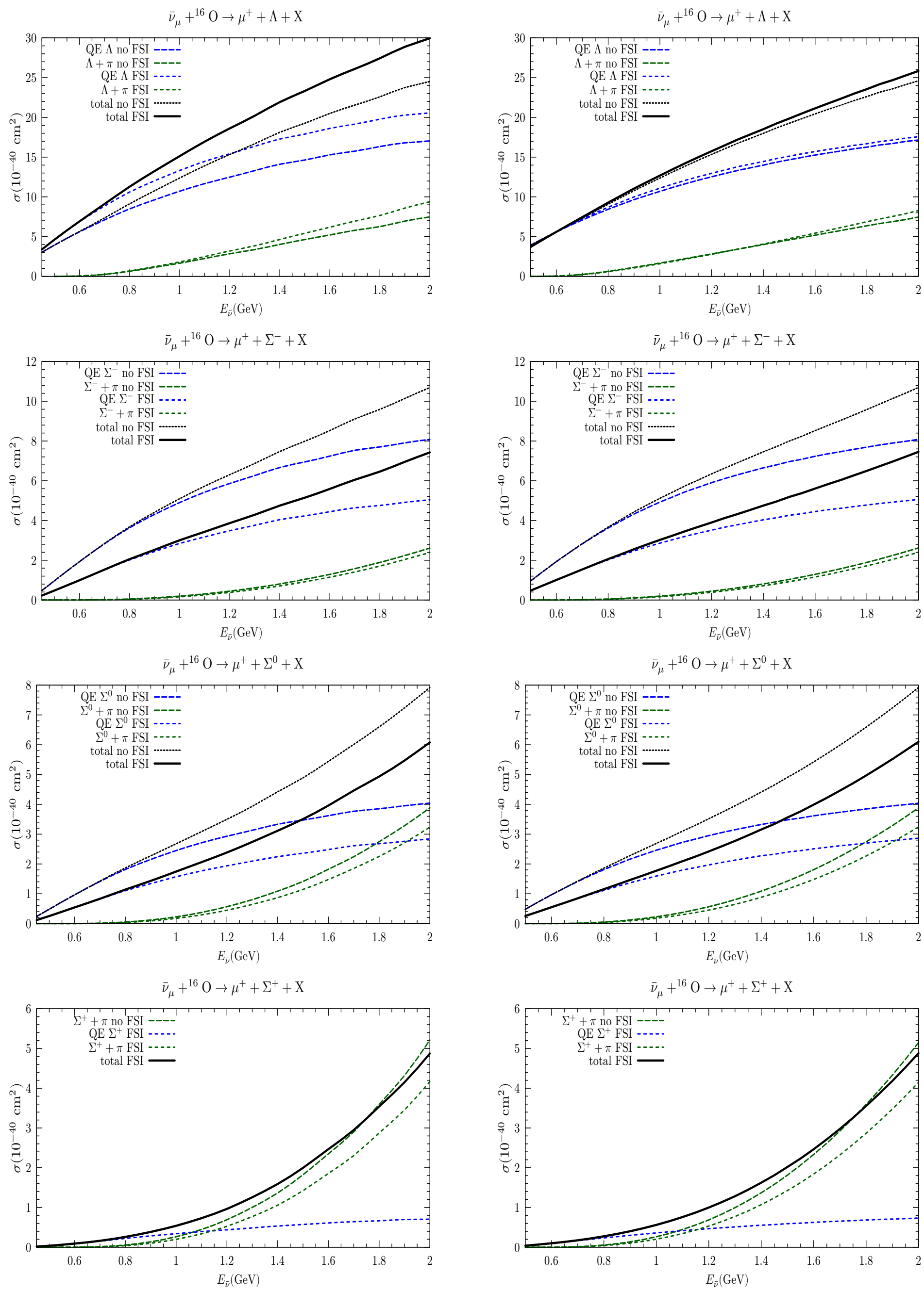

Figure 4.15: Integrated cross sections for QE production, $Y\pi$ production and the sum of both contributions with and without FSI for ^{16}O. In the left panels, we apply the FSI code without considering the hyperon potentials. Meanwhile, in the right panels, we use the improved FSI simulation. Note that in the case of QE interactions, the Σ^+ particle appears only as a result of FSI effects.

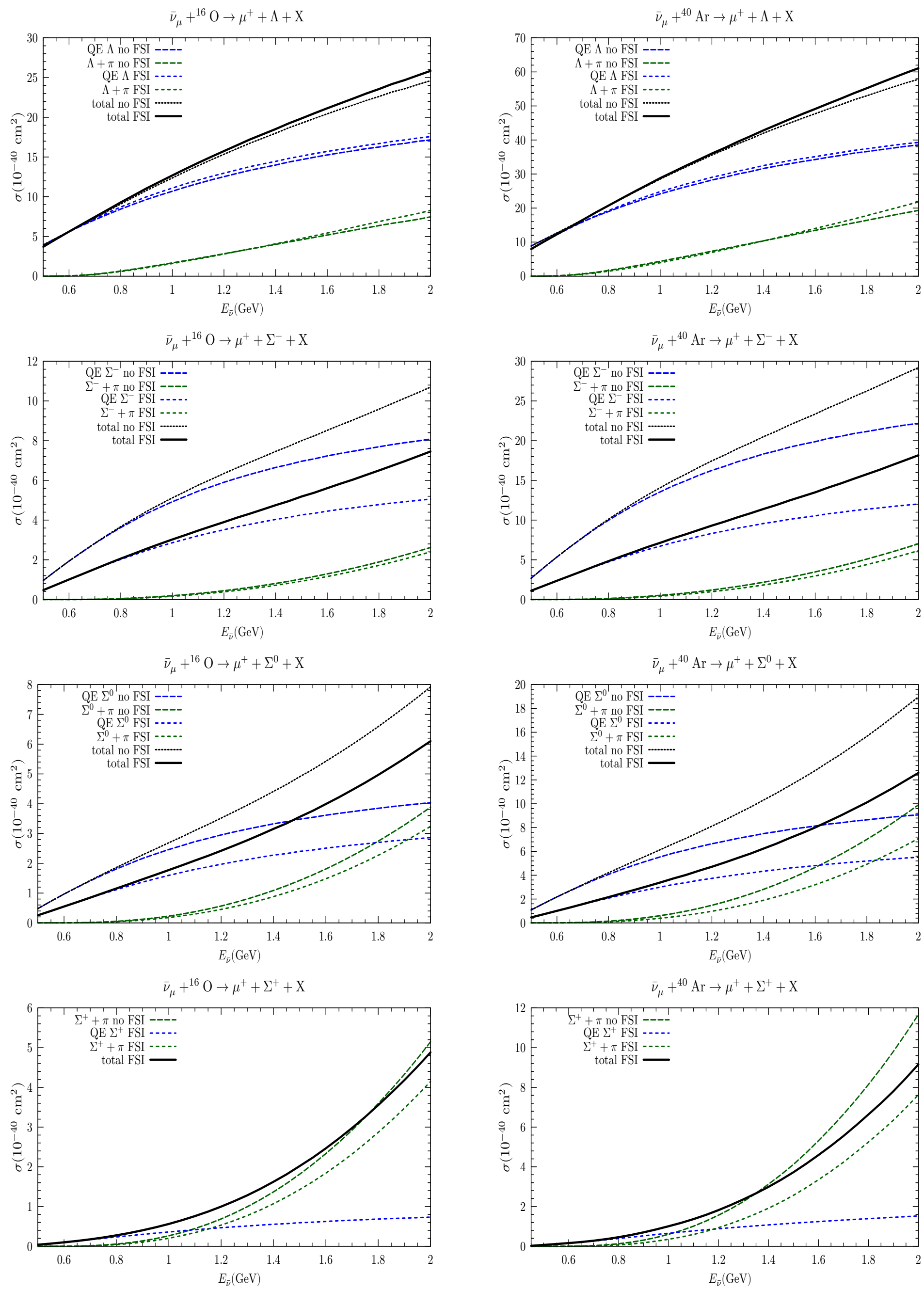

Figure 4.16: Total cross sections for quasielastic hyperon production, hyperon-pion production and the sum of both contributions with and without FSI for ^{16}O (left panels) and ^{40}Ar (right panels). Note that in the case of QE the Σ^+ particle appears only as a result of FSI effects.

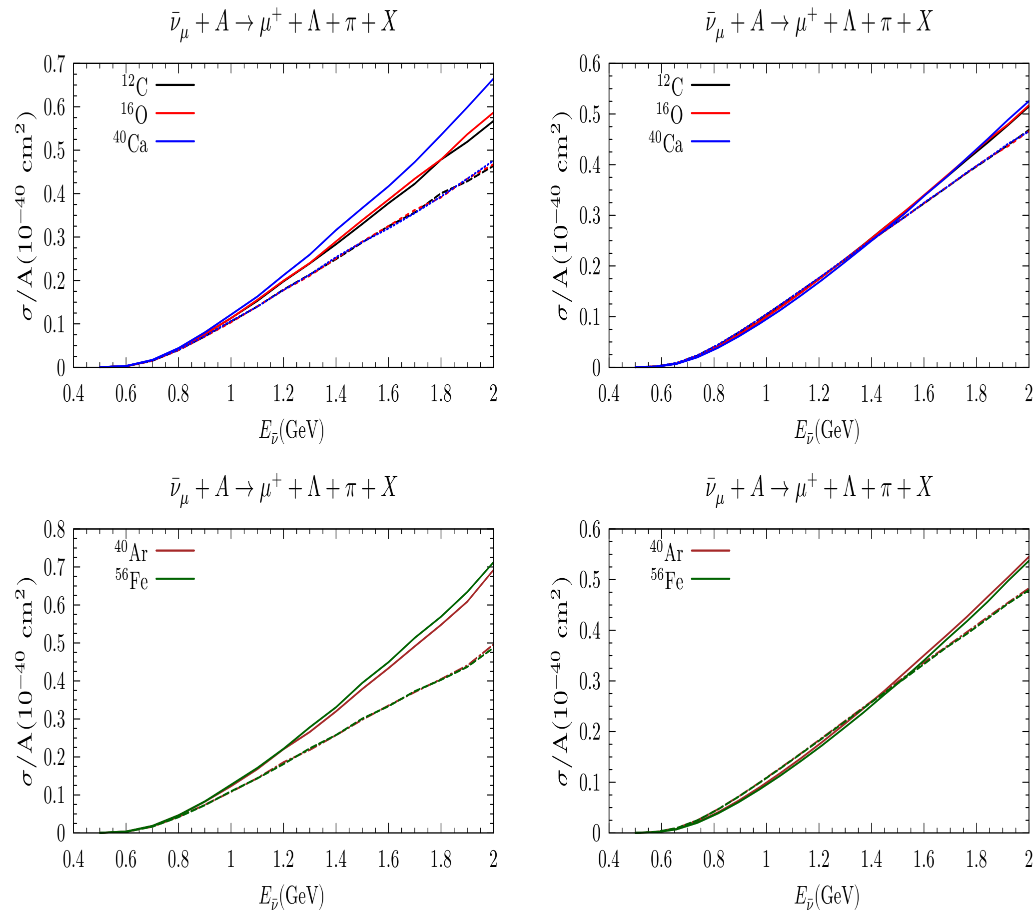

Figure 4.17: Integrated cross sections divided by the number of nucleons for the $\Lambda\pi$ production with and without FSI as a function of the antineutrino energy comparing the results for symmetric nuclei (^{12}C, ^{16}O and ^{40}Ca) (top panels) and asymmetric ones (^{40}Ar and ^{56}Fe) (bottom panels). The dashed lines correspond to the values without FSI effects. In the left panels, we show the results for or the simplest FSI model; while in the right ones, we present the results with the enhanced FSI.

In Figs. 4.17-4.18, we compare the integrated cross sections for $\Lambda\pi$ and $\Sigma\pi$ productions on symmetric nuclei such as ^{12}C, ^{16}O, and ^{40}Ca, and on asymmetric nuclei ^{40}Ar and ^{56}Fe. To make a comparison more correctly, we divided the integrated cross section by the mass number. This normalization was applied to all reactions involving $\Lambda\pi$ and $\Sigma^{-,0}\pi$ since both neutrons and protons contribute to these productions, as discussed in Chapter 2. However, for $\Sigma^+\pi$ production without FSI, we only divided by the number of protons, as neutrons do not contribute to the production. We also compare between the two different FSI simulations, but only for the case of $\Lambda\pi$ production, where, as shown in Fig. 4.15, is the reaction mostly affected by the inclusion of the hyperon-nucleus potential in the FSI simulation. The integrated cross section for Σ production exhibits minimal changes from one type of FSI to the other. We observe that the cross sections per nucleon without FSI are nearly indistinguishable among nuclei of the same category (symmetric or asymmetric). However, we observe that the integrated cross section without the effect of FSI is not exactly the same for symmetric and asymmetric nuclei, particularly in the $\Lambda\pi$ production. It is important to remember (see Sec. 4.1) that the result of the total cross section for primary $\Lambda\pi$ production off neutrons is twice that off protons. In fact, when dividing the total cross section by the number of nucleons, it is a bit larger for asymmetric nuclei. This is due to the greater number of neutrons in these nuclei compared to the number of protons (see Fig. 4.1 on Sec. 4.1).

In Fig. 4.17, we compare both types of FSI simulations. In the left panels, we display the results applying the simplest intranuclear cascade simulation. In the right panels, we present the cross section with and without the enhanced FSI. In this figure, we can observe the same behavior as we have seen previously in Fig. 4.15. In the left panels, we can see that the Lambda production cross section increases significantly with the FSI effect, and the size of the selected nucleus influences it. A larger nuclear size correlates with an augmented integrated cross section under the effect of the FSI. In contrast, in the right panels, where we have used the enhanced FSI simulation, this effect is not as pronounced. The growth in Λ production due to FSI is smaller, and significant differences due to the nucleus size are not evident. The results including the simplest FSI effects increase with the size of the nucleus of the nucleus because the hyperons travel a longer path before exiting the nucleus, and this implies more scattering processes in its way, with more possibilities for initially produced Σ's to become final Λ's. But this is different for the enhanced FSI. In this case, due to the presence of the Λ potential, and its possibility of getting trapped inside the nucleus, the nuclear size does not seem to increase significantly the cross section. To conclude the discussion of this figure, we compare the FSI on the left side (the simple one) with the FSI on the right side (the improved one). With the enhanced FSI, due to the Lambda absorption effect, the FSI curves in the left panels are considerably reduced, and the reduction is even more pronounced with increasing nuclear size. This makes sense because if the size is larger, the Λ travels a longer path, and there are, a priori, more chances for it to lose a significant amount of energy and get trapped.

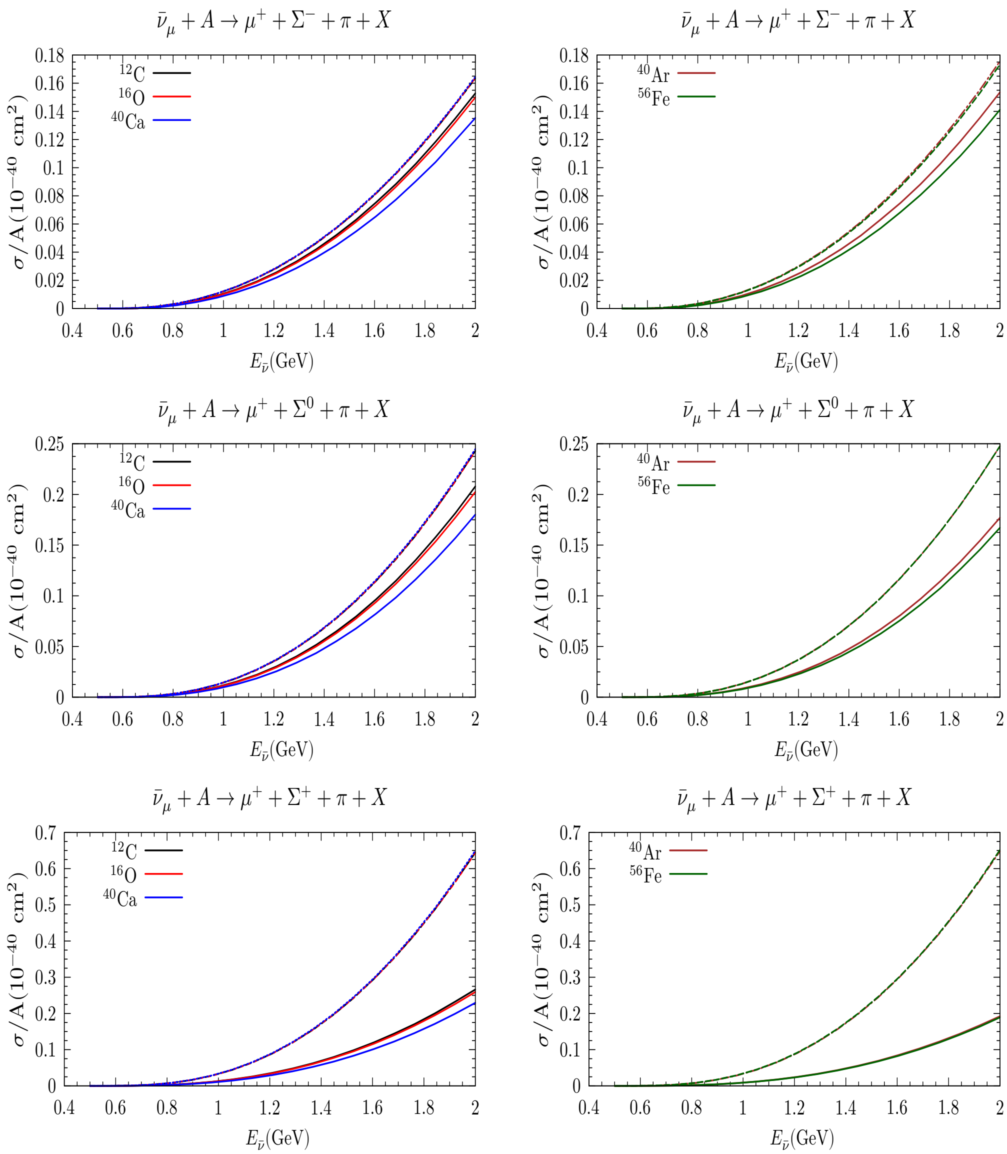

Figure 4.18: Integrated cross sections divided by the number of nucleons for the $\Sigma\pi$ production with and without the effect of the enhanced FSI as a function of the antineutrino energy comparing the results for symmetric nuclei (^{12}C, ^{16}O and ^{40}Ca) (left panels) and asymmetric ones (^{40}Ar and ^{56}Fe) (right panels). The dashed lines correspond to the values without FSI effects.

In Fig. 4.18, we present the results solely for the integrated cross section divided by the mass number for the $\Sigma\pi$ production, with and without the enhanced

FSI. In these cases, we omit the comparison with the simplest FSI because in Fig. 4.15 we already observed that the results for Σ production are similar with both FSI approximations. The reader can discern that, in $\Sigma\pi$ production, the effect of the FSI grows with the size of the nucleus. This is because the longer the trajectory inside the nucleus, the more possibilities there are for the Σ hyperon to transform into a Λ, as it is an exothermic reaction. This implies that the Σ can undergo a transformation into a Λ even when possessing the minimum energy, corresponding to the mass of this particle, except for Pauli-blocking effects in the nuclear medium. Conversely, the reverse transformation proves more intricate, as the Lambda, having a lower mass than the Sigma, necessitates an initial energy input to transition into a Σ.

In summary, we observe the same effect as in Fig. 4.16, comparing the left and right panels; the difference between the lines of the results with and without FSI is larger in all cases for heavier nuclei. For the Λ production, the integrated cross section with the effect of the final state interaction increases slightly. But the increment is not as pronounced as with the simpler FSI, because we take into account the potential and the possibility of the particle getting trapped inside the nucleus. However, the results for Σ production decrease with FSI. This is precisely for the same reason explained in the preceding paragraph: the heavier the nucleus is, the smaller cross section has with FSI, because there is a larger possibility for the transformation $\Sigma \to \Lambda$.

4.2.2 Hyperons kinetic energy spectra

In Figs. [4.19-4.20], we present the hyperon kinetic energy distributions for ^{16}O at $E_{\bar{\nu}} = 1, 2$ GeV, with and without FSI effects. We focus on comparing again the two types of hyperon production and their combined results. The choice of an incoming neutrino energy of 1 GeV, specifically with this target, has been made to facilitate the comparison of our results with previous studies of quasielastic hyperon production [85, 87]. Additionally, we extend our study to provide results for higher energy (2 GeV) to explore the region where the $Y\pi$ mechanism may have more relevance, as demonstrated in the preceding subsection. The shaded areas in Figs. [4.19-4.20] correspond to $T_Y \leq 50$ MeV. For hyperon kinetic energies below this value, the results are not meaningful and are included solely for illustrative purposes. As previously discussed, the semiclassical approximation used for FSI becomes questionable at low hyperon energies. Furthermore, the hyperon potential is no longer negligible compared to its kinetic energy, which would lead to changes in the energy spectra, as can be seen in Ref. [88]. Even if less accurate, we show results in this low energy region as they reflect the amount of produced hyperons and the impact of enhanced FSI.

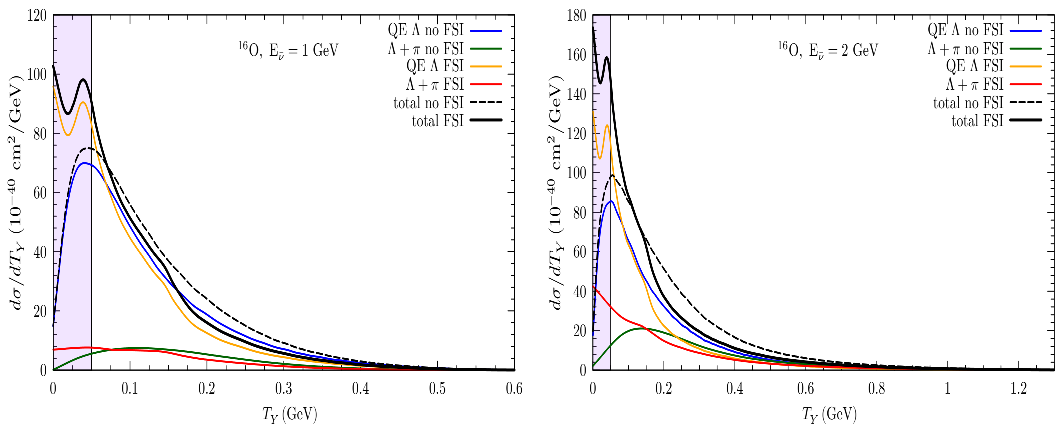

Figure 4.19: Hyperon kinetic energy distributions for the quasielastic hyperon production, hyperon-pion production and the sum of both contributions for Λ, with and without FSI for ^{16}O, at $E_{\bar{\nu}} = 1$ GeV (left panel) and $E_{\bar{\nu}} = 2$ GeV (right panel), respectively. The shaded areas correspond to $T_Y \leq 50$ MeV.

The first observation upon examining Figs. 4.19 and 4.20 is that, as discussed in the preceding subsection, the QE mechanism (blue line corresponds to the spectra without FSI, yellow line with FSI) is predominant. Additionally, we can observe the growing significance of the $Y\pi$ mechanism at higher antineutrino energies (the green line corresponds to the results without FSI and the red line with FSI). This becomes evident in the right panels of both figures. It can also be observed that the results for the hyperon kinetic energy distribution are much higher for Λ production than for the production of any of the Σ's. We find that our results for the QE mechanism without considering the FSI effects are fully consistent with those in Fig. 3 of Ref. [87]. In the case of distributions with FSI, we can see that our results are very similar to those obtained for Σ production. However, when examining the outcomes related to Λ production, we identify certain discrepancies. Our FSI simulation incorporates the real part of hyperon potentials within the cascade process. And, in addition, we take into account the effect of the potential on the hyperon trajectories solving the Hamilton equations of classical motion. This novelty is not included in the FSI simulations of Ref. [87]. On the other hand, there are some discrepancies with the FSI curves of Ref. [85]. This is because of a wrong implementation of the Pauli blocking which led to an underestimation of FSI effects in that study.

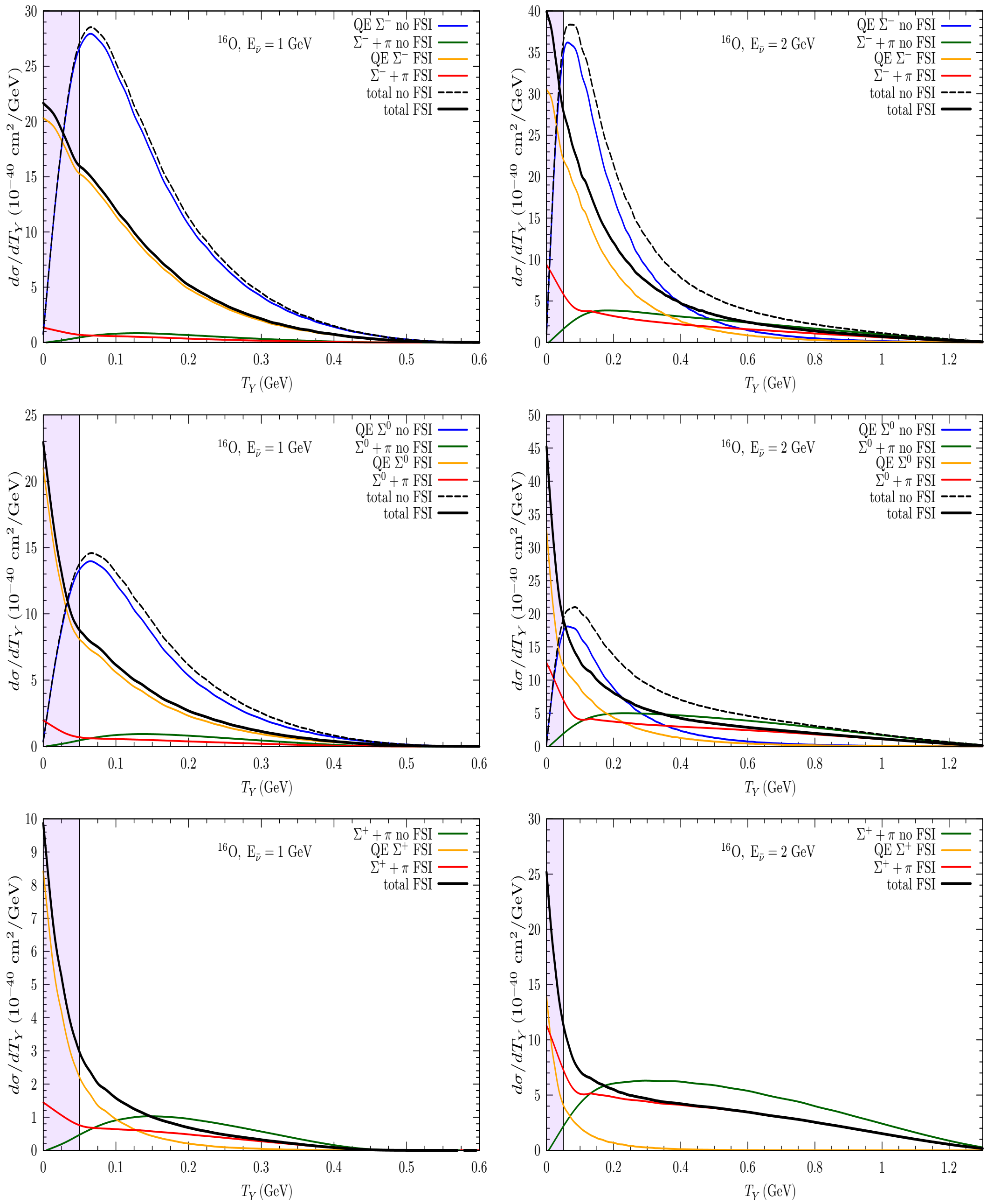

Figure 4.20: Hyperon kinetic energy distributions for the quasielastic hyperon production, hyperon-pion production and the sum of both contributions for Σ^- (top), Σ^0 (middle) and Σ^+ (bottom), with and without FSI for ^{16}O, at $E_{\bar{\nu}} = 1$ GeV (left panels) and $E_{\bar{\nu}} = 2$ GeV (right panels), respectively. The shaded areas correspond to $T_Y \leq 50$ MeV.

As it was also seen in Figs. 4.16, at 1 GeV the contributions for QE mechanism are much larger than $Y\pi$ production, with the exception of the Σ^+ channel, where primary QE production is absent. In this particular case, for hyperon kinetic energies just above 100 MeV, inelastic mechanisms compete with QE Σ^+ production. However, in the other three channels, changes caused by the $Y\pi$ mechanisms are minor. Nevertheless, as we showed earlier, at 2 GeV the relative significance of the $Y\pi$ mechanism is greater. This mechanism becomes predominant for Σ^+ production except at low hyperon kinetic energy. It is also important for the Σ^0 production, constituting the main contribution above 300 MeV. Additionally, for Λ and Σ^- production, this mechanism represents a substantial portion of the total contribution of these hyperon productions.

The consequences of the effects of FSI are clearly illustrated in the Figs. 4.19 and 4.20. Because, besides the clear transformation from one type of hyperon to another, there is a clear shape distortion caused by a significant events displacement towards low kinetic energies because "in each interaction" hyperons transfer a fraction of their energy to the scattered nucleon. In fact, the kinetic energy distributions in the presence of FSI are peaked at low energies. This feature is most important for both Λ and Σ^+, a large fraction of which are emitted when FSI is accounted for. We compare, in Fig. 4.21, the Λ kinetic energy distribution with the different FSI simulations explained in Sect. 3.4. The potential reduces the distribution, especially at lower kinetic energies. Furthermore, the Λ hyperon with kinetic energy below the potential value is going to be trapped by the nucleus. We recommend the reader to observe carefully that the y axis values in both panels are different.

In Fig. 4.22, we show the Λ and Σ hyperon kinetic energy distributions for ^{12}C at $E_{\bar{\nu}} = 2$ GeV. For this nucleus, the FSI effects are practically the same as those observed in the figures displaying the results for ^{16}O at the same antineutrino energy. The increase in Λ production is attributed to the ease with which Σ converts into Λ. The effect of the potential and the possibility of Lambda getting trapped in the nucleus create a compensatory effect. The disappearance of "Σ's into Λ's" through quasielastic processes ($\Sigma^- + p \to \Lambda + n$, $\Sigma^0 + n \to \Lambda + n$, $\Sigma^+ + n \to \Lambda + p$, among others) is quite significant. Therefore, while $\Sigma \to \Lambda$ processes predominate for low-energy hyperons, the reverse process is energetically forbidden for low energies. As already mentioned, Σ^+ hyperons can only be produced through secondary collisions in the case of QE processes. We have a non-zero kinetic energy distribution for Σ^+ production without FSI coming from the primary $\Sigma^+\pi$ channel.

As previously mentioned, the hyperon potentials utilized in the enhanced FSI simulation are $V(r) = -30\rho/\rho_0$ MeV for Λ and $V(r) = 0$ MeV for Σ's. To further

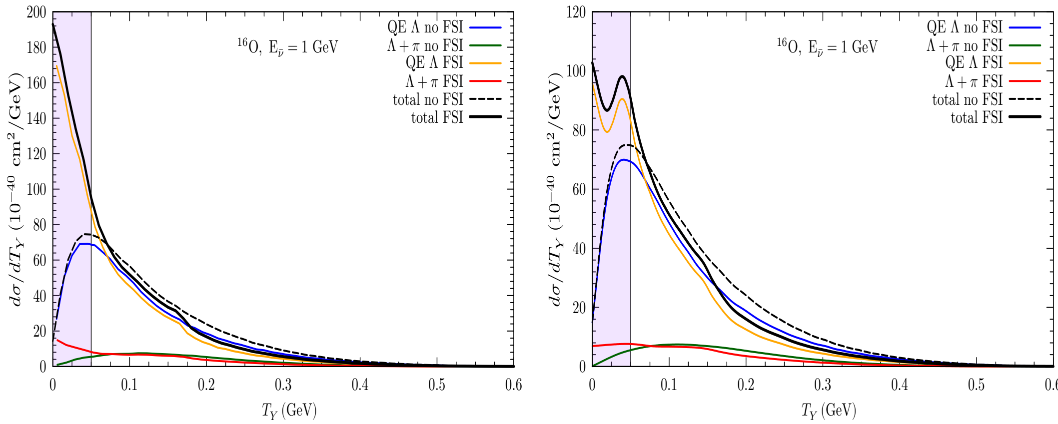

Figure 4.21: Hyperon kinetic energy distributions for the quasielastic production, $Y\pi$ production and the sum of both contributions for Λ, with and without FSI for ^{16}O at $E_{\bar{\nu}} = 1$ GeV. In the left panel, we apply the simplest FSI simulation without considering the hyperon potential. Meanwhile, in the right panel, we display the results with FSI, which includes the Λ potential and the possibility of absorption by the nucleus.

validate the credibility of our FSI model, we aim to make a modest comparison between our results for ^{12}C with those obtained in the Ref. [88]. The authors of this work studied the FSI and the response to changes in the potentials. However, a comprehensive comparison is not feasible since they exclusively present hyperon kinetic energy distributions for quasielastic Λ and Σ^0 production. Additionally, they convoluted these kinetic energy distributions with the flux used in NOvA experiment, which employs carbon as the nuclear target. Nevertheless, an observation reveals similarities in the shape between our QE distributions for these hyperons and those depicted in Figs. 15(b) and 16(b) of Ref. [88] (in those figures the authors used similar hyperon potentials). The results for Σ^- production maintain a ratio of approximately $1/2$ with Σ^0 ones in the QE scenario without FSI. In contrast, our results do not manifest this ratio when the effects of hyperon final state interactions are considered.

4.2.3 Transferred hyperons

In section 3.4, we have described the steps followed in both intranuclear cascade Monte Carlo simulations that we have used to describe the final state interaction. In our calculations, we take into account the elastic and inelastic interactions of the hyperons with the nucleons in the nuclear medium. Following the steps of

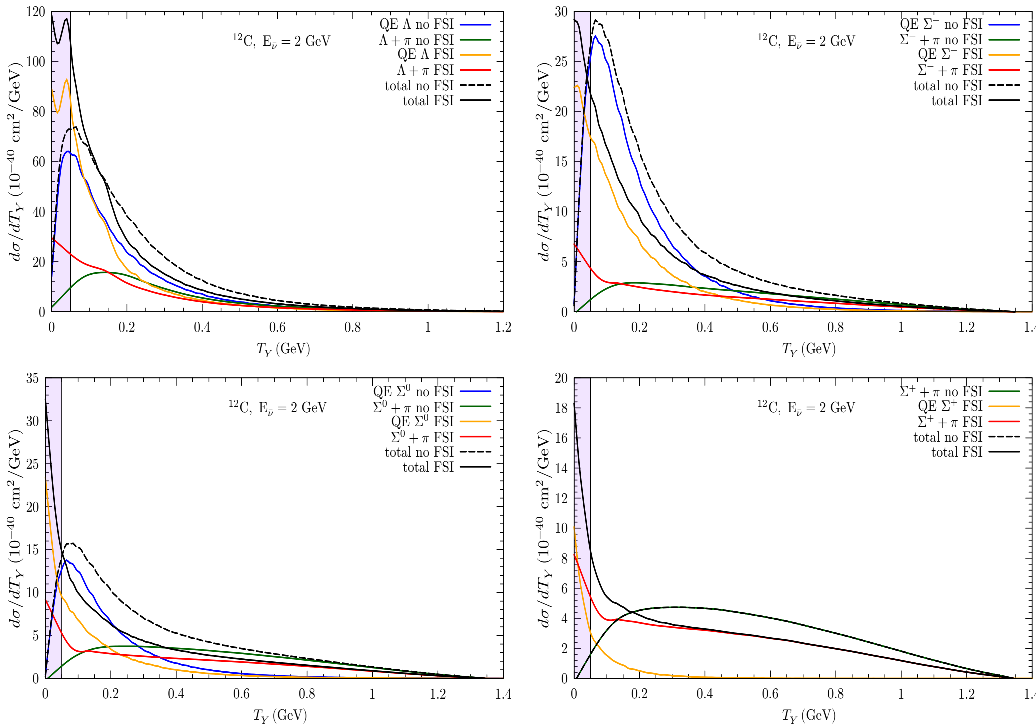

Figure 4.22: Hyperon kinetic energy distributions for the quasielastic hyperon production, hyperon-pion production and the sum of both contributions for the reaction $\bar{\nu}_\mu +^{12}\mathrm{C} \rightarrow \mu^+ + \mathrm{Y} + \mathrm{X}$ with and without enhanced FSI at $E_{\bar{\nu}} = 2$ GeV. The shaded areas correspond to $T_Y \leq 50$ MeV.

the hyperon on its way out of the nucleus. In this subsection, we solely consider the enhanced FSI because the main difference found is in Λ production. This simulation is more realistic as it takes into account the hyperon nuclear potential and the possibility of getting trapped inside the nucleus.

For the understanding of the behaviour of the hyperons leaving the nucleus, we want to show the following figures (Figs. 4.23 and 4.24). We display how the transfer between hyperons occurs due to elastic and inelastic collisions with the nucleons in their path toward exiting the nucleus ($YN \rightarrow Y'N'$). For this purpose, we only present results for the $Y\pi$ mechanism since it is the main focus of this thesis. Additionally, the FSI simulation remains consistent for both hyperon production mechanisms, and as we are not considering the fate of the pions at the moment, these figures serve as representative forms for both mechanisms. In summary, in this subsection, we display the transfer from a fixed initial hyperon to the other four possible hyperons, including itself. We also observe the reverse

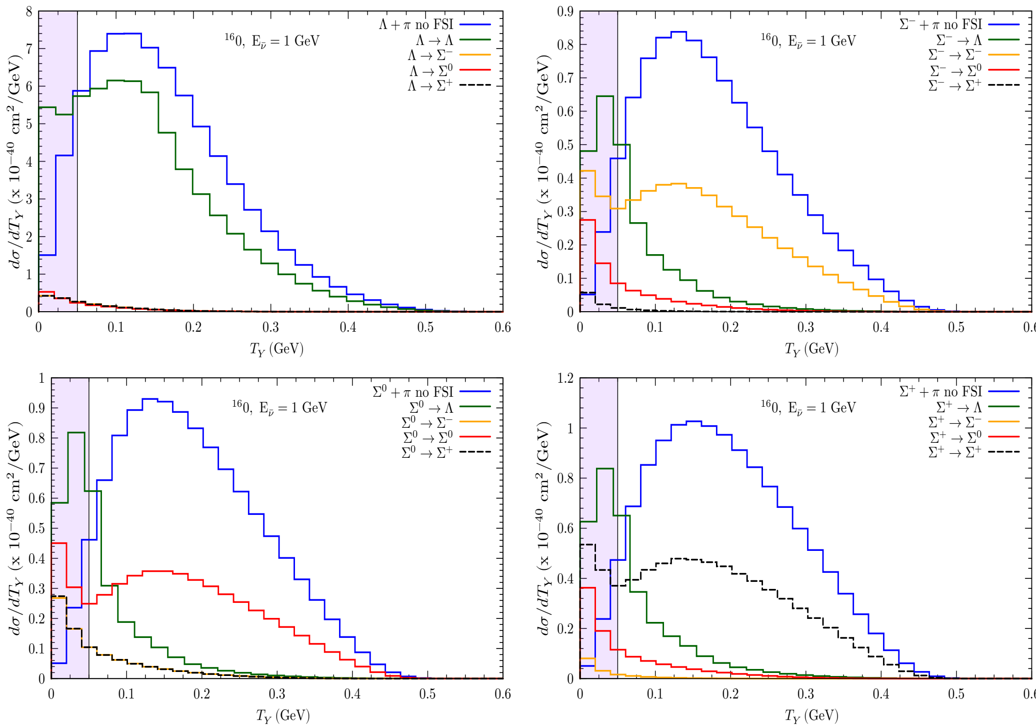

Figure 4.23: Transfer between hyperons due to the effect of enhanced FSI in the hyperon-pion mechanism for the reaction $\bar{\nu}_\mu +^{16} \mathrm{O} \rightarrow \mu^+ + \mathrm{Y} + \pi$ at $E_{\bar{\nu}} = 1$ GeV, comparison with the hyperon kinetic energy distributions without FSI for the same mechanism (blue line).

process, examining how each of the possible initial hyperons contributes to each fixed final hyperon.

In Fig. 4.23, we showcase the hyperon transfer due to the intranuclear cascade effect. The figure shows the kinetic energy distribution for the four possible hyperons. The blue histogram represents the "initial" hyperon and a pion production without FSI. At the same time, the green illustrates the transfer from the initial hyperon to Λ, the yellow to Σ^-, the red to Σ^0, and the dashed black line to Σ^+. We observe that each hyperon mostly contributes to itself through the elastic scattering. Besides primarily contributing to themselves, all the Σ hyperons significantly contribute to the Λ, especially at low kinetic energies.

In Fig. 4.24, the kinetic energy distribution for the $Y\pi$ production with the enhanced FSI effect is depicted by the blue line for each final hyperon. We can compare these values with the transferred hyperons. In this figure, it is important to note that although it may seem in Fig. 4.23 that the initial Λ hardly contributes

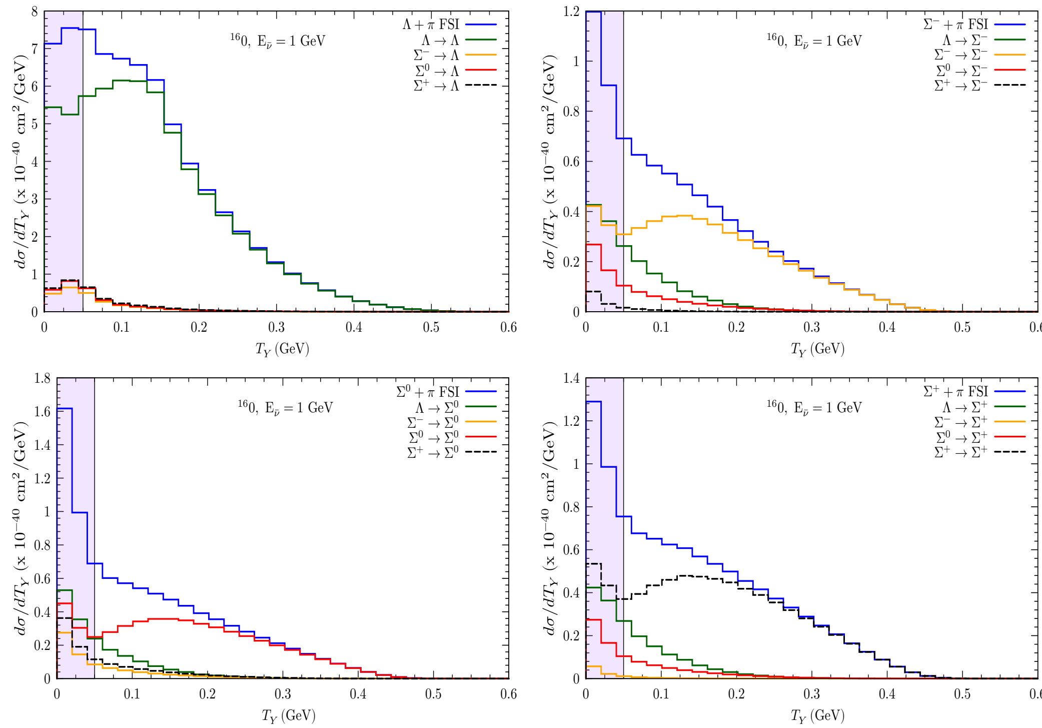

Figure 4.24: Transferred hyperons due to the effect of enhanced FSI in the hyperon-pion mechanism for the reaction $\bar{\nu}_\mu +^{16} \mathrm{O} \to \mu^+ + \mathrm{Y} + \pi$ at $E_{\bar{\nu}} = 1$ GeV.

to final Σ, it indeed does, especially at low energies. Here the reader needs to understand that this is due to an effect of the different scales in the production of Λ and Σ. In other words, the production of Λ is much more probable (has a higher cross section) than that of Σ, and what appears as a small effect on the scale of Λ is magnified on the scale of Σ.

4.2.4 Angular distributions

Now we examine the angular distributions considering the final particles, the hyperon and the lepton, in this particular case, the muon. In the following figures (4.25,4.26 and 4.27), we depict the angular distribution against the cosine of the angle formed between the outgoing hyperon and the muon. The selected nucleus to showcase the behavior of angular distributions is ^{40}Ar. As mentioned earlier, many current and future experiments utilize it as a target material. We set the antineutrino energy to 2 GeV to better observe the differences between the lines corresponding to the QE and $Y\pi$ cases. Note that in many cases, the primary pion produced in the $Y\pi$ mechanisms is absorbed by the nucleus and is not detected. We have found that $d\sigma/d\cos\theta_{Yl}$, where θ_{Yl} is the angle between the final lepton and the emitted hyperon, is particularly sensitive to the production mechanisms, showing different behavior for the QE and $Y\pi$ processes. This could eventually help to distinguish them from the data and study their relative importance.

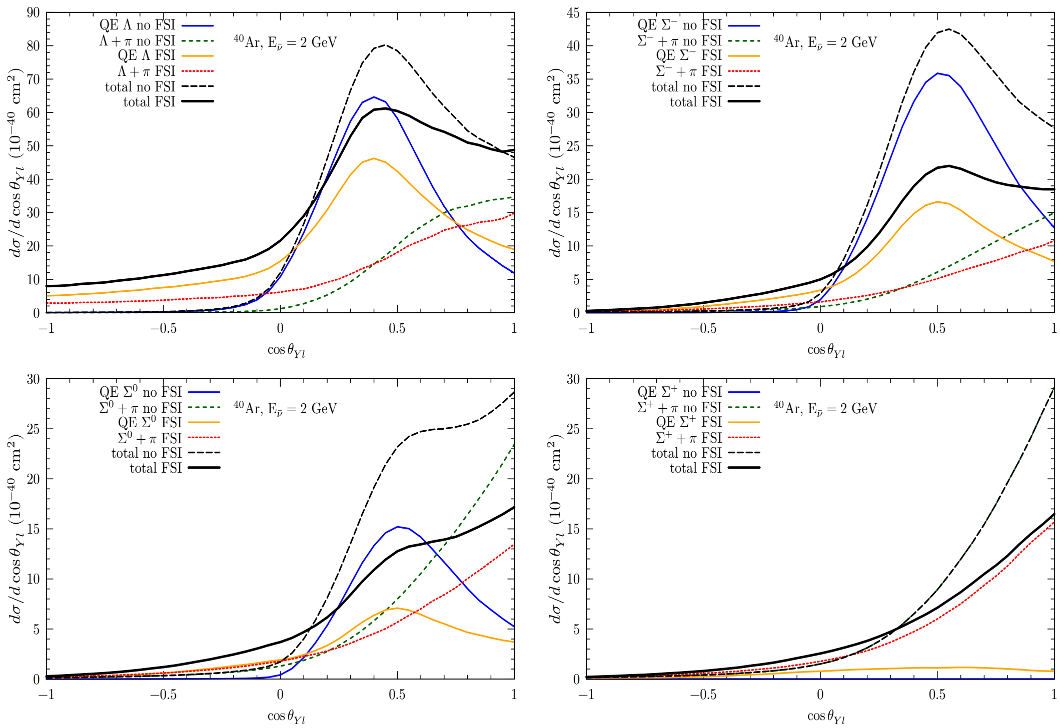

Figure 4.25: Angular distributions for the quasielastic hyperon production, hyperon-pion production and the sum of both contributions with and without FSI, including the Lambda potential, for the reaction $\bar{\nu}_\mu +^{40}\mathrm{Ar} \rightarrow \mu^+ + \mathrm{Y} + \mathrm{X}$ at $E_{\bar{\nu}} = 2$ GeV.

We present the results in the Fig. 4.25. The curves show the values for both the quasielastic mechanism and the $Y\pi$ production, with and without the effect of enhanced FSI, as well as the sum of both contributions. The dashed black line represents the total sum without FSI, while the solid black line represents the total sum with FSI. For all channels, the $Y\pi$ contributions are forward peaked and display a monotonous growth as a function of the cosine. In the case of $\Lambda\pi$ production, both with and without FSI, the curves exhibit a slower monotonic growth compared to those of $\Sigma\pi$ production. This is due to the potential for these particles to get trapped by the nucleus when their kinetic energy is lower than the potential. On the other hand, for the QE processes, there is a peak around cos $\theta_{Yl} \approx 0.4$, which is also reflected in the sum of both contributions. This peak is primarily driven by phase space and is also visible in the vector and axial parts of the hadronic current. The peak position hardly changes with the neutrino energy and is largely unaffected by FSI. The presence of such a structure for the QE mechanism and its properties are in line with the findings of Ref. [88], as can be seen in Figs. 23 and 24 of that reference. Clearly, this peak seems to be absent in the results for Σ^+ production, but it is an artefact of the scale of the graph because the quasielastic contribution is too small. If only the curve for the quasielastic case with FSI were displayed, the peak around the same cosine value as for the other hyperons would be visible. The total result without FSI, to the Σ^+ production, corresponds only to the inelastic channel. We compare the quasielastic mechanism with and without the effect of FSI for Λ, Σ^-, and Σ^0. In all cases, we observe that the FSI curve flattens, especially for the Λ hyperon, showing relatively significant values outside the peak around cos $\theta_{Yl} \approx 0.4$. Although this effect can also be observed for the production of Σ^0 and Σ^-.

In Fig. 4.26, we present the results for the angular distribution for both mechanisms of hyperon production and the sum of both contributions. We show the same figures as in Fig. 4.25 to ^{16}O in this case. The purpose of presenting this second figure is to compare between two different nuclei, one symmetric and light (^{16}O), and the other asymmetric and heavier (^{40}Ar). We aim to assess whether the nature of the utilized nucleus affects the shape of the angular distribution. However, as mentioned earlier, the behavior of the angular distribution is primarily attributed to the phase space of each mechanism. So, comparing Figs. 4.25 and 4.26, we can see that, as expected, the shape of the angular distributions for the four possible hyperons and the two production mechanisms remains similar for the two different nuclei. Exerting its influence solely on the angular distribution values owing to the different nuclear sizes and number of protons and neutrons of the two nuclei.

In Fig. 4.27, we present the angular distributions for the cosine of the angle between the final hyperon and muon regarding Λ production with ^{40}Ar as the nuclear target at $E_{\bar{\nu}} = 2$ GeV. This figure presents a comparison between the two different final state interaction simulations. Therefore, we only display the results considering the effects of the FSI for both contributions and their sum. In the upper panel, we applied the simplest FSI code where the hyperon moves in a straight line and is not under the influence of its potential. In this scenario, the Λ would always exit the nucleus. Meanwhile, the lower panel exhibits the results for

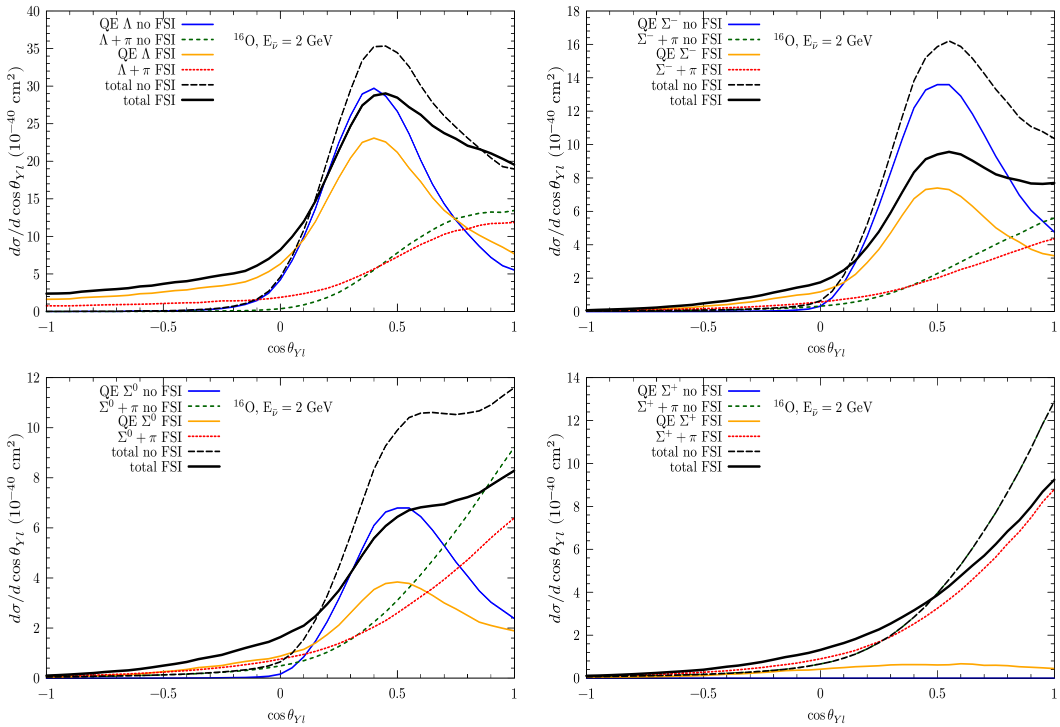

Figure 4.26: Angular distributions for the quasielastic hyperon production, hyperon-pion production and the sum of both contributions with and without FSI, including the Lambda potential, for the reaction $\bar{\nu}_\mu +^{16} \mathrm{O} \rightarrow \mu^+ + \mathrm{Y} + \mathrm{X}$ at $E_{\bar{\nu}} = 2$ GeV.

the Λ production applying the enhanced FSI simulation, which takes into account the Λ potential and the possibility of being confined within the nucleus. Upon comparison, a noticeable reduction in the Λ angular distribution is evident due to the potential in both mechanisms. Interestingly, the distribution shape remains unaltered by FSI; it does not affect its form. We are not comparing the angular distributions of the Σ hyperons as they do not exhibit significant differences. This discrepancy arises because the hyperon potential under consideration affects only the production and travel of Λ in the intranuclear cascade, and not so much that of Σ hyperons.

4.2.5 Double differential cross sections

We have observed that the inelastic mechanism of $Y\pi$ production is relatively important, at least when compared to the QE mechanism. We have also noted

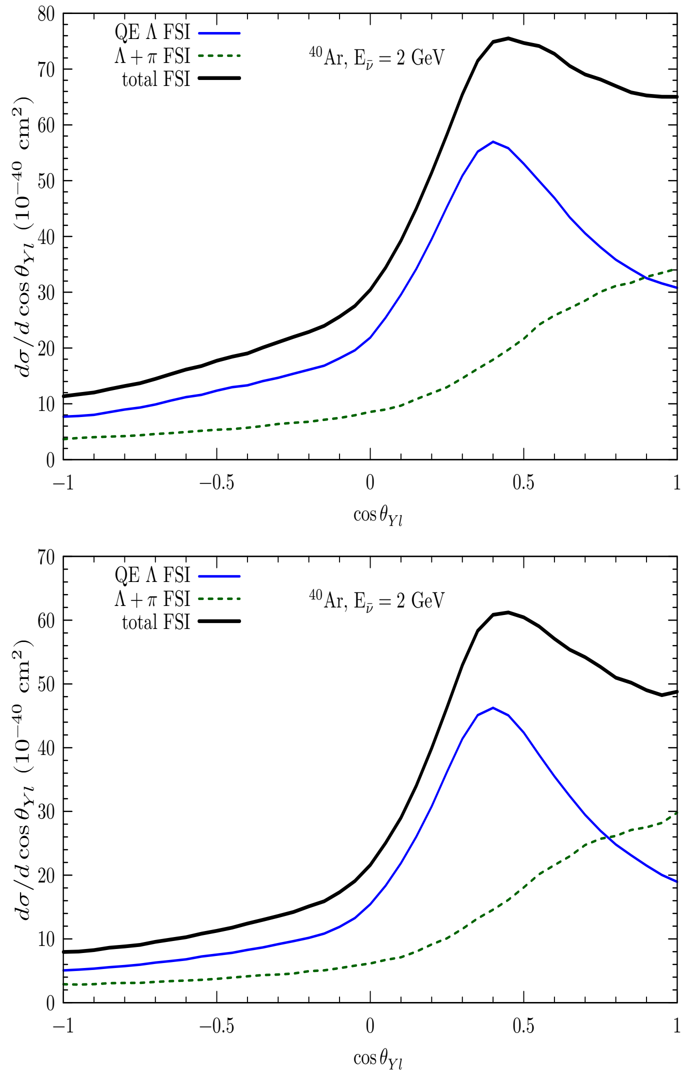

Figure 4.27: Comparison of the angular distributions for quasielastic hyperon production, hyperon-pion production, and the sum of both contributions with both FSI simulations for the reaction $\bar{\nu}_\mu +^{40}\text{Ar} \to \mu^+ + \Lambda + \text{X}$ at $E_{\bar{\nu}} = 2$ GeV. In the top panel, we present the distributions with FSI that do not include the Lambda potential; while in the bottom panel, we show the same distribution taking into account the potential.

that the angular distributions of the two mechanisms are clearly different: the QE production centers around a peak near $\cos\theta_{Yl} \approx 0.4$, while the hyperon-pion mechanism displays a monotonic growth and is forward peaked. Now, we present the double differential cross sections in both the hyperon kinetic energy and the relative angle between the muon and the outgoing hyperon to further visually compare the differences between both hyperon production mechanisms. The figures (4.28, 4.29, 4.30 and 4.31) display results with and without FSI, where the FSI considers the Λ potential and the possibility of this particle being trapped inside the nucleus during the final state interaction process. In this case, we do not compare the enhanced FSI results with the simplest simulation since, as observed, it primarily affects the slight reduction of the cross section with FSI at low values of Λ kinetic energy. In the previous section, we confirmed that the angular distribution of Λ with FSI remains unchanged in shape when transitioning between simulation types. Our aim in this subsection, along with the presented figures, is to compare, at a fixed antineutrino energy $E_{\bar{\nu}} = 2$ GeV for ^{40}Ar, both mechanisms. This is shown here for the case there would be a future experimental interest in distinguishing the mechanisms of production of the detected hyperons. In all the subsequent figures, on the left-hand side, the double differential cross sections are presented both without and with the FSI effect for the QE mechanism. Meanwhile, the right-hand panels show the results for the hyperon-pion inelastic production with and without FSI. It is important to remember that primary production of Σ^+ (without the FSI effect) cannot occur from the quasielastic mechanism. Therefore, its place in the following figures remains empty.

With a quick glance at Figs. 4.28, 4.29, 4.30 and 4.31 on the following pages, the reader notices a clear distinction between the color distributions in the left panels compared to those on the right. Looking first at the y-axis of the figures, as expected, we can see that the hyperon-pion production values are forward peaked for all hyperons. In contrast, the quasielastic results are centered around $\cos\theta_{Yl} \approx 0.4$. Looking now at the x-axis, it is important to note that we have set the range from 0 to 1.2 GeV in the hyperon kinetic energy. This allows us not only to compare well between the two production mechanisms but also to compare the production of different hyperons to gain a more comprehensive understanding of the behavior of both contributions before examining how hyperon production behaves when convoluted with the fluxes of current and future experiments. We recommend the reader to note that the colors in the figures of the double differential cross section do not correspond to the same values. We want to focus primarily on which points in these double distributions accumulate the highest number of hyperon production events and ascertain whether both contributions are easily distinguishable.

In Fig. 4.28, we present the double differential cross sections in the kinetic energy of the Λ and the relative angle between this hyperon and the outgoing muon.

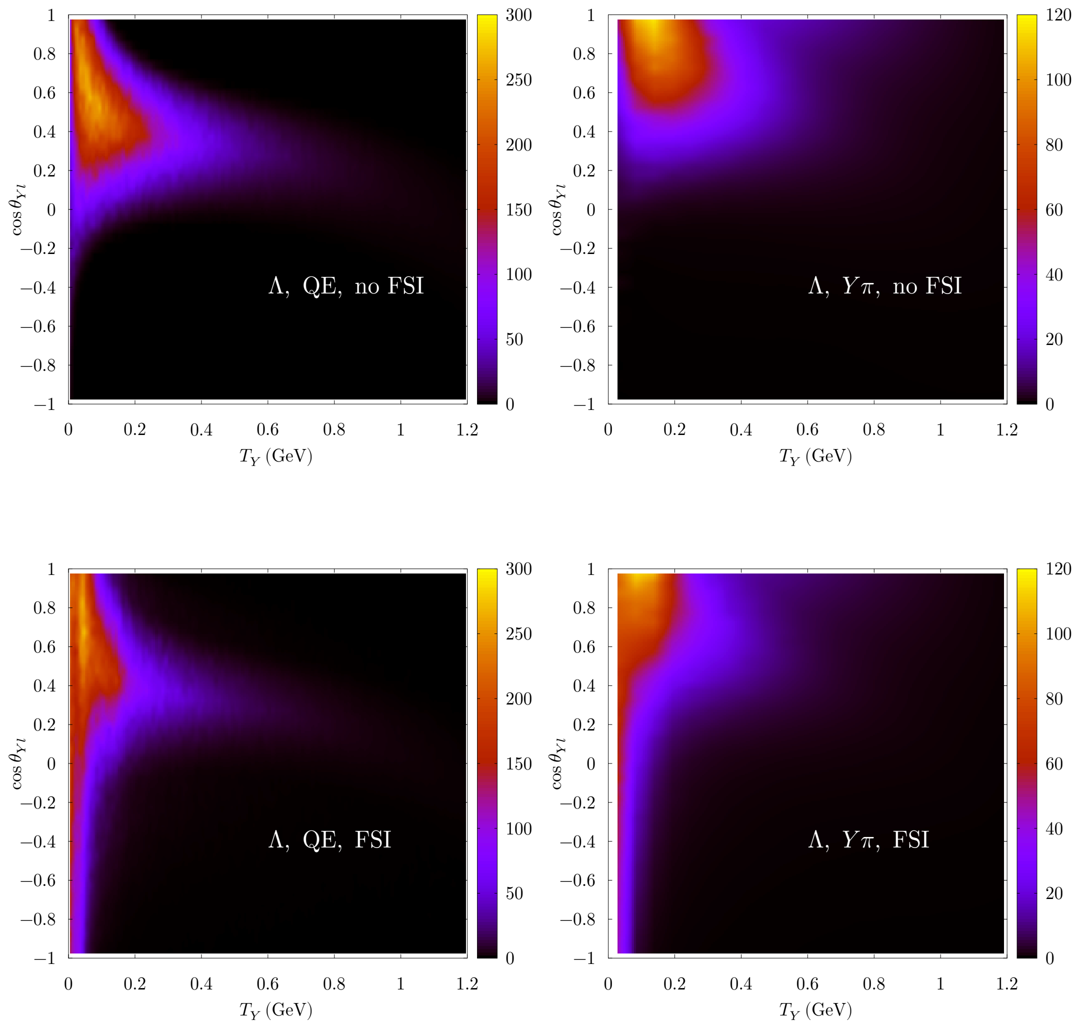

Figure 4.28: Double differential cross sections in hyperon kinetic energy and cosine of the relative angle between the hyperon and final muon. We compare the quasielastic production (left panels) and hyperon-pion mechanisms (right panels), both with (bottom panels) and without (top panels) the effects of the enhanced FSI for the reaction $\bar{\nu}_\mu +^{40} \mathrm{Ar} \rightarrow \mu^+ + \Lambda + \mathrm{X}$ at $E_{\bar{\nu}} = 2$ GeV. The units of the color scale are given in units of $10^{-40}\mathrm{cm}^2/\mathrm{GeV}$.

The shape of the distributions differs significantly between both contributions, as we mentioned, due to their distinct angular distribution. Within each mechanism, comparing results with and without FSI shows that the shape in the plane is not preserved, neither for the QE nor the $Y\pi$. The trend is that, for both mechanisms when there is FSI, the distribution shifts towards lower values of kinetic energy, and regions of negative cosines start to populate. The primary effect of FSI on Λ production is that most events accumulate at lower kinetic energies; and in both cases, they are more evenly spread across the cosine of the relative angle. It is important to remember that in this case, by imposing the potential of the Λ, many of these particles at low kinetic energies get trapped inside the nucleus. However, if we were to compare it with the simpler FSI simulation, which omits potentials and the possibility of particle trapping, the shapes of the distributions would be very similar. The notable difference lies in the event count within each distribution. We want to recall that although almost all curves of the angular distributions for different hyperons flatten, the one that flattens the most and has a higher cross-section outside the peak is the production of the Λ. That becomes evident when we look at the bottom panels of Fig. 4.28.

Something similar to what happens in the production of Λ can be observed in the production of Σ^- and Σ^0. Looking now at Figs. 4.29 and 4.30, we can see how the shape of the double distributions is driven by the angular distribution. For the quasielastic case, the highest accumulation of events is centered around the mentioned cosine value, whereas for the Sigma-pion production, it is forward peaked. For the production of these hyperons, we also observe that the visual impact of the FSI is as noticeable in the quasielastic case as in the hyperon-pion production. This visual effect is also evident in the case of the lambda. Similarly to the quasielastic production of Λ, when the FSI effect is applied, the values spread out towards cosines beyond the peak around the maximum cosine value, similar to the production of Λ, it flattens and spreads towards negative cosine values. Whereas without FSI, the values are more centralized around that point. We also observe that with the FSI effect, the maxima concentrate at smaller kinetic energies of Σ, as expected for both mechanisms.

The most particular case in our comparison among the most crucial hyperon production mechanisms with strangeness-changing charged currents is the production of Σ^+. We can show it in Fig. 4.31, the empty panel corresponds to the QE contribution without FSI. As we have mentioned on several occasions, this hyperon cannot be directly produced through the QE mechanism. Consequently, its production through this mechanism with FSI also holds no particular significance when compared to $Y\pi$ production. The form of the distributions with and without FSI for hyperon-pion production is very similar, similar to the rest of the double differentials.

In summary, the shapes of the double differential cross sections between the

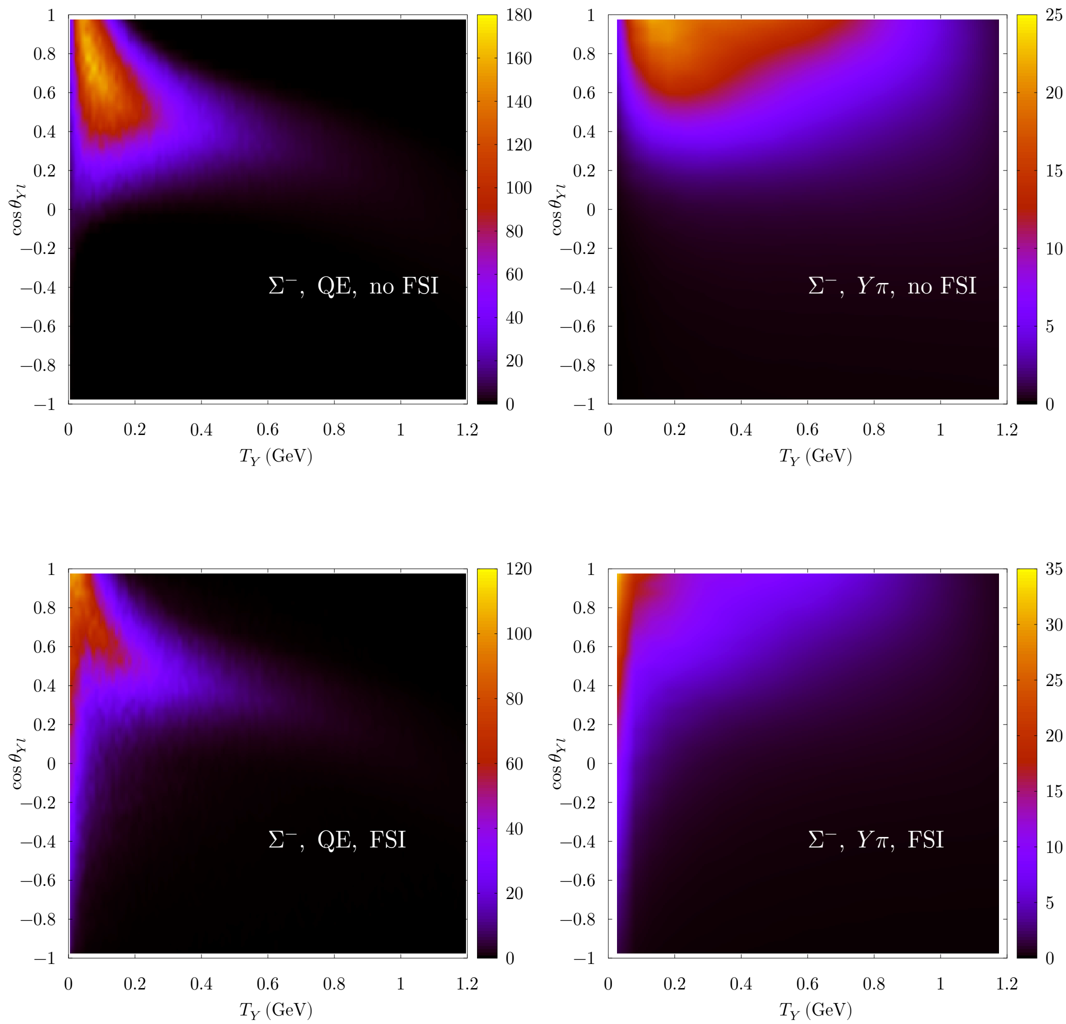

Figure 4.29: Double differential cross sections in hyperon kinetic energy and cosine of the relative angle between the hyperon and final muon. We compare the quasielastic production (left panels) and hyperon-pion mechanisms (right panels), both with (bottom panels) and without (top panels) the effects of the enhanced FSI for the reaction $\bar{\nu}_\mu +^{40}$ Ar $\rightarrow \mu^+ + \Sigma^- + \mathrm{X}$ at $E_{\bar{\nu}} = 2$ GeV. The units of the color scale are given in units of $10^{-40}\mathrm{cm}^2/\mathrm{GeV}$.

two studied mechanisms for hyperon production are clearly different. As we observed in the previous subsection, it was easy to differentiate between both con-

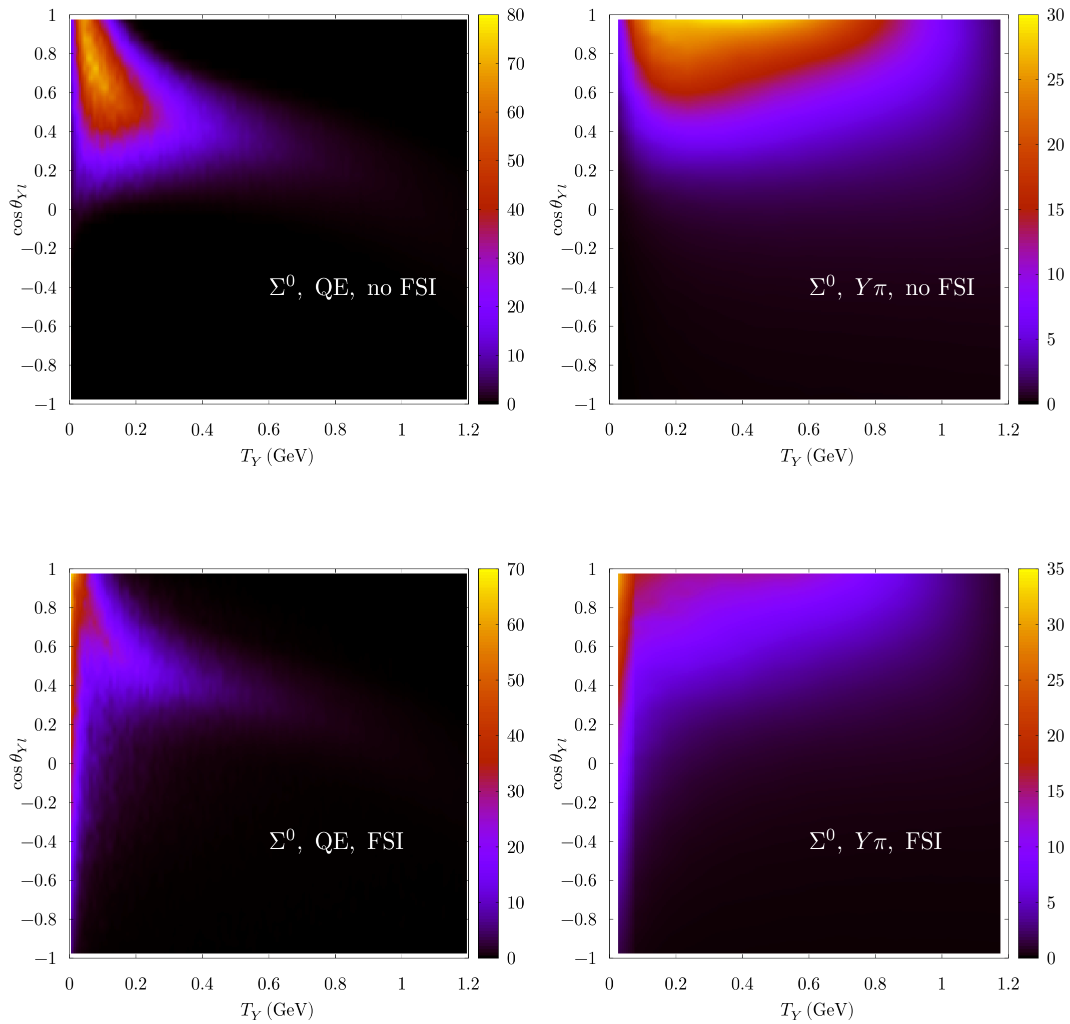

Figure 4.30: Double differential cross sections in hyperon kinetic energy and cosine of the relative angle between the hyperon and final muon. We compare the quasielastic production (left panels) and hyperon-pion mechanisms (right panels), both with (bottom panels) and without (top panels) the effects of the enhanced FSI for the reaction $\bar{\nu}_\mu + ^{40}\mathrm{Ar} \rightarrow \mu^+ + \Sigma^0 + \mathrm{X}$ at $E_{\bar{\nu}} = 2$ GeV. The units of the color scale are given in units of $10^{-40}\mathrm{cm}^2/\mathrm{GeV}$.

tributions with angular distributions. Additionally, we observe that the shapes of the double differential cross sections remain consistent among the production

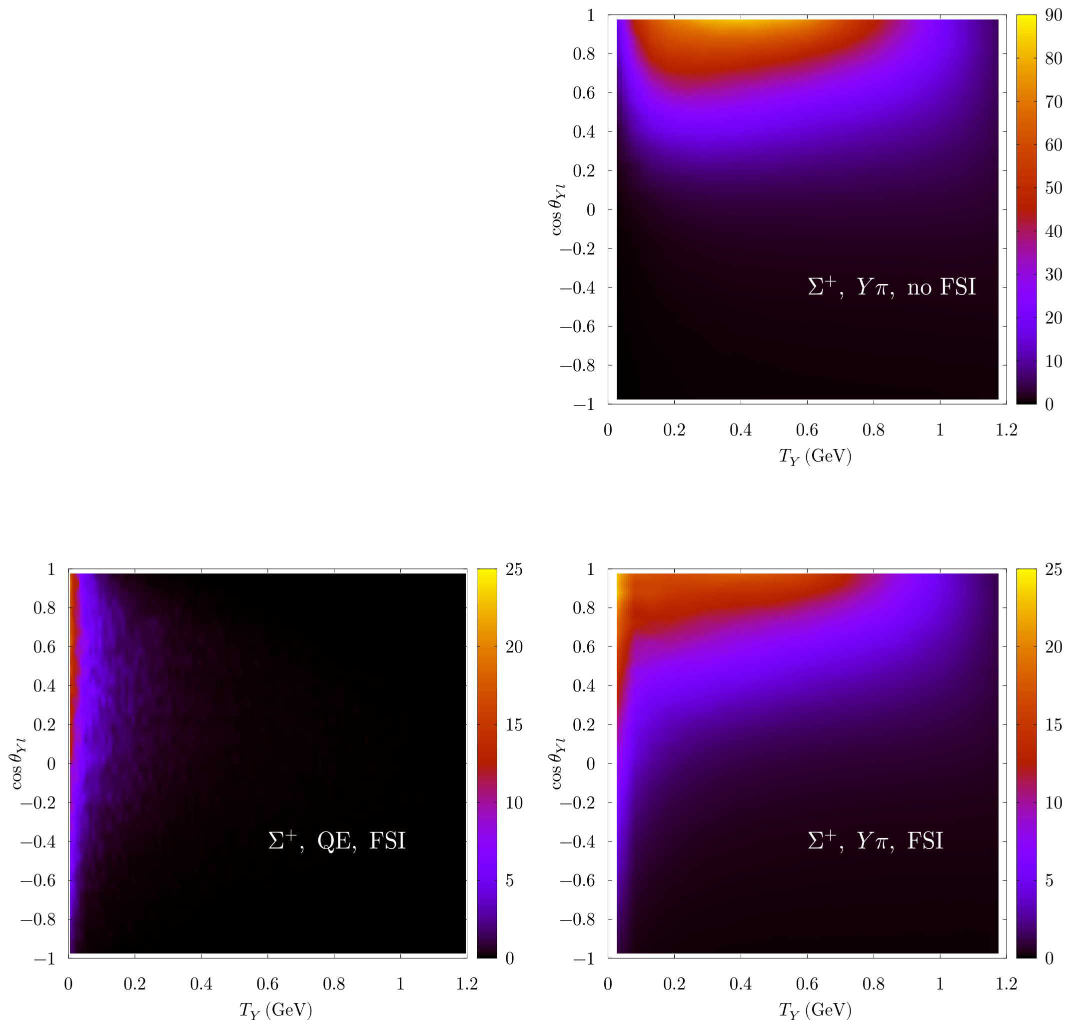

Figure 4.31: Double differential cross sections in hyperon kinetic energy and cosine of the relative angle between the hyperon and final muon. We compare the quasielastic production (left panels) and hyperon-pion mechanisms (right panels), both with (bottom panels) and without (top panels) the effects of the enhanced FSI for the reaction $\bar{\nu}_\mu +^{40}\mathrm{Ar} \rightarrow \mu^+ + \Sigma^+ + \mathrm{X}$ at $E_{\bar{\nu}} = 2$ GeV. The units of the color scale are given in units of $10^{-40}\mathrm{cm}^2/\mathrm{GeV}$. There is not a QE Σ^+ production without FSI.

of different hyperons within the same type of contribution with and without FSI, with the most exceptional case being Σ^+ as it is not directly produced via QE.

4.2.6 Pion absorption

Although the main purpose of this thesis revolves around evaluating hyperon production, it is important and interesting to consider the effects of the final state interaction of pions produced through the $Y\pi$ processes. Detecting these pions would provide us with a deeper understanding of the underlying physics. The primary interaction between hyperon and nucleon can occur throughout the entire volume of the nucleus, allowing produced pions to scatter, alter their energy, direction, and charge, or be absorbed. A comprehensive calculation of these effects would require a cascade simulation for the pions, although this is not the focus of this thesis. However, as explained in Sec. 3.4, we estimate reasonably the effect of pion absorption. To estimate the absorption of the pions by the nucleus, we employed an eikonal approximation. This approach has been previously utilized in the analysis of pion production processes in nuclei induced by pions [154] or neutrinos [155, 156].

First, we estimate the pion absorption rate at two different energies: 1 and 2 GeV. We perform the estimation for the four $Y\pi$ production channels. In tables 4.2 and 4.3, we show the pion absorption rate for ^{16}O, representing the light and symmetric nuclei and ^{40}Ar for the medium and antisymmetric ones. To verify how the change in antineutrino energy affects the pion absorption, and how the nuclear size and the type of hyperon being produced impact the absorption ratio of these mesons.

^{16}O	$E_{\bar{\nu}_\mu} = 1$ GeV	$E_{\bar{\nu}_\mu} = 2$ GeV
$\Lambda\pi$	56%	44%
$\Sigma^-\pi$	55%	35%
$\Sigma^0\pi$	55%	34%
$\Sigma^+\pi$	55%	33%

Table 4.2: Pion absorption rate for $Y\pi$ production for ^{16}O at $E_{\bar{\nu}_\mu} = 1$ and 2 GeV.

If we compare both tables 4.2-4.3, we observe that as the antineutrino energy increases, the absorption decreases for all hyperons. Additionally, although there is high pion absorption for all hyperons, the greatest absorption is observed for Λ production, especially at high antineutrino energies. However, at low antineutrino energies, the absorption is similar between Λ production and the rest of the considered hyperons. Observing the invariant mass spectra $\frac{d\sigma}{dW}$ for all reactions on the nucleon, we can clearly see that for the $\Lambda\pi$ reactions, the spectrum is concentrated at invariant masses very close to Σ^*. However, for the $\Sigma\pi$ reactions, the invariant mass spectrum is not as concentrated there but extends, with higher intensity, towards higher invariant masses. This implies that, on average, the pions emitted from the $\Lambda\pi$ reaction are slower than those from the $\Sigma\pi$ reactions. Slower pions are more prone to absorption than their faster counterparts.

^{40}Ar	$E_{\bar{\nu}_\mu} = 1$ GeV	$E_{\bar{\nu}_\mu} = 2$ GeV
$\Lambda\pi$	67%	53%
$\Sigma^-\pi$	66%	45%
$\Sigma^0\pi$	64%	43%
$\Sigma^+\pi$	63%	41%

Table 4.3: Pion absorption rate for $Y\pi$ production for ^{40}Ar at $E_{\bar{\nu}_\mu} = 1$ and 2 GeV.

As expected, the absorption of pions increases with the size of the nucleus used as a target, as the meson has a longer distance to travel before exiting the nucleus. Just to give some approximate numbers for the pion absorption rate, this ranges from 55 - 70% at 1 GeV of antineutrino energy (from the lightest (^{12}C and ^{16}O) to heaviest nuclei (^{40}Ca, ^{40}Ar and ^{56}Fe), to 30 - 50% at 2 GeV of the antineutrino energy, again from lighter to heavier nuclei. We do not observe significant differences between ^{40}Ca and ^{40}Ar, with the former being a symmetric nucleus and the latter an asymmetric one. The pion absorption rate at both antineutrino energies is very similar for both nuclei.

We compared the pion absorption rates with the integrated cross section for $Y\pi$ production where the pion was not absorbed versus the integrated cross section considering pion absorption. Next, we study if the shape of the distributions in both hyperon kinetic energy and angular distribution is significantly affected when pion absorption is taken into account. We compare these distributions with those that do not consider pion absorption. In Figs. 4.32 and 4.33, we present the distributions in the hyperon kinetic energy and the angular distribution, respectively, for the production of the four possible hyperons in ^{16}O. We also compare the two antineutrino energies ($E_{\bar{\nu}_\mu} = 1$ and 2 GeV), displaying the curves considering and not considering the possibility of pion absorption.

The figures presented (Figs. 4.32 and 4.33) do not illustrate how pion absorption impacts the reduction in cross sections concerning the two consistent antineutrino energies. This is because the values of the distributions vary significantly with the antineutrino energy. However, notable differences are observed between the lines at the same antineutrino energy, particularly around the peak

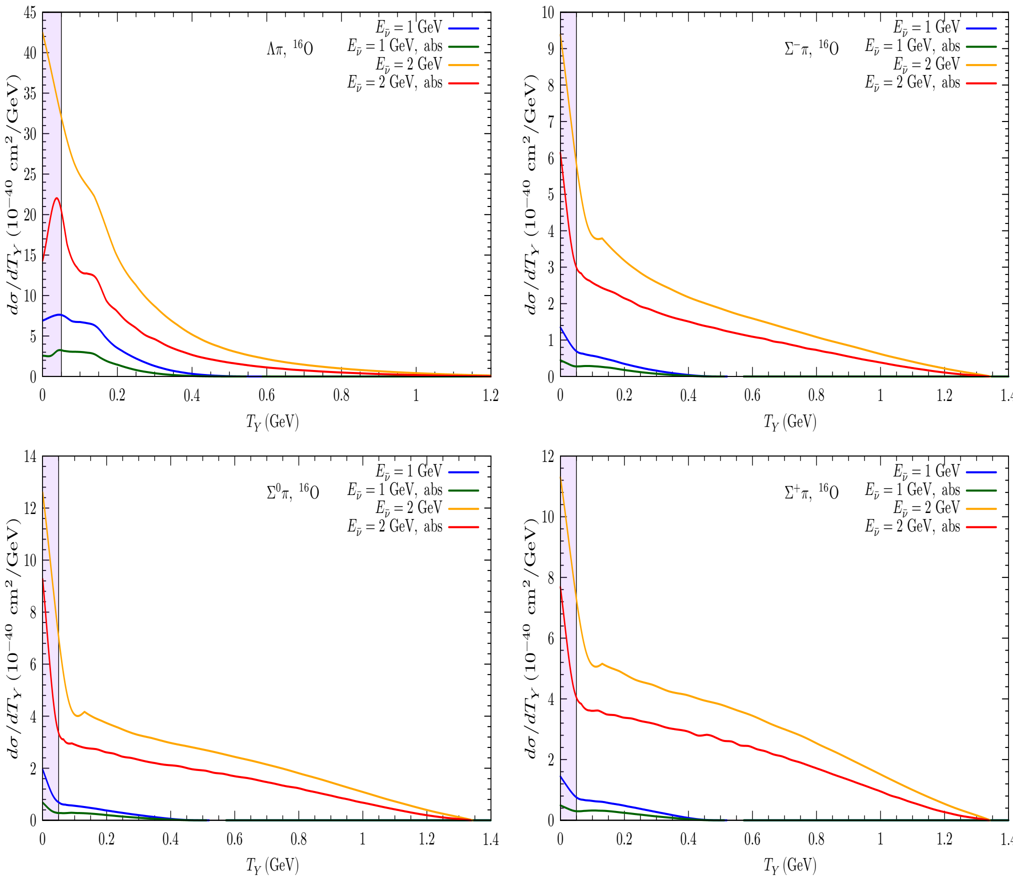

Figure 4.32: Hyperon kinetic energy distributions for the hyperon-pion mechanisms with the enhanced FSI including and not the absorption of the pions for the reaction $\bar{\nu}_\mu +^{16} \mathrm{O} \rightarrow \mu^+ + \mathrm{Y} + \pi + \mathrm{X}$ at $E_{\bar{\nu}} = 1$ and 2 GeV.

of each hyperon production distribution. These disparities are noticeable when comparing the gaps between curves at the same energy, with and without considering absorption. Notably, we find it is larger for the Λ production than for the production of any of the Σ's, notably at higher antineutrino energies, consistent with the findings shown in table 4.2.

In Fig. 4.34, we present the kinetic energy and angular distributions at a constant antineutrino energy of 2 GeV for two nuclei, ^{40}Ca and ^{40}Ar. These nuclei share the same mass number, but they have different number of protons and neutrons. In the left panels, we display the kinetic energy distribution of the four hyperons, comparing results for both nuclei with and without pion absorption. Conversely, in the right panels, the angular distribution is represented, following

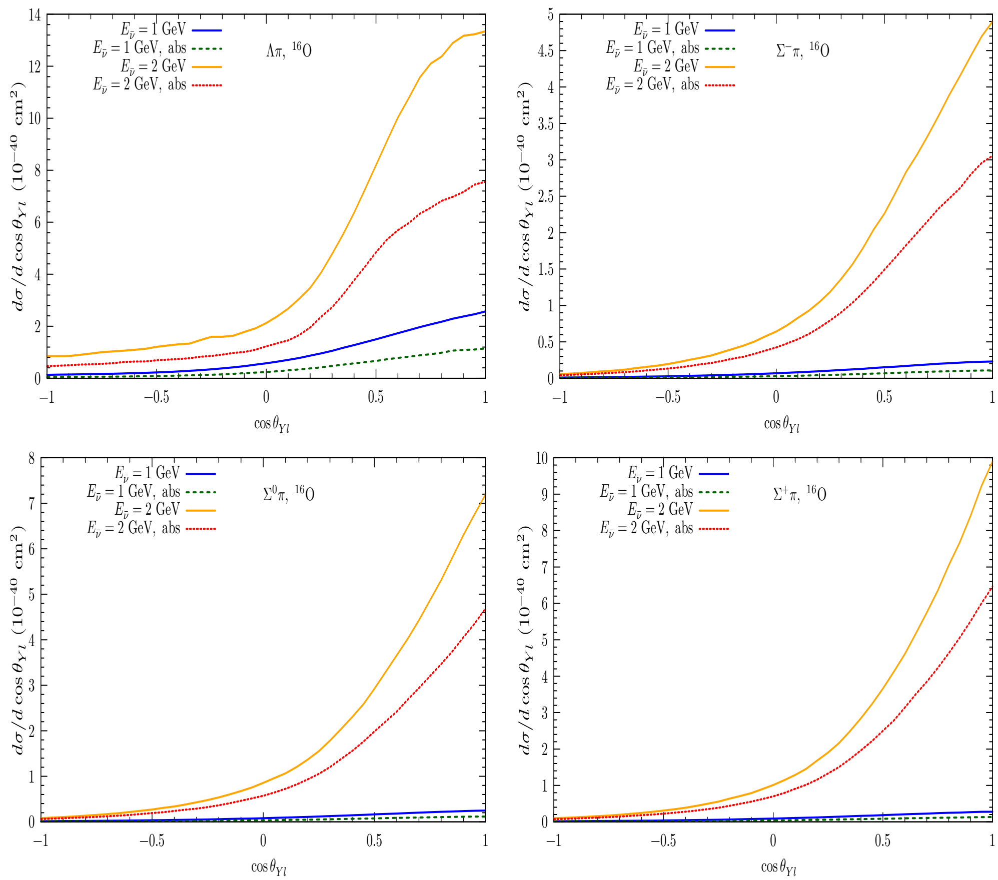

Figure 4.33: Angular distributions for the hyperon-pion mechanism with the enhanced FSI including and not the absorption of the pions for the reaction $\bar{\nu}_\mu +^{16}\mathrm{O} \rightarrow \mu^+ + \mathrm{Y} + \pi + \mathrm{X}$ at $E_{\bar{\nu}} = 1$ and 2 GeV.

the same comparison of results with and without pion absorption for both nuclei. Observing the behavior of pion absorption by the nuclei in different hyperon-pion productions. We can first note that for $\Lambda\pi$ production there are no significant differences between the results on both nuclei for the two distributions, both with and without pion absorption. It could be said that the lines are nearly identical, but upon a closer inspection, one can notice that in the curves corresponding to distributions without absorption, the line for ^{40}Ar remains slightly above.

The differences between the results with and without absorption could stem from the slightly different absorption rates of the two nuclei. When comparing at 2 GeV, the absorption rate for Λ production from ^{40}Ar (Tab. 4.3) and ^{40}Ca (Tab. 4.4) is slightly higher for ^{40}Ar, which might account for that minimal difference.

^{40}Ca	$E_{\bar{\nu}_\mu} = 1$ GeV	$E_{\bar{\nu}_\mu} = 2$ GeV
$\Lambda\pi$	66%	51%
$\Sigma^-\pi$	63%	43%
$\Sigma^0\pi$	63%	41%
$\Sigma^+\pi$	63%	40%

Table 4.4: Pion absorption rate for $Y\pi$ production for ^{40}Ca at $E_{\bar{\nu}_\mu} = 1$ and 2 GeV.

The distribution for the Λ is slightly higher in ^{40}Ar than in ^{40}Ca, which is also related to the fact that there are more neutrons in ^{40}Ar. This is because the primary production of $\Lambda\pi$ in neutrons is twice that in protons. A similar pattern is also observed in the distributions corresponding to $\Sigma^0\pi$ production. However, in the case of Σ^- and Σ^+ production, noticeable differences between the results for both distributions and the two nuclei can be observed. In the case of these two hyperons, we observe completely different behaviors. While the curves with and without absorption in ^{40}Ar are higher for the $\Sigma^-\pi$ production because it has more neutrons than ^{40}Ca, the results are lower than those corresponding to ^{40}Ca for $\Sigma^+\pi$ because this nucleus has more protons than ^{40}Ar. If we compare the pion absorption ratios from Tables 4.3 and 4.4, we notice a significant similarity between the two nuclei, although the absorption is slightly higher for ^{40}Ar. However, as we have observed, this slight difference in the ratios is not clearly reflected in all the distributions.

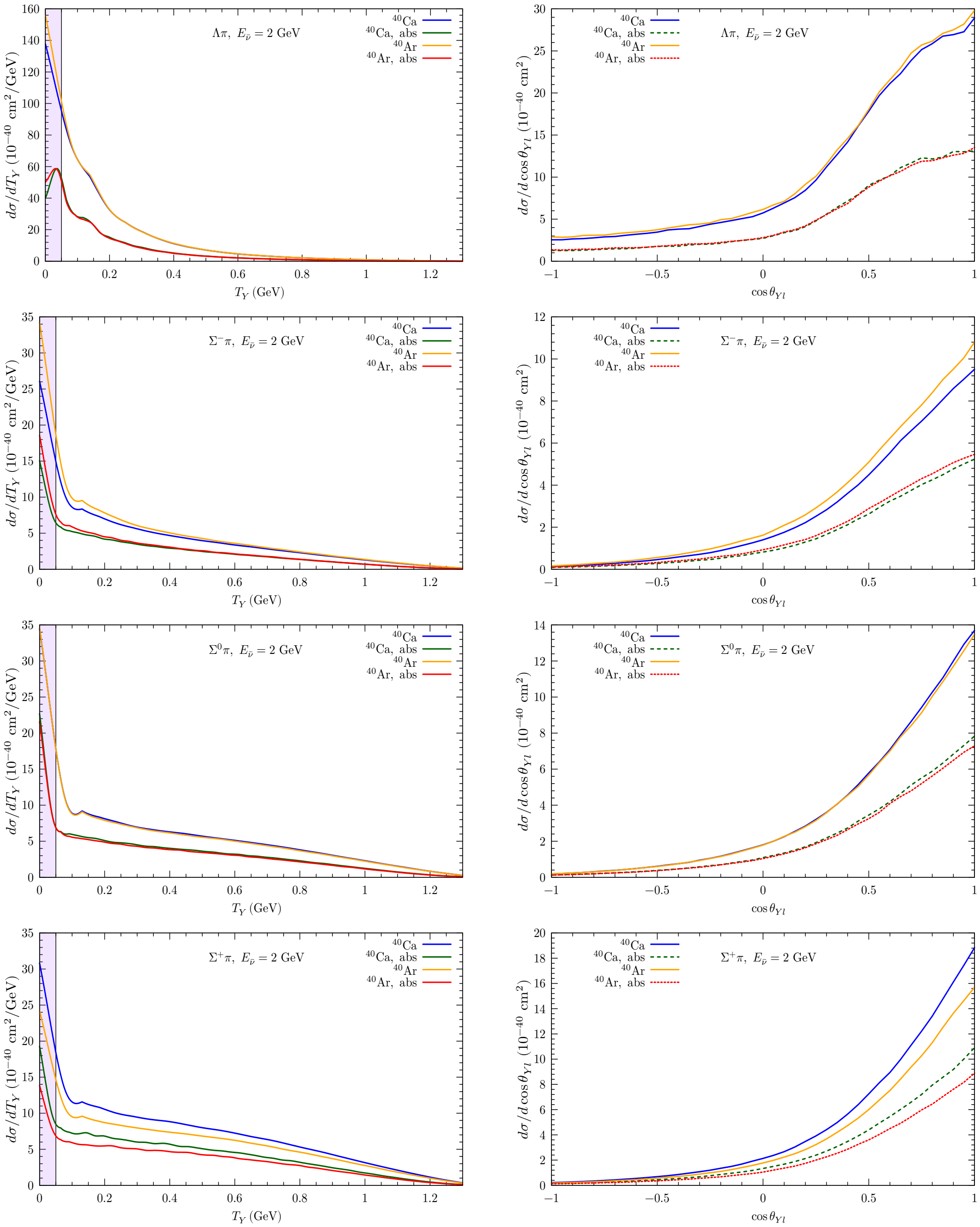

Figure 4.34: Hyperon kinetic energy (left panels) and angular distributions (right panels) for ^{40}Ca (symmetric nucleus) and ^{40}Ar (antisymmetric nucleus) comparing the hyperon-pion mechanism with the enhanced FSI including and not the absorption of the pions at $E_{\bar{\nu}} = 2$ GeV.

Chapter 5

Comparisons with MicroBooNE measurement

The experimental information for hyperon production induced by low energies antineutrinos is still very scarce, as was discussed in the introduction. However, this could change soon. Starting with the few experiments that reported strange baryon production, there is just a handful of Λ and Σ production events observed at several bubble chambers: Gargamelle [75, 76, 77], ANL [78], BNL [79, 80], Fermilab [82, 81] and SKAT [83]. The majority of the experiments that reported hyperon production events are from before the 1990s. Currently, experiments are reporting or awaiting results on the production of strange baryons such as MicroBooNE and SBND at Fermilab. Recently, the first measurement of $\bar{\nu}_\mu + {}^{40}\text{Ar} \to \mu^+ + \Lambda + X$, where X denotes the final state content without strangeness, has been reported by the MicroBooNE Collaboration [59]. So far only five Λ events have been identified analyzing the exposure of the MicroBooNE liquid argon detector to the off-axis NUMI beam at FNAL.

Fortunately, the situation is bound to improve. Soon, the statistics of MicroBooNE events are going to increase as already collected data as already collected data, which are awaiting for analysis, are analyzed and presented [59]. For instance, the Short Baseline Near Detector (SBND) at Fermilab is expected to accumulate around 8000 Λ's and 4500 Σ^+ in only three years of operation [60, 61][1].

[1]This estimation was obtained by the MicroBooNE collaboration using the GENIE event generator [164] for a 6.6×10^{20} protons on target exposure.

5.1 Hyperon kinetic energy distribution

At Fermilab, and using the NUMI beam and their liquid argon time projection chamber (LArTPC) detector, the MicroBooNE collaboration has reported five Λ events. Soon, a fourfold increase with already collected data is expected [59]. Clearly, the statistics is too low to discriminate between models or to analyze transition form factors, axial masses or other parameters of the theory. Nonetheless, these data already can provide useful information on the total cross section and the quality of data that can be anticipated.

In the first place, after folding the theoretical cross section with the experimental flux, we have calculated the restricted phase space cross section σ_*, related to the total cross section in the way explained in the supplemental material of Ref. [59], and that basically takes into account the detection thresholds of the Λ decay products. The restricted phase space cross section can be calculated as

$$\sigma_* = F\sigma, \tag{5.1}$$

$$F = \frac{1}{\sigma}\int_0^\infty f(p_\Lambda)\frac{d\sigma}{dp_\Lambda}dp_\Lambda, \tag{5.2}$$

where $f(p_\Lambda)$ is the fraction of Λ baryons decaying via $\Lambda \to p + \pi^-$ that will be above the detection thresholds as a function of their momentum p_Λ.

We apply the same restrictions in the phase space to our calculation in order to compare our results with MicroBooNE data in Tab. 5.1. The model agrees

	σ_* ($\times 10^{-40}$cm^2/Ar)
MicroBooNE	$2.0^{+2.1}_{-1.6}$
QE + $Y\pi$, full model	2.13
QE contr.	1.44
$Y\pi$ contr.	0.69

Table 5.1: Restricted phase space cross section, σ_*, for Λ production as defined in Ref. [59] and measured by the MicroBooNE collaboration and compared with our theoretical models for QE Λ and $\Lambda\pi$ production.

well with the data. In this restricted phase space, and for this flux, the relative importance of the $Y\pi$ mechanism as a source of pions and Λ's is considerably enhanced. In fact, as can be seen in Table 5.1, the $Y\pi$ contribution accounts for one third of the total flux-averaged cross section in the restricted phase space, σ_*.

The value of σ_* we obtain, including both QE and $Y\pi$ contributions, agrees with the MicroBooNE experimental result, whose discriminating power is still limited by the very low statistics. According to Ref. [59], the measured σ_* value is also consistent with the predictions from the GENIE [164] and NuWro [88] event generators. It should be remarked that neither of the two includes $Y\pi$ channels. In addition, in the case of GENIE FSI is not accounted for. This shortcoming could seriously affect the results for this observable, σ_*, because FSI sends many hyperons to low energies below the detection threshold. NuWro includes FSI, however, for the Λ case, its effects seem to be minimal [88]. Our findings imply that the $\Lambda\pi$ contribution, which is dominated by $\Sigma^*(1385)$ excitation, is a very important ingredient for the analysis and interpretation of the experimental results awaited at MicroBooNE and SBND.

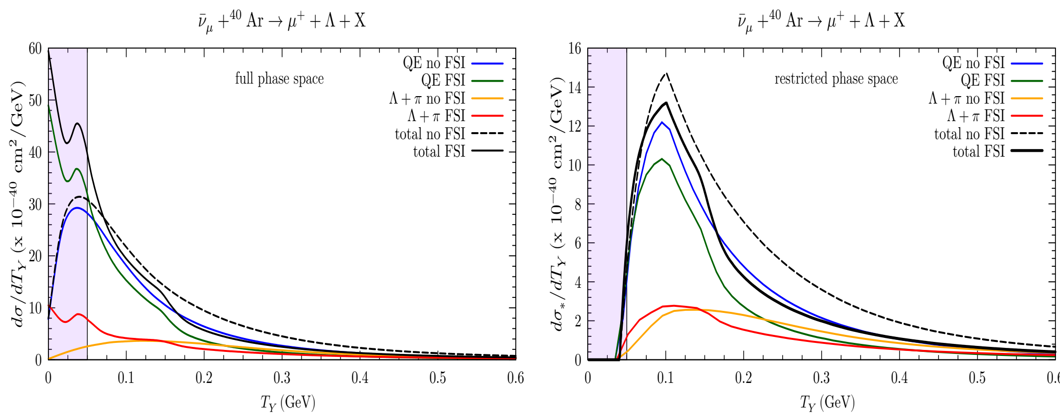

Figure 5.1: Flux-folded Λ kinetic energy spectra for QE and $\Lambda\pi$ processes, and the sum of both contributions, with and without FSI, for the reaction measured in Ref. [59]. The MicroBooNE flux has been taken from the supplemental material of the above reference. On the left panel we show the distributions without any restriction in the phase space due to the experimental detection thresholds; while on the right one we display the same distributions after applying the experimental restriction on the phase space, as explained in the supplemental material of Ref. [59].

Finally, although the experimental energy distribution of the hyperon events is not available, it is instructive to examine in detail how the restrictions of the phase space affect the different mechanisms. We plot the differential cross section for Λ production as a function of the hyperon kinetic energy averaged over the flux used by MicroBooNE in their simulations, in Fig. 5.1. According to our model, with the corresponding flux of relatively low energies and with the full phase space, the

QE mechanisms are the strongly predominant contribution. $Y\pi$ for Λ production constitutes just a minor addition. However, in the restricted phase space and due to the detection thresholds, we better explore the higher energies part of the $d\sigma/dT_Y$ distribution. That region is more richly populated with hyperons coming from $Y\pi$ events and as a consequence their relative weight becomes more appreciable and could reach a 30% of the total with the current MicroBooNE configuration. If we compare the distribution with FSI with respect to the one without FSI, a clear enhancement at low kinetic energies is apparent which reveals a strong $\Sigma \to \Lambda$ conversion. The QE contribution is predominant while the $Y\pi$ one brings only a minor increase. According to our estimates based on Eq. 3.50, half of the primarily produced pions will be absorbed and the rest are part of the final hadronic system X without strange particles. However, the MicroBooNE measurement has phase space restrictions dictated by the detection thresholds of the $\Lambda \to p\pi^-$ decay products used to identify the hyperon. To correct for this we multiply our prediction by the fraction of Λ decays with p and π^- above detection threshold. This quantity as a function of the hyperon momentum is readily provided by MicroBooNE in the Supplemental Material of Ref. [59]. The result is displayed in the right panel of Fig. 5.1. One immediately notices that the detector is blind to Λ's with $T_\Lambda < 40$ MeV, accounting for a large fraction of the cross section. The opportunity to understand better FSI and test models in this challenging region is unfortunately missed. Interestingly, this physics will be enabled in large-volume pressurized argon time projection chambers such as the one under development by DUNE [165, 166], where reconstruction thresholds in the few-MeV range are anticipated for hadrons.

5.1.1 Pion absorption

To delve into a more detailed examination of the potential impact of pion absorption within the nucleus on the $Y\pi$ process, we present, in Table 5.2, the pion absorption ratio derived from the cross sections convoluted with the MicroBooNE flux, considering both the full phase space and the restricted phase space. We can see that the percentage of absorbed pions is practically half for both cases, with and without restriction in the phase space.

On the other hand, we also present Figure 5.2. In blue, we show the results for QE production with FSI; in green, the $Y\pi$ process; and in yellow, the same, but considering pion absorption. The solid black line represents the combined contributions of QE + $Y\pi$ with FSI and without absorption, while the dashed black line represents the sum of the QE contribution and the segment corresponding to the difference in the $Y\pi$ cross section with and without pion absorption. If we

^{40}Ar	full phase space	restricted phase space
$\Lambda\pi$	48%	49%

Table 5.2: Pion absorption rate for $\Lambda\pi$ production off ^{40}Ar convoluted with the MicroBooNE flux.

compare the $\Lambda\pi$ production lines, we can see that with absorption, it is practically half compared to without considering it. The difference between them would be the percentage of inelastic events that could be confused with quasielastic processes. If we look at the dashed black line, we see that it is considerably more significant than the quasielastic line and could experimentally lead to an error. Both types of events could be confused.

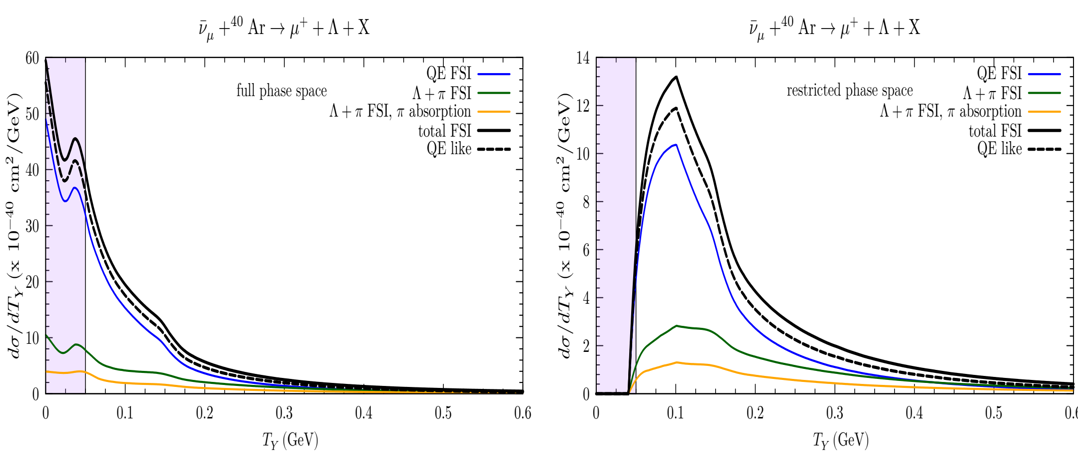

Figure 5.2: Flux-folded Λ kinetic energy spectra for QE and $\Lambda\pi$ processes with and without considering pion absorption in the nucleus. The sum of both contributions without considering pion absorption, and the sum of the QE contribution and the difference between $\Lambda\pi$ processes with and without considering pion absorption for the reaction measured in Ref. [59]. On the left panel, we show the distributions without any restriction in the phase space due to the experimental detection thresholds; while on the right one, we display the same distributions after applying the experimental restriction on the phase space.

5.2 Angular distribution

The results obtained for the angular distribution in the cosine of the angle between the muon and the Λ hyperon were calculated without restrictions in the phase space. We present in Fig.5.3 the angular distribution flux-folded with the effect of the final state interactions. The preservation of the observed shape in the results presented in subsection 4.2.4 is evident, as anticipated, given the lack of influence from the convolution with the flux of this experiment. It would be of particular interest to ascertain experimentally whether it is feasible to distinguish hyperons originating from each process by measuring the angle formed between the trajectories of the hyperon and the muon. Because, as we have seen in the previous section, due to the absorption of pions by the nucleus, there will be events corresponding to $\Lambda\pi$ production that will be confused with truly quasielastic events.

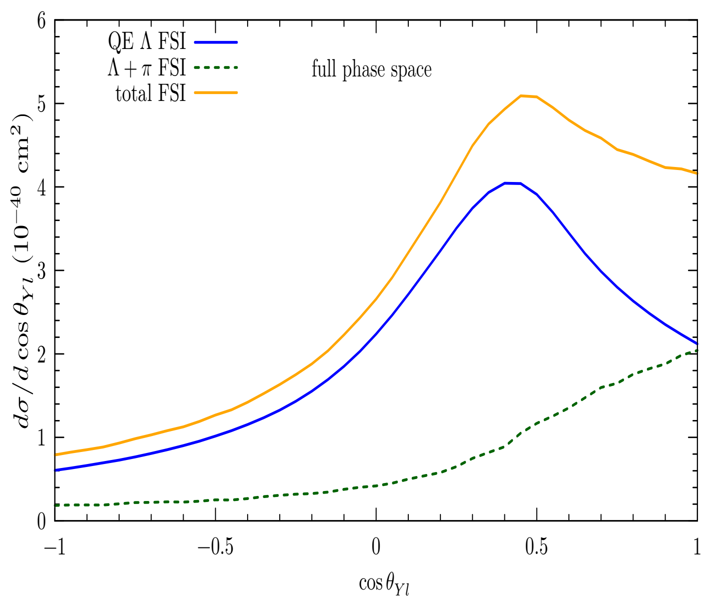

Figure 5.3: Flux-folded Λ angular distributions for QE and $\Lambda\pi$ processes with FSI, and the sum of both contributions for the reaction measured in Ref. [59].

5.3 Flux-folded double differential cross sections

In this section, we examine the shape of the double differential cross sections in the kinetic energy of the Λ and the cosine of the angle formed between the outgoing muon and the hyperon. In Figs. 5.4 and 5.5, we present the results for both quasielastic production and the $\Lambda\pi$ process, with and without the FSI effect, convoluted with the flux used by the MicroBooNE collaboration. If we compare the figures 5.4 and 4.28, where we represent the same double differential cross section without being convoluted with any experimental flux, we can see that, in the case of panels with FSI, they are distributed differently due to the flux. In the case of quasielastic production, the bulk of the double differential cross section focuses on cosine values above zero, whereas in the case without convolution with the flux, it was less centralized. For the $\Lambda\pi$ process, the opposite occurs. The effect of applying FSI also persists, flattening the shape towards negative cosine values for both quasielastic production and $\Lambda\pi$ production. However, the peak of events continues to be centered around the cosine value of 0.4 for QE and forward for $\Lambda\pi$. The shape remains despite the convolution with the flux, as expected. Therefore, the idea that it is interesting to consider the angle formed between the outgoing muon and the hyperon to try to differentiate between the two hyperon production processes is reinforced.

In Fig. 5.5, we also present the double differential cross sections convoluted with the flux, but in this case, applying the restrictions in the phase space already incorporated in Sects. 5.1 and 5.2 due to the detection thresholds of the MicroBooNE experiment. If we now compare Figs. 5.4 and 5.5, we observe, as expected, that we would no longer see anything for kinetic energies of Λ below 40 MeV. We also see that the greater number of events is concentrated more in this second figure due to the effect of the restriction in the phase space of the experimental setup.

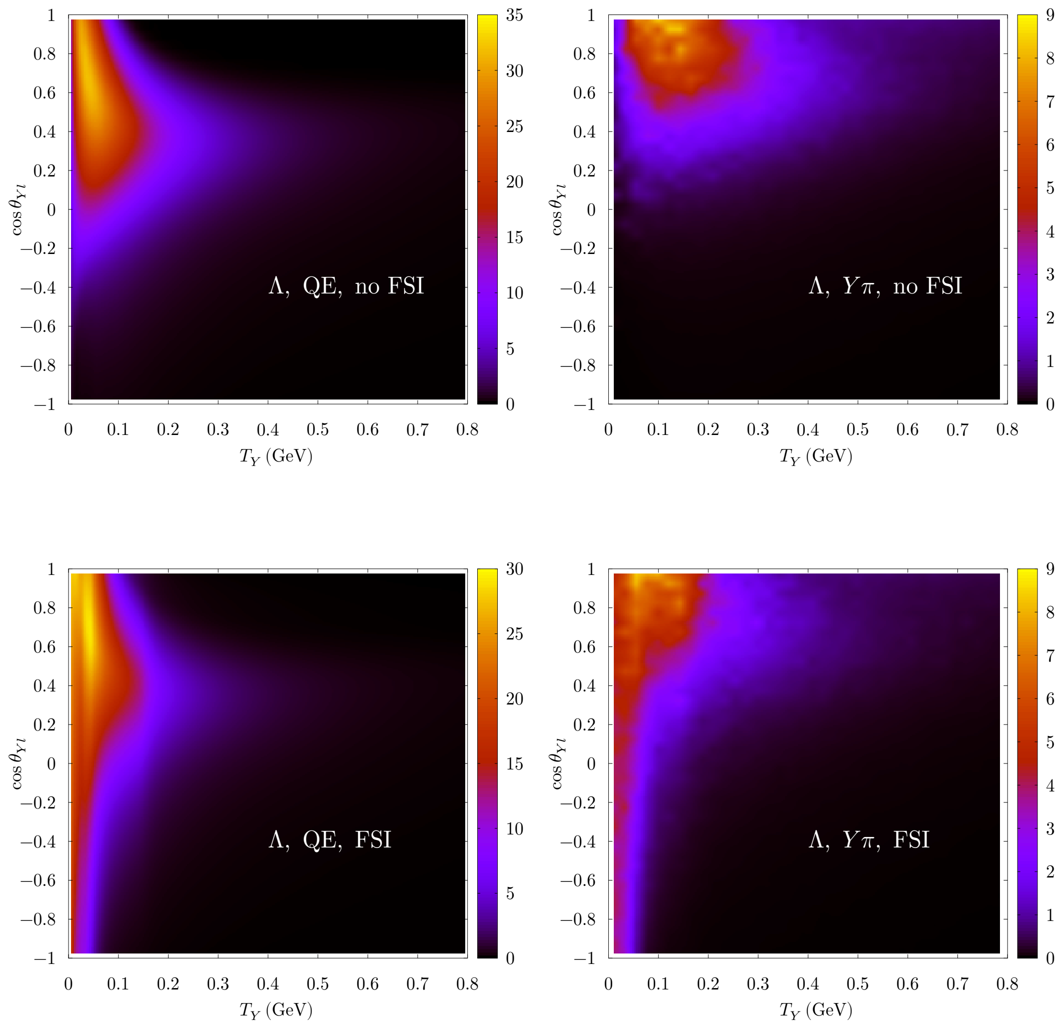

Figure 5.4: Flux-convoluted (with the MicroBooNE flux) double differential cross sections in kinetic energy and cosine of the angle between muon and hyperon. We compare the quasielastic hyperon production (left panels) and hyperon-pion mechanism (right panels) with (bottom panels) and without FSI (upper panels) for Λ production, in the reaction $\bar{\nu}_\mu + ^{40}\mathrm{Ar} \to \mu^+ + \Lambda + \mathrm{X}$. The units of the color scale are given in units of $10^{-40}\mathrm{cm}^2/\mathrm{GeV}$.

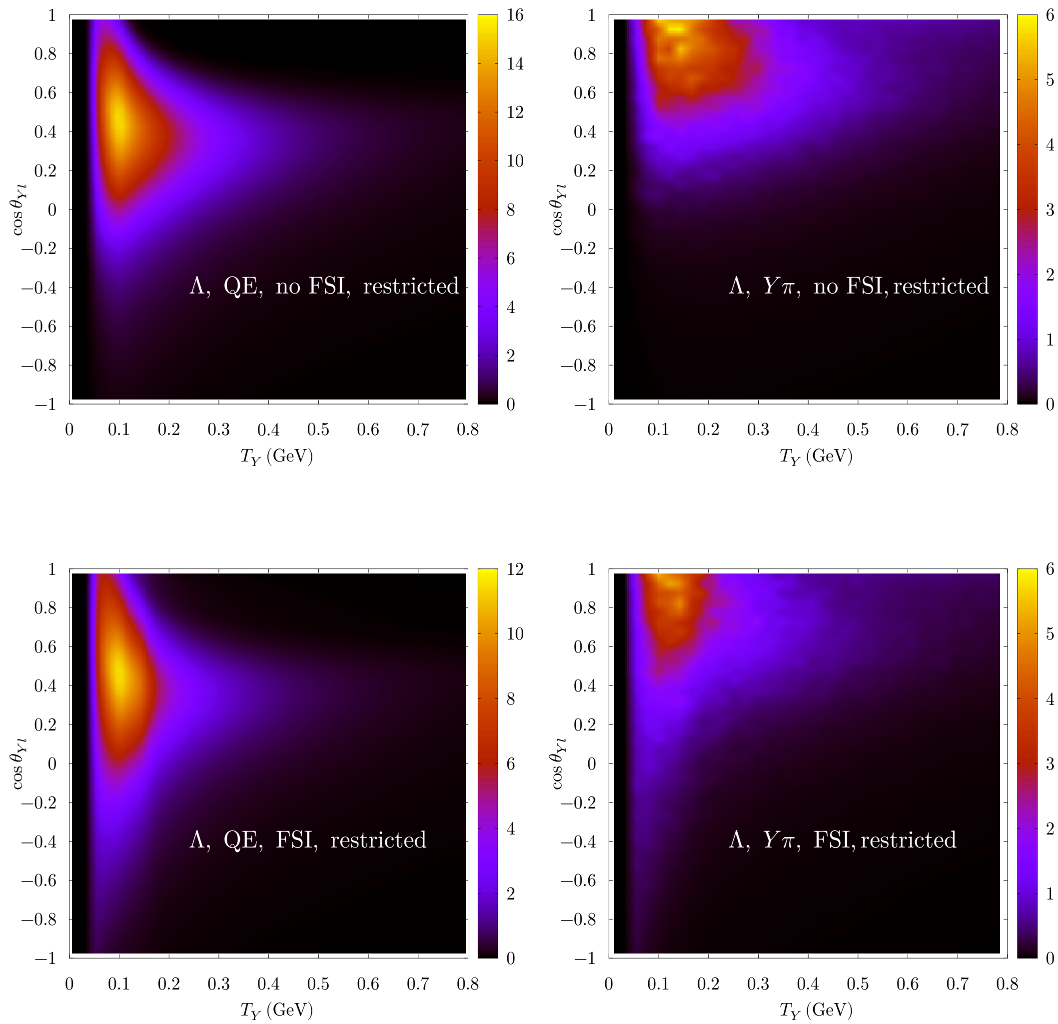

Figure 5.5: Flux-convoluted (with the MicroBooNE flux) double differential cross sections in kinetic energy and cosine of the angle between muon and hyperon with the restriction in the phase space. We compare the quasielastic hyperon production (left panels) and hyperon-pion mechanism (right panels) with (bottom panels) and without FSI (upper panels) for Λ production, in the reaction $\bar{\nu}_\mu +^{40}$ Ar $\rightarrow \mu^+ + \Lambda + \mathrm{X}$. The units of the color scale are given in units of $10^{-40}\mathrm{cm}^2/\mathrm{GeV}$.

5.4 SBND prediction

As we saw in the previous section, the first measurement of Λ quasielastic production off ^{40}Ar has been reported by the MicroBooNE collaboration. However, the data of Λ quasielastic production recorded between 2017 and 2020 is still awaiting to be analysed [59]. Meanwhile, the SBND collaboration expects to obtain larger statistics of hyperon production [60, 61]. It is expected to accumulate 8000 Λ and 4500 Σ^+ in only three years of operation. The Short-Baseline Near Detector (SBND) is the near detector of the Short-Baseline Neutrino (SBN) program located along the Booster Neutrino Beamline (BNB) at Fermilab. The LArTPC detector is larger than that of MicroBooNE and is filled with more tons of liquid argon, 270 tons compared to MicroBooNE's 170 tons. Therefore, the statistics are expected to be higher. They plan to take measurements continuously for 5 years and expect to observe 7000 interactions daily. They use the BNB flux, in our case, we focus solely on the muonic antineutrino component of the neutrino flux, from which we want to present in this section some predictions for the measurements of the experiment based in our model developed along this thesis. The flux used in SBND has, more or less, the same shape as that of MicroBooNE, but it is indeed more intense. This is because SBND is closer to the antineutrino source, situated at 110 meters compared to MicroBooNE's 470 meters. In these results we do not apply thresholds in the particle energies, as we want to show the possible behaviour of both contributions when we convolute with the flux used in their simulations. It is important to note that if we were to consider the experiment phase space restrictions, the cross sections would be reduced, and the shapes of the energy spectra would change. Furthermore, they would differ among the various hyperons.

As mentioned, they expect to obtain 8000 Λ and 4500 Σ^+ in only three years [60, 61]. The difficulty in detecting these hyperons lies in their short mean lifetime ($< 10^{-10}$ s) and the products of their decay. In light of the potential observation of all four hyperons, we have opted to present the outcomes for each of these hyperons' decays individually in Table 5.3.

Hyperon	Decay products
Λ	$p+\pi^-//n+\pi^0$
Σ^-	$n+\pi^-$
Σ^0	$\Lambda+\gamma$
Σ^+	$p+\pi^0//n+\pi^+$

Table 5.3: Decay products of the hyperons.

5.4.1 Hyperon spectra

We represent the energy spectrum for the production of the four hyperons, as having more statistics would make it more likely to detect any of the four possible channels. The hyperon kinetic energy distribution convoluted with the $\bar{\nu}_\mu$ SNBD flux in neutrino mode is shown in Fig. 5.6. We present the results for both QE production and $Y\pi$ processes with and without FSI, always considering hyperon potentials. We also show the sum of both contributions.

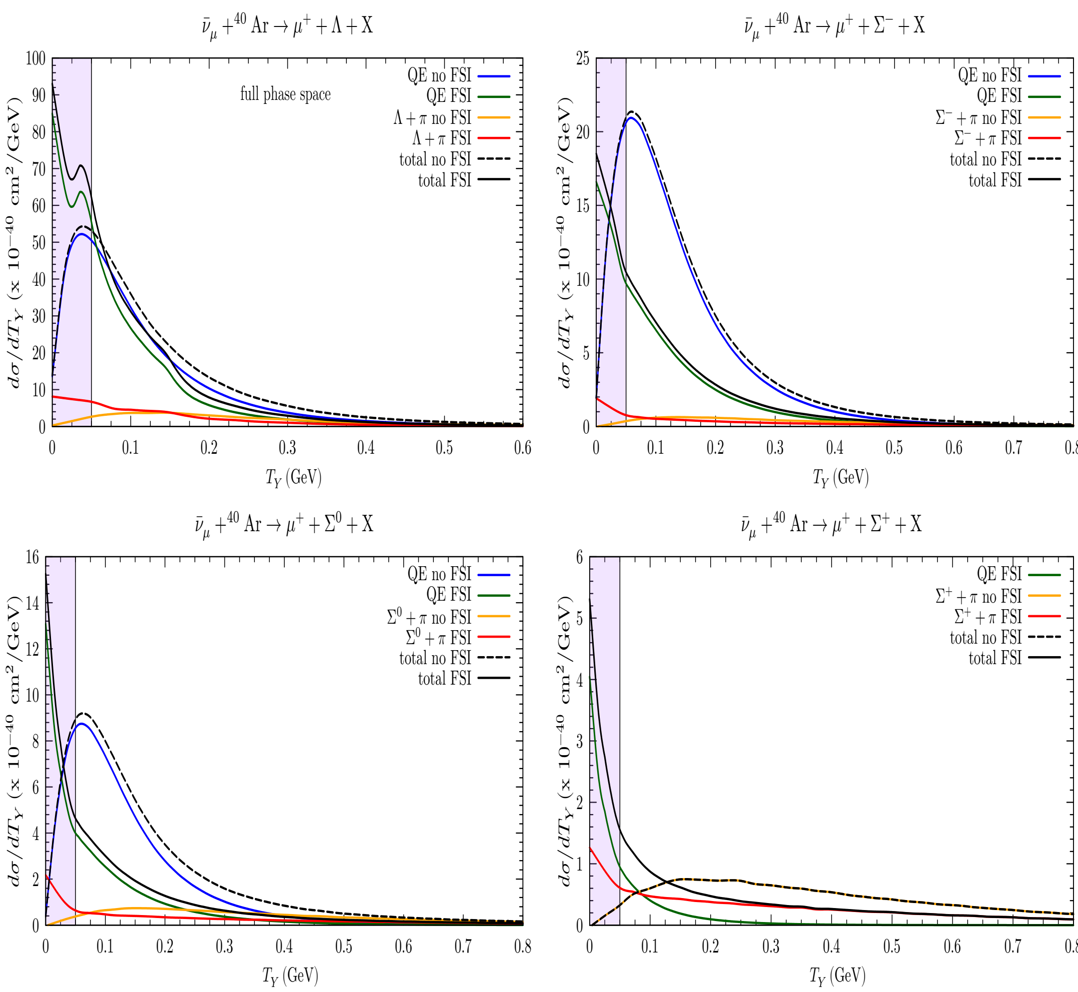

Figure 5.6: Flux-convoluted hyperon kinetic energy distributions for the quasielastic, hyperon-pion processes and the sum of both contributions, with and without FSI, for Λ and Σ's production. Convoluted with the $\bar{\nu}_\mu$ BNB flux. The nuclear target is ^{40}Ar.

In the Fig. 5.6, we can observe that the differences between the two processes with FSI are more pronounced for the production of Λ's than in the previous case, convoluting with the flux used in MicroBooNE 5.1. This may be due to the different shape of the flux in SBND, as we have already explained. The difference between the spectra of the two hyperon production modes is also significant for Σ^- and Σ^0, with Σ^+ being the only hyperon in which the impact of the inelastic production is crucial. Studying the production of Σ^+ induced by antineutrinos would be incomplete without considering the $Y\pi$ process. Since the energy distributions are comparable for both processes, exploring how the constraints in the phase space might influence the outcomes is of interest, particularly when the Σ^+ hyperons with lower kinetic energy are likely to remain undetected. We can venture to state, considering the higher values of the inelastic process compared to QE at higher hyperon kinetic energies, that the significance or weight of $\Sigma^+\pi$ production would be greater. Therefore, we consider it of vital importance that this type of hyperon production process, along with a pion, be included in the event generators utilized by experiments.

Process	π absorption rate
$\Lambda\pi$	40%
$\Sigma^-\pi$	48%
$\Sigma^0\pi$	52%
$\Sigma^+\pi$	53%

Table 5.4: Pion absorption rate for $Y\pi$ production for the cross sections convoluted with the SBND flux.

In the table 5.4, we show the pion absorption rate for all the reactions. The cross sections are convoluted with the flux used by SBND. The pion absorption range varies between 40% (for Λ) and 53% (for Σ^+). In Fig. 5.7, we depict the kinetic energy distributions of the four hyperons. We show the distributions for QE (blue line) and $Y\pi$ with FSI, the latter with (yellow line) and without (green line) considering pion absorption. The solid black line represents the total sum with FSI without considering absorption, and the dashed line shows the sum of the QE contribution plus the portion of the cross section corresponding to $Y\pi$ production where the pion has been absorbed. The reason for showing this last line is that, in principle, experimentally, that pion cannot be measured, and considering the entire obtained cross section as purely quasielastic could lead to a misinterpretation. We observe that, in the case of Λ, Σ^0 and Σ^-, the most significant differences between the green lines and the yellow ones occur at low hyperon energies. Meanwhile, for Σ^+, the differences seem that remain similar across all considered kinetic energies. The estimation we have made for the pion absorption ratio indicates that more than half of the pions produced in the $\Sigma^+\pi$ process would be absorbed by the nucleus. This could paint a different picture than the one shown in Fig. 5.6 and accounting as quasielastic events half of those coming from inelastic processes.

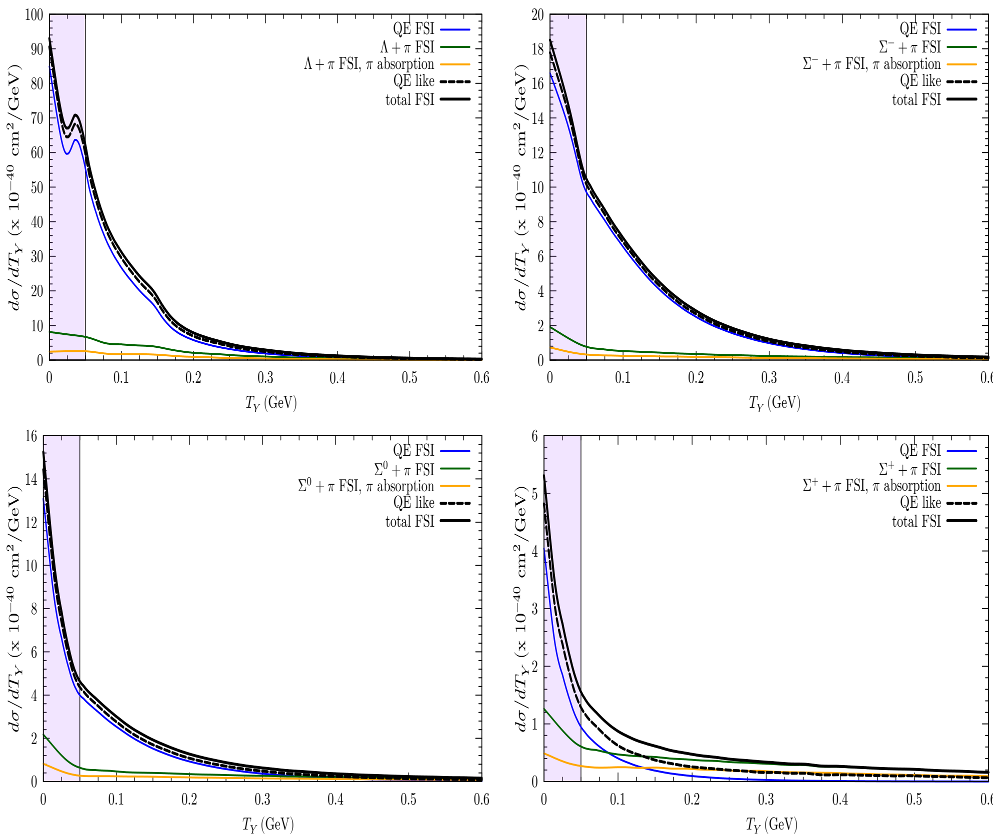

Figure 5.7: Hyperon kinetic energy distributions for the quasielastic and hyperon-pion processes, with and without considering pion absorption in the nucleus. The sum of both contributions without considering pion absorption, and the sum of the QE contribution and the difference between $Y\pi$ processes with and without considering pion absorption for Λ and Σ's production. Convoluted with the $\bar{\nu}_\mu$ SBND flux.

5.4.2 Angular distributions

In this section, we want to show the angular distribution for the four possible hyperons in the cosine of the angle between the muon and the produced hyperon.

We present the results with FSI. We can observe in Fig. 5.8 that the form of both contributions is clearly different, as we already saw in Subsection 4.2.4. There is a bump in the quasielastic mechanism around cosine equal $\sim$ 0.4-0.5. And the hyperon-pion production still has the same angular behavior, it is forward peaked. In this figure, we can also observe that, in the case of Σ^0 and Σ^+ production, the inelastic process $Y\pi$ holds competitive significance with quasielastic (QE) production, being even more important for Σ^+. Once again, we obtain results that underscore the importance of considering the $Y\pi$ mechanism in experimental analyses.

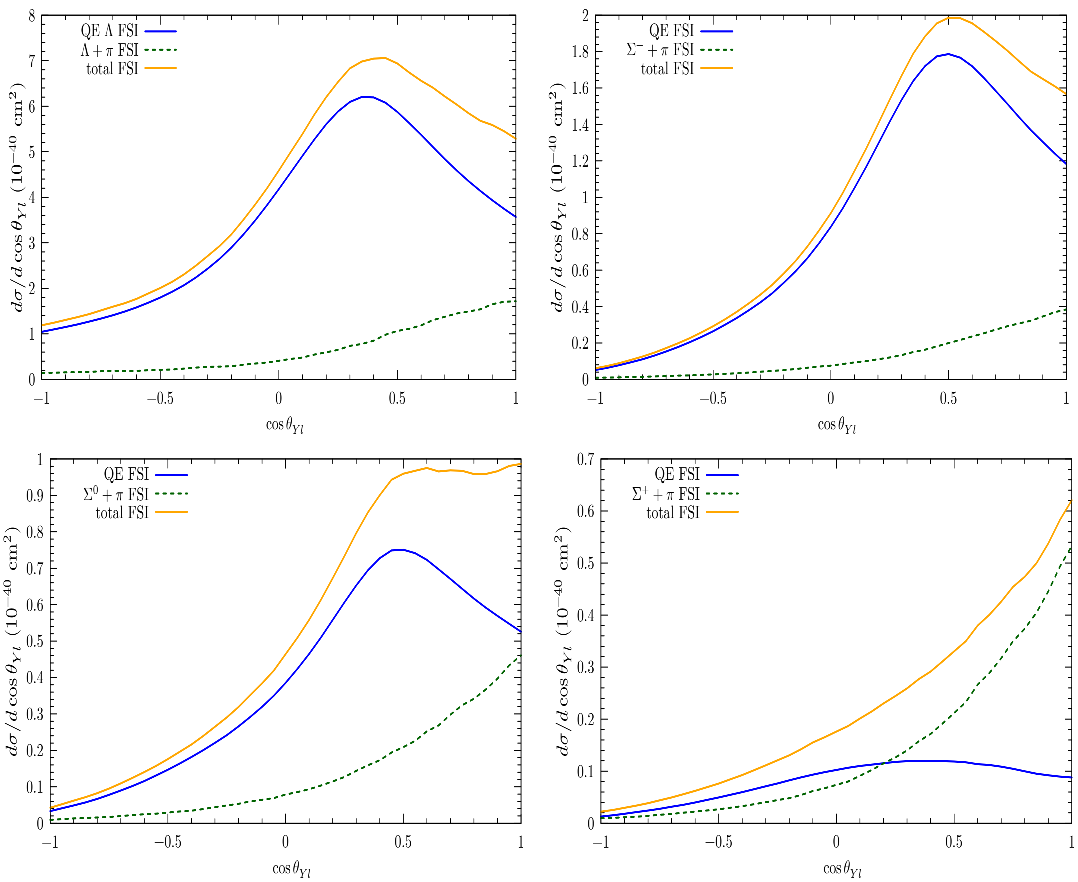

Figure 5.8: Angular distributions for the quasielastic, hyperon-pion processes and the sum of both contributions with FSI for Λ and Σ's production. Convoluted with the $\bar{\nu}_\mu$ BNB flux for SBND.

5.4.3 Double differential cross sections

We present the double differential cross sections, in hyperon kinetic energy and the cosine of the relative angle between the muon and the hyperon, convoluted with the muonic antineutrino flux from the SBND experiment. As mentioned earlier, this flux is very similar in shape to that of MicroBooNE but is more intense due to SBND being a short-baseline neutrino experiment. Therefore, we expect to find similar figures for the Λ results without applying phase space restrictions as those obtained in Section 5.3. We present results for the production of all four possible hyperons for both types of production mechanisms, with and without FSI (Figs. 5.9,5.10, 5.11 and 5.12). However, we will focus primarily on Λ production to compare with MicroBooNE results, and on Σ^+ production since, in this case, inelastic production will be competitively important alongside quasielastic production. If we compare with the figures in subsection 4.2.5, where we showed the double differential cross sections without convolution with any flux, we see that the shape is maintained for the results without FSI in the figures of this subsection. Although it is true that under the influence of the flux and its shape, the peak intensity tends to accumulate at lower hyperon kinetic energies. However, the results with FSI are different because the flux shifts the peaks to very low hyperon kinetic energies, with a significant portion of the statistics accumulating at values below 0.2 GeV. This effect is observed in both contributions to hyperon production. As we have seen so far, the main difference between both contributions lies in where the maximum accumulates in the cosine of the angle between the muon and the hyperon.

In Fig. 5.9, we show the double differential cross section for Λ production. We observe that the shape is maintained both in the accumulation in cosine and in the hyperon kinetic energy. The main differences with the results convoluted with the MicroBooNE flux (Sec. 5.3) are that in the case of the SBND flux, the shape and position of the flux maximum are somewhat different between them. In the case of quasielastic production of Λ with FSI, the events are also distributed towards negative values of the cosine of the angle between muon and hyperon, and in the case of the MicroBooNE flux, they are more centered on the representative peak of this quasielastic process.

On the other hand, Figs. 5.10 and 5.11 for the production of Σ^- and Σ^0 are practically very similar, as expected. The expected shape for each type of production with and without FSI is maintained. The main difference between them lies in the intensity of the cross section in each case, with a higher value for the production of Σ^-.

Finally, the results for the production of Σ^+ are shown in Fig. 5.12. We can see that, focusing only on the results with FSI, the two contributions would be easily distinguishable, as we have seen throughout all the results obtained in this thesis. The contribution of quasielastic production is lower than for the other Σ's because, without FSI, this hyperon cannot be produced.

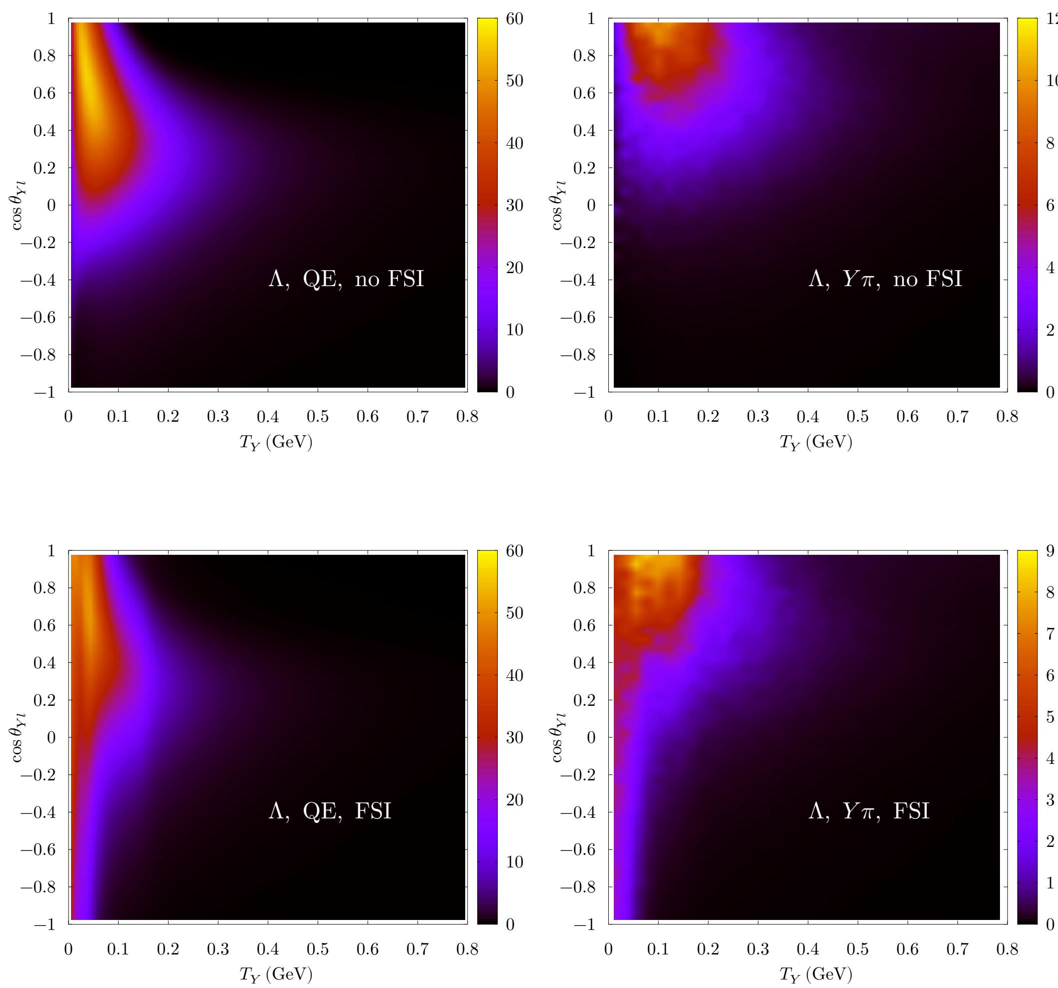

Figure 5.9: SBND flux-folded double differential cross sections in kinetic energy and angle comparing the quasielastic hyperon production (left figures) and hyperon-pion mechanism (right figures), with (bottom ones) and without FSI (upper figures) for Λ production, in the reaction $\bar{\nu}_\mu +^{40}\text{Ar} \to \mu^+ + \Lambda + \text{X}$. The units of the color scale are given in units of $10^{-40}\text{cm}^2/\text{GeV}$.

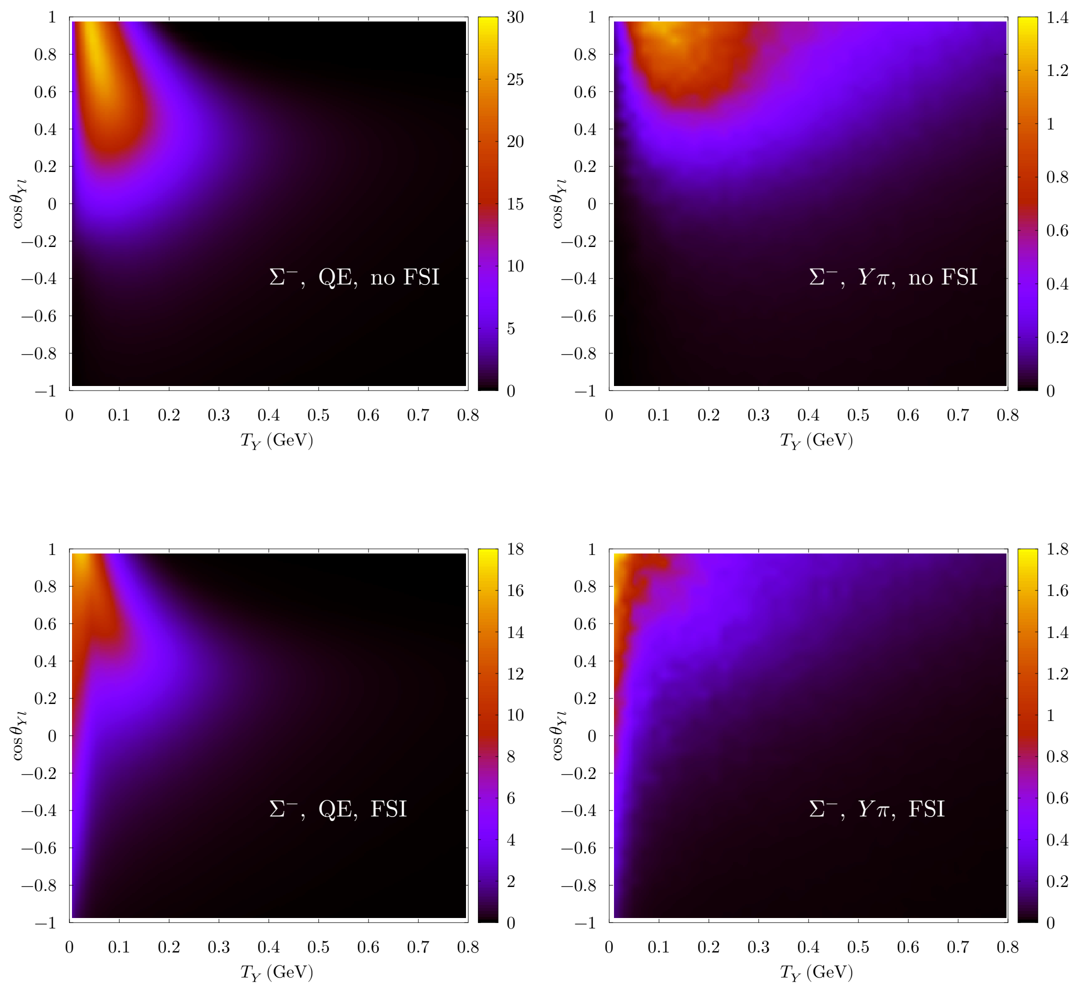

Figure 5.10: SBND flux-folded double differential cross sections in kinetic energy and angle comparing the quasielastic hyperon production (left figures) and hyperon-pion mechanism (right figures), with (bottom ones) and without FSI (upper figures) for Σ^- production, in the reaction $\bar{\nu}_\mu +^{40}\mathrm{Ar} \to \mu^+ + \Sigma^- + \mathrm{X}$. The units of the color scale are given in units of $10^{-40}\mathrm{cm}^2/\mathrm{GeV}$.

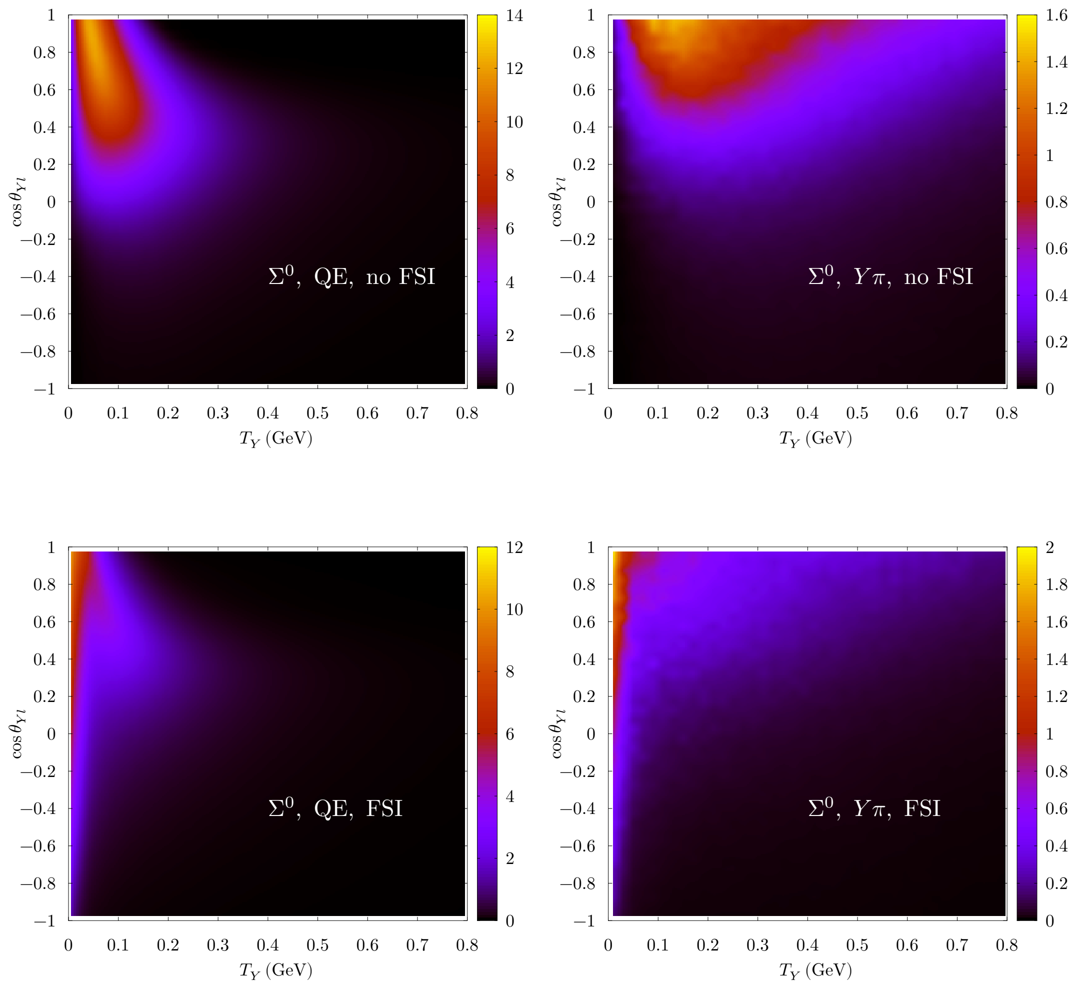

Figure 5.11: SBND flux-folded double differential cross sections in kinetic energy and angle comparing the quasielastic hyperon production (left figures) and hyperon-pion mechanism (right figures), with (bottom ones) and without FSI (upper figures) for Σ^0 production, in the reaction $\bar{\nu}_\mu +^{40}\mathrm{Ar} \to \mu^+ + \Sigma^0 + \mathrm{X}$. The units of the color scale are given in units of $10^{-40}\mathrm{cm}^2/\mathrm{GeV}$.

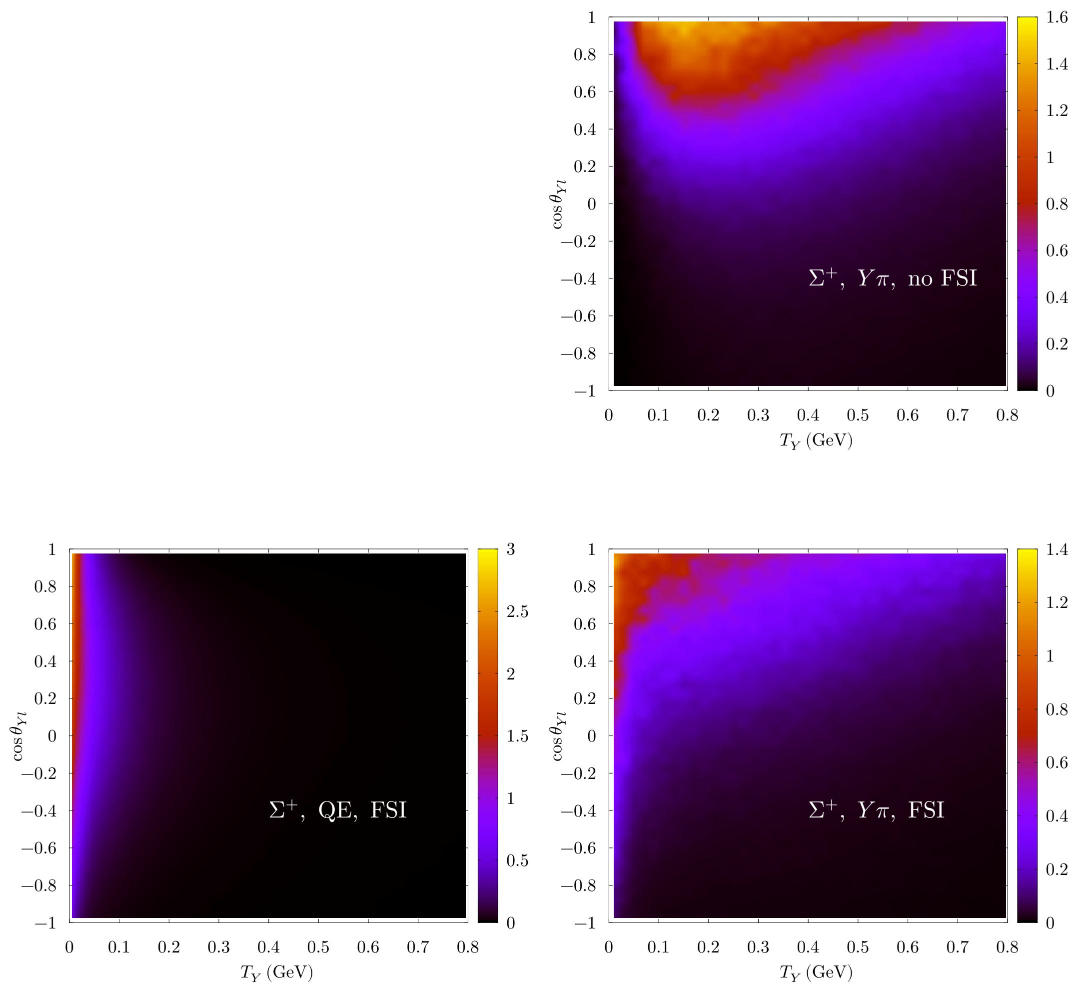

Figure 5.12: SBND flux-folded double differential cross sections in kinetic energy and angle comparing the quasielastic hyperon production (left figures) and hyperon-pion mechanism (right figures), with (bottom ones) and without FSI (upper figures) for Σ^+ production, in the reaction $\bar{\nu}_\mu + ^{40}\text{Ar} \rightarrow \mu^+ + \Sigma^+ + \text{X}$. The units of the color scale are given in units of $10^{-40}\text{cm}^2/\text{GeV}$.

Chapter 6

Conclusions

In this PhD thesis, we have investigated Cabibbo-suppressed hyperon production induced by antineutrinos driven by the strangeness-changing weak charged current. The possible hyperons are a Σ or Λ particle. The purpose of this thesis is to study hyperon production considering nuclear targets. In our model, we take into account quasielastic production, which is the primary mechanism for producing hyperons in the antineutrino energy range below 2 GeV, and the inelastic mechanism where the hyperon is produced along with a pion. The antineutrino-nucleus cross sections serve as essential inputs for the analysis of neutrino scattering and oscillation experiments. One of the primary components influencing the antineutrino-nucleus cross sections is the primary model of antineutrino-nucleon interaction. The quasielastic mechanism has been previously studied both with nuclear and nucleon targets. However, hyperon-pion production has not been studied before. Therefore, we began by studying this reaction on nucleon targets and then proceeded to study both mechanisms with nuclear targets, where numerous nuclear effects must be taken into account. Additionally, due to the recent experimental detection of Λ particle production by the MicroBooNE experiment, we compare our theoretical model with the results obtained by the collaboration. For this, we obtain cross sections convoluted with the flux used by the experiment. We also present our results for cross sections convoluted with the SBND experiment's flux

Therefore, we have begun studying Cabibbo-suppressed reactions of hyperon production off nucleons along with a single emitted pion by antineutrinos. The model is based on the lowest order effective SU(3) chiral Lagrangians in the presence of an external weak charged current and contains Born and the lowest-lying decuplet resonant mechanisms that can contribute to these reaction channels. It is well-known that its Cabibbo-enhanced counterpart is largely driven by the weak excitation of the $\Delta(1232)$ resonance; hence, in our model, we have also considered the relevant $\Sigma^*(1385)$ resonance ($S = -1$), which belongs to the same decuplet as the Δ.

One of the most prominent conclusions drawn from our study of hyperon-pion production from free nucleons is the significant role played by the resonances we considered. In fact, we have found that the $\Sigma^*(1385)$ mechanism prevails notably in the $\Lambda\pi$ reactions but holds less significance in the $\Sigma\pi$ channels. Our deduction leans towards its reduced importance in the latter due to the strong decay of this resonance into a Λ and a π. Additionally, we have observed the significance of crossed Δ or nucleon-pole diagrams, especially in some of the $\Sigma\pi$ reactions. This might suggest that including the N^* resonances in the u-channel could be necessary. However, the lack of experimental data on these reactions refrains us from making definitive claims in this regard. We have also studied the flux-convoluted total cross sections of these reaction channels with the antineutrino fluxes of past (MiniBooNE, SciBooNE) and current (T2K near and far detectors, Minerva) neutrino oscillation and scattering experiments.

Similarly, we have compared our findings with others in the recent and past literature. We have confirmed that the $\Lambda(1405)$ resonance plays a significant role near the threshold for $\Sigma\pi$ production. This is attributed to its S-wave character, contrasting with the P-wave character of the Σ^* resonance. However, as higher antineutrino energies are reached, other mechanisms and higher partial waves start to play a notable role. On the other hand, the $\Lambda(1405)$ resonance has no impact on $\Lambda\pi$ production due to the lack of coupling resulting from the conservation of strong isospin. Hence, we consider our results producing final $\Lambda\pi$ hadrons more reliable for the range of antineutrino energies explored in this thesis. On the other hand, based on the results obtained for the flux-convoluted total cross sections from various neutrino experiments, the figures seem to suggest that these cross sections could be measured in the Minerva experiment, especially those for the final production of $\Lambda\pi$. Nevertheless, it is true that compared to $\Delta S = 0$ pion production, the smallness of the cross section makes πY processes challenging to detect. This implies that the feasibility of detecting these channels in experiments is also limited. We have not provided our results for higher antineutrino energies, as our model does not account for processes such as hyperon production associated with a kaon, which begin to have an impact at certain antineutrino energies. The caution here is that we have had to apply the invariant mass cut to ensure the reliability of our primary interaction model.

Next, we have studied the production of Σ and Λ hyperons in nuclei induced by antineutrinos, in the energy region where associated strangeness production

($\Delta S = 0$) and secondary hyperon production induced by $\bar{K}$ nuclear re-scattering are still negligible. Hyperon production in this energy range primarily proceeds through quasielastic scattering, which has been also considered here, where a charged lepton and a hyperon are emitted. In addition, hyperon-pion production reactions had not been studied with nuclear targets to date, whereas quasielastic scattering has been previously explored. Nuclear effects were accounted by using the impulse approximation and a local Fermi gas description of the initial nuclear state. We have compared two versions of the final state interaction (FSI) experienced by hyperons in the nucleus. One uses a simpler approach, while the other accounts for the potential of the hyperons. However, in this thesis, we only consider the potential of the Lambda due to the limited experimental information available about the potential of the Sigma. An attractive nuclear mean field potential for Λ hyperons has been introduced for this. The final state interaction between the produced hyperon and the spectator nucleons was considered by using a Monte Carlo intranuclear cascade.

The predominant process at the range of antineutrino energies considered in this thesis is the quasielastic production. The additional increase due to the mass of the pion in the $Y\pi$ production leads to a higher threshold compared to quasielastic (QE) mechanisms. Nevertheless, these hyperon-pion production processes become relevant compared to YK production at lower energies, and their cross sections exhibit a more rapid growth with antineutrino energy compared to quasielastic scattering. Additionally, the $\Sigma^*(1385)$, which strongly decays into $\Lambda\pi$ and $\Sigma\pi$, is situated near the threshold. In fact, this mechanism is dominant in the $\Lambda\pi$ production channel, which has a lower threshold than the $\Sigma\pi$ one. This threshold effect allows the phase space to have grown for the $\Lambda\pi$ reaction when the $\Sigma\pi$ starts to be feasible. Our investigation reveals that the $Y\pi$ channels play a significant role in characterizing hyperon production within nuclei. Specifically, they contribute significantly to Σ^+ production and generate a substantial portion of the total cross section in other channels. Their relative importance amplifies with increasing energy. Neglecting these mechanisms would introduce biases in experimental analysis and result interpretation. This holds true, for example, in endeavors to constrain nucleon-to-hyperon transition form factors or extract information about hyperon potentials using neutrino scattering. While it is possible to discriminate $Y\pi$ events by detecting emitted pions, this feasibility is limited for a considerable portion of these events due to intranuclear pion absorption and detection thresholds. In this context, we have determined that distributions of lepton-hyperon relative angles serve as useful observables for distinguishing between quasielastic and $Y\pi$ processes. In any case, a thorough consideration of inelastic $Y\pi$ production in event generators used by experiments, such as GENIE or NuWro, is imperative. Additionally, due to hyperon final state interactions, there is an increase in Λ production caused by $\Sigma \to \Lambda$ conversion in both models of FSI. Furthermore, primary produced hyperons lose energy in colliding with nucleons, thereby shifting energy distributions significantly towards lower energies. On the other hand, the lepton-hyperon angular distributions are influenced by the final-state interaction, causing the curves to flatten and populate negative cosine values.

Moreover, final state interactions (FSI) experienced by pions in nuclear targets can effectively distort the final signal, altering the identity of the ultimate pion through mechanisms like charge exchange; however, this could be offset by secondary pions produced from hyperons. A more detailed analysis of the effects of final state interactions on pions has not been the focus of this thesis. We have observed that pion absorption by the nucleus decreases with the increase in antineutrino energy. Pions are long-lived particles and they have a significant probability of being absorbed in the nucleus. We consider it important to take into account the absorption probability in $Y\pi$ processes as it can lead to confusion between inelastic and quasielastic events.

Finally, we have studied Λ production on argon in the conditions of the recent MicroBooNE measurement. This implies folding with the antineutrino flux and imposing the proper acceptance cuts. The relative high detection threshold and small acceptance for low energy Λ's strongly reduces the fraction of events that can be identified and increases the relative importance of inelastic $Y\pi$ with respect to QE ones. In our result for the phase space restricted flux averaged cross section, which is consistent with the low-statistics experimental value, the $\Lambda\pi$ mechanism accounts for one third of the total cross section. Additionally, as the SBND experiment aims to gather more statistics for the production of Λ and Σ^+, we have investigated the production of all four hyperons convoluted with the muonic antineutrino flux provided by the experiment. In this case, we do not impose restrictions on the cross section. However, we can confirm that, since the Σ^+ hyperon cannot be primarily produced through quasielastic production, the $Y\pi$ mechanism must be taken into consideration. It should be included in the neutrino event generators used by experimental setups. To conclude, we posit that our model exhibits potential suitability for integration within Monte Carlo event generators as the primary interaction. This integration would allow for simulating the propagation of the $Y\pi$ pair within the nuclear medium while incorporating pertinent nuclear effects. When considering nuclear targets and comparing between quasielastic and inelastic production, specifically involving the co-production of a hyperon and a pion, our investigation underscores the significance of the $Y\pi$ process. While not the dominant reaction process, it garners increased relevance with the rise of the antineutrino energy. Our comparative analysis with MicroBooNE experimental findings revealed that this process contributes substantially a noteworthy fraction. However, it is pertinent to acknowledge that these experimental determinations were constrained by limited statistical precision. More data on hyperon production from MicroBooNE and SBND are eagerly awaited to learn more about this rare but interesting process.

Appendix A

Conventions

Metric tensor:

The convention followed for the metric tensor is

$$g_{\mu\nu} = g^{\mu\nu} = \begin{pmatrix} 1 & 0 & 0 & 0 \\ 0 & -1 & 0 & 0 \\ 9 & 0 & -1 & 0 \\ 0 & 0 & 0 & -1 \end{pmatrix}. \tag{A.1}$$

And for the Levi-Civita symbol

$$\epsilon^{0123} = +1. \tag{A.2}$$

Dirac and Pauli matrices:

Dirac matrices are denoted by γ^μ, where μ represents the spacetime index. The Dirac matrices in the Dirac-Pauli representation are given by:

$$\gamma^0 = \begin{pmatrix} I & 0 \\ 0 & -I \end{pmatrix}, \quad \gamma^i = \begin{pmatrix} 0 & \sigma^i \\ -\sigma^i & 0 \end{pmatrix}, \quad \gamma^5 = \gamma_5 = \begin{pmatrix} 0 & I \\ I & 0 \end{pmatrix} \tag{A.3}$$

where I is the identity matrix in two dimensions and σ^i are the Pauli matrices:

$$\sigma^1 = \begin{pmatrix} 0 & 1 \\ 1 & 0 \end{pmatrix}, \quad \sigma^2 = \begin{pmatrix} 0 & -i \\ i & 0 \end{pmatrix}, \quad \sigma^3 = \begin{pmatrix} 1 & 0 \\ 0 & -1 \end{pmatrix}. \tag{A.4}$$

From the Dirac matrices we define

$$\sigma^{\mu\nu} = \frac{i}{2}[\gamma^\mu, \gamma^\nu]. \tag{A.5}$$

The Dirac matrices have the following properties:

- Hermiticity:

$$\gamma^{0\dagger} = \gamma^0,\ \gamma^{i\dagger} = -\gamma^i,\ \gamma^{5\dagger} = \gamma^5. \tag{A.6}$$

- Anticommutation relation:

$$\{\gamma^\mu, \gamma^\nu\} = \gamma^\mu\gamma^\nu + \gamma^\nu\gamma^\mu = 2g^{\mu\nu}I, \tag{A.7}$$

where $g^{\mu\nu}$ is the metric tensor.

$$\{\gamma^\mu, \gamma^5\} = 0, \tag{A.8}$$

- Commutation relation:

$$[\gamma^5, \sigma^{\mu\nu}] = 0, \tag{A.9}$$

Gell-Mann matrices:
The Gell-Mann matrices represent the generators of the SU(3) group given by

$$\begin{aligned}
\lambda^1 &= \begin{pmatrix} 0 & 1 & 0 \\ 1 & 0 & 0 \\ 0 & 0 & 0 \end{pmatrix}, \quad \lambda^2 = \begin{pmatrix} 0 & -i & 0 \\ i & 0 & 0 \\ 0 & 0 & 0 \end{pmatrix}, \quad \lambda^3 = \begin{pmatrix} 1 & 0 & 0 \\ 0 & -1 & 0 \\ 0 & 0 & 0 \end{pmatrix} \\
\lambda^4 &= \begin{pmatrix} 0 & 0 & 1 \\ 0 & 0 & 0 \\ 1 & 0 & 0 \end{pmatrix}, \quad \lambda^5 = \begin{pmatrix} 0 & 0 & -i \\ 0 & 0 & 0 \\ i & 0 & 0 \end{pmatrix}, \quad \lambda^6 = \begin{pmatrix} 0 & 0 & 0 \\ 0 & 0 & 1 \\ 0 & 1 & 0 \end{pmatrix} \\
\lambda^7 &= \begin{pmatrix} 0 & 0 & 0 \\ 0 & 0 & -i \\ 0 & i & 0 \end{pmatrix}, \quad \lambda^8 = \frac{1}{\sqrt{3}} \begin{pmatrix} 1 & 0 & 0 \\ 0 & 1 & 0 \\ 0 & 0 & -2 \end{pmatrix}
\end{aligned} \tag{A.10}$$

The Gell-Mann matrices have the following properties:

- Hermiticity:

$$(\lambda^a)^\dagger = \lambda^a. \tag{A.11}$$

- Tracelessness:

$$\mathrm{Tr}(\lambda^a) = 0. \tag{A.12}$$

- Commutation relations:

$$[\lambda^a, \lambda^b] = 2if^{abc}\lambda^c, \tag{A.13}$$

where f^{abc} are the structure constants of the SU(3) group.

Dirac spinor normalization: We use $u_s(\mathbf{p})$ to denote particles with helicity s, momentum p and energy $E = \sqrt{\mathbf{p}^2 + m^2}$ and $v_s(\mathbf{p})$ to denote the antiparticles. The adjoint is given by

$$\bar{u}_s(\mathbf{p}) = u_s(\mathbf{p})^\dagger \gamma^0. \tag{A.14}$$

Our Dirac spinor normalization fulfill the following equations

$$\bar{u}_s(\mathbf{p}) u_r(\mathbf{p}) = 2m\delta_{sr}, \tag{A.15}$$

$$\bar{v}_s(\mathbf{p}) v_r(\mathbf{p}) = -2m\delta_{sr}, \tag{A.16}$$

$$\bar{u}_s(\mathbf{p}) v_r(\mathbf{p}) = \bar{v}_s(\mathbf{p}) u_r(\mathbf{p}) = 0. \tag{A.17}$$

Cabibbo-Kobayashi-Masakawa matrix: The CKM matrix is a unitary matrix in quantum chromodynamics that describes the mixing of different flavor states of quarks in weak decays or transitions, is given by

$$V_{CKM} = \begin{pmatrix} V_{ud} & V_{us} & V_{ub} \\ V_{cd} & V_{cs} & V_{cb} \\ V_{td} & V_{ts} & V_{tb} \end{pmatrix}. \tag{A.18}$$

$$|V_{CKM}| = \begin{pmatrix} 0.97373 \pm 0.00031 & 0.2243 \pm 0.0008 & (3.82 \pm 0.20) \times 10^{-3} \\ 0.221 \pm 0.004 & 0.975 \pm 0.006 & (40.8 \pm 1.4) \times 10^{-3} \\ (8.6 \pm 0.2) \times 10^{-3} & (41.5 \pm 0.9) \times 10^{-3} & 1.014 \pm 0.029 \end{pmatrix}. \tag{A.19}$$

Appendix B

SU(3) relations between the amplitudes

In this appendix, we derive the relations between the amplitudes (currents) for the seven reaction channels on free nucleons discussed in this thesis, using SU(3) group theoretical arguments.

To begin, we need to establish the correspondence between the physical states and the mathematical (or SU(3)) states for the meson and baryon states of the octet prior to applying the Wigner-Eckart theorem. Additionally, we have to identify the irreducible tensor operator belonging to the $\{8\}$ representation of SU(3) group that drives the strangeness-changing weak transition.

As discussed after Eq. 2.52, the strangeness-changing weak charged current (without the V_{us} Cabibbo-Kobayashi-Maskawa matrix element) carries "magnetic" quantum numbers of SU(3) $(I, I_3, Y) = \left(\frac{1}{2}, -\frac{1}{2}, -1\right)$ (I, the isospin; I_3, the third component of the isospin and Y the hypercharge). In other words, it carries the same quantum numbers as the K^- or the Ξ^- particles. At the quark level, this current operator can be expressed as

$$
\begin{aligned}
j^{\mu}_{\Delta S=-1} &= \overline{Q}\gamma^{\mu}(1-\gamma_5)(F_4 - iF_5)Q \\
&= -\sqrt{2}\,\overline{Q}\,K^{\mu\,\{8\}}_{\left(\frac{1}{2},-\frac{1}{2},-1\right)}\,Q,
\end{aligned}
\tag{B.1}
$$

where

$$
Q = (u\ d\ s)^{\mathrm{T}}, \tag{B.2}
$$

$$
K^{\mu\,\{8\}}_{\left(\frac{1}{2},-\frac{1}{2},-1\right)} = -\frac{1}{\sqrt{2}}\gamma^{\mu}(1-\gamma_5)(F_4 - iF_5), \tag{B.3}
$$

with $F_i = \frac{\lambda_i}{2}$ (being λ_i the Gell-Mann matrices (Appendix A)). The current operator $K^{\mu\,\{8\}}_{\left(\frac{1}{2},-\frac{1}{2},-1\right)}$ is an irreducible tensor belonging to the $\{8\}$ representation of the

SU(3) group, carrying the corresponding SU(3) quantum numbers of this representation explicitly written in the subindex. Therefore, to this operator, we can apply the Wigner-Eckart theorem of SU(3) [167]. From this point onward, we work with this operator, assuming that we are no longer dealing with individual quarks, and that the vector and axial-vector Dirac and Lorentz structure can be more complex than simply $\gamma^\mu(1-\gamma_5)$, which is the structure at the quark level only.

For simplicity in notation, we refer to the strangeness-changing current operator simply as

$$j^\mu_{\rm sc} \equiv j^\mu_{\Delta S=-1} = -\sqrt{2}\, K^{\mu\,\{8\}}_{\left(\frac{1}{2},-\frac{1}{2},-1\right)}, \tag{B.4}$$

and we proceed to calculate all the transition matrix elements driven by the above current between initial nucleon states and final $\Sigma\pi$ and $\Lambda\pi$ states. In order to do so, we have to fix the phases between the physical states and the corresponding mathematical states for which the SU(3) Clebsch-Gordan coefficients have been calculated [130, 167] in order to appropriately use the Wigner-Eckart theorem. For the physical states we have in this thesis, the phase fixing conventions for mesons and baryons are as follows:

$$\begin{aligned}
&|p\rangle = \left|\{8\}\,;\frac{1}{2},\frac{1}{2},1\right\rangle && |n\rangle = \left|\{8\}\,;\frac{1}{2},-\frac{1}{2},1\right\rangle \\
&\left|\Sigma^+\right\rangle = -\left|\{8\}\,;1,1,0\right\rangle && \left|\Sigma^0\right\rangle = \left|\{8\}\,;1,0,0\right\rangle \\
&\left|\Sigma^-\right\rangle = \left|\{8\}\,;1,-1,0\right\rangle && |\Lambda\rangle = \left|\{8\}\,;0,0,0\right\rangle \\
&\left|\pi^+\right\rangle = -\left|\{8\}\,;1,1,0\right\rangle && \left|\pi^0\right\rangle = \left|\{8\}\,;1,0,0\right\rangle \\
&\left|\pi^-\right\rangle = \left|\{8\}\,;1,-1,0\right\rangle ,
\end{aligned} \tag{B.5}$$

where the convention here is to label the mathematical states as $|\{\mathbf{N}\}\,;I,I_3,Y\rangle$.

The next step involves calculating the transition matrix elements $\langle Y\pi|\, j^\mu_{\rm sc}\,|N\rangle$. In order to do this, we need to first couple the tensor product of the $\{8\}$ representations for baryons and mesons. It is completely necessary to express the tensor product $|Y\pi\rangle$ in the coupled basis using the Clebsch-Gordan coefficients. These coefficients can be found in Ref. [130], and it is important to pay attention to the signs associated with some physical states of eq. (B.5). To ensure completeness, we provide these expressions below, although they are straightforward.

$$\left|\Lambda\pi^0\right\rangle = \sqrt{\frac{3}{10}}\left|\{27\}\,;1,0,0\right\rangle - \frac{1}{2}\left|\{10\}\,;1,0,0\right\rangle - \frac{1}{2}\left|\{\overline{10}\}\,;1,0,0\right\rangle + \sqrt{\frac{1}{5}}\left|\{8\}\,;1,0,0\right\rangle \tag{B.6}$$

$$\begin{aligned}\left|\Lambda\pi^-\right\rangle &= \sqrt{\frac{3}{10}}\left|\{27\}\,;1,-1,0\right\rangle - \frac{1}{2}\left|\{10\}\,;1,-1,0\right\rangle - \frac{1}{2}\left|\{\overline{10}\}\,;1,-1,0\right\rangle \\ &+ \sqrt{\frac{1}{5}}\left|\{8\}\,;1,-1,0\right\rangle\end{aligned} \tag{B.7}$$

$$\begin{aligned}\left|\Sigma^+\pi^-\right\rangle &= -\sqrt{\frac{1}{6}}\left|\{27\}\,;2,0,0\right\rangle - \sqrt{\frac{1}{12}}\left|\{10\}\,;1,0,0\right\rangle + \sqrt{\frac{1}{12}}\left|\{\overline{10}\}\,;1,0,0\right\rangle - \sqrt{\frac{1}{3}}\left|\{8'\}\,;1,0,0\right\rangle \\ &+ \sqrt{\frac{1}{120}}\left|\{27\}\,;0,0,0\right\rangle + \sqrt{\frac{1}{5}}\left|\{8\}\,;0,0,0\right\rangle - \sqrt{\frac{1}{8}}\left|\{1\}\,;0,0,0\right\rangle\end{aligned} \tag{B.8}$$

$$\begin{aligned}\left|\Sigma^0\pi^0\right\rangle &= \sqrt{\frac{2}{3}}\left|\{27\}\,;2,0,0\right\rangle + \sqrt{\frac{1}{120}}\left|\{27\}\,;0,0,0\right\rangle + \sqrt{\frac{1}{5}}\left|\{8\}\,;0,0,0\right\rangle \\ &- \sqrt{\frac{1}{8}}\left|\{1\}\,;0,0,0\right\rangle\end{aligned} \tag{B.9}$$

$$\begin{aligned}\left|\Sigma^-\pi^+\right\rangle &= -\sqrt{\frac{1}{6}}\left|\{27\}\,;2,0,0\right\rangle + \sqrt{\frac{1}{12}}\left|\{10\}\,;1,0,0\right\rangle - \sqrt{\frac{1}{12}}\left|\{\overline{10}\}\,;1,0,0\right\rangle + \sqrt{\frac{1}{3}}\left|\{8'\}\,;1,0,0\right\rangle \\ &+ \sqrt{\frac{1}{120}}\left|\{27\}\,;0,0,0\right\rangle + \sqrt{\frac{1}{5}}\left|\{8\}\,;0,0,0\right\rangle - \sqrt{\frac{1}{8}}\left|\{1\}\,;0,0,0\right\rangle\end{aligned} \tag{B.10}$$

$$\begin{aligned}\left|\Sigma^0\pi^-\right\rangle &= \sqrt{\frac{1}{2}}\left|\{27\}\,;2,-1,0\right\rangle + \sqrt{\frac{1}{12}}\left|\{10\}\,;1,-1,0\right\rangle - \sqrt{\frac{1}{12}}\left|\{\overline{10}\}\,;1,-1,0\right\rangle \\ &+ \sqrt{\frac{1}{3}}\left|\{8'\}\,;1,-1,0\right\rangle\end{aligned} \tag{B.11}$$

$$\begin{aligned}\left|\Sigma^-\pi^0\right\rangle &= \sqrt{\frac{1}{2}}\left|\{27\}\,;2,-1,0\right\rangle - \sqrt{\frac{1}{12}}\left|\{10\}\,;1,-1,0\right\rangle + \sqrt{\frac{1}{12}}\left|\{\overline{10}\}\,;1,-1,0\right\rangle \\ &- \sqrt{\frac{1}{3}}\left|\{8'\}\,;1,-1,0\right\rangle .\end{aligned} \tag{B.12}$$

Now we calculate the matrix elements $\langle Y\pi|\, j^\mu_{\rm sc}\, |N\rangle$, but this time we express the bras $\langle Y\pi|$ in terms of the coupled basis as given in Eqs. (B.6)-(B.12). After that, we apply the Wigner-Eckart theorem to each matrix element because now we have an irreducible tensor operator between states belonging to irreducible representations of the SU(3) group. For completeness, below we provide the expression of the Wigner-Eckart theorem for SU(3), which can also be found in [167],

$$\begin{aligned}&\langle\{\mu_3\}\,;(\nu_3)|\,T^{\{\mu_2\}}_{(\nu_2)}\,|\{\mu_1\}\,;(\nu_1)\rangle = \\ &\sum_{\gamma}\begin{pmatrix} \{\mu_1\} & \{\mu_2\} & \{\mu_3\}_\gamma \\ (\nu_1) & (\nu_2) & (\nu_3) \end{pmatrix}\langle\{\mu_3\}|\,|T^{\{\mu_2\}}|\,|\{\mu_1\}\rangle_\gamma\,.\end{aligned} \tag{B.13}$$

In the above expression, the indices μ_i refer to the irreducible representations of the SU(3) group, while the indices ν_i collectively refer to the (I, I_3, Y) "magnetic" quantum numbers of the representation μ_i. The factor enclosed in parentheses corresponds to the SU(3) Clebsch-Gordan coefficient. Lastly, the last term in Eq. (B.13) denotes the reduced matrix element, which is completely independent of the "magnetic" quantum numbers. It is worth noting that, in principle, a sum over γ should be performed, which would involve summing over all instances where $\{\mu_3\}$ irreducible representation is contained in the tensor product $\{\mu_1\}\otimes\{\mu_2\}$. However, in our case, there is not such a sum because in the bras of Eq. (B.13) always correspond to a definite $\{\mu_3\}_\gamma$ representation.

Once we have evaluated the $\langle Y\pi|\,j^\mu_{\text{sc}}\,|N\rangle$ matrix elements for all the cases considered in our study, we can write the following 7×6 matrix relating the previous matrix elements with the reduced matrix elements,

$$\begin{pmatrix} j^\mu_{p\to\Lambda\pi^0} \\ j^\mu_{n\to\Lambda\pi^-} \\ j^\mu_{p\to\Sigma^+\pi^-} \\ j^\mu_{p\to\Sigma^0\pi^0} \\ j^\mu_{p\to\Sigma^-\pi^+} \\ j^\mu_{n\to\Sigma^0\pi^-} \\ j^\mu_{n\to\Sigma^-\pi^0} \end{pmatrix} = \begin{pmatrix} \frac{\sqrt{3}}{10} & \frac{1}{\sqrt{48}} & \frac{-1}{\sqrt{48}} & \frac{-\sqrt{3}}{10} & 0 & 0 \\ \frac{\sqrt{3}}{\sqrt{50}} & \frac{1}{\sqrt{24}} & \frac{-1}{\sqrt{24}} & \frac{-\sqrt{3}}{\sqrt{50}} & 0 & 0 \\ \frac{1}{40} & \frac{1}{12} & \frac{1}{12} & \frac{1}{10} & \frac{-1}{6} & \frac{-1}{8} \\ \frac{1}{40} & 0 & 0 & \frac{1}{10} & 0 & \frac{-1}{8} \\ \frac{1}{40} & \frac{-1}{12} & \frac{-1}{12} & \frac{1}{10} & \frac{1}{6} & \frac{-1}{8} \\ 0 & \frac{-1}{\sqrt{72}} & \frac{-1}{\sqrt{72}} & 0 & \frac{1}{\sqrt{18}} & 0 \\ 0 & \frac{1}{\sqrt{72}} & \frac{1}{\sqrt{72}} & 0 & \frac{-1}{\sqrt{18}} & 0 \end{pmatrix} \begin{pmatrix} j^\mu_{\{27\}} \\ j^\mu_{\{10\}} \\ j^\mu_{\{\overline{10}\}} \\ j^\mu_{\{8\}} \\ j^\mu_{\{8'\}} \\ j^\mu_{\{1\}} \end{pmatrix}, \tag{B.14}$$

where $j^\mu_{N\to Y\pi}$ is a shorthand notation for $\langle Y\pi|\,j^\mu_{\text{sc}}\,|N\rangle$, while $j^\mu_{\{\mathbf{N}\}}$ denotes the reduced matrix element $\langle\{\mathbf{N}\}|\,|j^\mu_{\text{sc}}|\,|\{8\}\rangle$. Here, j^μ_{sc} given by Eq. (B.4), and $\{\mathbf{N}\}$ represents any of the irreducible representations of the SU(3) group appearing in the Clebsch-Gordan series of the tensor product of two octets, given in Eq. (2.32).

It is important to note that the coefficient matrix of Eq. (B.14) has more rows than columns, because for these $\Delta S = -1$ weak strangeness-changing transitions there are only 6 independent reduced matrix elements, $j^\mu_{\{\mathbf{N}\}}$. However, not all 6 matrix elements of the left-hand side of Eq. (B.14) can be considered truly independent, because the rank of the coefficient matrix is not 6, it is lower. This is expected because there are additional independent transition matrix elements that can be driven by the weak strangeness-changing operator of Eq. (B.4). Examples of these include, for instance, the $\left\langle N'\bar{K}\right| j^{\mu}_{\rm sc} \left|N\right\rangle$ (studied in Ref. [117]), the $\left\langle \Xi K\right| j^{\mu}_{\rm sc} \left|N\right\rangle$ (studied in Ref. [119]), or the $\left\langle Y\eta\right| j^{\mu}_{\rm sc} \left|N\right\rangle$ matrix elements.

Indeed, the rank of the coefficient matrix of eq. (B.14) is 3. It is easy to realize that the first and second rows of this matrix are proportional to each other. If one multiplies the second row by a factor $\frac{1}{\sqrt{2}}$, one obtains the coefficients of the first row. This indicates that only one of the matrix elements $j^{\mu}_{p\to\Lambda\pi^0}$ or $j^{\mu}_{n\to\Lambda\pi^-}$ can be considered independent. The relation between them is given by

$$\left\langle \Lambda\pi^0\right| j^{\mu}_{\rm sc} \left|p\right\rangle = \frac{1}{\sqrt{2}} \left\langle \Lambda\pi^-\right| j^{\mu}_{\rm sc} \left|n\right\rangle . \tag{B.15}$$

Due to this relation between the amplitudes for $\Lambda\pi$ production, the cross section for $n \to \Lambda\pi^-$ channel is twice as large as that for the $p \to \Lambda\pi^0$ channel, as can be observed in Fig. 4.1.

Another noticeable relation can be observed by examining the last two rows of the matrix of Eq. (B.14). One row is the negative of the other, thus implying that

$$\left\langle \Sigma^0\pi^-\right| j^{\mu}_{\rm sc} \left|n\right\rangle = -\left\langle \Sigma^-\pi^0\right| j^{\mu}_{\rm sc} \left|n\right\rangle . \tag{B.16}$$

This is the reason because of the cross sections for $\Sigma\pi$ production reactions off neutrons are exactly the same, as discussed in the caption of Fig. 4.2, as well as the flux-averaged cross sections shown in the last two rows of table 4.1.

However, we have decided to choose as independent strangeness-changing matrix elements $\left\langle \Lambda\pi^-\right| j^{\mu}_{\rm sc} \left|n\right\rangle$, $\left\langle \Sigma^+\pi^-\right| j^{\mu}_{\rm sc} \left|p\right\rangle$ and $\left\langle \Sigma^-\pi^+\right| j^{\mu}_{\rm sc} \left|p\right\rangle$. This choice is possible because by taking the second, third and fifth rows of the matrix in Eq. (B.14), we can form a 3×6 sub-matrix with at least one 3×3 determinant that is non-zero. In other words, these rows are linearly independent [1]. With this choice, we can express three $j^{\mu}_{\{\mathbf{N}\}}$ reduced matrix elements in terms of the above linearly independent explicit amplitudes and the other three remaining reduced matrix

[1] One could have taken equally other 3 different amplitudes with the same properties of linear independence, but we have decided to make this choice.

elements [2]. The result is,

$$j^{\mu}_{\{8\}} = \frac{5}{6}\left(j^{\mu}_{\{10\}} - j^{\mu}_{\{\overline{10}\}}\right) + j^{\mu}_{\{27\}} - 5\sqrt{\frac{2}{3}}\,j^{\mu}_{n\to\Lambda\pi^-} \tag{B.17}$$

$$j^{\mu}_{\{8'\}} = \frac{1}{2}\left(j^{\mu}_{\{10\}} + j^{\mu}_{\{\overline{10}\}}\right) + 3\left(j^{\mu}_{p\to\Sigma^-\pi^+} - j^{\mu}_{p\to\Sigma^+\pi^-}\right) \tag{B.18}$$

$$j^{\mu}_{\{1\}} = \frac{2}{3}\left(j^{\mu}_{\{10\}} - j^{\mu}_{\{\overline{10}\}}\right) + j^{\mu}_{\{27\}} - 4\sqrt{\frac{2}{3}}\,j^{\mu}_{n\to\Lambda\pi^-} - 4\left(j^{\mu}_{p\to\Sigma^-\pi^+} + j^{\mu}_{p\to\Sigma^+\pi^-}\right). \tag{B.19}$$

Finally, by substituting the expressions for $j^{\mu}_{\{\mathbf{N}\}}$ given in Eqs. (B.17)-(B.19) in the right-hand side of the linear system of Eq. (B.14), and carrying out the matrix multiplication, we obtain Eq. (B.15) for the first row. Additionally, we also obtain the following relationships

$$\left\langle \Sigma^0\pi^0\right| j^{\mu}_{\text{sc}} \left|p\right\rangle = \frac{1}{2}\left(\left\langle \Sigma^+\pi^-\right| j^{\mu}_{\text{sc}} \left|p\right\rangle + \left\langle \Sigma^-\pi^+\right| j^{\mu}_{\text{sc}} \left|p\right\rangle\right) \tag{B.20}$$

$$\left\langle \Sigma^0\pi^-\right| j^{\mu}_{\text{sc}} \left|n\right\rangle = \frac{1}{\sqrt{2}}\left(\left\langle \Sigma^-\pi^+\right| j^{\mu}_{\text{sc}} \left|p\right\rangle - \left\langle \Sigma^+\pi^-\right| j^{\mu}_{\text{sc}} \left|p\right\rangle\right) \tag{B.21}$$

$$\left\langle \Sigma^-\pi^0\right| j^{\mu}_{\text{sc}} \left|n\right\rangle = -\frac{1}{\sqrt{2}}\left(\left\langle \Sigma^-\pi^+\right| j^{\mu}_{\text{sc}} \left|p\right\rangle - \left\langle \Sigma^+\pi^-\right| j^{\mu}_{\text{sc}} \left|p\right\rangle\right) \tag{B.22}$$

for the fourth, sixth and seventh rows of Eq. (B.14), respectively. It is important to note that the relationships given in Eqs. (B.21) and (B.22) are fully consistent with the relation given previously in Eq. (B.16).

Finally, it is important to mention that these relations between the amplitudes are exact in the SU(3) limit, but when one uses the different physical masses of the involved particles, there will be SU(3) or SU(2) breaking effects. Nonetheless, these relations can be used to check that the $\mathcal{A}_i^{N\to Y\pi}$ constants of the tables 2.3 and 2.4 satisfy them. However, one has to be careful when checking these $\mathcal{A}_i^{N\to Y\pi}$ constants in some Born diagrams, where there are additional factors hidden in the standard definitions of the $f_i^{NY}(q^2)$ and $g_1^{NY}(q^2)$ form factors of tables 2.1 and 2.2.

[2]One cannot express the six $j^{\mu}_{\{\mathbf{N}\}}$ reduced matrix elements in terms only of the three explicit linear independent amplitudes, because there are more unknowns than linearly independent equations in the system, i.e, it is an underdetermined linear system.

Appendix C

Kinematics

C.1 Yπ production off free nucleons

One of the assumptions we make when doing the calculations in Sect. 2 is to select the reference frame where the initial nucleon is at rest ($\mathbf{p} = 0,\ p^0 = M$), the LAB frame. Initially, we take the direction of incident antineutrino ($\mathbf{k} = E_{\bar{\nu}}\hat{z}$) as the Z-axis. In this plane, we resolve the δ-function of hyperon 3-momentum, and we can generate the solid angles $d\Omega_{\hat{k}'}$ and $d\Omega_m$. But, to resolve the δ-function of energy conservation we integrate over the polar angle θ_m between $\mathbf{q}$ and $\mathbf{p_m}$ (eq. 2.12). To ease the solution of the δ-function of energy conservation, we need $\mathbf{q}$ to define a new Z'-axis. We achieve this by making a rotation in the scattering plane defined by $\mathbf{k}$ and $\mathbf{k'}$. The azimuthal angle of the pion, $\phi_{\widehat{p}_m}$, is measured in a perpendicular plane to $\mathbf{q}$ and its range is $\phi_{\widehat{p}_m} \in [0, 2\pi[$. This rotation does not change the value of energies or modules of the three-momenta, the initial nucleon is still at rest and $|\mathcal{M}|^2$ is invariant, as long as the scalar products of the particles' four-vectors in this expression are evaluated in the same reference system.

We are going to show how the expressions for 3-momenta would change when we perform a rotation in the scattering plane, around the Y-axis, with an angle α to be determined, to align $\mathbf{q}$ along the Z-axis.

Scattering plane :

- $\mathbf{k} = (0, 0, E_{\bar{\nu}})$
- $\mathbf{k}' = |\mathbf{k}'|\,(\sin\theta_l'\,, 0\,, \cos\theta_l')$
- $\mathbf{p} = (0, 0, 0)$
- $\mathbf{q} = \mathbf{k} - \mathbf{k}' = (-\,|\mathbf{k}'|\sin\theta_l'\,, 0\,, E_{\bar{\nu}} - |\mathbf{k}'|\cos\theta_l')$

We make a rotation $R_Y(\alpha)$ in the scattering plane, around the Y-axis, of angle α (to be determined) to put $\mathbf{q}$ along the Z-axis.

$$\mathbf{q}_{r_1} = R_Y(\alpha)\mathbf{q} = \begin{pmatrix} \cos\alpha & 0 & -\sin\alpha \\ 0 & 1 & 0 \\ \sin\alpha & 0 & \cos\alpha \end{pmatrix} \begin{pmatrix} -|\mathbf{k}'|\sin\theta_l' \\ 0 \\ E_{\bar{\nu}} - |\mathbf{k}'|\cos\theta_l' \end{pmatrix} \tag{C.1}$$

$$\mathbf{q}_{r_1} = \begin{pmatrix} -|\mathbf{k}'|\sin\theta_l' \cos\alpha - \sin\alpha(E_{\bar{\nu}} - |\mathbf{k}'|\cos\theta_l') \\ 0 \\ -|\mathbf{k}'|\sin\theta_l' \sin\alpha + \cos\alpha(E_{\bar{\nu}} - |\mathbf{k}'|\cos\theta_l') \end{pmatrix} = \begin{pmatrix} 0 \\ 0 \\ |\mathbf{q}| \end{pmatrix} \tag{C.2}$$

We impose that $\mathbf{q}_{r_1 x} = 0$,

$$-|\mathbf{k}'|\sin\theta_l'\cos\alpha - \sin\alpha(E_{\bar{\nu}} - |\mathbf{k}'|\cos\theta_l') = 0, \tag{C.3}$$

and then the tangent of the α-angle is

$$\tan\alpha = \frac{-|\mathbf{k}'|\sin\theta_l'}{E_{\bar{\nu}} - |\mathbf{k}'|\cos\theta_l'}, \tag{C.4}$$

the cosine and the sine are

$$\sin\alpha = \frac{-|\mathbf{k}'|\sin\theta_l'}{|\mathbf{q}|} \quad \cos\alpha = \frac{E_{\bar{\nu}} - |\mathbf{k}'|\cos\theta_l'}{|\mathbf{q}|} \tag{C.5}$$

The other 3-momenta are given by

- $\mathbf{k_{r_1}} = \begin{pmatrix} \cos\alpha & 0 & -\sin\alpha \\ 0 & 1 & 0 \\ \sin\alpha & 0 & \cos\alpha \end{pmatrix} \begin{pmatrix} 0 \\ 0 \\ E_{\bar{\nu}} \end{pmatrix} = \frac{E_{\bar{\nu}}}{|\mathbf{q}|} \begin{pmatrix} |\mathbf{k}'|\sin\theta_l' \\ 0 \\ E_{\bar{\nu}} - |\mathbf{k}'|\cos\theta_l' \end{pmatrix}$
- $\mathbf{k}'_{\mathbf{r_1}} = \begin{pmatrix} \cos\alpha & 0 & -\sin\alpha \\ 0 & 1 & 0 \\ \sin\alpha & 0 & \cos\alpha \end{pmatrix} |\mathbf{k}'| \begin{pmatrix} \sin\theta_l' \\ 0 \\ \cos\theta_l' \end{pmatrix} = |\mathbf{k}'| \begin{pmatrix} \sin(\theta_l' - \alpha) \\ 0 \\ \cos(\theta_l' - \alpha) \end{pmatrix}$
- $\mathbf{p_{r_1}} = (0, 0, 0)$
- $\mathbf{p_{m_{r_1}}} = |\mathbf{p_m}| \begin{pmatrix} \sin\theta_m\cos\phi_m \\ \sin\theta_m\sin\phi_m \\ \cos\theta_m \end{pmatrix}$
- $\mathbf{p_{Y_{r_1}}} = \mathbf{q_{r_1}} - \mathbf{p_{m_{r_1}}}$

It can be checked that, after the rotation, there is not any angular dependence on ϕ_l', thus allowing us to fix the angle to $\phi_l' = 0$.

C.2 $Y\pi$ production off nuclei

To describe the kinematics related to the $Y\pi$ production from nuclei, we need to set the frame where the Z-axis is defined by the neutrino momentum, and where the nucleus is at rest. We define the 3-momentum of the final lepton $\mathbf{k}'$ in spherical coordinates concerning the direction defined by $\mathbf{k}$, and the momentum transfer $\mathbf{q} = \mathbf{k} - \mathbf{k}'$.

Scattering plane :

- $\mathbf{k} = (0, 0, E_{\bar{\nu}})$
- $\mathbf{k}' = |\mathbf{k}'|\,(\sin\theta_l'\,, 0\,, \cos\theta_l')$
- $\mathbf{q} = \mathbf{k} - \mathbf{k}' = (-\,|\mathbf{k}'|\sin\theta_l'\,, 0\,, E_{\bar{\nu}} - |\mathbf{k}'|\cos\theta_l')$

where θ_l' is the scattering angle of the final lepton with respect to the incident neutrino direction in such a way that $\mathbf{k}\cdot\mathbf{k}' = E_{\bar{\nu}}\,|\mathbf{k}'|\cos\theta_l'$.

First rotation : In this case, the problem is that the δ-function of energy conservation fixes the cosine of the polar angle between $\mathbf{p}$ and $\mathbf{q}_m$ $(\cos\theta^0_{\widehat{pq}_m})$, being $\mathbf{p}$ the momentum of the nucleon in the local Fermi gas and $\mathbf{q}_m = \mathbf{q} - \mathbf{p}_m$ the difference between the transfer momentum and the momentum of the pion. And we have to integrate over the azimuthal angle of the nucleon momentum. To refer the components of $\mathbf{p}$ in spherical coordinates to the direction defined by $\mathbf{q_m}$, we need to align $\mathbf{q_m}$ along the Z-axis. First, we perform a rotation to bring $\mathbf{q}$ into the form $\mathbf{q_{r_1}} = (0, 0, |\mathbf{q}|)$, or in other words, by a suitable rotation, we can align the vector $\mathbf{q}$ along the Z-axis, denoted as $\mathbf{q_{r_1}}$, introducing an angle (α). This angle depends on the kinematics of $\mathbf{k}$ and $\mathbf{k}'$.

$$\mathbf{q}_{r_1} = R_Y(\alpha)\mathbf{q} = \begin{pmatrix} \cos\alpha & 0 & -\sin\alpha \\ 0 & 1 & 0 \\ \sin\alpha & 0 & \cos\alpha \end{pmatrix} \begin{pmatrix} -\,|\mathbf{k}'|\sin\theta_l' \\ 0 \\ E_{\bar{\nu}} - |\mathbf{k}'|\cos\theta_l' \end{pmatrix} \tag{C.6}$$

$$\mathbf{q}_{r_1} = \begin{pmatrix} -\,|\mathbf{k}'|\sin\theta_l'\,\cos\alpha - \sin\alpha(E_{\bar{\nu}} - |\mathbf{k}'|\cos\theta_l') \\ 0 \\ -\,|\mathbf{k}'|\sin\theta_l'\,\sin\alpha + \cos\alpha(E_{\bar{\nu}} - |\mathbf{k}'|\cos\theta_l') \end{pmatrix} = \begin{pmatrix} 0 \\ 0 \\ |\mathbf{q}| \end{pmatrix} \tag{C.7}$$

By imposing that $\mathbf{q}_{r_1 x} = 0$,

$$-\,|\mathbf{k}'|\sin\theta_l'\cos\alpha - \sin\alpha(E_{\bar{\nu}} - |\mathbf{k}'|\cos\theta_l') = 0, \tag{C.8}$$

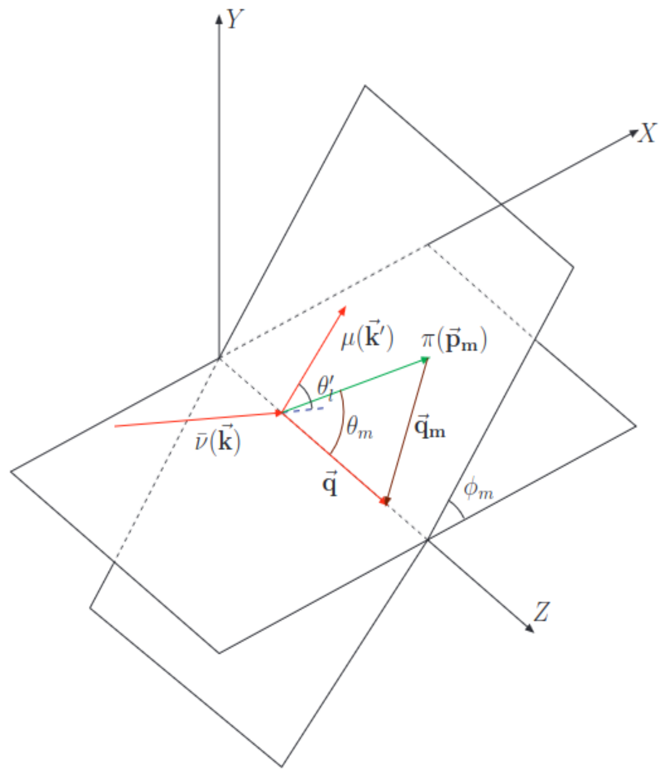

Figure C.1: Kinematic situation after performing the first rotation r_1, and the vector $\mathbf{q}$ (momentum transfer) is pointing along the Z-axis.

we obtain the tangent of the α-angle

$$\tan\alpha = \frac{-|\mathbf{k}'|\sin\theta'_l}{E_{\bar{\nu}} - |\mathbf{k}'|\cos\theta'_l}, \tag{C.9}$$

the cosine and the sine are given by

$$\sin\alpha = \frac{-|\mathbf{k}'|\sin\theta'_l}{|\mathbf{q}|}, \quad \cos\alpha = \frac{E_{\bar{\nu}} - |\mathbf{k}'|\cos\theta'_l}{|\mathbf{q}|}. \tag{C.10}$$

This first rotation is exactly the same as for the kinematics of the $Y\pi$ production from free nucleons. Therefore, in the same way, we obtain the rest of the 3-momenta

- $\mathbf{k_{r_1}} = \begin{pmatrix} \cos\alpha & 0 & -\sin\alpha \\ 0 & 1 & 0 \\ \sin\alpha & 0 & \cos\alpha \end{pmatrix} \begin{pmatrix} 0 \\ 0 \\ E_{\bar{\nu}} \end{pmatrix} = \frac{E_{\bar{\nu}}}{|\mathbf{q}|} \begin{pmatrix} |\mathbf{k}'|\sin\theta'_l \\ 0 \\ E_{\bar{\nu}} - |\mathbf{k}'|\cos\theta'_l \end{pmatrix}$

- $\mathbf{k'_{r_1}} = \begin{pmatrix} \cos\alpha & 0 & -\sin\alpha \\ 0 & 1 & 0 \\ \sin\alpha & 0 & \cos\alpha \end{pmatrix} |\mathbf{k'}| \begin{pmatrix} \sin\theta'_l \\ 0 \\ \cos\theta'_l \end{pmatrix} = |\mathbf{k'}| \begin{pmatrix} \sin(\theta'_l - \alpha) \\ 0 \\ \cos(\theta'_l - \alpha) \end{pmatrix}$

- $\mathbf{p_{m_{r_1}}} = |\mathbf{p_m}| \begin{pmatrix} \sin\theta_m \cos\phi_m \\ \sin\theta_m \sin\phi_m \\ \cos\theta_m \end{pmatrix}$

We define the meson 3-momentum, with its components referred to the frame where $\mathbf{q_{r_1}}$ defines the Z-axis, where θ_m is the angle relative between the transferred momentum and the pion one.

Now we calculate the $\mathbf{q_{m_{r_1}}}$ vector, which is the difference between the transferred momentum $\mathbf{q}$ and the momentum of the pion, with both vectors in the same frame.

- $\mathbf{q_{m_{r_1}}} = \mathbf{q_{r_1}} - \mathbf{p_{m_{r_1}}} = \begin{pmatrix} -|\mathbf{p_m}| \sin\theta_m \cos\phi_m \\ -|\mathbf{p_m}| \sin\theta_m \sin\phi_m \\ |\mathbf{q}| - |\mathbf{p_m}| \cos\theta_m \end{pmatrix}$

Second rotation : Now we want to rotate the vector $\mathbf{q_m}$ in such a way that it lies along the Z-axis. The $\mathbf{q_{m_{r_1}}}$ vector is in the reaction plane, thus we perform a rotation by an angle ϕ around the Z-axis, such that $\mathbf{q_{m_{r_2}}} = R_Z(\phi)\mathbf{q_{m_{r_1}}}$ lies on the "original" scattering plane, i.e., on the XZ plane.

$$\mathbf{q_{m_{r_2}}} = R_Z(\phi)\mathbf{q_{m_{r_1}}} = \begin{pmatrix} \cos\phi & -\sin\phi & 0 \\ \sin\phi & \cos\phi & 0 \\ 0 & 0 & 1 \end{pmatrix} \begin{pmatrix} -|\mathbf{p_m}| \sin\theta_m \cos\phi_m \\ -|\mathbf{p_m}| \sin\theta_m \sin\phi_m \\ |\mathbf{q}| - |\mathbf{p_m}| \cos\theta_m \end{pmatrix} \tag{C.11}$$

$$\mathbf{q_{m_{r_2}}} = \begin{pmatrix} -|\mathbf{p_m}| \sin\theta_m (\cos\phi_m \cos\phi - \sin\phi_m \sin\phi) \\ -|\mathbf{p_m}| \sin\theta_m (\cos\phi_m \sin\phi + \sin\phi_m \cos\phi) \\ |\mathbf{q}| - |\mathbf{p_m}| \cos\theta_m \end{pmatrix} \tag{C.12}$$

When imposing that $\mathbf{q_m}_{r_2 y} = 0$,

$$-|\mathbf{p_m}| \sin\theta_m (\cos\phi_m \sin\phi + \sin\phi_m \cos\phi) = 0, \rightarrow \sin(\phi_m + \phi) = 0, \tag{C.13}$$

we obtain the rotation angle $\phi = -\phi_m$,

$$\mathbf{q_{m_{r_2}}} = \begin{pmatrix} -|\mathbf{p_m}| \sin\theta_m \\ 0 \\ |\mathbf{q}| - |\mathbf{p_m}| \cos\theta_m \end{pmatrix} \tag{C.14}$$

Third rotation : The last rotation we perform is a rotation around the Y-axis by an angle β such that $\mathbf{q_{m_{r_3}}} = R_Y(\beta)\mathbf{q_{m_{r_2}}}$, ensuring that $\mathbf{q_{m_{r_3}}}$ has only a Z-component and is aligned with the Z-axis.

$$\mathbf{q_{m_{r_3}}} = R_Y(\beta)\mathbf{q_{m_{r_2}}} = \begin{pmatrix} \cos\beta & 0 & -\sin\beta \\ 0 & 1 & 0 \\ \sin\beta & 0 & \cos\beta \end{pmatrix} \begin{pmatrix} -\left|\mathbf{p_m}\right|\sin\theta_m \\ 0 \\ \left|\mathbf{q}\right| - \left|\mathbf{p_m}\right|\cos\theta_m \end{pmatrix} \tag{C.15}$$

$$\mathbf{q_{m_{r_3}}} = \begin{pmatrix} -\left|\mathbf{p_m}\right|\sin\theta_m \, \cos\beta - \sin\beta(\left|\mathbf{q}\right| - \left|\mathbf{p_m}\right|\cos\theta_m) \\ 0 \\ -\left|\mathbf{p_m}\right|\sin\theta_m \sin\beta + \cos\beta(\left|\mathbf{q}\right| - \left|\mathbf{p_m}\right|\cos\theta_m) \end{pmatrix} \tag{C.16}$$

We impose that $\mathbf{q_{m_{r_3 x}}} = 0$,

$$-\left|\mathbf{p_m}\right|\sin\theta_m \, \cos\beta - \sin\beta(\left|\mathbf{q}\right| - \left|\mathbf{p_m}\right|\cos\theta_m) = 0, \tag{C.17}$$

we calculate the tangent of β-angle

$$\tan\beta = \frac{-\left|\mathbf{p_m}\right|\sin\theta_m}{\left|\mathbf{q}\right| - \left|\mathbf{p_m}\right|\cos\theta_m}, \tag{C.18}$$

the cosine and the sine

$$\sin\beta = \frac{-\left|\mathbf{p_m}\right|\sin\theta_m}{\left|\mathbf{q_m}\right|}, \quad \cos\beta = \frac{\left|\mathbf{q}\right| - \left|\mathbf{p_m}\right|\cos\theta_m}{\left|\mathbf{q_m}\right|}. \tag{C.19}$$

Now that we have seen the rotations we need to align the vector $\mathbf{q_m}$ with the Z-axis, $\mathbf{q_m} = (0, 0, \left|\mathbf{q_m}\right|)$ where $\left|\mathbf{q_m}\right|^2 = \left|\mathbf{q}\right|^2 + \left|\mathbf{p_m}\right|^2 - 2\left|\mathbf{q}\right|\left|\mathbf{p_m}\right|\cos\theta_m$, we rotate the rest of the 3-momenta, directly carrying out the two consecutive rotations $R_Y(\beta)R_Z(-\phi_m)$.

$$R_{r_1\to r_3} = R_Y(\beta)R_Z(-\phi_m) = \begin{pmatrix} \cos\beta\cos\phi_m & \cos\beta\sin\phi_m & -\sin\beta \\ -\sin\phi_m & \cos\phi_m & 0 \\ \sin\beta\cos\phi_m & \sin\beta\sin\phi_m & \cos\beta \end{pmatrix} \tag{C.20}$$

The 3-momenta, applying the two consecutive rotations $R_{r_1\to r_3}$, are given by

- $\mathbf{k_{r_3}} = E_{\bar\nu} \begin{pmatrix} -\cos\beta\cos\phi_m\sin\alpha - \sin\beta\cos\alpha \\ \sin\phi_m\sin\alpha \\ -\sin\beta\cos\phi_m\sin\alpha + \cos\beta\cos\alpha \end{pmatrix}$

- $\mathbf{k'_{r_3}} = \left|\mathbf{k'}\right| \begin{pmatrix} \cos\beta\cos\phi_m\sin(\theta'_l - \alpha) - \sin\beta\cos(\theta'_l - \alpha) \\ -\sin\phi_m\sin(\theta'_l - \alpha) \\ \sin\beta\cos\phi_m\sin(\theta'_l - \alpha) + \cos\beta\cos(\theta'_l - \alpha) \end{pmatrix}$

- $\mathbf{q_{r_3}} = |\mathbf{q}| \begin{pmatrix} -\sin\beta \\ 0 \\ \cos\beta \end{pmatrix}$

- $\mathbf{p_{m_{r_3}}} = |\mathbf{p_m}| \begin{pmatrix} -\sin(\beta - \theta_m) \\ 0 \\ \cos(\beta - \theta_m) \end{pmatrix}$

In this reference frame where $\mathbf{q_{m_{r_3}}}$ lies along the Z-axis, we can proceed to define the 3-momentum of the nucleon

- $\mathbf{p_{r_3}} = |\mathbf{p}| \begin{pmatrix} \sin\theta^0_{\widehat{pq}_m} \cos\phi_{\widehat{pq}_m} \\ \sin\theta^0_{\widehat{pq}_m} \sin\phi_{\widehat{pq}_m} \\ \cos\theta^0_{\widehat{pq}_m} \end{pmatrix}$

where the cosine of the angle between the nucleon momentum $\mathbf{p}$ and $\mathbf{q_m}$ is given by

$$\cos\theta^0_{\widehat{pq}_m} = \frac{(E(\mathbf{p}) + q^0 - E_m(\mathbf{p_m}))^2 - |\mathbf{p}|^2 - |\mathbf{q_m}|^2 - M_Y^2}{2\,|\mathbf{p}|\,|\mathbf{q_m}|}, \tag{C.21}$$

and it is fixed by the δ-function of energy conservation.

Bibliography

[1] W. Pauli, Phys. Today **31N9**, 27 (1978)

[2] E. Fermi, Z. Phys. **88** (1934), 161-177 doi:10.1007/BF01351864

[3] E. Fermi, Nuovo Cim. **11** (1934), 1-19 doi:10.1007/BF02959820

[4] M. Goeppert-Mayer, Phys. Rev. **48** (1935), 512-516 doi:10.1103/PhysRev.48.512

[5] E. Majorana, Nuovo Cim. **14** (1937), 171-184 doi:10.1007/BF02961314

[6] C. L. Cowan, F. Reines, F. B. Harrison, H. W. Kruse and A. D. McGuire, Science **124** (1956), 103-104 doi:10.1126/science.124.3212.103

[7] B. Pontecorvo, Zh. Eksp. Teor. Fiz. **37** (1959), 1751-1757

[8] R. P. Feynman and M. Gell-Mann, Phys. Rev. **109** (1958), 193-198 doi:10.1103/PhysRev.109.193

[9] G. Danby, J. M. Gaillard, K. A. Goulianos, L. M. Lederman, N. B. Mistry, M. Schwartz and J. Steinberger, Phys. Rev. Lett. **9** (1962), 36-44 doi:10.1103/PhysRevLett.9.36

[10] K. Kodama *et al.* [DONUT], Phys. Lett. B **504** (2001), 218-224 doi:10.1016/S0370-2693(01)00307-0

[11] N. Cabibbo, Phys. Rev. Lett. **10** (1963), 531-533 doi:10.1103/PhysRevLett.10.531

[12] M. Kobayashi and T. Maskawa, Prog. Theor. Phys. **49** (1973), 652-657 doi:10.1143/PTP.49.652

[13] Christian Spiering, The European Physical Journal H **37** (2012), 515-565 doi:10.1140/epjh/e2012-30014-2 [arXiv:1207.4952 [astro-ph.IM]]

[14] R. Davis, Jr., D. S. Harmer and K. C. Hoffman, Phys. Rev. Lett. **20** (1968), 1205-1209 doi:10.1103/PhysRevLett.20.1205

[15] K. Hirata *et al.* [Kamiokande-II], Phys. Rev. Lett. **58** (1987), 1490-1493 doi:10.1103/PhysRevLett.58.1490

[16] Y. Fukuda *et al.* [Super-Kamiokande], Phys. Rev. Lett. **81** (1998), 1562-1567 doi:10.1103/PhysRevLett.81.1562

[17] Q. R. Ahmad *et al.* [SNO], Phys. Rev. Lett. **89** (2002), 011301 doi:10.1103/PhysRevLett.89.011301 [arXiv:nucl-ex/0204008 [nucl-ex]].

[18] K. Eguchi *et al.* [KamLAND], Phys. Rev. Lett. **90** (2003), 021802 doi:10.1103/PhysRevLett.90.021802 [arXiv:hep-ex/0212021 [hep-ex]].

[19] L. Shtembari [GERDA], PoS **ICHEP2022** (2022), 614 doi:10.22323/1.414.0614

[20] A. S. Inácio [SNO+], PoS **PANIC2021** (2022), 274 doi:10.22323/1.380.0274

[21] C. Adams *et al.* [NEXT], [arXiv:2305.09435 [nucl-ex]].

[22] A. K. Soma [nEXO], Springer Proc. Phys. **277** (2022), 531-534 doi:10.1007/978-981-19-2354-8_97

[23] L. Alvarez-Ruso *et al.* [NuSTEC], Prog. Part. Nucl. Phys. **100** (2018), 1-68 doi:10.1016/j.ppnp.2018.01.006

[24] A. de Gouvêa, I. Mocioiu, S. Pastore, L. E. Strigari, L. Alvarez-Ruso, A. M. Ankowski, A. B. Balantekin, V. Brdar, M. Cadeddu and S. Carey, *et al.* [arXiv:2209.07983 [hep-ph]].

[25] P. Taule, M. Escudero and M. Garny, Phys. Rev. D **106** (2022) no.6, 063539 doi:10.1103/PhysRevD.106.063539 [arXiv:2207.04062 [astro-ph.CO]].

[26] B. Batell, J. Berger, V. Brdar, A. D. Bross, J. M. Conrad, P. deNiverville, V. De Romeri, B. Dutta, S. Foroughi-Abari and M. Hostert, *et al.* [arXiv:2207.06898 [hep-ph]].

[27] C. Athanassopoulos *et al.* [LSND], Phys. Rev. C **54** (1996), 2685-2708 doi:10.1103/PhysRevC.54.2685 [arXiv:nucl-ex/9605001 [nucl-ex]].

[28] S. L. Glashow, Nucl. Phys. **22** (1961), 579-588 doi:10.1016/0029-5582(61)90469-2

[29] S. Weinberg, Phys. Rev. Lett. **19** (1967), 1264-1266 doi:10.1103/PhysRevLett.19.1264

[30] A. Salam, Conf. Proc. C **680519** (1968), 367-377 doi:10.1142/9789812795915_0034

[31] M. Goldhaber, L. Grodzins and A. W. Sunyar, Phys. Rev. **109** (1958), 1015-1017 doi:10.1103/PhysRev.109.1015

[32] G. B. Adera and B. I. S. Van der Ventel, Int. J. Mod. Phys. E **20** (2011), 2475 doi:10.1142/S0218301311020460 [arXiv:1112.5567 [nucl-th]].

[33] T. Leitner, O. Buss, L. Alvarez-Ruso and U. Mosel, Phys. Rev. C **79** (2009), 034601 doi:10.1103/PhysRevC.79.034601 [arXiv:0812.0587 [nucl-th]].

[34] A. Meucci, C. Giusti and F. D. Pacati, Nucl. Phys. A **739** (2004), 277-290 doi:10.1016/j.nuclphysa.2004.04.108 [arXiv:nucl-th/0311081 [nucl-th]].

[35] J. E. Amaro, M. B. Barbaro, J. A. Caballero, T. W. Donnelly and C. F. Williamson, Phys. Lett. B **696** (2011), 151-155 doi:10.1016/j.physletb.2010.12.007 [arXiv:1010.1708 [nucl-th]].

[36] J. A. Caballero, J. E. Amaro, M. B. Barbaro, T. W. Donnelly, C. Maieron and J. M. Udias, Phys. Rev. Lett. **95** (2005), 252502 doi:10.1103/PhysRevLett.95.252502 [arXiv:nucl-th/0504040 [nucl-th]].

[37] J. E. Amaro, M. B. Barbaro, J. A. Caballero, T. W. Donnelly and J. M. Udias, Phys. Rev. C **75** (2007), 034613 doi:10.1103/PhysRevC.75.034613 [arXiv:nucl-th/0612056 [nucl-th]].

[38] J. Nieves, J. E. Amaro and M. Valverde, Phys. Rev. C **70** (2004), 055503 [erratum: Phys. Rev. C **72** (2005), 019902] doi:10.1103/PhysRevC.70.055503 [arXiv:nucl-th/0408005 [nucl-th]].

[39] V. Pandey, N. Jachowicz, T. Van Cuyck, J. Ryckebusch and M. Martini, Phys. Rev. C **92** (2015) no.2, 024606 doi:10.1103/PhysRevC.92.024606 [arXiv:1412.4624 [nucl-th]].

[40] E. Hernandez, J. Nieves and M. Valverde, Phys. Rev. D **76**, 033005 (2007) doi:10.1103/PhysRevD.76.033005 [arXiv:hep-ph/0701149 [hep-ph]].

[41] K. Xie, J. Gao, T. J. Hobbs, D. R. Stump and C. P. Yuan, [arXiv:2303.13607 [hep-ph]].

[42] J. L. Hewett, H. Weerts, R. Brock, J. N. Butler, B. C. K. Casey, J. Collar, A. de Gouvea, R. Essig, Y. Grossman and W. Haxton, *et al.* doi:10.2172/1042577 [arXiv:1205.2671 [hep-ex]].

[43] M. C. Gonzalez-Garcia, P. C. de Holanda, C. Pena-Garay and J. W. F. Valle, Nucl. Phys. B **573** (2000), 3-26 doi:10.1016/S0550-3213(99)00709-9 [arXiv:hep-ph/9906469 [hep-ph]].

[44] P. Adamson *et al.* [MINOS+], Phys. Rev. Lett. **125** (2020) no.13, 131802 doi:10.1103/PhysRevLett.125.131802 [arXiv:2006.15208 [hep-ex]].

[45] M. A. Ramírez *et al.* [T2K], [arXiv:2305.09916 [hep-ex]].

[46] D. Grant [IceCube–PINGU], AIP Conf. Proc. **1666** (2015) no.1, 100004 doi:10.1063/1.4915572

[47] V. Carretero [KM3NeT], PoS **ICRC2023** (2023), 996 doi:10.22323/1.444.0996

[48] Z. Xie [Hyper-Kamiokande], PoS **NOW2022** (2023), 024 doi:10.22323/1.421.0024

[49] J. Huang [JUNO], PoS **ICRC2023** (2023), 1120 doi:10.22323/1.444.1120

[50] Z. Chen, [arXiv:2309.05989 [hep-ex]].

[51] H. de Kerret *et al.* [Double Chooz], Nature Phys. **16** (2020) no.5, 558-564 doi:10.1038/s41567-020-0831-y [arXiv:1901.09445 [hep-ex]].

[52] X. Zhang [PROSPECT], Springer Proc. Phys. **213** (2018), 187-191 doi:10.1007/978-981-13-1316-5_35

[53] C. D. Shin *et al.* [RENO], JHEP **04** (2020), 029 doi:10.1007/JHEP04(2020)029 [arXiv:1911.04601 [hep-ex]].

[54] A. A. Aguilar-Arevalo *et al.* [MiniBooNE], Phys. Rev. D **88** (2013) no.3, 032001 doi:10.1103/PhysRevD.88.032001 [arXiv:1301.7067 [hep-ex]].

[55] K. Hiraide *et al.* [SciBooNE], Phys. Rev. D **78** (2008), 112004 doi:10.1103/PhysRevD.78.112004 [arXiv:0811.0369 [hep-ex]].

[56] P. Abratenko *et al.* [MicroBooNE], Phys. Rev. D **102** (2020) no.11, 112013 doi:10.1103/PhysRevD.102.112013 [arXiv:2010.02390 [hep-ex]].

[57] M. A. Acero *et al.* [NOvA], Phys. Rev. D **107** (2023) no.5, 052011 doi:10.1103/PhysRevD.107.052011 [arXiv:2109.12220 [hep-ex]].

[58] G. Yang [DUNE], PoS **NuFact2021** (2022), 003 doi:10.22323/1.402.0003

[59] P. Abratenko *et al.* [MicroBooNE], Phys. Rev. Lett. **130** (2023) no.23, 231802 doi:10.1103/PhysRevLett.130.231802 [arXiv:2212.07888 [hep-ex]].

[60] D. Brailsford [SBND], J. Phys. Conf. Ser. **888** (2017) no.1, 012186 doi:10.1088/1742-6596/888/1/012186

[61] P. A. Machado, O. Palamara and D. W. Schmitz, Ann. Rev. Nucl. Part. Sci. **69** (2019), 363-387 doi:10.1146/annurev-nucl-101917-020949

[62] K. Abe *et al.* [T2K], Nature **580** (2020) no.7803, 339-344 [erratum: Nature **583** (2020) no.7814, E16] doi:10.1038/s41586-020-2177-0 [arXiv:1910.03887 [hep-ex]].

[63] M. Sajjad Athar, A. Fatima and S. K. Singh, [arXiv:2206.13792 [hep-ph]].

[64] L. Alvarez-Ruso *et al.* [GENIE], Eur. Phys. J. ST **230** (2021) no.24, 4449-4467 doi:10.1140/epjs/s11734-021-00295-7 [arXiv:2106.09381 [hep-ph]].

[65] Y. Hayato and L. Pickering, Eur. Phys. J. ST **230** (2021) no.24, 4469-4481 doi:10.1140/epjs/s11734-021-00287-7 [arXiv:2106.15809 [hep-ph]].

[66] D. Zhuridov, J. T. Sobczyk, C. Juszczak and K. Niewczas, J. Phys. G **48** (2021) no.5, 055002 doi:10.1088/1361-6471/abdade [arXiv:2007.14426 [hep-ph]]

[67] J. Isaacson, W. I. Jay, A. Lovato, P. A. N. Machado and N. Rocco, Phys. Rev. D **107** (2023) no.3, 033007 doi:10.1103/PhysRevD.107.033007 [arXiv:2205.06378 [hep-ph]].

[68] G. Battistoni, P. R. Sala, M. Lantz, A. Ferrari and G. Smirnov, Acta Phys. Polon. B **40** (2009), 2491-2505

[69] K. Gallmeister, U. Mosel and J. Weil, Phys. Rev. C **94** (2016) no.3, 035502 doi:10.1103/PhysRevC.94.035502 [arXiv:1605.09391 [nucl-th]].

[70] R. L. Workman *et al.* [Particle Data Group], PTEP **2022** (2022), 083C01 doi:10.1093/ptep/ptac097

[71] Degrange, B., Fontaine, G., & Fleury, P. 2013, Physics Today, 66, 8. doi:10.1063/PT.3.1989

[72] G. D. Rochester and C. C. Butler, Nature **160** (1947), 855-857 doi:10.1038/160855a0

[73] A. J. Seriff, R. B. Leighton, C. Hsiao, E. W. Cowan and C. D. Anderson, Phys. Rev. **78** (1950) no.3, 290 doi:10.1103/PhysRev.78.290

[74] C. F. Powell, Nuovo Cim. **11** (1954) no.2suppl, 165-197 doi:10.1007/BF02781081

[75] T. Eichten, H. Faissner, S. Kabe, W. Krenz, J. Von Krogh, J. Morfin, K. Schultze, J. Lemonne, J. Sacton and W. Van Doninck, *et al.* Phys. Lett. B **40** (1972), 593-596 doi:10.1016/0370-2693(72)90490-X

[76] O. Erriquez, M. T. Fogli Muciaccia, S. Natali, S. Nuzzo, A. Halsteinslid, K. Myklebost, A. Rognebakke, O. Skjeggestad, S. Bonetti and D. Cavalli, *et al.* Phys. Lett. B **70** (1977), 383-386 doi:10.1016/0370-2693(77)90683-9

[77] O. Erriquez, M. T. Fogli-Muciaccia, S. Natali, S. Nuzzo, A. Halsteinslid, C. Jarlskog, K. Myklebost, A. Rognebakke, O. Skjeggestad and B. Tvedt, *et al.* Nucl. Phys. B **140** (1978), 123-140 doi:10.1016/0550-3213(78)90316-4

[78] S. J. Barish, M. Derrick, L. G. Hyman, P. Schreiner, R. Singer, R. P. Smith, H. Yuta, V. E. Barnes, D. D. Carmony and A. F. Garfinkel, *et al.* Phys. Rev. Lett. **33** (1974), 1446 doi:10.1103/PhysRevLett.33.1446

[79] G. Fanourakis, L. K. Resvanis, G. Grammatikakis, P. Tsilimigras, A. Vayaki, U. Camerini, W. F. Fry, R. J. Loveless, J. H. Mapp and D. D. Reeder, Phys. Rev. D **21** (1980), 562 doi:10.1103/PhysRevD.21.562

[80] N. J. Baker, P. L. Connolly, S. A. Kahn, H. G. Kirk, M. J. Murtagh, R. B. Palmer, N. P. Samios and M. Tanaka, Phys. Rev. D **24** (1981), 2779-2786 doi:10.1103/PhysRevD.24.2779

[81] D. Son, G. A. Snow, S. Chang, S. Kunori, P. H. Steinberg, D. Zieminska, R. A. Burnstein, J. Hanlon, H. A. Rubin and R. Engelmann, *et al.* Phys. Rev. D **28** (1983), 2129 doi:10.1103/PhysRevD.28.2129

[82] V. V. Ammosov, V. A. Gapienko, G. S. Gapienko, A. G. Denisov, V. I. Klyukhin, V. I. Koreshev, P. V. Pitukhin, V. I. Sirotenko,

Z. U. Usubov and V. G. Zaets, *et al.* Z. Phys. C **36** (1987), 377-381 doi:10.1007/BF01573931

[83] J. Brunner *et al.* [SKAT], Z. Phys. C **45** (1990), 551 doi:10.1007/BF01556267

[84] M. Rafi Alam, M. Sajjad Athar, S. Chauhan and S. K. Singh, Int. J. Mod. Phys. E **25**, no.02, 1650010 (2016) doi:10.1142/S0218301316500105 [arXiv:1509.08622 [hep-ph]].

[85] S. K. Singh and M. J. Vicente Vacas, Phys. Rev. D **74**, 053009 (2006) doi:10.1103/PhysRevD.74.053009 [arXiv:hep-ph/0606235 [hep-ph]].

[86] F. Akbar, M. Sajjad Athar, A. Fatima and S. K. Singh, Eur. Phys. J. A **53**, no.7, 154 (2017) doi:10.1140/epja/i2017-12340-4 [arXiv:1704.04580 [hep-ph]].

[87] J. E. Sobczyk, N. Rocco, A. Lovato and J. Nieves, Phys. Rev. C **99** (2019) no.6, 065503 doi:10.1103/PhysRevC.99.065503 [arXiv:1901.10192 [nucl-th]].

[88] C. Thorpe, J. Nowak, K. Niewczas, J. T. Sobczyk and C. Juszczak, Phys. Rev. C **104** (2021) no.3, 035502 doi:10.1103/PhysRevC.104.035502 [arXiv:2010.12361 [hep-ph]].

[89] P. Dennery, Phys. Rev. **127**, 664-670 (1962) doi:10.1103/PhysRev.127.664

[90] E. Hernández, J. Nieves and M. J. Vicente Vacas, Phys. Rev. D **87**, no.11, 113009 (2013) doi:10.1103/PhysRevD.87.113009 [arXiv:1304.1320 [hep-ph]].

[91] L. Alvarez-Ruso, S. K. Singh and M. J. Vicente Vacas, Phys. Rev. C **59**, 3386-3392 (1999) doi:10.1103/PhysRevC.59.3386 [arXiv:nucl-th/9804007 [nucl-th]].

[92] I. Budagov, D. C. Cundy, C. Franzinetti, W. B. Fretter, H. W. K. Hopkins, C. Manfredotti, G. Myatt, F. A. Nezrick, M. Nikolic and T. B. Novey, *et al.* Phys. Lett. B **29**, 524-528 (1969) doi:10.1016/0370-2693(69)90041-0

[93] W. Krenz *et al.* [Gargamelle Neutrino Propane and Aachen-Brussels-CERN-Ecole Poly-Orsay-Padua], Nucl. Phys. B **135**, 45-65 (1978) doi:10.1016/0550-3213(78)90213-4

[94] D. Coplowe *et al.* [MINERvA], Phys. Rev. D **102**, no.7, 072007 (2020) doi:10.1103/PhysRevD.102.072007 [arXiv:2002.05812 [hep-ex]].

[95] A. A. Aguilar-Arevalo *et al.* [MiniBooNE], Phys. Rev. D **83**, 052007 (2011) doi:10.1103/PhysRevD.83.052007 [arXiv:1011.3572 [hep-ex]].

[96] B. Eberly *et al.* [MINERvA], Phys. Rev. D **92** (2015) no.9, 092008 doi:10.1103/PhysRevD.92.092008 [arXiv:1406.6415 [hep-ex]].

[97] A. Rodriguez *et al.* [K2K], Phys. Rev. D **78**, 032003 (2008) doi:10.1103/PhysRevD.78.032003 [arXiv:0805.0186 [hep-ex]].

[98] M. Benitez Galan, M. R. Alam and I. Ruiz Simo, Phys. Rev. D **104** (2021) no.7, 073005 doi:10.1103/PhysRevD.104.073005 [arXiv:2108.06393 [hep-ph]].

[99] M. B. Galan, L. Alvarez-Ruso, M. Rafi Alam, I. Ruiz Simo and M. J. Vicente Vacas, Phys. Rev. D **109** (2024) no.3, 033001 doi:10.1103/PhysRevD.109.033001 [arXiv:2305.17004 [hep-ph]].

[100] X. L. Ren, E. Oset, L. Alvarez-Ruso and M. J. Vicente Vacas, Phys. Rev. C **91**, no.4, 045201 (2015) doi:10.1103/PhysRevC.91.045201 [arXiv:1501.04073 [hep-ph]].

[101] J. J. Wu and B. S. Zou, Few Body Syst. **56**, no.4-5, 165-183 (2015) doi:10.1007/s00601-015-0973-0 [arXiv:1307.0574 [hep-ph]].

[102] J. Finjord and F. Ravndal, Nucl. Phys. B **106**, 228-236 (1976) doi:10.1016/0550-3213(76)90379-5

[103] H. K. Dewan, Phys. Rev. D **24**, 2369-2378 (1981) doi:10.1103/PhysRevD.24.2369

[104] R. P. Feynman, M. Kislinger and F. Ravndal, Phys. Rev. D **3**, 2706-2732 (1971) doi:10.1103/PhysRevD.3.2706

[105] N. Cabibbo and F. Chilton, Phys. Rev. **137** (1965), B1628-B1634 doi:10.1103/PhysRev.137.B1628

[106] N. Cabibbo, E. C. Swallow and R. Winston, Ann. Rev. Nucl. Part. Sci. **53**, 39-75 (2003) doi:10.1146/annurev.nucl.53.013103.155258 [arXiv:hep-ph/0307298 [hep-ph]].

[107] S. J. Barish, Y. Cho, M. Derrick, T. Dombeck, L. G. Hyman, B. Musgrave, P. Schreiner, R. Singer, R. P. Smith and D. Swanson, *et al.* Phys. Rev. Lett. **36**, 179 (1976) doi:10.1103/PhysRevLett.36.179

[108] J. A. Formaggio and G. P. Zeller, Rev. Mod. Phys. **84** (2012), 1307-1341 doi:10.1103/RevModPhys.84.1307 [arXiv:1305.7513 [hep-ex]].

[109] L. Alvarez-Ruso *et al.* [NuSTEC], Prog. Part. Nucl. Phys. **100**, 1-68 (2018) doi:10.1016/j.ppnp.2018.01.006 [arXiv:1706.03621 [hep-ph]].

[110] L. Alvarez-Ruso, Y. Hayato and J. Nieves, New J. Phys. **16**, 075015 (2014) doi:10.1088/1367-2630/16/7/075015 [arXiv:1403.2673 [hep-ph]].

[111] T. Katori and M. Martini, J. Phys. G **45**, no.1, 013001 (2018) doi:10.1088/1361-6471/aa8bf7 [arXiv:1611.07770 [hep-ph]].

[112] U. Mosel, Ann. Rev. Nucl. Part. Sci. **66**, 171-195 (2016) doi:10.1146/annurev-nucl-102115-044720 [arXiv:1602.00696 [nucl-th]].

[113] U. Mosel, J. Phys. G **46**, no.11, 113001 (2019) doi:10.1088/1361-6471/ab3830 [arXiv:1904.11506 [hep-ex]].

[114] M. Gell-Mann and M. Levy, Nuovo Cim. **16** (1960), 705 doi:10.1007/BF02859738

[115] J. W. Cronin, Conf. Proc. C **680828** (1968), 281-303

[116] M. Rafi Alam, I. Ruiz Simo, M. Sajjad Athar and M. J. Vicente Vacas, Phys. Rev. D **82**, 033001 (2010) doi:10.1103/PhysRevD.82.033001 [arXiv:1004.5484 [hep-ph]].

[117] M. R. Alam, I. R. Simo, M. S. Athar and M. J. Vicente Vacas, Phys. Rev. D **85**, 013014 (2012) doi:10.1103/PhysRevD.85.013014 [arXiv:1111.0863 [hep-ph]].

[118] M. Rafi Alam, I. Ruiz Simo, M. Sajjad Athar and M. J. Vicente Vacas, Phys. Rev. D **87**, 053008 (2013) doi:10.1103/PhysRevD.87.053008 [arXiv:1211.4947 [hep-ph]].

[119] M. Rafi Alam and I. Ruiz Simo, Phys. Rev. D **100**, no.3, 033001 (2019) doi:10.1103/PhysRevD.100.033001 [arXiv:1906.07049 [hep-ph]].

[120] S. Scherer and M. R. Schindler, Lect. Notes Phys. **830**, pp.1-338 (2012) doi:10.1007/978-3-642-19254-8

[121] R. L. Workman *et al.* [Particle Data Group], PTEP **2022** (2022), 083C01 doi:10.1093/ptep/ptac097

[122] V. Shtabovenko, R. Mertig and F. Orellana, Comput. Phys. Commun. **256**, 107478 (2020) doi:10.1016/j.cpc.2020.107478 [arXiv:2001.04407 [hep-ph]].

[123] V. Shtabovenko, R. Mertig and F. Orellana, Comput. Phys. Commun. **207**, 432-444 (2016) doi:10.1016/j.cpc.2016.06.008 [arXiv:1601.01167 [hep-ph]].

[124] R. Mertig, M. Bohm and A. Denner, Comput. Phys. Commun. **64**, 345-359 (1991) doi:10.1016/0010-4655(91)90130-D

[125] J. M. Gaillard and G. Sauvage, Ann. Rev. Nucl. Part. Sci. **34** (1984), 351-402 doi:10.1146/annurev.ns.34.120184.002031

[126] J. D. Bjorken and S. D. Drell, "Relativistic quantum fields," International Series in Pure and Applied Physics. McGraw-Hill Book Company, New York-St.Louis-San Francisco-Toronto-London-Sydney (ISBN-10: 0-07-005494-0)

[127] S. S. Gershtein and Y. B. Zeldovich, Zh. Eksp. Teor. Fiz. **29** (1955), 698-699

[128] S. Weinberg, Phys. Rev. **112**, 1375-1379 (1958) doi:10.1103/PhysRev.112.1375

[129] M. S. Athar and S. K. Singh, Cambridge University Press, 2020, ISBN 978-1-108-77383-6, 978-1-108-48906-5 doi:10.1017/9781108489065

[130] P. S. J. McNamee and F. Chilton, Rev. Mod. Phys. **36**, 1005-1024 (1964) doi:10.1103/RevModPhys.36.1005

[131] S. Galster, H. Klein, J. Moritz, K. H. Schmidt, D. Wegener and J. Bleckwenn, Nucl. Phys. B **32**, 221-237 (1971) doi:10.1016/0550-3213(71)90068-X

[132] A. Fatima, M. Sajjad Athar and S. K. Singh, Phys. Rev. D **98**, no.3, 033005 (2018) doi:10.1103/PhysRevD.98.033005 [arXiv:1806.08597 [hep-ph]].

[133] A. Fatima, M. S. Athar and S. K. Singh, Front. in Phys. **7**, 13 (2019) doi:10.3389/fphy.2019.00013 [arXiv:1807.08314 [hep-ph]].

[134] Y. Nambu, Phys. Rev. Lett. **4**, 380-382 (1960) doi:10.1103/PhysRevLett.4.380

[135] M. N. Butler, M. J. Savage and R. P. Springer, Nucl. Phys. B **399**, 69-88 (1993) doi:10.1016/0550-3213(93)90617-X [arXiv:hep-ph/9211247 [hep-ph]].

[136] M. Doring, E. Oset and S. Sarkar, Phys. Rev. C **74**, 065204 (2006) doi:10.1103/PhysRevC.74.065204 [arXiv:nucl-th/0601027 [nucl-th]].

[137] G. M. Radecky, V. E. Barnes, D. D. Carmony, A. F. Garfinkel, M. Derrick, E. Fernandez, L. Hyman, G. Levman, D. Koetke and B. Musgrave, *et al.* Phys. Rev. D **25**, 1161-1173 (1982) [erratum: Phys. Rev. D **26**, 3297 (1982)] doi:10.1103/PhysRevD.25.1161

[138] T. Kitagaki, H. Yuta, S. Tanaka, A. Yamaguchi, K. Abe, K. Hasegawa, K. Tamai, S. Kunori, Y. Otani and H. Hayano, *et al.* Phys. Rev. D **34**, 2554-2565 (1986) doi:10.1103/PhysRevD.34.2554

[139] H. De Vries, C. W. De Jager and C. De Vries, Atom. Data Nucl. Data Tabl. **36** (1987), 495-536 doi:10.1016/0092-640X(87)90013-1

[140] I. Vidana, A. Polls, A. Ramos and M. Hjorth-Jensen, Nucl. Phys. A **644** (1998), 201-220 doi:10.1016/S0375-9474(98)00599-5

[141] J. L. Rodríguez-Sánchez, J. C. David, J. Hirtz, J. Cugnon and S. Leray, Phys. Rev. C **98** (2018) no.2, 021602 doi:10.1103/PhysRevC.98.021602

[142] T. Harada and Y. Hirabayashi, Nucl. Phys. A **759** (2005), 143-169 doi:10.1016/j.nuclphysa.2005.04.025

[143] P. K. Saha, H. Noumi, D. Abe, S. Ajimura, K. Aoki, H. C. Bhang, K. Dobashi, T. Endo, Y. Fujii and T. Fukuda, *et al.* Phys. Rev. C **70** (2004), 044613 doi:10.1103/PhysRevC.70.044613 [arXiv:nucl-ex/0405031 [nucl-ex]].

[144] J. Rowley *et al.* [CLAS], Phys. Rev. Lett. **127** (2021) no.27, 272303 doi:10.1103/PhysRevLett.127.272303

[145] T. Nanamura *et al.* [J-PARC E40], PTEP **2022** (2022) no.9, 093D01 doi:10.1093/ptep/ptac101

[146] K. Miwa *et al.* [J-PARC E40], Phys. Rev. C **104** (2021) no.4, 045204 doi:10.1103/PhysRevC.104.045204

[147] K. Miwa *et al.* [J-PARC E40], Phys. Rev. Lett. **128** (2022) no.7, 072501 doi:10.1103/PhysRevLett.128.072501

[148] G. Alexander, U. Karshon, A. Shapira, G. Yekutieli, R. Engelmann, H. Filthuth and W. Lughofer, Phys. Rev. **173** (1968), 1452-1460 doi:10.1103/PhysRev.173.1452

[149] B. Sechi-Zorn, B. Kehoe, J. Twitty and R. A. Burnstein, Phys. Rev. **175** (1968), 1735-1740 doi:10.1103/PhysRev.175.1735

[150] J. M. Hauptman, J. A. Kadyk and G. H. Trilling, Nucl. Phys. B **125** (1977), 29-51 doi:10.1016/0550-3213(77)90222-X

[151] F. Eisele, H. Filthuth, W. Foehlisch, V. Hepp and G. Zech, Phys. Lett. B **37** (1971), 204-206 doi:10.1016/0370-2693(71)90053-0

[152] G. R. Charlton, J. Badier, E. Barrelet, I. Makarovisch, J. Pernegr, J. R. Hubbard, A. Leveque, C. Louedec, L. Moscoso and D. Revel, Phys. Lett. B **32** (1970), 720-722 doi:10.1016/0370-2693(70)90454-5

[153] R. Engelmann, H. Filthuth, V. Hepp, E. Kluge, Phys. Lett. **21**, 5, (1966) 587-589, doi:10.1016/0031-9163(66)91310-2

[154] E. Oset and M. J. Vicente-Vacas, Nucl. Phys. A **454** (1986), 637-652 doi:10.1016/0375-9474(86)90110-7

[155] S. K. Singh, M. Sajjad Athar and S. Ahmad, Phys. Rev. Lett. **96** (2006), 241801 doi:10.1103/PhysRevLett.96.241801 [arXiv:nucl-th/0601045 [nucl-th]].

[156] X. Zhang and B. D. Serot, Phys. Rev. C **86** (2012), 035504 doi:10.1103/PhysRevC.86.035504 [arXiv:1208.1553 [nucl-th]].

[157] E. Oset and L. L. Salcedo, Nucl. Phys. A **468** (1987), 631-652 doi:10.1016/0375-9474(87)90185-0

[158] L. L. Salcedo, E. Oset, M. J. Vicente-Vacas and C. Garcia-Recio, Nucl. Phys. A **484** (1988), 557-592 doi:10.1016/0375-9474(88)90310-7

[159] A. A. Aguilar-Arevalo *et al.* [MiniBooNE], Phys. Rev. D **88** (2013) no.3, 032001 doi:10.1103/PhysRevD.88.032001 [arXiv:1301.7067 [hep-ex]].

[160] K. Hiraide *et al.* [SciBooNE], Phys. Rev. D **78** (2008), 112004 doi:10.1103/PhysRevD.78.112004 [arXiv:0811.0369 [hep-ex]].

[161] K. Abe *et al.* [T2K], Phys. Rev. D **87** (2013) no.1, 012001 doi:10.1103/PhysRevD.87.012001 [arXiv:1211.0469 [hep-ex]].

[162] K. Abe *et al.* [T2K], Phys. Rev. D **91** (2015) no.7, 072010 doi:10.1103/PhysRevD.91.072010 [arXiv:1502.01550 [hep-ex]].

[163] L. Aliaga *et al.* [MINERvA], Phys. Rev. D **94** (2016) no.9, 092005 doi:10.1103/PhysRevD.94.092005 [arXiv:1607.00704 [hep-ex]].

[164] C. Andreopoulos, A. Bell, D. Bhattacharya, F. Cavanna, J. Dobson, S. Dytman, H. Gallagher, P. Guzowski, R. Hatcher and P. Kehayias, *et al.* Nucl. Instrum. Meth. A **614** (2010), 87-104 doi:10.1016/j.nima.2009.12.009 [arXiv:0905.2517 [hep-ph]

[165] V. Hewes *et al.* [DUNE], Instruments **5** (2021) no.4, 31 doi:10.3390/instruments5040031 [arXiv:2103.13910 [physics.ins-det]].

[166] A. Abed Abud *et al.* [DUNE], [arXiv:2203.06281 [hep-ex]].

[167] J. J. de Swart, Rev. Mod. Phys. **35** (1963), 916-939 [erratum: Rev. Mod. Phys. **37** (1965), 326-326] doi:10.1103/RevModPhys.35.916

[168] P. A. Zyla *et al.* [Particle Data Group], PTEP **2020** (2020) no.8, 083C01 doi:10.1093/ptep/ptaa104

[169] D. Drakoulakos *et al.* [MINERvA], [arXiv:hep-ex/0405002 [hep-ex]].

[170] K. Abe *et al.* [T2K], Nucl. Instrum. Meth. A **659**, 106-135 (2011) doi:10.1016/j.nima.2011.06.067 [arXiv:1106.1238 [physics.ins-det]].

[171] H. Chen *et al.* [MicroBooNE], FERMILAB-PROPOSAL-0974.

[172] K. Abe *et al.* [Hyper-Kamiokande Proto-], PTEP **2015**, 053C02 (2015) doi:10.1093/ptep/ptv061 [arXiv:1502.05199 [hep-ex]].

[173] R. Acciarri *et al.* [DUNE], [arXiv:1601.05471 [physics.ins-det]].

[174] R. Acciarri *et al.* [DUNE], [arXiv:1512.06148 [physics.ins-det]].

[175] D. Rein and L. M. Sehgal, Annals Phys. **133**, 79-153 (1981) doi:10.1016/0003-4916(81)90242-6

[176] C. Wilkinson, P. Rodrigues, S. Cartwright, L. Thompson and K. McFarland, Phys. Rev. D **90**, no.11, 112017 (2014) doi:10.1103/PhysRevD.90.112017 [arXiv:1411.4482 [hep-ex]].

[177] E. A. Paschos, L. Pasquali and J. Y. Yu, Nucl. Phys. B **588**, 263-280 (2000) doi:10.1016/S0550-3213(00)00486-7 [arXiv:hep-ph/0005255 [hep-ph]].

[178] O. Lalakulich, T. Leitner, O. Buss and U. Mosel, Phys. Rev. D **82**, 093001 (2010) doi:10.1103/PhysRevD.82.093001 [arXiv:1007.0925 [hep-ph]].

[179] K. S. Kuzmin, V. V. Lyubushkin and V. A. Naumov, Acta Phys. Polon. B **37**, 2337-2348 (2006) [arXiv:hep-ph/0606184 [hep-ph]].

[180] J. J. Wu, T. Sato and T. S. H. Lee, Phys. Rev. C **91**, no.3, 035203 (2015) doi:10.1103/PhysRevC.91.035203 [arXiv:1412.2415 [nucl-th]].

[181] T. Leitner, O. Buss, U. Mosel and L. Alvarez-Ruso, Phys. Rev. C **79**, 038501 (2009) doi:10.1103/PhysRevC.79.038501 [arXiv:0812.1787 [nucl-th]].

[182] M. Kabirnezhad, Phys. Rev. D **97**, no.1, 013002 (2018) doi:10.1103/PhysRevD.97.013002 [arXiv:1711.02403 [hep-ph]].

[183] U. Mosel and K. Gallmeister, Phys. Rev. C **96**, no.1, 015503 (2017) doi:10.1103/PhysRevC.96.015503 [arXiv:1708.04528 [nucl-th]].

[184] M. V. Ivanov, J. M. Udias, A. N. Antonov, J. A. Caballero, M. B. Barbaro and E. M. de Guerra, Phys. Lett. B **711**, 178-183 (2012) doi:10.1016/j.physletb.2012.03.072 [arXiv:1203.5970 [nucl-th]].

[185] A. Nikolakopoulos, R. González-Jiménez, K. Niewczas, J. Sobczyk and N. Jachowicz, Phys. Rev. D **97**, no.9, 093008 (2018) doi:10.1103/PhysRevD.97.093008 [arXiv:1803.03163 [nucl-th]].

[186] C. Barbero, G. López Castro and A. Mariano, Phys. Lett. B **728**, 282-287 (2014) doi:10.1016/j.physletb.2013.12.006 [arXiv:1311.3542 [nucl-th]].

[187] M. Martini, M. Ericson, G. Chanfray and J. Marteau, Phys. Rev. C **80**, 065501 (2009) doi:10.1103/PhysRevC.80.065501 [arXiv:0910.2622 [nucl-th]].

[188] J. E. Sobczyk, E. Hernández, S. X. Nakamura, J. Nieves and T. Sato, Phys. Rev. D **98**, no.7, 073001 (2018) doi:10.1103/PhysRevD.98.073001 [arXiv:1807.11281 [hep-ph]].

[189] D. L. Yao, L. Alvarez-Ruso, A. N. Hiller Blin and M. J. Vicente Vacas, Phys. Rev. D **98**, no.7, 076004 (2018) doi:10.1103/PhysRevD.98.076004 [arXiv:1806.09364 [hep-ph]].

[190] D. L. Yao, L. Alvarez-Ruso and M. J. Vicente Vacas, Phys. Lett. B **794**, 109-113 (2019) doi:10.1016/j.physletb.2019.05.036 [arXiv:1901.00773 [hep-ph]].

[191] S. Ahmad, M. Sajjad Athar and S. K. Singh, Phys. Rev. D **74**, 073008 (2006) doi:10.1103/PhysRevD.74.073008 [arXiv:nucl-th/0607069 [nucl-th]].

[192] R. González-Jiménez, N. Jachowicz, K. Niewczas, J. Nys, V. Pandey, T. Van Cuyck and N. Van Dessel, Phys. Rev. D **95**, no.11, 113007 (2017) doi:10.1103/PhysRevD.95.113007 [arXiv:1612.05511 [nucl-th]].

[193] O. Lalakulich and E. A. Paschos, Phys. Rev. D **71**, 074003 (2005) doi:10.1103/PhysRevD.71.074003 [arXiv:hep-ph/0501109 [hep-ph]].

[194] O. Lalakulich, E. A. Paschos and G. Piranishvili, Phys. Rev. D **74**, 014009 (2006) doi:10.1103/PhysRevD.74.014009 [arXiv:hep-ph/0602210 [hep-ph]].

[195] S. S. Gershtein, Y. Y. Komachenko and M. Y. Khlopov, Sov. J. Nucl. Phys. **32** (1980), 861 IFVE-80-63.

[196] W. Y. Lee, E. Maddry, P. Sokolsky, L. Teig, A. Bross, T. Chapin, L. Holloway, L. Nodulman, T. O'Halloran and C. Y. Pang, *et al.* Phys. Rev. Lett. **38**, 202 (1977) doi:10.1103/PhysRevLett.38.202

[197] H. J. Grabosch *et al.* [SKAT], Z. Phys. C **41**, 527 (1989) doi:10.1007/BF01564697

[198] C. L. McGivern *et al.* [MINERvA], Phys. Rev. D **94**, no.5, 052005 (2016) doi:10.1103/PhysRevD.94.052005 [arXiv:1606.07127 [hep-ex]].

[199] Y. Kurimoto *et al.* [SciBooNE], Phys. Rev. D **81**, 033004 (2010) doi:10.1103/PhysRevD.81.033004 [arXiv:0910.5768 [hep-ex]].

[200] O. Erriquez, M. T. Fogli-Muciaccia, S. Natali, S. Nuzzo, A. Halsteinslid, K. Myklebost, A. Rognebakke, O. Skjeggestad, S. Bonetti and D. Cavalli, *et al.* Phys. Lett. B **73**, 350-354 (1978) doi:10.1016/0370-2693(78)90532-4

[201] K. Abe *et al.* [T2K], Phys. Rev. D **95**, no.1, 012010 (2017) doi:10.1103/PhysRevD.95.012010 [arXiv:1605.07964 [hep-ex]].

[202] T. Bolognese, J. P. Engel, J. L. Guyonnet and J. L. Riester, Phys. Lett. B **81**, 393-396 (1979) doi:10.1016/0370-2693(79)90361-7

[203] M. Derrick, E. Fernandez, L. Hyman, G. Levman, D. Koetke, B. Musgrave, P. Schreiner, R. Singer, A. Snyder and S. Toaff, *et al.* Phys. Rev. D **23**, 569 (1981) doi:10.1103/PhysRevD.23.569

[204] N. J. Baker, A. M. Cnops, P. L. Connolly, S. A. Kahn, M. J. Murtagh, R. B. Palmer, N. P. Samios and M. Tanaka, Phys. Rev. D **23**, 2495-2498 (19) doi:10.1103/PhysRevD.23.2495

[205] F. J. Hasert, W. Krenz, J. Von Krogh, D. Lanske, J. Morfin, K. Schultze, H. Weerts, G. H. B. Coremans, H. Mulkens and J. Sacton, *et al.* Phys. Lett. B **59**, 485-489 (1975) doi:10.1016/0370-2693(75)90352-4

[206] M. Pohl, M. Dewit, C. Vander Velde-Wilquet, P. Vilain, D. Haidt, C. Matteuzzi, B. Degrange, T. Francois, P. Van Dam and M. Jaffre, *et al.* Lett. Nuovo Cim. **24**, 540-544 (1979) doi:10.1007/BF02725470

[207] D. Allasia *et al.* [AMSTERDAM-BOLOGNA-PADUA-PISA-SACLAY-TURIN], Z. Phys. C **20**, 95-100 (1983) doi:10.1007/BF01573212

[208] B. Eberly *et al.* [MINERvA], Phys. Rev. D **92**, no.9, 092008 (2015) doi:10.1103/PhysRevD.92.092008 [arXiv:1406.6415 [hep-ex]].

[209] T. Le *et al.* [MINERvA], Phys. Lett. B **749**, 130-136 (2015) doi:10.1016/j.physletb.2015.07.039 [arXiv:1503.02107 [hep-ex]].

[210] A. A. Aguilar-Arevalo *et al.* [MiniBooNE], Phys. Rev. D **83**, 052009 (2011) doi:10.1103/PhysRevD.83.052009 [arXiv:1010.3264 [hep-ex]].

[211] K. S. Kuzmin and V. A. Naumov, Phys. Atom. Nucl. **72** (2009), 1501-1512 doi:10.1134/S1063778809090105

[212] M. R. Alam, M. S. Athar, S. Chauhan and S. K. Singh, J. Phys. G **42** (2015) no.5, 055107 doi:10.1088/0954-3899/42/5/055107 [arXiv:1409.2145 [hep-ph]].

[213] J. Gasser and H. Leutwyler, Nucl. Phys. B **250**, 465-516 (1985) doi:10.1016/0550-3213(85)90492-4

[214] S. Weinberg, Phys. Rev. Lett.**19**, 1264-1266 (1967) doi:10.1103/PhysRevLett.19.1264

[215] J. A. Oller, M. Verbeni and J. Prades, JHEP **09**, 079 (2006) doi:10.1088/1126-6708/2006/09/079 [arXiv:hep-ph/0608204 [hep-ph]].

[216] E. Oset and A. Ramos, Nucl. Phys. A **635** (1998), 99-120 doi:10.1016/S0375-9474(98)00170-5 [arXiv:nucl-th/9711022 [nucl-th]].

[217] T. Le *et al.* [MINERvA], Phys. Lett. B **749** (2015), 130-136 doi:10.1016/j.physletb.2015.07.039 [arXiv:1503.02107 [hep-ex]].

[218] C. L. McGivern *et al.* [MINERvA], Phys. Rev. D **94** (2016) no.5, 052005 doi:10.1103/PhysRevD.94.052005 [arXiv:1606.07127 [hep-ex]].

[219] P. Hamacher-Baumann, X. Lu and J. Martín-Albo, Phys. Rev. D **102** (2020) no.3, 033005 doi:10.1103/PhysRevD.102.033005 [arXiv:2005.05252 [physics.ins-det]].

[220] X. G. Lu, D. Coplowe, R. Shah, G. Barr, D. Wark and A. Weber, Phys. Rev. D **92** (2015) no.5, 051302 doi:10.1103/PhysRevD.92.051302 [arXiv:1507.00967 [hep-ex]].

[221] A. Faessler, T. Gutsche, B. R. Holstein, M. A. Ivanov, J. G. Korner and V. E. Lyubovitskij, Phys. Rev. D **78** (2008), 094005 doi:10.1103/PhysRevD.78.094005 [arXiv:0809.4159 [hep-ph]].